Modelling carbon isotopes to examine ocean circulation and the marine carbon cycle

Jennifer Ellen Dentith

Submitted in accordance with the requirements for the degree of
Doctor of Philosophy

The University of Leeds

School of Earth and Environment

November 2019

Declaration

The candidate confirms that the work submitted is her own, except where work which has formed part of jointly authored publications has been included. The contribution of the candidate and the other authors to this work has been explicitly indicated below. The candidate confirms that appropriate credit has been given within the thesis where reference has been made to the work of others.

The work in Chapter 2 of the thesis has appeared in publication as follows:

Dentith, J. E., Ivanovic, R. F., Gregoire, L. J., Tindall, J. C., and Smith, R. S. (2019). Ocean circulation drifts in multi-millennial climate simulations: the role of salinity corrections and climate feedbacks. *Climate Dynamics*, 52(3-4), 1761-1781.

The candidate was responsible for conducting the background research, designing and running the simulations, analysing and presenting the results, and writing the manuscript. The co-authors advised on all aspects of the work, including: analysing the model output; placing the work in a broader scientific context; and, structuring and developing the manuscript. R.S.S. also supplied the VFLUX modification and the HadCM3 model output.

Acknowledgements

There are a number of people who I would like to thank for their contributions to this work:

Firstly, my supervisors: Ruza Ivanovic, Lauren Gregoire, Julia Tindall, and Laura Robinson, for their invaluable guidance and for being so generous with their time. In particular, I am grateful to Ruza and Lauren for their endless enthusiasm, for always encouraging me to pursue my interests, and for supporting me to work out the whys; to Julia for the many hours spent helping me to derive new equations and debug coding errors; and to Laura for sharing her expertise and passion for palaeoceanography, which renewed my interest in the subject when my enthusiasm was waning.

My collaborators, Robin Smith and Paul Valdes, for supplying code used in Chapters 2, 3, and 4 of this thesis, and for sharing their expertise about the FAMOUS General Circulation Model and its ongoing development. I am also grateful to Alex Jahn for helpful email exchanges about implementing carbon isotopes into General Circulation Models.

My friends and fellow PhD students in the Palaeo@Leeds and Physical Climate Change research groups: Ilkka Matero, Lauren Marshall, Matt Rowlinson, and Niall Gandy, for helping me with Python coding and for providing moral support. Also, thanks to Niall for proof reading my thesis, and to Claire Harnett for always being on call for coffee and cake breaks.

Lastly, thank you to my family for their unwavering support, and to James Woodman for proof reading and helping me with LaTeX, but more importantly, for being there every step of the way.

This project was funded by the Natural Environment Research Council (NERC) SPHERES Doctoral Training Partnership (DTP), #NE/L002574/1. Numerical climate model simulations made use of the N8 High Performance Computing (HPC) Centre of Excellence (funded by the N8 consortium and the Engineering and Physical Sciences Research Council (EPSRC), #EP/K000225/1) and ARC2, part of the HPC facilities at the University of Leeds, UK.

Abstract

Understanding how the Meridional Overturning Circulation (MOC) might change in response to anthropogenic climate change has important repercussions for predictions of surface climate and the carbon cycle, but our ability to interpret future changes in the context of natural variability is limited by the short observational record (approximately 15 years). Key insights into the temporal variability of the MOC can be gained from geochemical tracers (e.g. carbon isotope ratios, δ^{13}C and Δ^{14}C) in geological archives. However, interpreting proxy records is complex because the isotopes respond to both physical and biogeochemical processes. Isotope-enabled models enable us to directly compare simulated and observed values, and investigate plausible mechanisms for the measured signals. Nonetheless, carbon isotopes are not routinely included in numerical climate models because of the computational cost of fully spinning up the deep ocean circulation and the marine carbon cycle (which requires run lengths between 5000 and 15,000 years).

This thesis uses carbon isotopes to investigate ocean circulation and the marine carbon cycle in FAMOUS, a fully coupled atmosphere-ocean General Circulation Model that offers a unique balance between speed and complexity. Using the most recent published generation of the model, this study demonstrates that small regional salinity drifts (that occur because of inaccuracies in the formulation of the hydrological budget) can lead to significant changes in the representation of the MOC in multi-millennial climate simulations, even under constant pre-industrial boundary conditions and when the global hydrological budget has been forcibly closed. An earlier generation of the model, which provides a more accurate and stable representation of the pre-industrial MOC, is therefore used for the implementation and validation of a new carbon isotope scheme (^{13}C and ^{14}C). The simulated δ^{13}C distributions capture the physical and biogeochemical behaviour of the model well, but are offset from observed values because of inaccuracies in the biological pump and the large-scale ocean circulation. The Δ^{14}C tracer is less sensitive to these biases and shows good agreement to observations, both spatially and temporally, which demonstrates the skill of the model in representing carbon uptake and transport. Radiocarbon ages are typically interpreted in terms of ventilation, but comparing the simulated ^{14}C ages to idealised water ages suggests that ^{14}C is only a good ventilation tracer in well-mixed regions, where the physical component of the solubility pump is a more dominant control on dissolved inorganic carbon distributions than the chemical component. The local balance between physical and biogeochemical processes should therefore be considered when interpreting $\Delta^{14}C$ in proxy records to avoid drawing erroneous conclusions about palaeocean circulation.

Overall, this study demonstrates the utility of including carbon isotopes in numerical climate models: it aids our interpretation of geochemical tracers in geological archives, and provides a sensitive and holistic tuning diagnostic for evaluating and improving model performance.

Contents

List of Figures

List of Tables

Abbreviations

Data sets

CARINA	CARbon dioxide IN the Atlantic Ocean
GEOSECS	GEochemical Ocean SEctions Study
GLODAP	GLobal Ocean Data Analysis Project
INDIGO	INDIen Gaz Ocean
PACIFICA	PACIFic ocean Interior CArbon
SAVE	South Atlantic Ventilation Experiment
TTO	Transient Tracers in the Ocean
WOCE	World Ocean Circulation Experiment

Numerical climate models

Bern3D+C	Bern 3-dimensional Earth system Model of Intermediate Complexity (with carbon cycle)
CCSM2/3/4	Community Climate System Model (version 2, 3 or 4)
CESM	Community Earth System Model
CISM	Community Ice Sheet Model
CLIMBER-2	CLIMate and BiosphERe group Earth system Model of Intermediate Complexity (version 2)
CSIRO Mk3L (-COAL)	Commonwealth Scientific and Industrial Research Organisation climate system model (version 3) - Low resolution (with the Carbon of the Ocean, Atmosphere and Land biogeochemical model)
CSM1	Climate System Model (version 1)
ECCO	Estimating the Circulation & Climate of the Ocean
EMIC	Earth system Model of Intermediate Complexity
FAMOUS	Fast Met Office/U.K. Universities Simulator
FM1	FAMOUS-MOSES1
FM2	FAMOUS-MOSES2.2
GCM	General Circulation Model

GENIE	Grid ENabled Integrated Earth system model
GFDL:	Geophysical Fluid Dynamics Laboratory
CM2Mc	Climate Model with MOM (version 2) - Low resolution
MOM	Modular Ocean Model
HadAM3	Hadley Centre Atmosphere Model (version 3)
HadCM3	Hadley Centre Coupled atmosphere-ocean General Circulation Model (version 3)
HadCM3L	Hadley Centre Coupled atmosphere-ocean General Circulation Model (version 3) - Low resolution
HadGEM3-GC3.1	Hadley Centre Global Environment Model (version 3) - Global Coupled (version 3.1)
HadOCC	Hadley Centre Ocean Carbon Cycle model
HadOM3	Hadley Centre Ocean Model (version 3)
Hamburg LSG OGCM	Hamburg Large Scale Geostrophic Ocean General Circulation Model
HAMOCC3.1	HAMburg Ocean Carbon Cycle model version (3.1)
LOVECLIM	LOch–Vecode-Ecbilt-CLio-agIsm Model
MIT2.8	Massachusetts Institute of Technology General Circulation Model (version 2.8)
MoBidiC	Modéle Bidimensionnel du Climat
MOSES	Met Office Surface Exchange Scheme
PISCES	Pelagic Interactions Scheme for Carbon and Ecosystem Studies
UM	Unified Model
UVic ESM	University of Victoria Earth system model

General

AABW	Antarctic Bottom Water
ACC	Antarctic Circumpolar Current
AMOC	Atlantic Meridional Overturning Circulation
B	Bermuda
BB	Bay of Biscay
CE	Common Era
CS	Caribbean Sea
DIC	dissolved inorganic carbon
DP	Drake Passage
EEA_UP	eastern equatorial Atlantic upwelling zone
EEP_UP	eastern equatorial Pacific upwelling zone
G	Grimsey

GB	German Bight
GeB	Georges Bank
GNAIW	Glacial North Atlantic Intermediate Water
GrB	Grand Banks
HS	Hudson Strait
ki-fract-only	Simulation that only includes kinetic fractionation effects
kyr	thousand years
L95	Simulation with biological fractionation calculated as per Laws et al. (1995)
L97	Simulation with biological fractionation calculated as per Laws et al. (1997)
LGM	Last Glacial Maximum
LS	Labrador Sea
MOC	Meridional Overturning Circulation
NADW	North Atlantic Deep Water
NE	Northeast Channel
NH_ASG	Northern Hemisphere Atlantic sub-tropical gyre
NH_DWF	Northern Hemisphere deep water formation region
no-asgx-fract	Simulation without fractionation during air-sea gas exchange
no-bio-fract	Simulation without biological fractionation effects
NS	Nova Scotia
OCMIP	Ocean Carbon-Cycle Model Intercomparison Project
OG	Oyster Ground
p.p.m.	parts per million
P-E	precipitation minus evaporation
$p\mathrm{CO}_2$	partial pressure of CO_2
POC	particulate organic carbon
psu	practical salinity units
QUICK	Quadratic Upstream Interpolation for Convective Kinematics
PUMA	Providing Unified Model Access
RAPID/MOCHA	Rapid Climate Change/ Meridional Overturning Circulation Heatflux Array
RMSE	root mean square error
S	Siglufjörður
S13	Schmittner et al. (2013)
SB	Sable Bank
SFLUX	Simulation with surface flux correction
SH_ASG	Southern Hemisphere Atlantic sub-tropical gyre

SH_DWF	Southern Hemisphere deep water formation region
SH_PSG	Southern Hemisphere Pacific sub-tropical gyre
std	Simulation with biological fractionation calculated as per Popp et al. (1989)
SO_UP	Southern Ocean upwelling zone
SSMI	Special Sensor Microwave Imager
SSS	sea surface salinity
SST	sea surface temperature
Sv	sverdrup
T	Tromsø
VFLUX	Simulation with volumetric flux correction
VSF	virtual salinity flux

Nomenclature

$\delta^{13}\mathrm{C}$	$^{13}\mathrm{C}/^{12}\mathrm{C}$ ratio of a sample relative to a standard (‰)
$^{13}D/^{12}D$	$^{13}\mathrm{C}/^{12}\mathrm{C}$ ratio of detritus
$^{13}C/^{12}C$	$^{13}\mathrm{C}/^{12}\mathrm{C}$ ratio of dissolved inorganic carbon
$\delta^{13}\mathrm{C}_{\mathrm{DIC}}$	$^{13}\mathrm{C}/^{12}\mathrm{C}$ ratio of dissolved inorganic carbon relative to a standard (‰)
$^{13}P/^{12}P$	$^{13}\mathrm{C}/^{12}\mathrm{C}$ ratio of phytoplankton
$\delta^{13}\mathrm{C}_{\mathrm{POC}}$	$^{13}\mathrm{C}/^{12}\mathrm{C}$ ratio of particulate organic carbon relative to a standard (‰)
$^{13}A/^{12}A$	$^{13}\mathrm{C}/^{12}\mathrm{C}$ ratio of the atmosphere
$\delta^{13}\mathrm{C}_{\mathrm{atm}}$	$^{13}\mathrm{C}/^{12}\mathrm{C}$ ratio of the atmosphere relative to a standard (‰)
$^{13}Z/^{12}Z$	$^{13}\mathrm{C}/^{12}\mathrm{C}$ ratio of zooplankton
$\delta^{14}\mathrm{C}$	$^{14}\mathrm{C}/^{12}\mathrm{C}$ ratio of a sample relative to a standard (‰)
$\Delta^{14}\mathrm{C}$	$^{14}\mathrm{C}/^{12}\mathrm{C}$ ratio of a sample relative to a standard, corrected for isotopic fractionation effects and normalised to the mean value for terrestrial wood (‰)
$^{14}C/^{12}C$	$^{14}\mathrm{C}/^{12}\mathrm{C}$ ratio of dissolved inorganic carbon
$^{14}A/^{12}A$	$^{14}\mathrm{C}/^{12}\mathrm{C}$ ratio of the atmosphere
$\Delta^{14}\mathrm{C}_{\mathrm{atm}}$	$^{14}\mathrm{C}/^{12}\mathrm{C}$ ratio of the atmosphere relative to a standard, corrected for isotopic fractionation effects and normalised to the mean value for terrestrial wood (‰)
F	Air-sea gas flux of $\mathrm{DI^{12}C}$ ($\mathrm{mol\,m^{-2}\,yr^{-1}}$)
$F_{13/12}$	Air–sea gas flux of $\mathrm{DI^{13}C}/\mathrm{DI^{12}C}$ ($\mathrm{mol\,m^{-2}\,yr^{-1}}$)
$F_{14/12}$	Air–sea gas flux of $\mathrm{DI^{14}C}/\mathrm{DI^{12}C}$ ($\mathrm{mol\,m^{-2}\,yr^{-1}}$)
CO_2^*	Aqueous $\mathrm{CO_2}$ concentration ($\mathrm{\mu mol\,l^{-1}}$)
β_{D}	Assimilation efficiency associated with zooplankton grazing on detritus (0.5)
β_{P}	Assimilation efficiency associated with zooplankton grazing on phytoplankton (0.7)
α_{k}	Constant kinetic fractionation factor (0.99919)
t	Current timestep
λ_D	Detrital remineralisation rate (0.02 to $0.1\,\mathrm{d^{-1}}$)
γ	Detrital sinking rate ($10\,\mathrm{m\,d^{-1}}$)

$\alpha_{\mathrm{POC}\leftarrow\mathrm{aq}}$	Equilibrium fractionation factor between aqueous CO_2 and particulate organic carbon
E	Evaporation rate ($\mathrm{kg\,m^{-2}\,s^{-1}}$)
a_{ice}	Fractional ice cover
ε	Isotopic enrichment factor
α_{CaCO3}	Isotopic fractionation during calcium carbonate production
α_{p}	Isotopic fractionation during photosynthesis
dz	Layer depth (cm)
KMT	Maximum depth of the ocean (m)
k	Model level
m_{P}	Phytoplankton mortality due to overpopulation (mmol-N $\mathrm{m^{-3}}$)
η_{P}	Phytoplankton respiration (mmol-N $\mathrm{m^{-3}}$)
μ	Phytoplankton specific growth rate ($\mathrm{d^{-1}}$)
R_{P}	Phytoplankton specific growth rate (mmol-N $\mathrm{m^{-3}}$)
PV	Piston velocity ($\mathrm{cm\,h^{-1}}$)
P	Precipitation rate ($\mathrm{kg\,m^{-2}\,s^{-1}}$)
β	Radioactive decay constant ($3.889\,15 \times 10^{-12}\,\mathrm{s^{-1}}$)
C_{sat}	Saturation concentration of atmospheric CO_2 ($\mathrm{mol\,m^{-3}}$)
Sc	Schmidt number for CO_2
C_{surf}	Surface aqueous CO_2 concentration ($\mathrm{mol\,m^{-3}}$)
$\alpha_{\mathrm{DIC}\leftarrow\mathrm{g}}$	Temperature-dependent fractionation between aqueous CO_2 and dissolved inorganic carbon
$\alpha_{\mathrm{aq}\leftarrow\mathrm{g}}$	Temperature-dependent fractionation during gas dissolution
a	Tuneable coefficient of air-sea gas exchange
u	Wind speed ($\mathrm{m\,s^{-1}}$)
G_{D}	Zooplankton grazing on detritus (mmol-N $\mathrm{m^{-3}}$)
G_{P}	Zooplankton grazing on phytoplankton (mmol-N $\mathrm{m^{-3}}$)
m_{Z}	Zooplankton mortality due to predation and natural causes (mmol-N $\mathrm{m^{-3}}$)

CHAPTER 1

Introduction

1.1 Scientific background

1.1.1 Ocean circulation and the marine carbon cycle

The oceans play a pivotal role in the climate system by storing and transporting large amounts of heat, freshwater, carbon and nutrients, and exchanging these properties with the atmosphere (Rhein et al., 2013), but the behaviour of large-scale ocean circulation in a warming world remains uncertain (Srokosz et al., 2012). Understanding the current state of ocean circulation, as well as the mechanisms for and consequences of past changes, can therefore provide valuable insights into how the system might change in the future, which has important repercussions for predictions of surface climate and the carbon cycle.

The Meridional Overturning Circulation (MOC) is the system of surface and bottom water currents that flows between all ocean basins, connecting the atmosphere with the deep sea reservoir on centennial-to-millennial timescales (Figure 1.1). The Atlantic MOC (AMOC) is characterised by warm, saline water flowing northwards in the shallow ocean, which is compensated at depth by a cold return flow (Kuhlbrodt et al., 2007; Srokosz et al., 2012; Ferreira et al., 2018). The shallow currents transport approximately 1.3 PW of heat from the tropics to the northern mid-latitudes (Srokosz et al., 2012), increasing temperatures in Western Europe by as much as 6 to 8 °C relative to similar latitudes in North America (Ferreira et al., 2018). In the modern Atlantic Ocean, there are two dominant water masses at depth: the southwards flowing North Atlantic Deep Water (NADW), which is cold (approximately 2 to 4 °C) and nutrient-depleted; and the northwards flowing Antarctic Bottom Water (AABW), which is nutrient-rich and approximately 2 °C colder than the overlying NADW cell (Talley, 2011). NADW can be further sub-divided into two components: an upper limb (<2000 m below sea level) that is formed by wintertime convection in the Labrador Sea; and a lower limb (>2000 m below sea level) that originates from open ocean convection in the Nordic Seas (Talley, 2011).

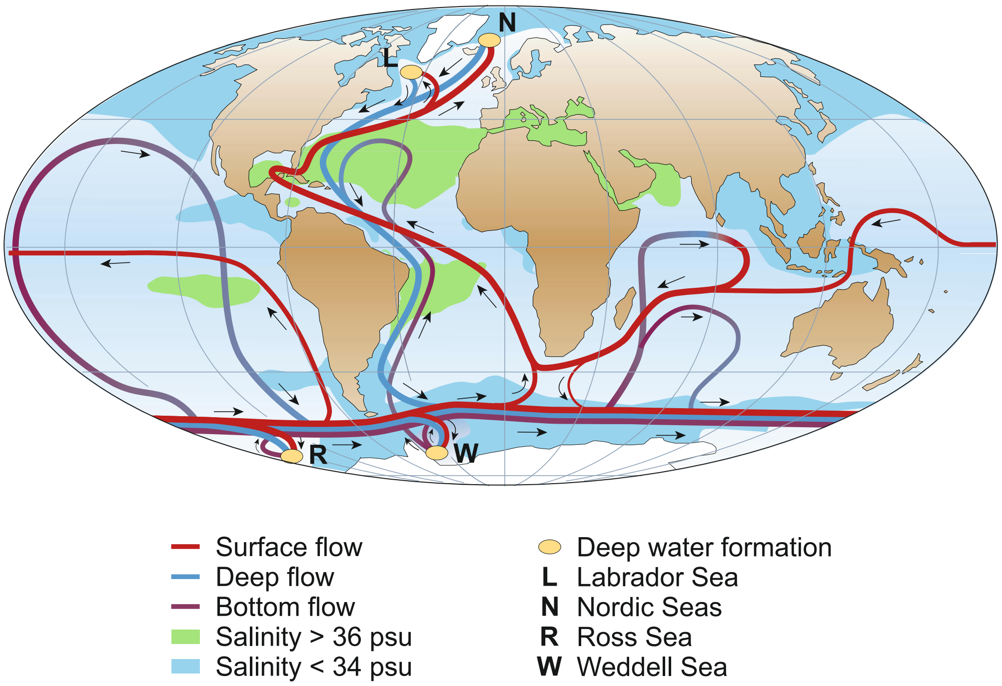

Figure 1.1: Schematic of present day large-scale ocean circulation adapted from Kuhlbrodt et al. (2007), following Rahmstorf (2002) and Broecker (1987). Near-surface currents (red) flow towards four high latitude deep water formation regions (yellow ovals) and recirculate at depth (blue and purple).

In recent years, it has been suggested that the AMOC is slowing down (Bryden et al., 2005b; Smeed et al., 2014; Rahmstorf et al., 2015; Jackson et al., 2016a), but the short observational record (approximately 15 years) limits our ability to interpret current trends in the context of natural variability. Numerical climate models predict further weakening of the AMOC (between 10 and 50 %) over the coming century in response to anthropogenic climate change (Gregory et al., 2005; Collins et al., 2013), however, uncertainties remain because most state-of-the-art models omit important processes such as Greenland ice melt (Swingedouw et al., 2006). Furthermore, the results could be sensitive to the forcing agent, with anthropogenic aerosols tending to strengthen the AMOC, thereby partially offsetting the weakening produced by greenhouse gases (Delworth and Dixon, 2006).

Key insights into the temporal variability of the AMOC can be gained from the geological record, which demonstrates that the AMOC has previously undergone large fluctuations on short (decadal) timescales (Alley, 2007). For example, proxy reconstructions and numerical climate models suggest that a significant weakening of the AMOC coincided with abrupt, centennial-to-millennial length cold reversals (Heinrich Stadial 1, 17,500 to 14,500 years ago, and the Younger Dryas, 12,700 to 11,500 years ago) during the last deglaciation (21,000 to 11,000 years ago; Broecker et al., 1989; Keigwin et al., 1991; McManus et al., 2004; Condron and Winsor, 2012; Valley et al., 2017; Ivanovic et al., 2018). Freshwater fluxes and iceberg calving are thought to have played a crucial role in triggering these events, but there is no overall consensus on the magnitude of AMOC reduction that is required to explain the marine and surface climate records. For example, some studies advocate a complete collapse of the AMOC during Heinrich Stadial 1 (McManus et al., 2004; Gherardi et al., 2005; Liu et al., 2009; Menviel et al., 2011), whilst others suggest that the AMOC was weaker but persistent (Bradtmiller et al., 2014; Roche et al., 2014; Ivanovic et al., 2018).

Changes in the strength and/or structure of the AMOC can also have significant repercussions for the carbon cycle, which might exacerbate or reduce the overall rates of anthropogenic climate change (Rhein et al., 2013), because the oceans contain around 50 times more carbon than the atmosphere (Sabine et al., 2004). The oceans are currently absorbing around 30 % of anthropogenic carbon emissions (Khatiwala et al., 2013), but proxy records suggest that they have acted as a CO_2 source under different circulation regimes in the past (e.g. Burke and Robinson, 2012).

Oceanic carbon exists in both dissolved and particulate, organic and inorganic states. The main constituent (98 %) is dissolved inorganic carbon (DIC), which is comprised of carbonic acid ($H_2CO_3^*$), bicarbonate ions (HCO_3^-), and carbonate ions (CO_3^{2-}). In the modern oceans, DIC concentrations at depth are around 15 % higher than in the surface ocean (Volk and Hoffert, 1985; Sarmiento and Gruber, 2006). The surface ocean is therefore within ±40 % of saturation with atmospheric CO_2, whilst the deep ocean is supersaturated with respect to the atmosphere (Takahashi et al., 1993). This has important repercussion for atmospheric CO_2 concentrations, because air-sea gas exchange is driven by the partial pressure (pCO$_2$) difference at the air-sea interface, which depends upon temperature, salinity, DIC, and alkalinity (a measure of the excess of bases over acids; Sarmiento and Gruber, 2006). If the carbon was evenly distributed throughout the depth of the ocean, pre-industrial atmospheric CO_2 concentrations would therefore have been approximately 50 % higher (Sarmiento and Gruber, 2006).

Three main mechanisms (or "pumps") maintain the vertical gradient: the *solubility pump*, the *soft-tissue pump* and the *carbonate pump*. In brief, the solubility pump is driven by the temperature dependence of the solubility of CO_2 in seawater, with increased solubility in cold (high latitude and deep ocean) waters relative to warm (low latitude and surface ocean) waters (Volk and Hoffert, 1985; Takahashi et al., 1993). The efficiency of the solubility pump in transferring carbon to depth therefore depends on the thermal stratification of the oceans and the saturation of the water, which is a function of surface residence times (Ito and Follows, 2003). In the shallow ocean, photosynthesis converts DIC into particulate organic carbon (POC), which is then transported into the abyssal ocean via active biotransport and gravitational settling, where it is remineralised and buried (Volk and Hoffert, 1985; Sarmiento and Gruber, 2006). This is referred to as the soft-tissue pump. Increasing the strength of the soft-tissue pump (i.e. higher rates of biological activity) reduces $p\mathrm{CO}_2$ in the surface ocean, which leads to increased oceanic carbon storage and a reduction in atmospheric CO_2 concentrations (Sarmiento and Toggweiler, 1984; Takahashi et al., 1993). Similarly, the formation of calcium carbonate (CaCO_3) shells in the upper ocean (mainly by coccolithophorids, foraminifera, and pteropods), and their subsequent dissolution or burial at depth is termed the carbonate pump (Volk and Hoffert, 1985; Sarmiento and Gruber, 2006). The carbonate pump has competing effects on $p\mathrm{CO}_2$, with the removal of calcium ions reducing alkalinity (increasing $p\mathrm{CO}_2$), and the removal of carbonate ions reducing DIC concentrations (decreasing $p\mathrm{CO}_2$). The effects on alkalinity are twice as strong as the effects on DIC, therefore the overall effect of a stronger carbonate pump is to increase $p\mathrm{CO}_2$ (Volk and Hoffert, 1985; Sarmiento and Gruber, 2006).

The marine carbon cycle operates across a wide range of timescales, ranging from days (in the POC pool) to millennia. Approximately 75 % of the global ocean volume interacts with the atmosphere via just 4 % of the surface ocean, with turnover times of around 1000 years (Sarmiento and Toggweiler, 1984). A further 16 % of the global ocean volume interacts with the atmosphere via 16 % of the surface ocean, with turnover times of approximately 10 to 100 years (Sarmiento and Toggweiler, 1984). Climate change and variability on timescales from seasons to millennia therefore reflects the close coupling between ocean circulation, the marine carbon cycle, and the atmosphere.

Understanding physical and biogeochemical changes in the oceans is hindered by a lack of long-term observations (Rhein et al., 2013). Ocean circulation can either be measured directly using instruments such as drifting buoys and Acoustic Doppler Current Profilers (Dohan et al., 2010), or inferred from density (temperature and salinity) distributions (Blanckenburg, 1999; Lynch-Stieglitz, 2001). Basin-scale sampling began in the late 1950s, with the initial focus being on near-surface temperature measurements (Rhein et al., 2013). In recent years, there has been a concerted effort to improve the quality and coverage of ocean observations, and increase the number of variables that are being recorded. For example, the RAPID/MOCHA array has been continuously monitoring the strength and structure of the AMOC at 26.5° N since 2004 (Rayner et al., 2011) and Argo profilers have been providing near-global, year-round temperature and salinity measurements in the uppermost 2000 m of the oceans since 2005 (Freeland and Cummins, 2005; Rhein et al., 2013). Nevertheless, sampling in the deep ocean (below 2000 m), which accounts for >50 % of the global ocean volume, remains sparse (Hood, 2009). Instrumental records of ocean biogeochemistry are shorter and less complete than the physical records, although major research programs have made significant contributions in recent decades. For example, the Global Ocean Data Analysis Project (GLODAP) measured the distribution of carbon-relevant oceanic tracers throughout the entire water column at approximately 12,000 hydrographic stations during the 1990s (Key et al., 2004), providing a snapshot of the anthropogenic CO_2 inventory. However, very few repeat measurements have been taken since the original surveys. To increase the utility of such data sets, a higher sampling frequency (2 to 3 years) is required (Hood, 2009). Thus, it is valuable to use proxy records to reconstruct past changes in ocean circulation and the marine carbon cycle, and to fill in the spatiotemporal gaps in modern data set.

1.1.2 Carbon isotopes

There are multiple proxies for ocean circulation, as outlined in Table 1.1. This study focusses on carbon isotopes because (1) we have a better understanding of the processes that control their distributions compared with other isotope systems (e.g. neodymium), (2) they respond to both physical and biogeochemical processes, so are able to provide a more holistic record of changes within the climate system, and (3) major oceanographic research programs provide a comprehensive database of measurements for the modern oceans that can be used as a benchmark against which to study isotopic ratios in geological archives.

Table 1.1: Examples of tracers of ocean circulation and the marine carbon cycle.

Proxy	Environmental variable(s)	Select references
δ^{13}C	Air-sea gas exchange, nutrients, productivity	Gruber and Keeling (2001); Oliver et al. (2010)
Δ^{14}C	Air-sea gas exchange, ventilation	Broecker et al. (1960, 2004); Sweeney et al. (2007)
δ^{18}O	Density, temperature, salinity	Lynch-Stieglitz et al. (1999a,b)
εNd	Water mass provenance	Rutberg et al. (2000); Piotrowski et al. (2004)
^{231}Pa/^{230}Th	Rate of overturning, scavenging	Marchal et al. (2000); Henry et al. (2016)
Grain size	Current intensity	Ledbetter and Johnson (1976); McCave et al. (1995)

There are three naturally occurring carbon isotopes: the stable isotopes ^{12}C (98.9 %) and ^{13}C (1.1 %), and the radioactive isotope ^{14}C (1.2×10^{-10} %), which is commonly referred to as radiocarbon (Key, 2001). The relative proportions of each isotope in a given oceanic pool (e.g. DIC or POC) are controlled by ocean circulation and mixing, and mass dependent fractionation during air-sea gas exchange (e.g. Zhang et al., 1995), photosynthesis (e.g. Sackett et al., 1965; Popp et al., 1989), and $CaCO_3$ formation (e.g. Emrich et al., 1970). Radiocarbon concentrations are also affected by atmospheric production rates (Damon et al., 1978) and radioactive decay (Godwin, 1962; Key, 2001). Carbon isotope data are typically reported in delta (δ) notation, which is the heavy (^{13}C or ^{14}C) to light (^{12}C) isotope ratio of a sample relative to a standard in per mil (‰) units (Stuiver and Polach, 1977). For ^{14}C, a correction is applied to account for the mass dependency of isotopic fractionation and to normalise all samples relative to the mean value of terrestrial wood in 1950 CE (Broecker and Walton, 1959; Key, 2001); this is denoted using $\Delta^{14}C$. The half-life of ^{14}C is 5730 years (Godwin, 1962; Key, 2001), which limits its use as a geochemical tracer to approximately the last 30,000 to 50,000 years (Reimer et al., 2009). In contrast, ^{13}C records extend over millions of years (e.g. Hodell and Venz-Curtis, 2006). Consequently, oceanic $\Delta^{14}C$ is usually used as a proxy for the length of time since a water parcel was last in contact with the atmosphere (which is typically referred to as the "ventilation" age; Broecker et al., 1960, 2004), whereas $\delta^{13}C$ is primarily used to track individual water masses (Sarnthein et al., 1994; Curry and Oppo, 2005), to study past changes in the carbon cycle (e.g. de la Fuente et al., 2015), and to investigate changes in ocean circulation on glacial-interglacial timescales (e.g. Spero and Lea, 2002; Campos et al., 2017). Both $\Delta^{14}C$ and $\delta^{13}C$ have also been used to constrain air-sea gas exchange rates (Gruber and Keeling, 2001; Marchitto and Broecker, 2006; Sweeney et al., 2007) and to estimate the uptake of anthropogenic carbon by the global oceans (e.g. Quay et al., 1992, 2003; Graven et al., 2012a).

Oceanographic surveys such as the Geochemical Ocean Sections Study (GEOSECS; Östlund et al., 1988) and the World Ocean Circulation Experiment (WOCE; Orsi and Whitworth III, 2005; Talley, 2007; Koltermann et al., 2011; Talley, 2013), and synthesis projects such as GLODAP (Key et al., 2004, 2015; Olsen et al., 2016), provide an indication of large-scale carbon isotope distributions in the modern oceans. However, as outlined in Section 1.1.1, these data sets provide a snapshot rather than a continuous record, because there have been few repeat measurements (typically taken decades apart; Hood, 2009). They are therefore insufficient for studying transient changes on sub-decadal timescales and for providing a baseline against which anthropogenic changes can be assessed in the context of natural variability.

Isotopic ratios in geological archives (including corals, sediment cores, and bivalves) can complement direct oceanographic measurements (e.g. Sherwood et al., 2008; Scourse et al., 2012) and can also be used to extend the record further back in time (e.g. Robinson et al., 2005; Burke and Robinson, 2012; Chen et al., 2015; Campos et al., 2017; de la Fuente et al., 2017). The carbonate skeletons of corals and bivalves record the isotopic ratio of the seawater from which they precipitated (Druffel, 1980; Adkins et al., 2002; Farmer et al., 2015). Similarly, the carbonate shells of planktonic and benthic foraminifera preserved in deep sea sediments record the isotopic ratios of the surface ocean and the water depth from which the core is taken, respectively (Shackleton, 1977). Corals can be independently dated using U-Th (e.g. Robinson et al., 2005) or excess ^{210}Pb (e.g. Sherwood et al., 2008), bivalves are dated using growth bands (e.g. Richardson, 2001), and foraminifera are typically dated using chronostratigraphy or ^{14}C (e.g. Bostock et al., 2004). One of the main shortcomings of using isotopic ratios in proxy records to reconstruct ocean circulation and the marine carbon cycle is that they are difficult to interpret because they reflect a complex interplay between physical processes and biogeochemical processes, both in the water column itself and during biomineralisation.

The simple interpretation of ^{14}C ages as ventilation ages in the ocean interior, for example, may be complicated by atmospheric production rates (on multi-millennial timescales; Damon et al., 1978), air-sea equilibration times (Campin et al., 1999), and the transport of ^{14}C from the surface ocean to depth via the sinking of particulate organic matter (Jain et al., 1997). Schmittner (2003) tuned glacial and present day simulations to have similar NADW formation rates and showed that increased sea ice cover in the Southern Ocean leads to older ^{14}C ages even for unchanged overturning. These results therefore demonstrate the potential inadequacy of interpreting palaeo Δ^{14}C distributions solely in terms of past deep water formation rates. Furthermore, primary productivity is sensitive to changes in the AMOC. For example, Schmittner (2005) simulated a 10 to 20 % decrease in global export production in response to a freshwater-induced AMOC collapse. However, the relative importance of how the change in overturning circulation versus the resultant change in the biological pump would be expressed in ^{14}C records has not explicitly been explored. Jain et al. (1997) estimated changes in the terrestrial biosphere and oceanic ^{14}C inventories using a six box biosphere model and an upwelling diffusion ocean model. Their results suggested that the transport of ^{14}C via the marine biological pump must be included for models to reproduce oceanic bomb ^{14}C inventories. However, beyond this study, the importance of the biological pump for oceanic ^{14}C distributions (and deep ocean ^{14}C concentrations, in particular) has largely been overlooked. Thus, one approach for filling in the spatiotemporal gaps in both modern and proxy data set, and for providing plausible physical and biogeochemical interpretations for observed signals, is to include carbon isotopes in numerical climate models.

1.1.3 Numerical climate models

Numerical climate models are valuable tools for studying Earth system processes over a range of spatiotemporal scales (Flato et al., 2013). State-of-the-art, high resolution, high complexity models that provide sophisticated representations of the main components of the Earth system (atmosphere, ocean, biosphere, sea ice, and biogeochemical cycles) are the most comprehensive tools for studying climate variability on seasonal-to-decadal timescales and for making projections of change in the near-future in response to anthropogenic forcing (e.g. Hazeleger et al., 2012; Flato et al., 2013; Hurrell et al., 2013; Menary et al., 2018). In the context of this thesis, the main limitation of such models is their computational expense. For example, HadGEM3-GC3.1 can be run at two resolutions: N216ORCA025 and N96ORCA1 (Menary et al., 2018). The N216ORCA025 configuration has a horizontal resolution of 60 km in the atmosphere and 0.25° in the ocean, and runs at approximately 1.4 model years per day on 4320 core processors. The N96ORCA1 configuration has a horizontal resolution of approximately 135 km in the atmosphere and 1° in the ocean (with refinement to 0.33° within 15° of the equator), and simulates approximately 2.3 years per day on 416 cores. It is therefore unfeasible to use a model of this complexity to study the components of the Earth system that evolve on millennial timescales, such as deep ocean circulation (England, 1995) and ocean biogeochemical cycles (Falkowski et al., 2000; Key et al., 2004).

At the opposite end of the scale, Earth system Models of Intermediate Complexity (EMICs) are capable of producing hundreds to thousands of years of output per day, making them ideal tools for studying slow (millennial) feedbacks within the climate system, such as those related to ice sheets, ocean biogeochemistry, and marine sediments (e.g. Ridgwell et al., 2007; Goosse et al., 2010; Huybrechts et al., 2011; Flato et al., 2013). This class of model operates at a much lower resolution than the state-of-the-art GCMs and typically represents many of the physical processes in an idealised manner or excludes them altogether (Flato et al., 2013). For example, the ocean component of GENIE has 36 × 36 equal-area grid cells in the horizontal and 8 vertical levels, and the atmosphere is represented by a simple 2-dimensional energy-moisture balance model (Ridgwell et al., 2007). GENIE is therefore capable of simulating more than 1000 years per hour on a desktop computer (Ridgwell et al., 2007). Other EMICs, such as the LOVECLIM Earth system model, offer increased resolution and complexity relative to GENIE, but are still capable of computing 600 years per day on a single Xeon processor (Goosse et al., 2010). Specifically, LOVECLIM has a horizontal resolution of $3^\circ \times 3^\circ$ and 20 vertical levels in the ocean, and 32×64 cells in its quasi-geostrophic atmosphere, which provides a simple representation of the relevant dynamic and thermodynamic processes required to study air-sea interactions over millennial timescales. In the context of this thesis, the main drawback of these models is that they do not provide sufficient complexity in their representation of ocean circulation, vertical mixing, and atmosphere-ocean interactions to study abrupt (decadal-to-centennial) changes in the climate system.

Low resolution GCMs have been developed to reduce the computational expense of running full complexity models, thereby bridging the gap between the state-of-the-art GCMs and the EMICs. These models still provide considerable detail in the complexity of the feedbacks between different Earth system processes, but have reduced spatial resolutions and longer timesteps relative to the parent models on which they are typically based. Examples include the CSIRO Mk3L climate system model (Phipps et al., 2011), and low-resolution versions of CCSM3 (Yeager et al., 2006) and the GFDL coupled climate model (Dixon et al., 2003). In the context of this thesis, a potential problem with these models is the possibility for drifts to occur because of the approximation, parameterisation, or complete omission of a number of physical processes (Covey et al., 2006; Gupta et al., 2012). Although the drifts may be small and therefore relatively unimportant over short (decadal-to-centennial) timescales, they could affect the stability of the ocean and the wider climatic regime over longer (millennial) timescales. Previous studies have examined the impact of drifts in climatic variables such as sea surface temperature and salinity, which are important for the stratification and circulation of the oceans, on timescales ranging from a few centuries (Bryan, 1998) to a few millennia (Covey et al., 2006). These studies have demonstrated that near-surface drifts are typically small, allowing sea surface temperatures, sea ice extent, and atmospheric circulation to remain realistic. The vast capacity of the deep ocean to store heat and salt has been highlighted as a potential problem in longer simulations, however. For example, the deep ocean cooled and became more saline, whilst the upper ocean freshened at a near-constant rate over the course of a relatively short (300 year) integration with CSM1 (Bryan, 1998). The author therefore postulated that the changes in the abyssal ocean would eventually manifest themselves in the shallow ocean, potentially causing the thermohaline circulation to collapse. Covey et al. (2006) agreed that models initialised for the present day could transition into a different equilibrium state because of drifts arising from systematic biases in the mean climate. Crucially, the importance of these slowly evolving drifts in multi-millennial (e.g. 10,000 year) simulations, which are required to fully spin-up deep ocean circulation and the marine carbon cycle, has not yet been explored.

Carbon isotopes are not routinely represented in numerical climate models because of the computational expense of fully spinning up deep ocean circulation and the marine carbon cycle (Bardin et al., 2014), however, there are multiple benefits to their inclusion. Reconstructing ocean circulation from proxy data is not simple and different tracers can produce conflicting interpretations. For example, there is no consensus on the strength and structure of the AMOC at the Last Glacial Maximum (LGM; approximately 21,000 years ago). Palaeonutrient tracers (e.g. δ^{13}C) have been used to infer a shoaling of the NADW cell and a concurrent reduction in the rate of overturning compared to modern (e.g. Duplessy et al., 1988; Marchitto et al., 2002; Curry and Oppo, 2005). Kinematic tracers (e.g. ^{231}Pa/^{230}Th) have also been interpreted as recording a 30 to 40 % slowdown in the glacial AMOC (McManus et al., 2004), although others have used them to demonstrate that glacial overturning occurred at a similar or higher rate than today (Yu et al., 1996). Numerical climate models also produce a range different of glacial AMOCs (shallower and weaker, no significant changes from modern, and stronger and deeper), despite having comparable circulation states in present day simulations (Otto-Bliesner et al., 2007). If these models were isotope-enabled, however, the simulated tracer distributions could be directly compared to the geological archives and plausible mechanisms for the observed signals could be investigated more coherently. Another advantage is that isotopic tracers can be used to diagnose model biases (Matsumoto et al., 2004; Jahn et al., 2015). Simulated temperatures and salinities are typically tuned to observations (Williamson et al., 2017), but carbon isotopes provide an independent constraint against which physical and biogeochemical model components can be evaluated.

A selection of existing ^{13}C and/or ^{14}C-enabled models is outlined in Table 1.2. In general, these are low resolution, intermediate complexity models. As previously discussed, such models are useful for studying slow (centennial-to-millennial) changes within the climate system, but they are not sophisticated enough to study abrupt (decadal-to-centennial) changes. Two of the models (PISCES and CESM) offer increased complexity and resolution, but they are computationally more expensive. For example, at

Table 1.2: Overview of existing carbon isotope-enabled models.

Model	**Resolution**	**Levels**	^{13}**C**	^{14}**C**	**Reference(s)**
GFDL (various)	[*]	12 to 28	✓	✓[1,2]	Toggweiler et al. (1989a,b); England and Rahmstorf (1999); Guilderson et al. (2000); Murnane and Sarmiento (2000); Galbraith et al. (2011)
Hamburg LSG OGCM & HAMOCC3.1	3.5° × 3.5°	11 to 22	✓	✓[1]	Hofmann et al. (1999, 2000); Butzin et al. (2005)
CLIMBER-2	2.5° × 3 basins	20	✓	✓[2]	Brovkin et al. (2002)
UVic ESM	1.8° × 3.6°	19	✓	✓[1]	Meissner et al. (2003); Schmittner et al. (2013); Koeve et al. (2015)
MoBidiC	5° × 3 basins	19	✓	✓[1]	Crucifix (2005)
PISCES	2° × 2°[†]	30	✓	✗	Tagliabue and Bopp (2008)
Bern3D+C	36 cells × 36 cells	32	✓	✓[2]	Tschumi et al. (2011)
CCSM	0.9° to 1.9° × 3.6°	25	✗	✓[1]	Graven et al. (2012a)
ECCO	1° × 1°	25	✗	✓[1]	Graven et al. (2012a); Koeve et al. (2015)
iLOVECLIM	3° × 3°	20	✓	✓[2]	Bouttes et al. (2015)
CESM	3° × 3°[‡]	60	✓	✓[1,3]	Jahn et al. (2015)
MIT2.8	2.8° × 2.8°	15	✗	✓[1]	Koeve et al. (2015)
CSIRO Mk3L-COAL	1.6° × 2.8°	21	✓	✓[1]	Buchanan et al. (2019)

[*] Ranges between 4.5° × 3.75° in the earliest configuration of the model (Toggweiler et al., 1989a,b) and a variable grid with finest resolution of 0.6° at the equator in the latest configuration (Galbraith et al., 2011).

[†] Mean resolution (enhanced meridional resolution at the equator).

[‡] 3° × 3° for model development, 1° × 1° for scientific application.

[1] ^{14}C is not transported through the carbon cycle. Changes in oceanic ^{14}C are calculated as a simple function of air-sea gas exchange, advection, and radioactive decay ("abiotic" implementation).

[2] ^{14}C is transported through the carbon cycle without accounting for isotopic fractionation during air-sea gas exchange, photosynthesis, and/or $CaCO_3$ formation.

[3] ^{14}C is cycled through the biological pump with isotopic fractionation effects ("biotic" implementation).

the time of their study, PISCES had only been spun-up for 3000 years and the $\delta^{13}C_{DIC}$ concentrations in the deep ocean were still drifting by 0.012 to 0.015 ‰ per century (Tagliabue and Bopp, 2008). Similarly, at the time of implementation, a 6010 year spin-up simulation with CESM took over 7 months to run (Jahn et al., 2015), although an accelerated spin-up technique for the ecosystem model has since been developed (Lindsay, 2017). Thus, carbon isotopes have yet to be implemented into a numerical climate model that is computationally efficient enough to fully spin-up the deep ocean circulation and marine carbon cycle without the need for offline or accelerated spin-up techniques, whilst still maintaining sufficient detail in the representation of ocean circulation, vertical mixing, and atmosphere-ocean interactions to study abrupt (decadal-to-centennial) changes in the climate system.

1.1.4 Limitations of previous studies and outstanding uncertainties

Although carbon isotopes have previously been implemented into a number of numerical climate models (Section 1.1.3), there remain several important gaps in our technical and scientific knowledge:

1. No modelling group has explored whether small drifts affect the stability of the climate system in multi-millennial (e.g. 10,000 year) simulations, which are required to fully spin-up deep ocean circulation and the marine carbon cycle.
2. Carbon isotopes have yet to be implemented into a numerical climate model that is computationally efficient enough to fully spin-up the deep ocean circulation and marine carbon cycle in a timely manner (without the need for offline or accelerated spin-up techniques), whilst still maintaining sufficient detail in the representation of the feedbacks between Earth system processes to study changes on decadal-to-centennial timescales.
3. No modelling group has used an independent age tracer to assess the importance of the biological pump for deep water ^{14}C concentrations, and thus the extent to which ^{14}C ages reflect the ventilation timescale of the oceans.

1.2 Research aim and overall approach

The aim of this thesis is to use carbon isotopes to investigate ocean circulation and the marine carbon cycle in a full complexity GCM. To address this aim, the first biotic implementation of oceanic carbon isotopes (^{13}C and ^{14}C) in the UK Met Office Unified Model version 4.5 (UM4.5; Valdes et al., 2017) is presented herein. In this implementation, the carbon isotopes are transported through the biological pump and are subject to isotopic fractionation during air-sea gas exchange and photosynthesis. Abiotic ^{14}C, which neither fractionates nor interacts with the marine carbon cycle, has previously been implemented into the ocean component of the UM4.5 (Palmer, 1998). However, this legacy code has not been maintained. At the outset of this study, numerical instabilities associated with the calculation of the abiotic tracer cause the model to crash. Hence, a minor update to this scheme is required. In this thesis, both the new and existing carbon isotope schemes are presented and evaluated, and the isotope-enabled model is used to address the outstanding uncertainties outlined in Section 1.1.4.

1.2.1 Choice of model

This study uses the Fast Met Office/U.K. Universities Simulator (FAMOUS; Jones et al., 2005; Smith et al., 2008a; Smith, 2012; Williams et al., 2013), which is a low resolution coupled atmosphere-ocean GCM based on HadCM3 (Gordon et al., 2000; Pope et al., 2000). Both are configurations of the UM4.5 (Valdes et al., 2017). The quasi-hydrostatic, primitive equation atmospheric model in FAMOUS (HadAM3) is 5° in latitude by 7.5° in longitude and has 11 vertical levels on a hybrid sigma-pressure coordinate system. The rigid lid ocean model (HadOM3) is based on the widely used Bryan and Cox code (Bryan, 1969; Cox, 1984). It is 2.5° in latitude by 3.75° in longitude, with 20 unevenly spaced vertical levels that provide a higher resolution in the surface ocean (10 m thickness) than at depth (600 m thickness). The atmosphere operates on a 1 h timestep whilst the ocean has a 12 h timestep. The two model components are coupled once per model day. The physical climate model is also coupled to both a land surface model (that can be run with either static or dynamic vegetation) and an ocean carbon cycle model: the Met Office Surface Exchange Scheme (MOSES; Cox et al., 1999; Essery et al., 2001, 2003) and the Hadley Centre Ocean Carbon Cycle model (HadOCC; Palmer, 1998; Palmer and Totterdell, 2001; Williams et al., 2013), respectively. More detailed descriptions of MOSES and HadOCC are provided in the model descriptions in Chapters 2 and 3, respectively.

FAMOUS has been systematically tuned for optimal performance and the resultant climatology is more realistic than expected for a model of this speed and resolution (Jones et al., 2005). Both the control climate and the climate sensitivity in FAMOUS are similar to that of HadCM3, although FAMOUS has a pronounced cold bias in the high latitude Northern Hemisphere (5 °C compared to HadCM3 and 7 °C compared to observations), which results in an overestimation of Arctic sea ice extent (Smith and Gregory, 2009). In terms of ocean circulation, FAMOUS simulates a single NADW formation region that extends from the Nordic Seas to the southern tip of Greenland, which is also the case in the parent model (Smith and Gregory, 2009). Previous studies with FAMOUS have simulated maximum AMOC stream function strengths between 12 Sv (Williams et al., 2014) and 17 Sv (Smith and Gregory, 2009), which compare well to other versions of the UM4.5 (10 to 19 Sv; Valdes et al., 2017) and to observations (14 to 19 Sv; Talley et al., 2003; Smeed et al., 2014). Where relevant, additional details regarding the representation of ocean circulation and the surface climate in FAMOUS are included in Chapters 2, 3, and 4.

With a full suite of oceanic tracers included, FAMOUS is capable of simulating approximately 400 years per wallclock day, which is more than 5 times the run speed of HadCM3 (Table 1.3). A 10,000 year simulation with FAMOUS therefore takes around 1 month to complete, compared to approximately 5 months with HadCM3, making it a more appropriate choice for model development work that involves fully spinning up the deep ocean circulation and the marine carbon cycle. Thus, FAMOUS is an excellent tool for validating a new oceanic carbon isotope scheme within the UM4.5 family. The new code will also be directly transferable into the higher resolution parent model (HadCM3) for future scientific application.

Table 1.3: Summary of the differences in resolution, timestep, and run time between FAMOUS and HadCM3.

		FAMOUS	**HadCM3**
Atmosphere	Horizontal resolution	5° × 7.5°	2.5° × 3.75°
	Vertical resolution (levels)	11	19
	Timestep (hours)	1	0.5
Ocean	Horizontal resolution	2.5° × 3.75°	1.25° × 1.25°
	Vertical resolution (levels)	20	20
	Timestep (hours)	12	1
Computational cost	Number of processors	16	32
	Run speed (years per day):		
	Standard oceanic tracers	600	70
	Full suite of oceanic tracers	400	60

FAMOUS currently has four options for the advection of oceanic tracers: upstream differencing, centred differencing, third-order Quadratic Upstream Interpolation for Convective Kinematics (QUICK; Leonard, 1979) and QUICK with flux limiter (Leonard, 1993), which is the default scheme. The advantage of QUICK advection schemes is that they do not incur the stability problems of centred differencing or the inaccuracies of numerical diffusion associated with upstream differencing (Leonard, 1979), whilst the addition of a flux limiter preserves positivity (Leonard, 1993). Indeed, Smith et al. (2008a) noted improvements in the distribution of DIC and the resultant air-sea gas exchange field when using the flux-limited third-order scheme relative to simpler formulations (e.g. centred differencing).

Overall, FAMOUS is a comparable tool to existing isotope-enabled models such as CSIRO Mk3L (Phipps et al., 2011; Buchanan et al., 2019) and the low resolution ("palaeo") configuration of CCSM3 (Yeager et al., 2006; Graven et al., 2012a). The combination of speed and complexity provided by this generation of the UM4.5 makes it ideal for running long (multi-millennial) climate simulations and large (hundred-member) ensembles. For example, FAMOUS was the first coupled atmosphere-ocean GCM to transiently simulate the whole of the last glacial cycle (120,000 years; Smith and Gregory, 2012). It was also used to perform more than 100 perturbed parameter simulations to investigate the climatic processes involved in developing and maintaining the equable climate of Early Eocene (Sagoo et al., 2013). FAMOUS has been coupled to the Glimmer thermomechanical ice sheet model to study the development of Northern Hemisphere ice sheets approximately 115,000 years ago (Gregory et al., 2012). More recently, Gregoire et al. (2016) investigated links between rapid North American ice sheet melt and abrupt climate change during the last deglaciation by forcing Glimmer-CISM with a transient FAMOUS simulation of the last 21,000 years. Similarly, Hopcroft et al. (2011) investigated the coupling between abrupt warming (Dansgaard-Oeschger) events and the global methane cycle during the last glacial period by driving a dynamic vegetation model with transient output from FAMOUS. In addition, FAMOUS has been used to investigate the climatic and oceanic impacts of freshwater input into different regions of the North Atlantic (Smith and Gregory, 2009) and it is the first coupled atmosphere-ocean GCM to exhibit AMOC bistability (“on” and “off” equilibrium states) in response to freshwater forcing (Hawkins et al., 2011). It has also been used to conduct idealised simulations examining the large-scale ocean circulation on a retrograde rotating Earth (Smith et al., 2008b) and on an aquaplanet (Smith et al., 2006). Thus, FAMOUS has proved to be an ideal model for addressing major Earth system research questions relating to the interplay between the atmosphere, ocean, ice sheets, and the carbon cycle on multi-millennial timescales.

1.3 Research questions

The overall aim of this thesis has been broken down into three main research questions, which are addressed by the work presented in Chapters 2, 3, and 4. Each chapter addresses at least one research question; some chapters address multiple research questions; and some research questions are addressed by multiple chapters (Table 1.4).

Table 1.4: Research questions and the chapters in which they are addressed.

Research question	**Thesis chapter(s)**
How important are small salinity drifts and biases in sea surface climate in multi-millennial simulations?	2
How accurately can modern carbon isotope distributions be simulated in a low resolution coupled atmosphere-ocean GCM?	3 and 4
To what extent can ^{14}C be interpreted as a ventilation tracer?	4

1.3.1 How important are small salinity drifts and biases in sea surface climate in multi-millennial simulations?

1.3.1.1 Scientific background

The oceans play a central role in the global hydrological cycle, with approximately 78 % of precipitation and 86 % of evaporation occurring over the sea surface (Schmitt, 1995). The balance between precipitation and evaporation is the main control on sea surface salinity distributions, with high salinity in regions where evaporation rates are greater than precipitation rates, and vice versa (Rhein et al., 2013). Ocean circulation, the melting and freezing of ice, and surface runoff also affect salinity more locally (Rhein et al., 2013). The salinity of seawater affects its density, therefore global salinity distributions are important for the vertical stratification and circulation of the oceans (Rhein et al., 2013).

Salinity drifts occur in numerical climate models because inaccuracies in the formulation of the hydrological budget can lead to the non-conservation of salt or freshwater (Bryan, 1998; Gupta et al., 2012). Like many models, the UM4.5 experiences salinity drifts because it operates without dynamical ice sheets to return freshwater stored as ice and snow back to the oceans via iceberg calving (Gordon et al., 2000; Pardaens et al., 2003). The importance of these drifts have previously been investigated to a limited extent in a 1400 year simulation with HadCM3 (Pardaens et al., 2003). The authors surmised that the long-term temperature and salinity drifts were not having a significant effect on the ocean circulation because the maximum overturning stream function of the NADW cell remained fairly constant throughout the simulation. However, in the North Atlantic, both the volume-weighted temperature and salinity were still linearly trending after 1400 years. Over longer timescales (e.g. 10,000 years), persistent drifts can affect the vertical stratification of the water column. They therefore have the potential to completely collapse the AMOC and invigorate a Pacific MOC (PMOC), even under constant pre-industrial boundary conditions (Bryan, 1998; Covey et al., 2006).

Deep water formation occurs where shallow sea water becomes denser than underlying water. This is typically where sea surface temperatures are cold (i.e. near the poles) and where sea surface salinity is relatively high (e.g. in regions of brine rejection from sea ice formation). In the modern oceans, four main deep water formation regions exist (Figure 1.1): the Nordic Seas and the Labrador Sea in the North Atlantic basin, and the Ross Sea and the Weddell Sea in the Southern Ocean (Kuhlbrodt et al., 2007). Thus, one of the most distinctive features of the modern MOC is the asymmetry between the Atlantic and Pacific basins (Figure 1.2).

The waters in the North Atlantic basin are the most saline in the global open oceans because of high regional evaporation rates (103 cm yr^{-1}), high through-flow rates associated with the North Atlantic Current, and the input of saline water from the South Atlantic

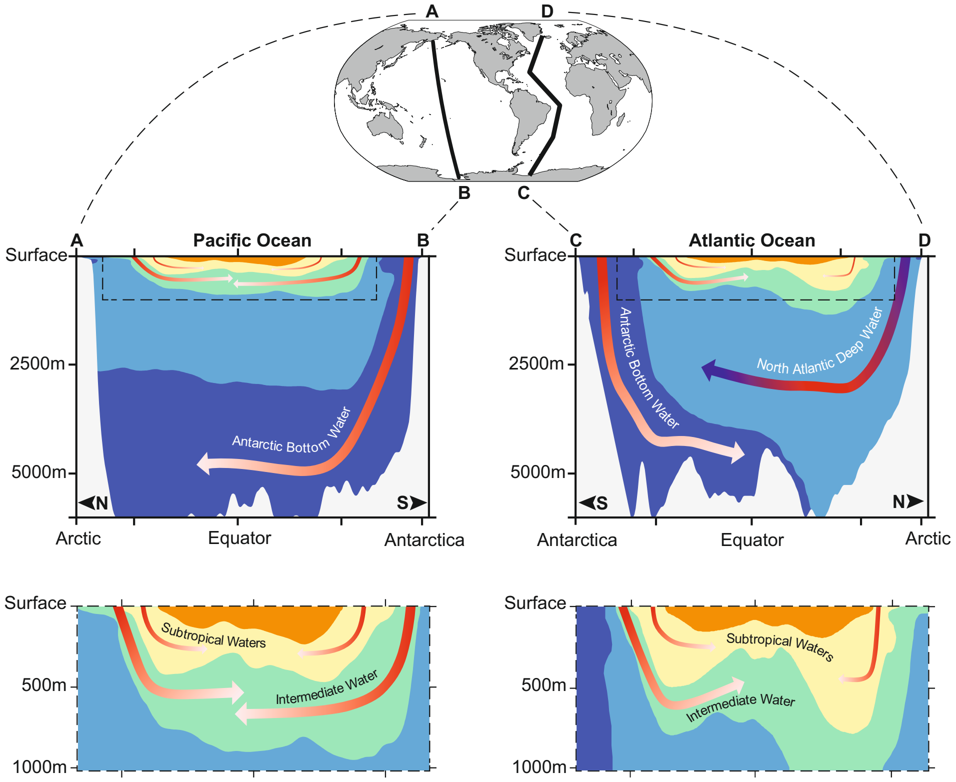

Figure 1.2: Schematic of present day stratification in the Atlantic (right) and Pacific (left) basins adapted from Rhein et al. (2013). Cold Antarctic Bottom Water (dark blue) sinks in the Southern Ocean and spreads northwards at depth. North Atlantic Deep Water (light blue) sinks to depth in the Labrador and Nordic Seas, spreading southwards above the Antarctic Bottom Water. In the upper ocean (detailed panels), cool intermediate waters (green) are formed in sub-polar regions, spreading equatorwards underneath warm sub-tropical waters (yellow), which are also transported towards the equator below warmer tropical waters (orange). Red arrows fading to white represent warming with time. Blue arrows transitioning to red then blue represent warming and subsequent cooling on decadal timescales.

(Warren, 1983). The average surface salinity in this region (34.9 psu) is comparable to that of the underlying water column (34.9 to 35.0 psu); therefore, the North Atlantic is primed for deep convection in the winter months (Warren, 1983). Thus, as outlined in Section 1.1.1, the modern AMOC consists of a near-surface, warm, northwards flow that is compensated at depth by colder, saline, southwards flowing waters (Kuhlbrodt et al., 2007; Srokosz et al., 2012; Ferreira et al., 2018).

In contrast, the North Pacific has low regional evaporation rates (55 cm yr^{-1}) and low flow rates through the surface layer, which promote much fresher surface waters (Warren, 1983). The average sea surface salinity in this region is 32.8 psu compared to 34.6 psu in the underlying waters (Zweng et al., 2013). Consequently, deep water does not form in the modern day Pacific Ocean because the relatively low density of the surface water stabilises the water column and limits downward convection (Warren, 1983; Menviel et al., 2012). Pacific overturning is therefore dominated by weak, southwards flowing

North Pacific Intermediate Water and northwards flowing AABW (Talley et al., 2003).

It has been speculated that the North Pacific may have been a site of deep water formation in the geological past. For example, Rae et al. (2014) suggested that a pronounced excursion in ^{14}C and boron isotope data in a northeast Pacific sediment core during Heinrich Stadial 1 was driven by the onset of deep convection in this region as a result of increased sea surface salinity. Similarly, using evidence from surface proxy data, marine ^{14}C ventilation ages and GCM simulations, Okazaki et al. (2010) identified major reorganisations in ocean circulation during the early stages of the last deglaciation, with relatively weak AMOC and North Pacific Deep Water extending to depths of 3 km. Modelling studies have also simulated a deep sinking branch of the PMOC in response to changing freshwater fluxes in the major ocean basins (Saenko et al., 2004; Chikamoto et al., 2012; Menviel et al., 2012), although this is not always the case (Ivanovic et al., 2017). It is therefore important to address whether small salinity drifts, which arise because of imbalances in the hydrological cycle, might act as gentle "hosing experiments" – modelling studies in which freshwater is systematically added to the ocean (e.g. Smith and Gregory, 2009) – thereby causing a reorganisation of the large-scale density driven circulation in multi-millennial climate simulations (i.e. producing erroneous deep water formation in the North Pacific under pre-industrial boundary conditions).

1.3.1.2 Research approach

To explore the influence of small but persistent salinity drifts and biases in sea surface climate in multi-millennial simulations with the FAMOUS GCM, the latest generation of the model (FAMOUS-MOSES2.2) is spun-up for 10,000 years under constant pre-industrial boundary conditions. The global volume-weighted drift in this simulation is $0.25\,\mathrm{psu\,kyr^{-1}}$, which results in a complete collapse of the AMOC and invigoration of a PMOC. In an attempt to close the global hydrological budget and prevent a reorganisation of the MOC from occurring, two different schemes for neutralising the unforced salinity drift are tested: surface flux correction (SFLUX) and volumetric flux correction (VFLUX). An earlier generation of the model (FAMOUS-MOSES1), which has a slightly different surface climate and therefore a different hydrological balance over the oceans, is also spun-up for 10,000 years to examine whether it is susceptible to the same changes in ocean circulation.

1.3.2 How accurately can modern carbon isotope distributions be simulated in a low resolution coupled atmosphere-ocean GCM?

1.3.2.1 Scientific background

Oceanic carbon isotope distributions are controlled by the interplay between physical and biogeochemical effects, with mass dependent fractionation occurring during air-sea gas exchange (e.g. Zhang et al., 1995), photosynthesis (e.g. Sackett et al., 1965), and $CaCO_3$

formation (e.g. Emrich et al., 1970). Briefly, marine phytoplankton preferentially take up ^{12}C rather than ^{13}C and ^{14}C during primary production, leaving the DIC pool relatively enriched in the heavier isotopes (high δ_{DIC} values). When the POC is remineralised at depth (without further fractionation), it releases a relatively low isotopic signature back into the DIC pool, thereby reducing the δ_{DIC} values. The same principles apply to $CaCO_3$ formation (which increases δ_{DIC} values in the shallow ocean) and dissolution (which decreases δ_{DIC} values in the deep ocean). Similarly, areas of net CO_2 invasion have relatively low δ_{DIC} values due to the preferential uptake of $^{12}CO_2$, whilst areas of net outgassing have relatively high δ_{DIC} values as $^{12}CO_2$ is preferentially released back into the atmosphere.

Empirical relationships for the different biogeochemical fractionation effects have been established from laboratory experiments, modern oceans and lakes, and the sedimentary record, but to-date there remains no single accepted parameterisation for the fractionation of carbon isotopes during photosynthetic CO_2 fixation. Early studies suggested a simple temperature dependence for fractionation during photosynthesis (Sackett et al., 1965), although the proposed ‰ per °C changes were not large enough to fully explain the observed δ^{13}C range (Wong and Sackett, 1978). In the late 1980s and early 1990s, numerous authors advocated the importance of aqueous CO_2 concentrations in the ambient environment (Popp et al., 1989; Rau et al., 1989; Jasper and Hayes, 1990; Hollander and McKenzie, 1991; Freeman and Hayes, 1992), however, these studies assumed that CO_2 enters the phytoplankton by passive diffusion and neglected physiological effects. Later studies therefore accounted for the effects of phytoplankton growth rate (Laws et al., 1995, 1997) and active bicarbonate transport (Burkhardt et al., 1999; Keller and Morel, 1999).

As there is no consensus on the most representative parameterisation, previous ^{13}C implementation studies have used a number of different equations, with the choice of scheme largely reflecting the complexity of the simulated biogeochemical and ecosystem processes. For example, simple Nitrogen-Phytoplankton-Zooplankton-Detritus models typically calculate photosynthetic fractionation as a function of the aqueous CO_2 concentration (e.g. LOVECLIM; Bouttes et al., 2015), whereas models that include multiple functional groups account for phytoplankton type-specific cell parameters (e.g. CESM; Jahn et al., 2015). In contrast, existing ^{14}C implementations have tended to follow the Ocean Carbon Cycle Model Intercomparison Project version 2 (OCMIP-2) protocol, which outlines the equations required to add abiotic ^{14}C to a model, and provides the initial conditions, run lengths, and standard input files for a suite of simulations (Orr et al., 2000).

New isotope schemes must be validated before they can confidently be used for scientific application. Two anthropogenic disturbances have perturbed the carbon isotope system since the 1850s (the Suess effect and the ^{14}C bomb pulse), thereby providing a natural experiment for evaluating the performance of isotope-enabled models. The Suess effect refers to the dilution of ^{13}C and ^{14}C in any carbon pool due to fossil fuel burning (Suess, 1955; Keeling, 1979). Fossil fuels formed millions of years ago from organic matter. They are therefore ^{13}C-depleted due to isotopic fractionation during photosynthesis and ^{14}C-free because of radioactive decay. In contrast, thermonuclear weapons testing during the 1950s and 1960s approximately doubled the amount of ^{14}C in the atmosphere (Mahadevan, 2001). Hence, the standard (OCMIP-2) approach for verifying the accuracy of new carbon isotope schemes is to prescribe these historical changes (following a spin-up simulation with fixed atmospheric δ^{13}C and Δ^{14}C) and to directly compare the simulated values to modern observations.

Model-data discrepancies in previous studies have been attributed to physical biases such as sluggish ocean circulation (Jahn et al., 2015) and restricted horizontal mixing (Buchanan et al., 2019), and biogeochemical biases such as high carbon export (Buchanan et al., 2019). Thus, this is a two-fold research question:

1. How well do the simulated carbon isotopes distributions represent processes such as ocean circulation, air-sea gas exchange, the marine carbon cycle in the model?
2. How well do the simulated isotope distributions compare to observations, both spatially and temporally?

1.3.2.2 Research approach

To explore the how accurately modern carbon isotope distributions can be simulated in a low resolution coupled atmosphere-ocean GCM, new code for stable ^{13}C (Chapter 3) and radioactive ^{14}C (Chapter 4) is developed and implemented into the ocean component of the FAMOUS GCM. The model is spun-up for 10,000 years under pre-industrial boundary conditions to allow the deep ocean circulation and the marine carbon cycle to reach steady state. The model is then run for a further 235 years with transient atmospheric CO_2, bomb ^{14}C and the ^{13}C-^{14}C Suess effect to produce output that is directly comparable to observations. In Chapter 3, the importance of the choice of biological fractionation parameterisation to the simulated stable carbon isotope distributions is tested via the inclusion of three different equations from the literature. The effects of fractionation during air-sea gas exchange and primary productivity on the simulated stable isotope distributions are also tested via an on-off sensitivity experiment. In Chapter 4, the model's ability to reproduce natural (pre-bomb) and anthropogenic (bomb) ^{14}C distributions is examined by comparing the simulated values to hydrographic observations, and the expression of the transient bomb signal is compared to natural archives from different water depths across the North Atlantic Ocean. Overall, this study considers how physical and biogeochemical processes affect carbon isotope distributions and how these new tracers can be used as a tuning target in future model development work.

1.3.3 To what extent can ^{14}C be interpreted as a ventilation tracer?

1.3.3.1 Scientific background

Oceanic ^{14}C distributions primarily reflect the pattern and intensity of ocean circulation, but they are also sensitive to atmospheric production rates (Damon et al., 1978), air-sea gas exchange (Campin et al., 1999), and biological activity (Jain et al., 1997). Campin et al. (1999) implemented two passive tracers ($\Delta^{14}C$ and water age) in a 3° × 3° ocean-only GCM to examine the relative contributions of circulation and air-sea gas exchange to large-scale ^{14}C distributions, and thus the extent to which ^{14}C can be interpreted as a ventilation tracer. The authors identified a decoupling between the ^{14}C age and the actual age of the oceans under both pre-industrial and glacial boundary conditions. Specifically, the newly formed NADW and AABW in the model had similar absolute ages, indicating similar rates of renewal, but the ^{14}C age of the AABW was systematically older than its water age and the ^{14}C age of the NADW. There were two main reasons for these differences: the timescale for isotopic $^{14}CO_2$ equilibration between the ocean and the atmosphere (5 to 10 years; Toggweiler et al., 1989a; Lynch-Stieglitz, 2003; Sarmiento and Gruber, 2006) compared to surface water residence times (e.g. 2 years for Antarctic Surface Waters; Lynch-Stieglitz et al., 1995), and the presence of compacted sea ice in the Ross and Weddell Seas, which prevented air-sea gas exchange from occurring. In the Southern Ocean, strong westerlies at approximately 60° S promoted intense northward Ekman transport and upwelling of old (^{14}C-depleted) Circumpolar Deep Water. In the deep water formation regions southwards of this divergence zone, the surface waters had relatively low ^{14}C concentrations because (1) they had short residence times with respect to the rates of $^{14}CO_2$ air-sea gas exchange and (2) they were isolated from the well ventilated (^{14}C-rich) sub-tropical surface waters. In contrast, newly formed NADW was closer to equilibrium with the atmosphere because it had been transported northwards from the sub-tropics via surface currents before sinking in the high latitudes (Figure 1.1). The differences between the ^{14}C ages and the water ages increased significantly under glacial boundary conditions. The globally averaged ^{14}C ages were roughly the same in both simulations, but the mean water age in the glacial simulation was 150 years younger than in the pre-industrial simulation, suggesting faster rates of overturning at the LGM than at present. Thus, the authors concluded that interpreting ^{14}C ages in terms of ventilation alone may lead to erroneous conclusions regarding ocean circulation and how it has changed in the past.

Koeve et al. (2015) also examined how slow and incomplete $^{14}CO_2$ air-sea gas exchange affects $\Delta^{14}C$ distributions in the interior ocean in the context of model evaluation. The authors defined the *preformed age* as the ^{14}C age of water relating to ^{14}C equilibration between the ocean and the atmosphere, which they deduced is very sensitive to air-sea gas exchange rates and is moderately sensitive to sea ice cover. The *bulk age* of the water was defined as the age due to circulation plus the preformed age. The relative contribution of the preformed age to the bulk age was found to vary between the three models used in the study, and also regionally within each model, with an average contribution of 50 %. The choice of gas exchange constant (within parametric uncertainty) was found to have such a strong influence on the ^{14}C ages that the authors concluded that the preformed age is a better metric than the bulk age for evaluating and tuning the circulation in ocean models.

Following Toggweiler et al. (1989a), biological effects are typically neglected in ^{14}C implementations. Only one previous study has accounted for isotopic fractionation during air-sea gas exchange and primary production, and a further four models transport ^{14}C through the carbon cycle without fractionation effects (Table 1.2). Thus, whilst potential problems have been identified with using ^{14}C as a ventilation tracer due to the influence of air-sea gas exchange, the decoupling between the ^{14}C age and the actual age of water due to biological effects has not yet been investigated.

1.3.3.2 Research approach

Two approaches are taken to examine the importance of the biological pump for ^{14}C concentrations in the deep ocean, and thus the extent to which ^{14}C can be interpreted as a ventilation tracer. Firstly, the new biotic ^{14}C scheme is compared to the existing abiotic ^{14}C scheme to determine the importance of the biological pump for deep water ^{14}C concentrations. The abiotic tracer is a simple function of air-sea gas exchange (without isotopic fractionation), advection, and radioactive decay. The new biotic tracer is additionally cycled through the marine carbon cycle and is affected by fractionation during air-sea gas exchange and photosynthesis. Secondly, the biotic ^{14}C concentrations are converted to ages as per Stuiver and Polach (1977). A simple water age tracer is also added to the model, which counts the length of time since the water in a single grid cell was last in contact with the atmosphere. Unlike the ^{14}C, the water age tracer is not affected by air-sea gas exchange or biology; it is only a function of the large-scale ocean circulation. The differences between both the abiotic-biotic and the ^{14}C age-water age tracer pairs are examined across a range of locations (e.g. deep water formation regions, sub-tropical gyres, and upwelling zones) and water depths to identify whether interpreting ^{14}C as a ventilation tracer is more or less valid in certain oceanographic and biogeochemical settings.

1.4 Publications and collaborations

All of the written work presented in this thesis is my own. The following three results chapters are structured as individual research articles, beginning with a brief literature review and a self-contained methodology. These have either already been published (Chapter 2) or are ready to submit to peer-reviewed journals (Chapters 3 and 4).

The work in Chapter 2 of this thesis has appeared in publication as follows:
Dentith, J. E., Ivanovic, R. F., Gregoire, L. J., Tindall, J. C., and Smith, R. S. (2019). Ocean circulation drifts in multi-millennial climate simulations: the role of salinity corrections and climate feedbacks. *Climate Dynamics*, 52(3-4), 1761-1781.
I was responsible for conducting the background research, designing and running the simulations, analysing and presenting the results, and writing the manuscript. My co-authors advised on all aspects of the work, including: analysing the model output; placing the work in a broader scientific context; and, structuring and developing the manuscript. R.S.S. also supplied the VFLUX modification and the HadCM3 model output. In addition, we acknowledge the contribution of Paul Valdes (University of Bristol), who supplied the SFLUX modification.

The work in Chapter 3 of this thesis has been prepared for submission to *Geoscientific Model Development*. My co-authors are my supervisors: R. F. Ivanovic, L. J. Gregoire, J. C. Tindall, and L. F. Robinson. I was responsible for conducting the background research, writing and implementing the code, designing and running the simulations, analysing the results, and preparing the manuscript. J.C.T. and L.J.G. provided technical support for deriving, discretising, and implementing the new isotopic equations. All of my co-authors contributed scientific expertise to help analyse the results and suggested ways to improve the manuscript. We acknowledge the contribution of Alexandra Jahn (University of Colorado), with whom we had helpful discussions about implementing carbon isotopes in GCMs. We also acknowledge the contribution of Robin Smith (University of Reading), who supplied the code to cap the oceanic CO_2 flux.

The work in Chapter 4 of this thesis has been prepared for submission to *Biogeosciences*. My co-authors are my supervisors: R. F. Ivanovic, L. J. Gregoire, J. C. Tindall, and L. F. Robinson; and external collaborator P. J. Valdes. I was responsible for conducting the background research, validating the existing abiotic ^{14}C scheme, writing and implementing the biotic ^{14}C code, running the simulations, analysing the results, and preparing the manuscript. J.C.T., L.J.G. and R.F.I. provided technical support for the isotope implementation work. R.F.I., L.J.G., L.F.R. and J.C.T. contributed scientific expertise to help analyse the results and suggested ways to improve the manuscript. P.J.V. wrote and implemented the idealised water age code. Again, we acknowledge Robin Smith for supplying the code to cap the oceanic CO_2 flux and Alexandra Jahn for helpful discussions about implementing carbon isotopes in GCMs.

CHAPTER 2

Ocean circulation drifts in multi-millennial climate simulations: the role of salinity corrections and climate feedbacks

Abstract

Low-resolution, complex General Circulation Models (GCMs) are valuable tools for studying the Earth system on multi-millennial timescales. However, slowly evolving salinity drifts can cause large shifts in climatic and oceanic regimes over thousands of years. We test two different schemes for neutralising unforced salinity drifts in the FAMOUS GCM: surface flux correction and volumetric flux correction. Although both methods successfully maintain a steady global mean salinity, local drifts and subsequent feedbacks promote cooling (≈4 °C over 6000 years) and freshening (≈2 psu over 6000 years) in the North Atlantic Ocean, and gradual warming (≈0.2 °C per millennium) and salinification (≈0.15 psu per millennium) in the North Pacific Ocean. Changes in the surface density in these regions affect the Meridional Overturning Circulation (MOC), such that, after several millennia, the Atlantic MOC (AMOC) is in a collapsed state, and there is a strong, deep Pacific MOC (PMOC). Furthermore, the AMOC exhibits a period of metastability, which is only identifiable with run lengths in excess of 1500 years. We also compare simulations with two different land surface schemes, demonstrating that small biases in the surface climate may cause regional salinity drifts and significant shifts in the MOC (weakening of the AMOC and the initiation then invigoration of PMOC), even when the global hydrological cycle has been forcibly closed. Although there is no specific precursor to the simulated AMOC collapse, the northwest North Pacific and northeast North Atlantic are important areas that should be closely monitored for trends arising from such biases.

2.1 Introduction

State-of-the-art, high resolution, high complexity General Circulation Models (GCMs) provide a sophisticated representation of the main components of the Earth system: the ocean, atmosphere, biosphere, and sea ice. As such, they are valuable tools for studying climate change on decadal to centennial timescales (e.g. Collins et al., 2011; Gent et al., 2011; Martin et al., 2011; Hazeleger et al., 2012; Flato et al., 2013; Hurrell et al., 2013; Hardiman et al., 2017). However, these models are extremely computationally expensive. They are therefore impractical for running the long simulations required to spin-up the components of the Earth system that evolve on millennial timescales, such as deep ocean circulation (England, 1995) and ocean biogeochemical cycles (Falkowski et al., 2000; Key et al., 2004). GCMs with significantly faster operational speeds, as a consequence of reduced spatial resolution and/or longer timesteps, are therefore important tools for Earth system modellers who run long integrations (e.g. to study palaeoclimate, the carbon cycle and ice sheet evolution). These models allow multi-millennial climate simulations to be conducted whilst still allowing considerable detail in the complexity of the feedbacks between different Earth system processes. Examples include FAMOUS (Jones et al., 2005; Smith et al., 2008a; Williams et al., 2013), the CSIRO Mk3L climate system model (Phipps et al., 2011), and low-resolution versions of CCSM3 (Yeager et al., 2006) and the GFDL coupled climate model (Dixon et al., 2003).

Models are neither complete nor perfect representations of reality because a number of physical processes are approximated, parameterised, or omitted altogether (Gupta et al., 2012). Drift is therefore an inherent problem in coupled GCMs that can occur even when no external forcing is applied (Covey et al., 2006; Gupta et al., 2012). Unforced drift can be characterised on two timescales: “fast adjustments” occur on annual to decadal timescales and typically relate to surface imbalances in heat, freshwater and (sometimes) biogeochemical fluxes; “slow adjustments” occur on centennial to millennial timescales and involve the response of deep ocean circulation and ocean biogeochemical cycles to the surface imbalances (Gupta et al., 2012). This study focuses on multi-millennial salinity drifts that primarily arise because of inaccuracies in the formulation of the hydrological budget, which lead to the non-conservation of salt or freshwater (Bryan, 1998; Gupta et al., 2012). Many GCMs experience salinity drifts because they operate without dynamical ice sheets to return freshwater stored as ice back to the oceans via iceberg calving (e.g. Gordon et al., 2000; Pardaens et al., 2003; Johns et al., 2006; Gupta et al., 2012). Some older GCMs also operate without a river routing system, which inhibits continental precipitation from being returned to the oceans (e.g. Bryan, 1998). The resultant drifts may be small when considered over a few decades or even centuries. However, over multiple millennia they can lead to large shifts in climatic and oceanic regimes (Bryan, 1998; Pardaens et al., 2003; Covey et al., 2006).

Accurate simulation of the hydrological budget at both the global and regional scales is an influential factor in determining the strength and structure of Meridional Overturning Circulation (MOC) and the location of deep water formation regions. In turn, these large-scale features are particularly important when studying ocean biogeochemical processes, the oceanic carbon cycle, and ocean heat transport. Surface freshwater fluxes reflect the balance of sea ice formation and melt, precipitation minus evaporation (P-E), and continental runoff. Together with ocean advection, they control sea surface salinity distributions. Salinity gradients influence ocean stratification and vertical mixing; therefore, any drifts in surface salinity could eventually propagate in to the deep ocean, affecting density driven circulation and poleward heat transport (Pardaens et al., 2003; Jin et al., 2017). Even small imbalances in the surface climate can result in large MOC shifts if maintained for multiple millennia (Pardaens et al., 2003), with the potential for both a total collapse of the Atlantic MOC (AMOC) and invigoration of the Pacific MOC (PMOC) under constant pre-industrial boundary conditions.

One approach for alleviating hydrological drift and maintaining a stable climate in long model integrations is to apply an artificial flux adjustment as a constant, predetermined freshwater flux. However, this approach is inherently non-physical (Gupta et al., 2012). Very simple representations of physical processes not otherwise included in the model, whose implementation are explicitly aimed at reducing drift, are therefore preferable. For example, HadCM3 applies a spatially uniform freshwater flux, equivalent to $0.1\,\mathrm{mm\,d^{-1}}$, to account for rainfall that runs into internal drainage basins (Gordon et al., 2000). Additionally, all versions of the UK Met Office Unified Model (UM) up to version 9 include a calibrated iceberg melt freshwater field to balance water losses associated with the accumulation of snow on the Antarctic and Greenland ice sheets (e.g. Gordon et al., 2000; Smith et al., 2008a; Collins et al., 2011; Martin et al., 2011), which is discussed further in Section 2.2.1.2.

In this study, we aim to minimise the effects of non-closure of the hydrological budget and get the best representation of both the strength and structure of large-scale pre-industrial ocean circulation in long (10,000 year) integrations with the FAMOUS GCM. The latest generation of FAMOUS has been developed to provide increased and more dynamic Earth system capabilities. However, persistent salinity drifts on the order of $0.25\,\mathrm{psu\,kyr^{-1}}$ result in a collapsed AMOC and invigorated PMOC when run lengths exceed 6000 years. To prevent (or at least reduce) this large drift, the hydrological cycle must be forcibly closed by applying a freshwater flux adjustment that corrects global mean ocean salinity. In this manuscript, we compare two different methods for neutralising unforced salinity drifts in the most recent generation of the model (Section 2.3). Despite both schemes successfully maintaining a steady global mean salinity, localised drifts and subsequent feedbacks alter the sea surface temperature, salinity and density in the northeast North Atlantic and northwest North Pacific Oceans, leading to a recurrence of the aforementioned abnormal MOCs. We therefore examine the effects of intrinsic biases in the surface climatologies of two different generations of the model in the context of the hydrological cycle and overturning circulation to address whether the switch between AMOC-dominance and PMOC-dominance is an inherent feature of long FAMOUS simulations (Section 2.4). The MOC abnormalities were only observed in the latest generation of the model, with an earlier version of the model maintaining a strong, though over-deep AMOC and no PMOC (similar to the ocean state observed today). Thus, we conclude with a discussion of whether tuning could improve the accuracy of the simulated MOCs in the latest version of the model (Section 2.5).

2.2 Methods

2.2.1 Model description

FAMOUS is a coupled ocean-atmosphere GCM based on the higher resolution HadCM3 (Gordon et al., 2000; Pope et al., 2000), a configuration of the UM version 4.5 (UM4.5; Jones et al., 2005; Smith et al., 2008a; Smith, 2012; Williams et al., 2013). The atmospheric component of FAMOUS is based on primitive equations and has a horizontal resolution of $7.5° \times 5°$, 11 vertical levels, and 1 h timestep. The oceanic component is a rigid lid model, which has a 12 h timestep, $3.75° \times 2.5°$ horizontal resolution, and 20 vertical levels that vary in thickness from 10 m at the surface to more than 600 m at depth. The uppermost 100 m of the ocean is divided into 7 levels and there are 13 layers in the first kilometre. The maximum depth of the ocean is 5500 m. The bathymetry of FAMOUS differs from that of HadCM3 in the North Atlantic Ocean and the Nordic Seas. The parent model has deep overflow channels in these regions, which improve the representation of North Atlantic Deep Water (NADW). However, these features are not included in FAMOUS because they were found to eliminate Atlantic-sector Antarctic Bottom Water (AABW) and unrealistically increase the strength of the AMOC. The horizontal resolution of FAMOUS does not permit flow through the Denmark Straits. Iceland has therefore been removed to increase northward heat transport in the Atlantic and prevent the unrealistic build-up of sea ice in the Nordic Seas. The spatial resolution of the model also means that the Bering Strait is shut to significant mass transport and effectively shut to tracer mass transport. This is of potential relevance to the ocean circulation drifts described in this study, because it reduces exchange between the Atlantic and Pacific Oceans through the Arctic. The ocean and atmosphere are coupled once per day. At the time of this study, FAMOUS simulates 400 to 600 model years per wall-clock day using 16 processors on Tier 2 (regional) and Tier 3 (local) High Performance Computers at the University of Leeds. This is an order of magnitude faster than HadCM3 and therefore is ideal for multi-millennial simulations (e.g. Smith and Gregory, 2012; Gregoire et al., 2012, 2015) or large ensembles (e.g. Gregoire et al., 2011; Sagoo et al., 2013).

Multiple generations of FAMOUS exist, as outlined by Williams et al. (2013). Each

FAMOUS simulation is denoted by a unique 5 letter UM index. Here, we use the simulations XFHCC (Smith, 2012) and XCVJO, which is an unpublished predecessor to XFHCU (Williams et al., 2013). The UM basis files for these simulations can be accessed via the Providing Unified Model Access (PUMA) service (`http://cms.ncas.ac.uk/wiki/PumaService`). Technical documentation and evaluations of model development work can be found in an ongoing special issue in Geoscientific Model Development (`http://www.geosci-model-dev.net/special_issue15.html`).

2.2.1.1 Land surface schemes in FAMOUS

All versions of FAMOUS published prior to Williams et al. (2013) used the Met Office Surface Exchange Scheme (MOSES) version 1 (Cox et al., 1999). MOSES1 calculates the surface-to-atmosphere fluxes of momentum, energy and water, and the vegetation-to-atmosphere fluxes of CO_2, incorporating the physiological impact of atmospheric CO_2, temperature and water vapour on photosynthesis and stomatal conductance (Cox et al., 1999; Valdes et al., 2017). The state of the land surface is defined in terms of four prognostic variables: temperature, canopy water, lying snow, and soil moisture (Cox et al., 1999). A significant drawback within the context of long-term Earth system modelling is that MOSES1 does not include the terrestrial carbon cycle or interactive vegetation (Williams et al., 2013; Valdes et al., 2017).

The latest generation of the model, optimised by Williams et al. (2013), includes a newer version of the land surface model, MOSES2.2 (Essery et al., 2001, 2003), as well as an update for the sea ice physics scheme and extra physics at the top of the atmosphere (Smith, 2012). MOSES2.2 upgrades all aspects of the land surface exchange and surface radiation schemes compared to MOSES1 (Valdes et al., 2017). An additional advance was the introduction of a tiled representation of surface types on the sub-grid scale, which allows heterogeneous surface characteristics to be modelled (Essery et al., 2001; Valdes et al., 2017). To calculate the energy balance for each grid cell, MOSES2.2 weights the properties of the different surface types and calculates the fluxes for the average surface (Essery et al., 2003). A detailed description of the differences between MOSES1 and MOSES2.2 is provided by Valdes et al. (2017).

2.2.1.2 Salinity drifts in FAMOUS

Salinity drifts occur in multi-millennial simulations in FAMOUS because the water budget is not fully closed (Pardaens et al., 2003; Smith et al., 2008a). The primary cause of this drift is the persistent accumulation of multi-year snow on the Greenland and Antarctic ice sheets without dynamic ice physics to allow transport to the coast or iceberg calving, resulting in insufficient freshwater being routed back to the global oceans. This is a feature of all versions of the UM4.5 family and is primarily addressed by the inclusion of a constant freshwater flux to represent iceberg melt (Smith et al., 2008a).

The meltwater field is calibrated in a standard pre-industrial control run to balance the model's global salinity drift and is applied uniformly in the areas adjacent to the ice sheets where icebergs should occur. An additional issue is that the rigid lid ocean model requires the use of a virtual salinity flux (VSF) at the surface, rather than a direct water forcing (Pardaens et al., 2003; Smith et al., 2008a). In FAMOUS, unlike other versions of the UM4.5 (e.g. Valdes et al., 2017), the VSF is calculated using the local sea surface salinity, which means that, although local effects may be more accurately represented, there is no guarantee that a globally balanced surface water forcing will translate into a globally balanced VSF.

Small drifts may also arise from evaporation over isolated inland seas, which have infinite capacity to fill up (from precipitation and continental runoff) and/or dry out (through evaporation), because the ocean's rigid lid ensures that the volume of these water masses remains constant. Modelled salinities are therefore capped at 45 psu to prevent them from becoming unrealistically salty in isolated bodies of water, such as the Hudson Bay and the Red Sea (Pardaens et al., 2003).

2.2.2 Experiment design

2.2.2.1 Salinity drifts

The global volume-weighted mean salinity drift in a 10,000 year pre-industrial equilibrium simulation with the standard version of FAMOUS-MOSES2.2 is 0.25 psu kyr^{-1} (not shown). A drift of this magnitude is unacceptable in multi-millennial simulations because it leads to a collapsed AMOC and invigorated PMOC even under constant pre-industrial boundary conditions. Two different modifications were independently incorporated into the latest generation of the model in an attempt to minimise the salinity drift: SFLUX and VFLUX. The SFLUX code modification sets a target for the global volume-weighted mean of salinity, calculates the difference between this target and the model value at each timestep, and applies a correction via a surface salinity flux. The salinity target was set to 34.65 psu to match the global volume-weighted salinity in the most recent standard spun-up version of FAMOUS (produced by Williams et al., 2013). On the other hand, VFLUX calculates the global average VSF at the surface, and applies a small salinity tendency equally at every grid cell throughout the depth of the ocean to cancel out any net salinity forcing. This ensures that there is no volume-averaged drift in global salinity. Both simulations were run for 10,000 years with constant pre-industrial boundary conditions and were initialised from an unpublished simulation (XCVJO), which was a precursor to the standard FAMOUS-MOSES2.2 simulation (produced by Williams et al., 2013). In Section 2.3, the effectiveness of the two salinity drift modifications will be assessed and the impact of each modification on the model's deep ocean circulation will be discussed.

2.2.2.2 Generations of FAMOUS

Two different generations of the model, FAMOUS-MOSES1 (FM1) and FAMOUS-MOSES2.2 (FM2), were also compared to investigate the effect that differences in the surface climatologies have on the hydrological cycle and large-scale ocean circulation. As with the salinity drift experiment (Section 2.2.2.1), both simulations were run for 10,000 years with constant pre-industrial boundary conditions. Both simulations were run using published model setups and were initialised from the end of 12,000 year (FM1 = XFHCC; Smith, 2012) and 7000 year (FM2 = XCVJO) spin-ups, respectively. FM1 was run with a standard salinity drift modification that ensures that changes in global ocean salinity due to the VSF formulation are consistent with the overall climatic water budget – see Smith et al. (2008a) for more details. However, if the water budget is drifting (e.g. because of snow accumulation or a poorly calibrated iceberg meltwater field), this modification does not eradicate the salinity drift. FM2 is the same simulation described in Section 2.2.2.1 that contains the VFLUX modification (see Table 2.1 for a summary of the key differences between the simulations presented in this study).

Table 2.1: Summary of the key differences between the simulations.

Simulation	Land surface scheme	Salinity drift correction
SFLUX	FAMOUS-MOSES2.2	Surface
VFLUX	FAMOUS-MOSES2.2	Volumetric
FM1	FAMOUS-MOSES1	Standard*
FM2	FAMOUS-MOSES2.2	Volumetric

* See Smith et al. (2008a) for more details.

In Section 2.4, results will be compared to HadCM3 because FAMOUS was originally tuned to reproduce both the equilibrium climate and climate sensitivity of the parent mode (Jones et al., 2005; Smith et al., 2008a; Smith, 2012). The HadCM3 simulation (AAXZK) that we compare to is part of the MOSES1 pre-industrial control run conducted by Gordon et al. (2000), which was a $\approx$ 400 year run initialised with modern climatology, but forced with pre-industrial boundary conditions. The initial conditions for AAXZK (henceforth "HadCM3") were the climate state from the year 360 of the simulation described by Gordon et al. (2000). We compare to a climatology that has been produced after a 240 year continuation with constant pre-industrial forcing. In addition, we compare to observations from the World Ocean Atlas 2013 version 2 (Locarnini et al., 2013; Zweng et al., 2013), since subsequent model development may have taken newer FAMOUS simulations away from the parent model.

2.3 Influence of salinity drift correction on ocean circulation

In this section, we compare the effect that the two salinity drift correction schemes (SFLUX and VFLUX) have on global salinity and the MOC in the most recent generation of the model (FM2). We focus our analyses on the Atlantic and Pacific Oceans, because one of the most distinctive features of the modern MOC is the asymmetry between these two basins (Saenko et al., 2004). Deep waters are currently formed in the Nordic and Labrador Seas in the Northern Atlantic Ocean, and the Ross and Weddell Seas in the Southern Ocean (Schmittner et al., 2007). In contrast, there is no deep water formation in the Pacific Ocean, because the relatively low density of the surface water stabilises the water column and limits downward convection (Warren, 1983; Menviel et al., 2012). Instead, modern Pacific overturning is dominated by weak, southwards flowing North Pacific Intermediate Water and northwards flowing AABW (Talley et al., 2003). However, the North Pacific has been postulated as a site of deep water formation in the geological past based on evidence from proxy records and modelling studies (e.g. Okazaki et al., 2010; Rae et al., 2014).

2.3.1 Evolution of salinity

Both salinity drift correction schemes are effective in maintaining a constant global salinity over the 10,000 year integration (Figure 2.1). However, in both simulations, there is a redistribution of salt from the Atlantic basin into the Pacific basin. Specifically, the Atlantic Ocean freshens by ≈0.26 psu during the first 1500 years of both simulations. In SFLUX, the Atlantic salinity plateaus at 34.81 psu between years 1500 and 4500, before increasing by ≈0.09 psu between years 4500 and 5250. There is a further increase of 0.04 psu between years 5250 and 7000. The regional salinity then stabilises at ≈ 34.94 psu during the final 3000 years of the simulation. In VFLUX, the Atlantic salinity drifts by <0.04 psu between years 1500 and 5750. The regional salinity then increases by 0.135 psu between years 5750 and 6750, before plateauing at ≈34.95 psu during the final 3250 years of the simulation. The Pacific Ocean salinity increases by ≈0.07 psu during the first 500 years of the SFLUX simulation. Continued salinification (≈0.12 psu) is simulated between years 500 and 3000, with a period of metastability between years 3000 and 4750. The basin freshens by ≈0.02 psu between years 4750 and 5250, with an additional 0.01 psu of freshening simulated between years 5250 and 7000. The regional salinity stabilises at ≈34.63 psu during the final 3000 years of the simulation. In VFLUX, the Pacific basin becomes ≈0.08 psu more saline during the first 750 years of the simulation. The regional salinity increases by a further ≈0.09 psu between years 750 and 5800 before freshening by ≈0.03 psu between years 5800 and 6750. The salinity plateaus at 34.6 psu during the final 3250 years of the simulation. Overall, the regional drifts are comparable between the two simulations, with the Atlantic freshening by 0.127 psu in SFLUX and 0.109 psu in VFLUX, and Pacific salinity increasing by 0.164 psu and

0.148 psu, respectively. The causes and effects of these drifts are discussed further in Section 2.3.3.

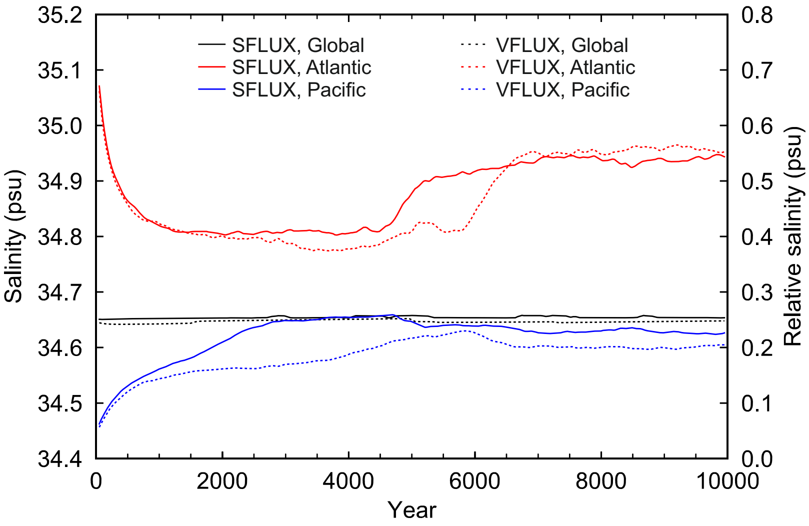

Figure 2.1: Volume-weighted mean salinity in SFLUX (solid line) and VFLUX (dashed line) calculated for the global ocean (black), Atlantic basin (red) and Pacific basin (blue). Data are calculated from annual climate means.

2.3.2 Meridional Overturning Circulation

The maximum MOC strength was calculated between 20° N and 80° N and at depths greater than 250 m. At the start of both simulations, the maximum strength of the AMOC is 14 to 15 Sv (1 Sv = 10^6 m^3 s^{-1}; Figure 2.2), broadly consistent with other FAMOUS control experiments and observations at the same latitude (Table 2.2). An initial decrease in strength of 4 to 5 Sv also occurs during the first 200 years of both simulations as a result of a coupling shock, because the model configuration matches the standard FM2 simulation (XFHCU, Williams et al., 2013), whereas the initialisation state is from an earlier, unpublished FM2 simulation (XCVJO), which has not been tuned or spun-up to a comparable steady-state. However, tests with different initialisations states suggest that this has little bearing on the final MOC configuration. In both simulations, the AMOC exhibits a period of metastability before it weakens to a maximum strength of 4 to 5 Sv. The duration of the period of metastability and the rate of AMOC collapse differs between the two simulations. In SFLUX, the maximum AMOC strength remains relatively stable (10 to 11 Sv) between years 200 and 1600 before gradually decreasing to a strength of ≈4 Sv 4750 years after the start of the simulation. In VFLUX, the AMOC is metastable for a longer period, fluctuating between 10 and 12 Sv until year 3800. A more rapid collapse then occurs, with a 7 Sv drop in strength simulated between years 3800 and 6000. This highlights the risk of carrying out too short model integrations. If the simulations had only been run for 1500 and 3500 years, respectively, the AMOC could have been misdiagnosed as having reached steady-state. However, the longer integrations demonstrate that this is not the case, with the AMOC only stabilising after a minimum run time of 5000 years. In both simulations, the initial maximum strength of Pacific overturning (6 Sv) is in good agreement with the strength of shallow sub-tropical gyre overturning in the North Pacific computed from hydrographic data (Talley et al., 2003). However, by the end of both simulations, a strong PMOC cell has established. In SFLUX, the maximum PMOC strength at the end of the simulation is ≈15.5 Sv, with the greatest rate of increase occurring during the first 2000 years. In VFLUX, the maximum strength of overturning at the end of the simulation is ≈14.5 Sv and the greatest rate of increase occurs between years 3400 and 6000. The lagged evolution of the MOCs in VFLUX relative to SFLUX results from the weaker surface forcing that arises from the salinity drift correction being applied to the whole ocean volume as opposed to a single layer.

Table 2.2: Maximum AMOC strength at 26.5° N.

Study	Model/Observations	AMOC strength (Sv)
This study	FM2 (initial)	14.5 ± 0.5
This study	FM1 (final)	20.0
Talley et al. (2003)	Observations	18.5 ± 5.0
Cunningham et al. (2007)	Observations	18.7 ± 5.6
Smith and Gregory (2009)	FM1	17.0
Kanzow et al. (2010)	Observations	18.7 ± 2.1
Hawkins et al. (2011)	FM1	19.0
Williams et al. (2014)	FM2	12.7 ± 0.4

The MOC responses are not limited to changes in strength; there are also structural changes (Figure 2.3 and Figure 2.4). In the Atlantic basin, NADW initially extends across all latitudes to depths of 3 km, with maximum strengths of ≈15 Sv (clockwise circulation; red colours in Figures 2.3a and 2.3b). The AABW cell (anti-clockwise circulation; blue colours in Figures 2.3a and 2.3b) fills the deep Atlantic southwards of 30° N and has a maximum strength of ≈5 Sv. After 10,000 years, the Atlantic overturnings are in a collapsed state (Figures 2.3c and 2.3d). Atlantic MOC collapses in FAMOUS have only previously been simulated in "hosing experiments" – modelling studies in which freshwater is systematically added to the ocean (e.g. Smith and Gregory, 2009). However, we postulate that the AMOC in the latest generation of the model (FM2) is primed to collapse in multi-millennial simulations without the need for freshwater forcing, as will be discussed further in Section 2.4. In the Pacific basin, the AABW cell initially fills the deep ocean, with maximum strengths in excess of 15 Sv (anti-clockwise circulation; Figures 2.4a and 2.4b). There is shallow mixing in the tropics (above 1 km) and very weak (<1 Sv), deep convection (<3 km) in the sub-polar North Pacific (clockwise circulation;

Figures 2.4a and 2.4b). However, by the end of the simulations, North Pacific Deep Water (NPDW) is the dominant water mass in the Northern Hemisphere, with maximum strengths of ≈15 Sv. The AABW cell has weakened (to a maximum strength of ≈9 Sv) and become more restricted in both lateral and vertical extent (Figures 2.4c and 2.4d). Both the strength and structure of the PMOC at the end of these simulations resembles the strong Pacific overturning cell simulated by Jackson et al. (2016b) in response to freshwater hosing compensated by the removal of freshwater from the surface ocean outside of the hosing region.

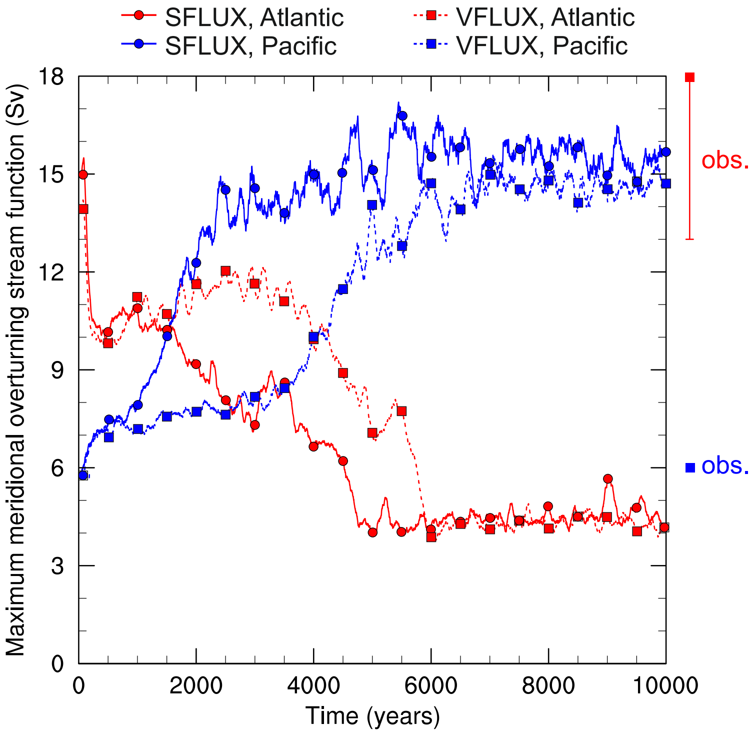

Figure 2.2: Maximum meridional overturning stream function in the Atlantic basin (red) and Pacific basin (blue) in SFLUX (solid line with circles) and VFLUX (dashed line with squares). The stream functions have been calculated between 20 and 80° N at depths greater than 250 m. Data are calculated from annual climate means. Observations show the range provided by Talley et al. (2003).

The changes in ocean circulation between the beginning and end of the simulations are reflected in the changes in the model's mixed layer depth (Figure 2.5), which provides a useful approximation for sites of vertical convection (e.g. Lavender et al., 2002). There is a decrease in Atlantic-sector mixing in both simulations, with the mixed layer reducing in depth by more than 150 m in the Nordic Seas (Figures 2.5a and 2.5c). The mixed layer in the Bering Sea deepens in excess of 160 m, as deep water formation is invigorated in this region (Figures 2.5b and 2.5d).

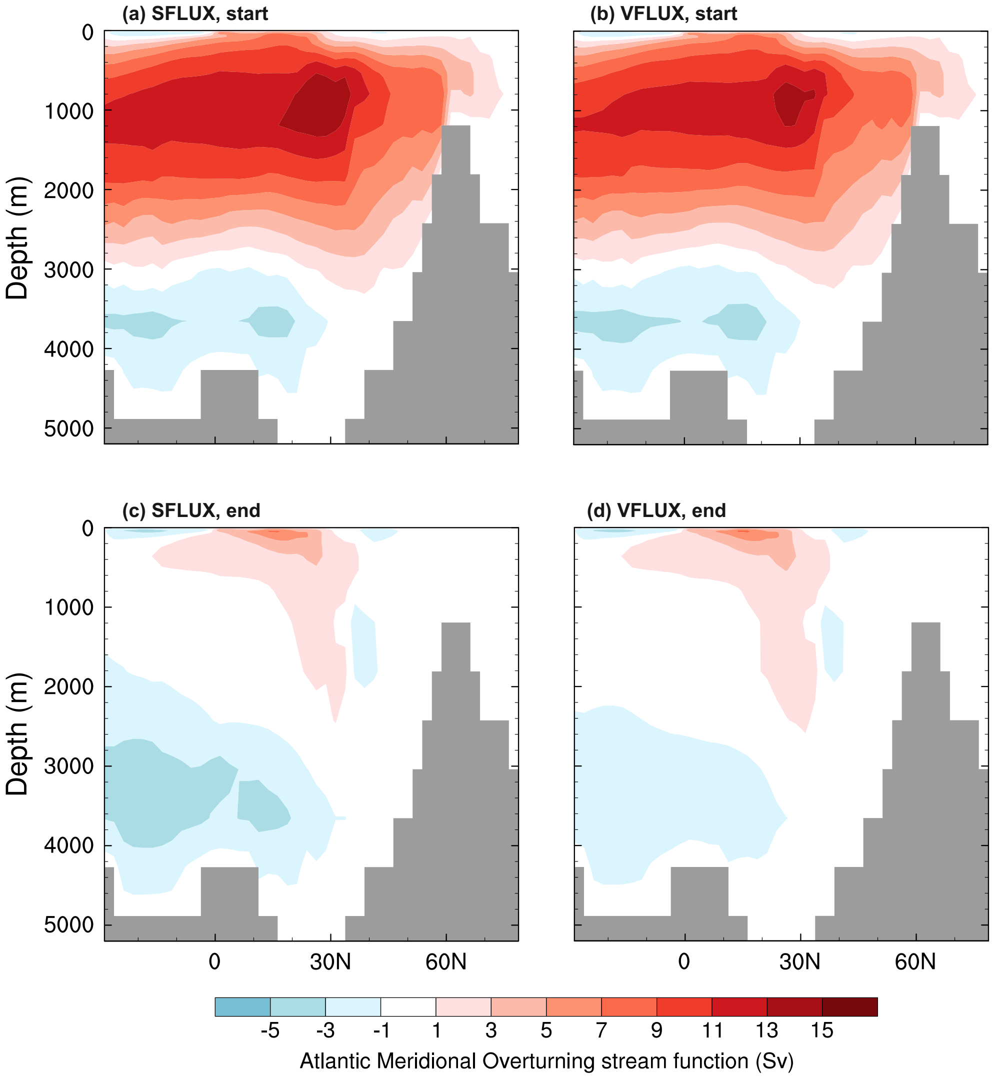

Figure 2.3: Atlantic Meridional Overturning Circulation in (a, c) SFLUX and (b, d) VFLUX at the start of the simulation (a, b) and after 10,000 years (c, d). Red colours show clockwise circulation, blue colours indicate anti-clockwise circulation. Data are calculated from 100 year annual climate means.

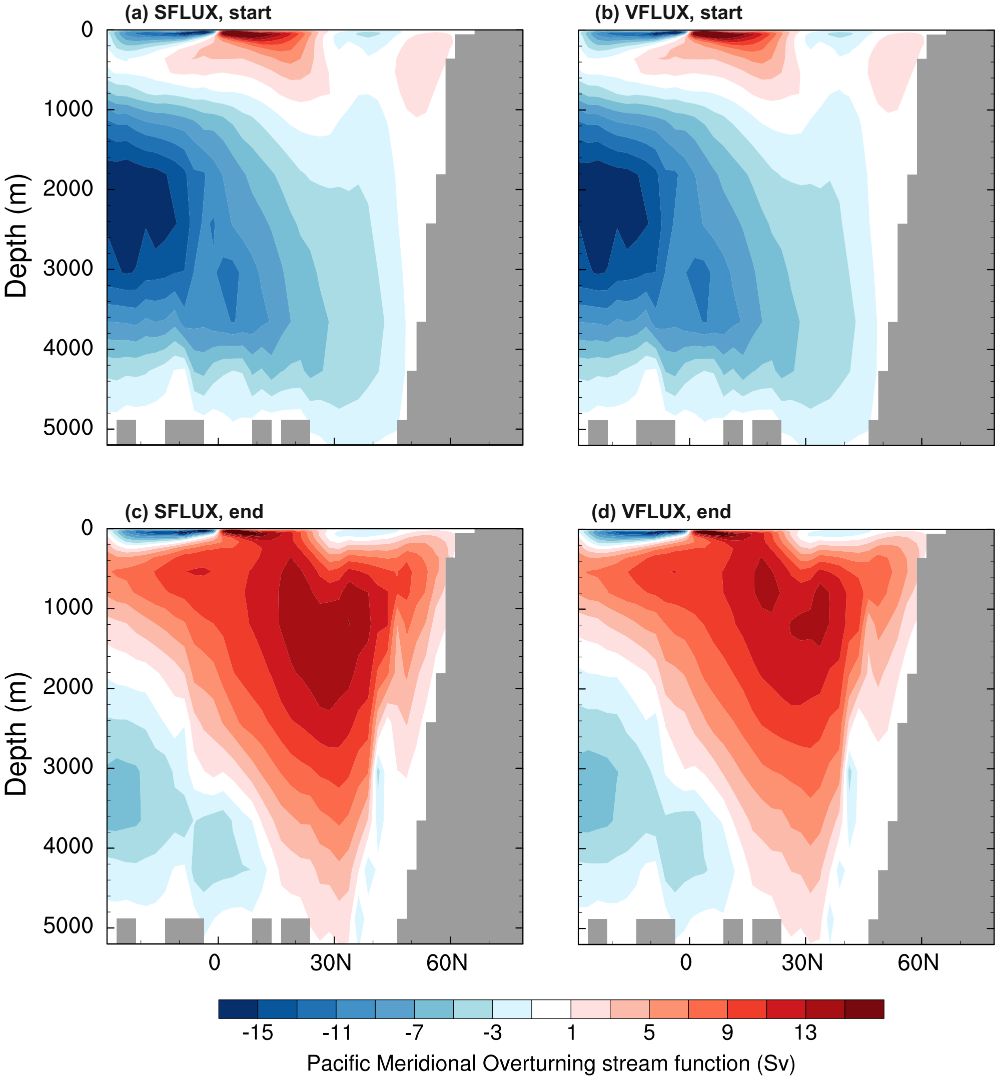

Figure 2.4: As for Figure 2.3, but for Pacific Meridional Overturning Circulation.

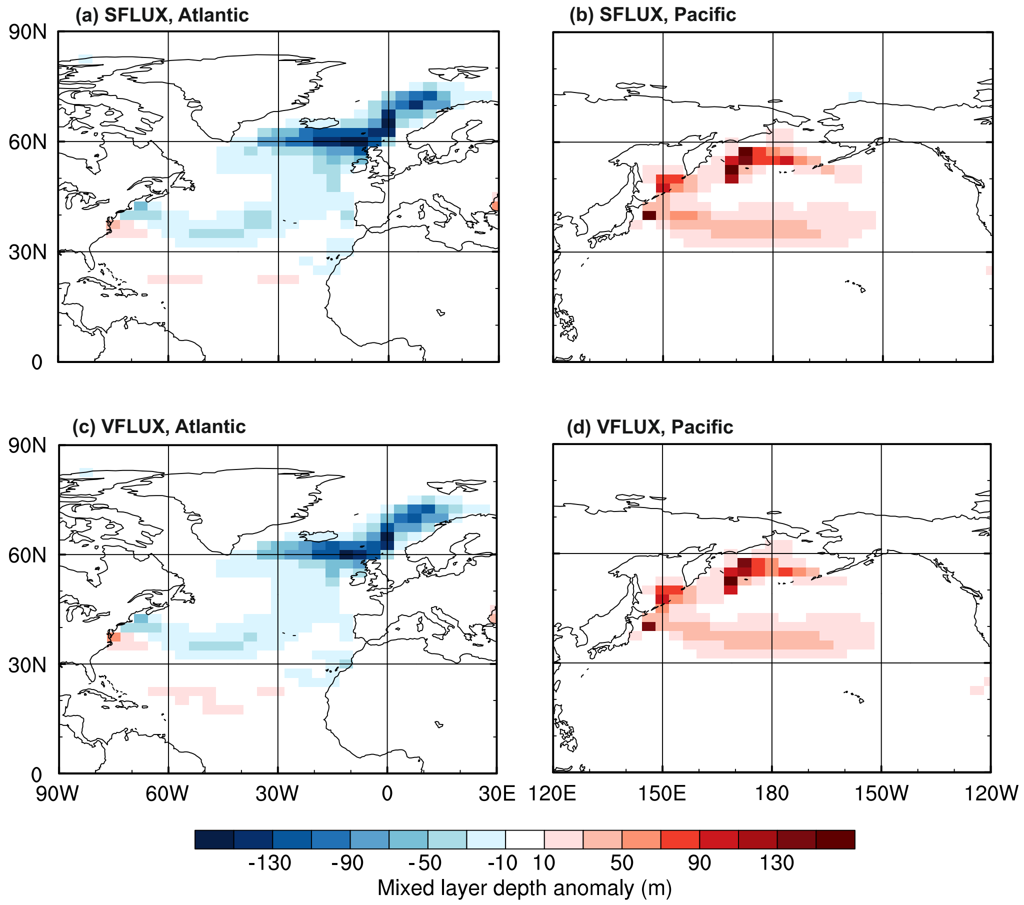

Figure 2.5: Change in mixed layer depth between the start and end of the simulation in (a, b) SFLUX and (c, d) VFLUX. Blue colours indicate shoaling of the mixed layer associated with a reduction in deep convection. Red colours show a deepening of the mixed layer associated with increased deep convection. Data are calculated from 100 year annual climate means.

2.3.3 Surface climatologies

Further information regarding both the drivers and impacts of the changes in ocean circulation between the start and end of the two simulations can be observed in the surface climatologies of the Bering Sea and the North Atlantic Ocean (Figure 2.6). During the first six millennia of both simulations, there is a small but persistent increase in sea surface temperature (SST; Figures 2.6a and 2.6b) and sea surface salinity (SSS; Figures 2.6c and 2.6d) in the northwest North Pacific Ocean, whilst the northeast North Atlantic Ocean surface becomes colder and fresher. After 6000 years, SSS in the Pacific region has risen by $\approx$0.85 psu in both simulations. Increasing SSS reduces the buoyancy of the surface waters (Figures 2.6g and 2.6h), thereby promoting sinking and an intensification of overturning circulation rates. This brings more relatively warm, salty equatorial waters northwards, thus contributing to the gradual salinification and the $\approx$0.2 °C per millennium temperature increase. As the sea surface warms, it becomes more evaporative (Figures 2.6e and 2.6f, thereby further increasing the SSS and invigorating the MOC. Thus, a positive feedback is initiated that links increasing SSSs and SSTs with enhanced evaporation and a strengthened MOC, and whilst warming partly counteracts the influence of rising salinity on density, it does not completely compensate for the effect. The surface climatologies then plateau during the final 4000 years of both simulations, consistent with the concurrent stabilisation of the MOCs.

The response in the North Atlantic basin is non-linear in both simulations. In SFLUX, the surface ocean freshens by more than 2 psu during the first half of the simulation, with ≈1 psu of this freshening occurring between years 4500 and 5000 (Figure 2.6c). In VFLUX, the SSS is stable during the first 3500 years of the simulation, with a gradual period of freshening occurring between 3500 and 5500 years. Between 5500 and 6000 years, a 1.25 psu drop in SSS is simulated (Figure 2.6d). As the surface ocean freshens, the waters become less dense (Figures 2.6g and 2.6h), inhibiting deep water formation and reducing the rate of overturning circulation. Consequently, colder waters accumulate in the region. This explains the ≈4 °C cooling that occurs in both simulations, ≈2 °C of which is concurrent with the periods of rapid freshening. Cooler waters are less evaporative; therefore, in the opposite feedback loop to the North Pacific, the freshness of the sea surface is enhanced.

Thus, although the salinity modifications maintain the global mean ocean salinity, the local salinity drifts and resultant changes in the MOC indicate that important imbalances exist in the simulation of the hydrological cycle. In both simulations, the northeast North Atlantic Ocean is initially ≈2.8 °C warmer and 0.7 psu saltier than the northwest North Pacific Ocean. However, by the end of the simulations, this relationship is reversed, with the North Atlantic region becoming ≈2.3 °C cooler and more than 2 psu fresher than the North Pacific region (Figures 2.6a – d). It is the positive feedbacks associated with these local drifts that change the density of the surface waters and promote the reversal from AMOC-dominance to PMOC-dominance in the model when the length of the simulation is sufficiently long.

It is important to address whether the switch between AMOC-dominance and PMOC-dominance is an inherent feature of long FAMOUS simulations, because the model is intended for multi-millennial simulations (as well as ensemble generation and examinations of model development). For example, it has already been used to better understand ice sheet dynamics (Gregoire et al., 2012, 2015) and associated sea level rises (Gregoire et al., 2016), and it will be used to conduct further long, transient climate simulations (Ivanovic et al., 2016). The abnormal overturning circulation states that we see here will impact the surface climate, the ocean carbon cycle, and tracer distributions. This abnormality has not previously been observed in a pre-industrial control run, despite long integrations having been conducted using both FM1 (4000 years, Smith et al., 2008; 12,000 years, Smith, 2012) and FM2 (3500 years, Williams et al., 2014). However, the

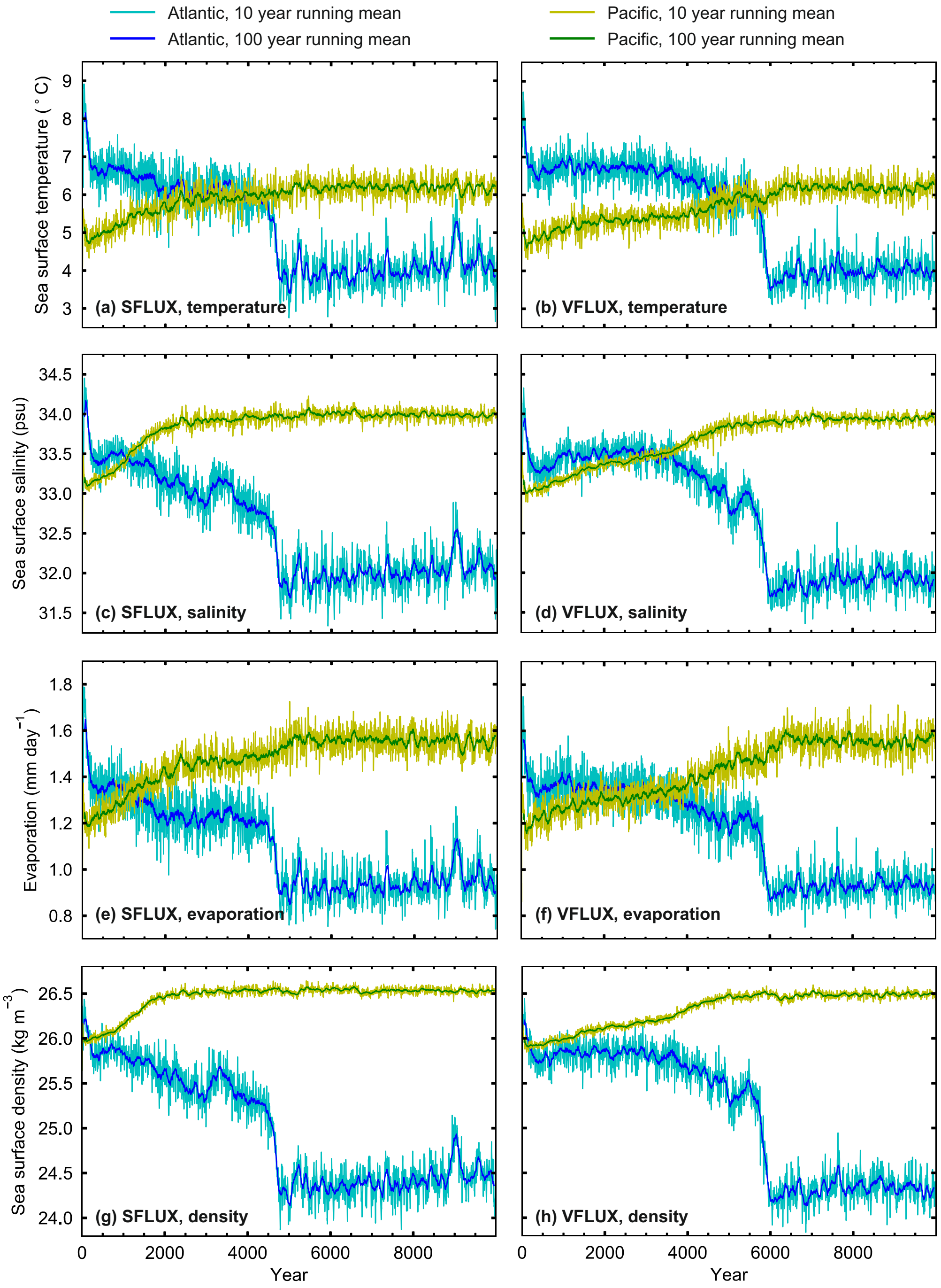

Figure 2.6: Northern North Atlantic and North Pacific (a, b) sea surface temperature, (c, d) sea surface salinity, (e, f) sea surface evaporation, and (g, h) sea surface density in SFLUX (left) and VFLUX (right). Atlantic data were averaged over the area between 50 to 70° N and 0 to 30° W. Pacific data were averaged over the area between 50 to 60° N and 165 to 195° E. These regions correspond to the areas that experience the largest changes in mixed layer depth between the start and end of the simulations, as shown in Figure 2.5.

maximum AMOC strength in FM2 reported by Williams et al. (2014) was at the lowermost limit of observational estimates (when the uncertainty ranges are taken into account; Table 2.2). We therefore postulate that overturning circulation is more sluggish in the latest generation of the model, and is primed to collapse when local surface imbalances pass a threshold during the course of multi-millennial simulations.

2.4 Comparison of FAMOUS-MOSES1 and FAMOUS-MOSES2.2

In this study, the collapsed AMOC and invigorated PMOC outlined in Section 2.3 are exclusive to the FM2 setup. In the following section, we will therefore investigate why these MOC changes are not seen in FM1 simulations, which have previously been shown to produce a reasonably strong AMOC (Table 2.2) and no identifiable PMOC. We examine differences in the initial surface climatologies of the two generations of the model, focussing on parameters that influence sea surface density, either directly or indirectly: precipitation, evaporation, SSS, SST and sea ice.

2.4.1 Meridional Overturning Circulation

The global volume-weighted mean salinity in FM2 is constant because of the inclusion of the aforementioned salinity drift modification (VFLUX). However, there is a redistribution of water between the Atlantic and Pacific basins because of enhanced evaporation over the Pacific and reduced evaporation over the Atlantic compared to FM1 and HadCM3 (discussed further in Section 2.4.2). As outlined in Section 2.3.2, FM2 therefore simulates a positive feedback loop that reduces the maximum AMOC strength from 14 Sv to 4 Sv and initiates a PMOC that reaches a maximum strength of 14.5 Sv.

In FM1, there is a small global salinity drift of ≈0.02 psu per millennium, with both basins freshening at a similar rate (Figure 2.7). In this simulation, the regional salinity drifts reflect the overall global salinity drift, which arises because the surface hydrological budget is not fully closed and the iceberg melt field is imperfectly calibrated (Section 2.2.1.2). As a result of these small salinity drifts, the AMOC gradually increases in strength from an initial value of 16.5 Sv, stabilising at ≈20 Sv after 3000 years (Figure 2.8). The strength of shallow sub-tropical gyre overturning in the Pacific is stable (≈4.5 Sv) throughout the FM1 simulation, and there is no NPDW formation.

Consequently, the MOC structures in FM1 provide a better representation of pre-industrial ocean circulation than FM2, compared to pre-industrial simulations with HadCM3 (e.g. Jackson and Vellinga, 2012) and observational estimates for the modern period (Talley et al., 2003). At the start of the FM1 simulation, NADW extends across all latitudes to depths of 3 km, with a maximum strength of 16.5 Sv. A weak AABW cell, with a maximum strength of 3 Sv, is also simulated below 3.5 km and south-

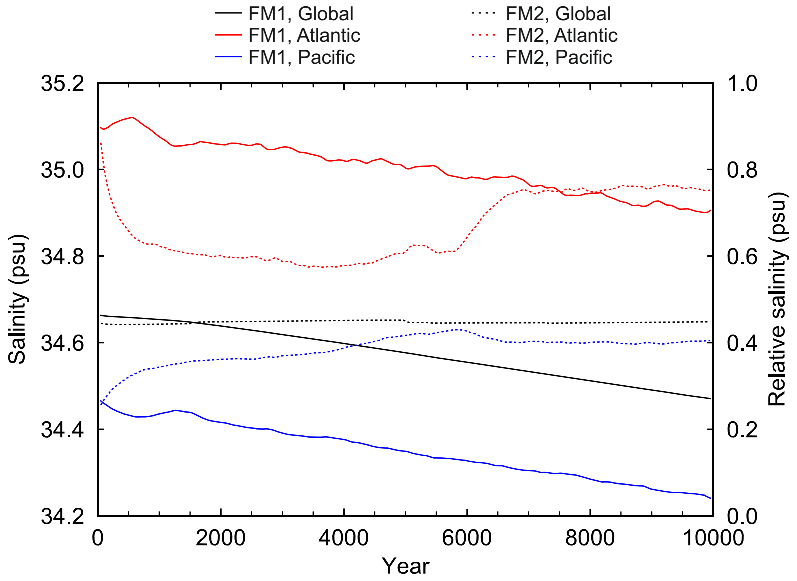

Figure 2.7: Volume-weighted mean salinity in FM1 (solid line) and FM2 (dashed line) calculated for the global ocean (black), Atlantic basin (red) and Pacific basin (blue). Data are calculated from annual climate means.

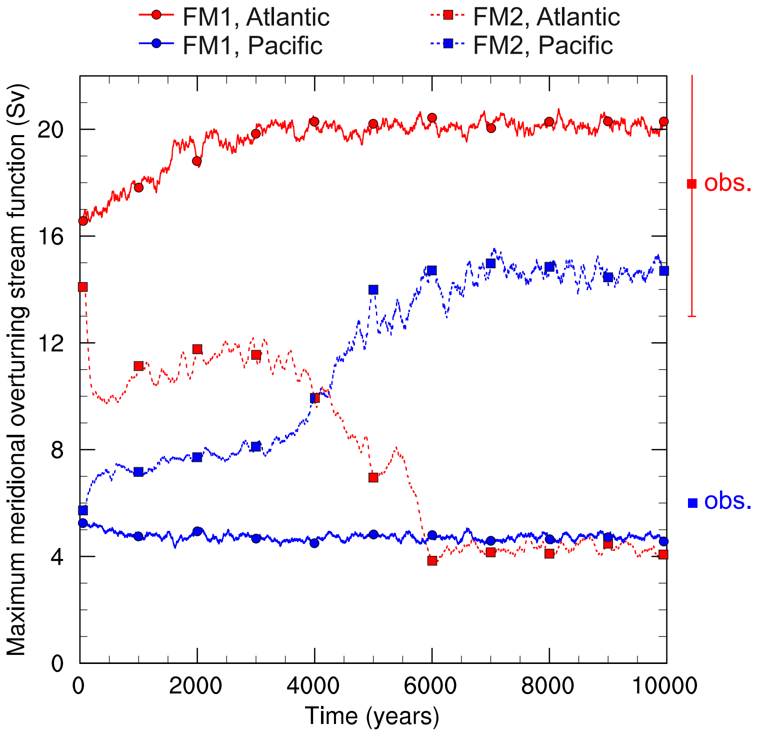

Figure 2.8: Maximum meridional overturning stream function in the Atlantic basin (red) and Pacific basin (blue) in FM1 (solid line with circles) and FM2 (dashed line with squares). The stream functions have been calculated between 20 and 80° N at depths greater than 250 m. Data are calculated from annual climate means. Observations show the range provided by Talley et al. (2003).

wards of 20° N (Figure 2.9a). By the end of the simulation, the NADW cell extends across all depths and latitudes, with a maximum strength of $\approx$20 Sv. There is no AABW cell because AABW formation in the Southern Ocean is too weak Figure 2.9c). This is a known limitation of the FAMOUS GCM (Smith, 2012; Williams et al., 2013), which demonstrates why single number metrics should not be used as comprehensive measures of the MOC. The over-deep NADW cell is an important model bias that also has implications for the ocean carbon cycle and ocean tracer distributions. However, this is not accounted for when quoting only the maximum AMOC strength.

Pacific circulation in FM1 remains stable throughout the simulation and is a closer match to modern observations than the abnormal PMOC that is simulated in FM2. Antarctic Bottom Water extends across almost all latitudes below 1 to 2 km and there is shallow convective mixing in the tropical Northern Hemisphere (Figures 2.9b and 2.9d).

2.4.2 Northern Hemisphere surface climatologies

The surface ocean in the Nordic Seas in FM2 is initially warmer and fresher than in FM1, whilst the Bering Sea is warmer, saltier and drier (due to a combination of reduced precipitation and increased evaporation). The temperature and salinity in these two regions affect the density of the surface waters with significant repercussions for deep water formation and density-driven circulation. These intrinsic biases are amplified by the positive MOC feedbacks that occur in FM2 (as outlined in Section 2.3.3), resulting in more substantial differences between the surface climatologies of the two generations of FAMOUS, the parent model, and observations after 10,000 years (Appendix A).

Differences exist between the simulations' hydrological cycles, as demonstrated by the precipitation, evaporation (Figure 2.10), and SSS anomalies (Figure 2.11). Initially, there are large differences in the annual mean P-E (ranging from –14.0 to 7.7 mm d^{-1}) between the three simulations in the Intertropical Convergence Zone, which primarily reflect differences in both the amount and structure of low latitude precipitation. Because this is a region of high rainfall (with >12 mm d^{-1} simulated in FAMOUS and >18 mm d^{-1} simulated in HadCM3), small shifts in the precipitation patterns create large anomalies, resulting in their disproportionate representation.

Elsewhere, the most striking P-E anomaly is in the northwest North Pacific, where both versions of FAMOUS simulate a relative drying (due to reduced precipitation) compared to HadCM3. The discrepancy is more pronounced in FM2 than FM1, because FM1 has a compensating bias between insufficient precipitation (Figure 2.10c) and insufficient evaporation (Figure 2.10d). Improvements in FM2 have increased evaporation rates over the North Pacific but have not substantially altered the precipitation rates. Consequently, the northwest North Pacific Ocean in FM2 is >1 psu more saline than in FM1 and >2 psu more saline than HadCM3. However, the majority of the global surface ocean in HadCM3 is too fresh compared to observations, with an average anomaly of approximately 1 psu

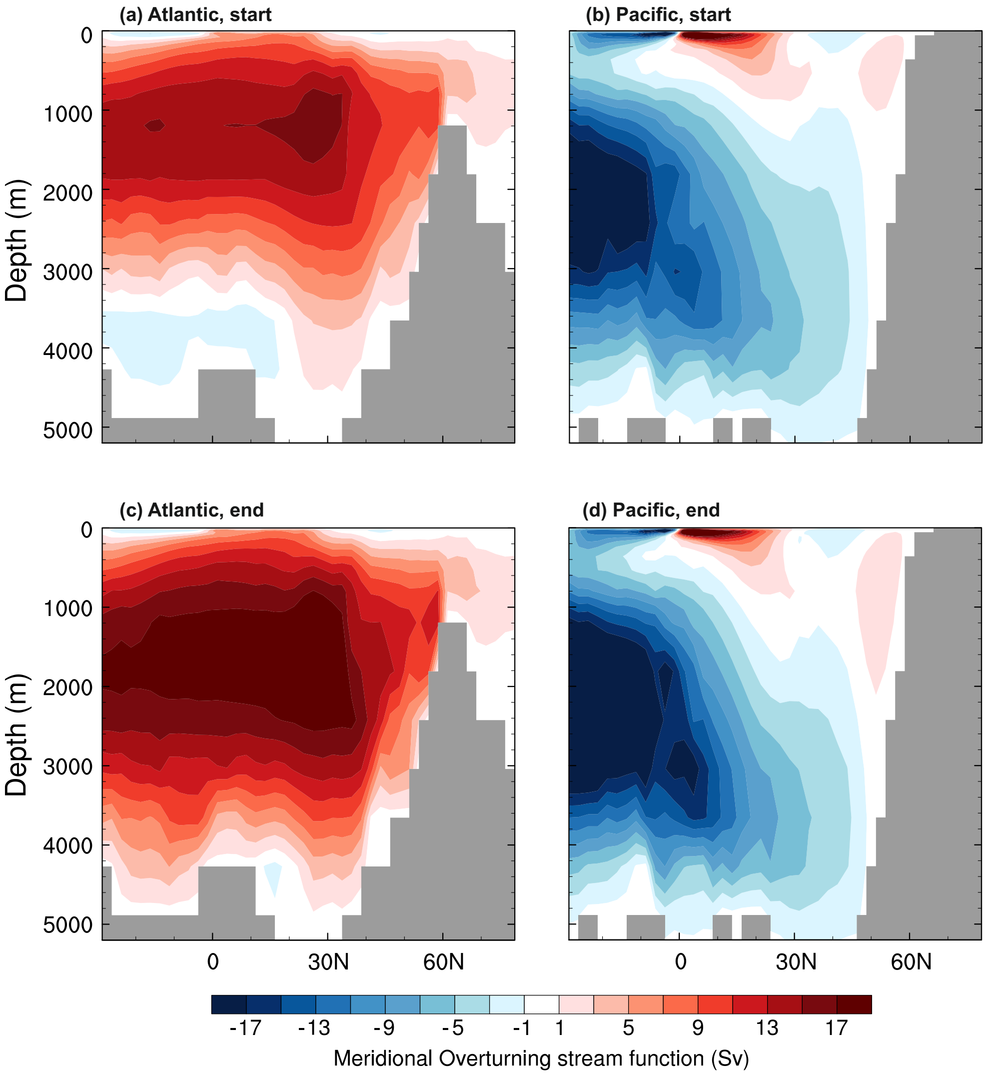

Figure 2.9: (a, c) Atlantic and (b, d) Pacific Meridional Overturning Circulation in FM1 at the start of the simulation (a, b) and after 10,000 years (c, d). Red colours show clockwise circulation, blue colours indicate anti-clockwise circulation. Data are calculated from 100 year annual climate means.

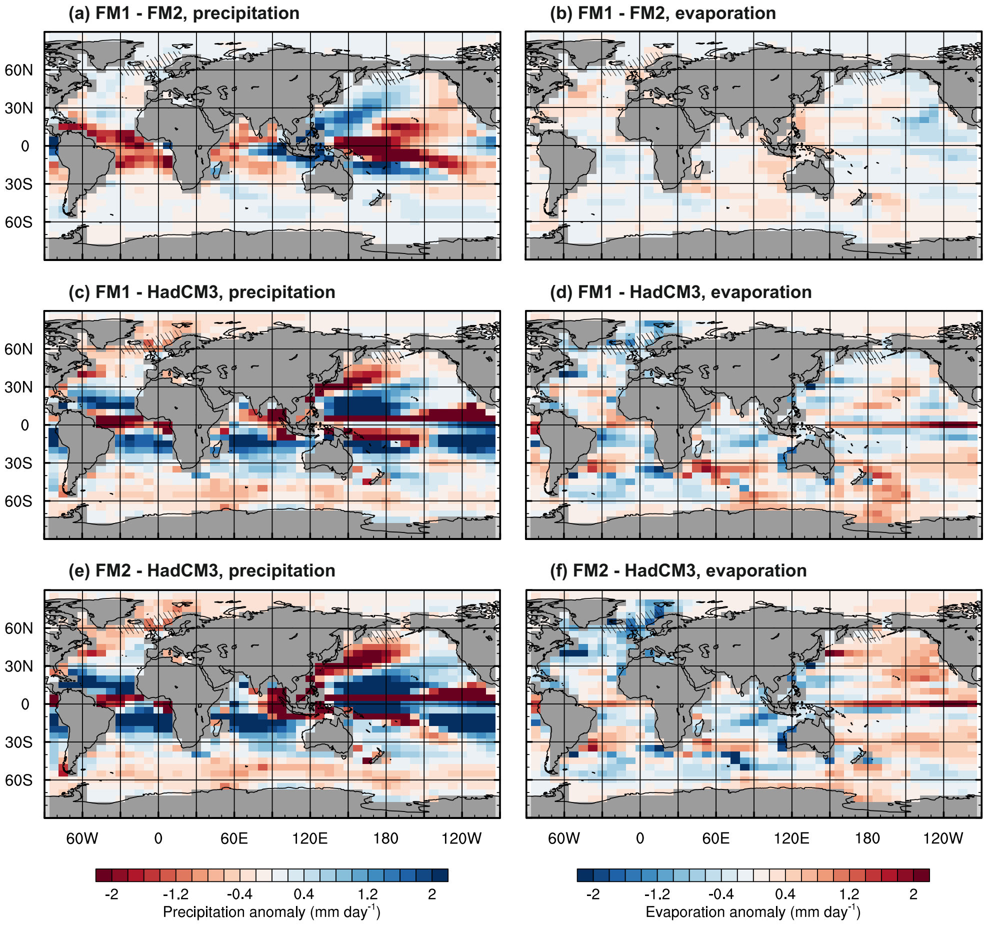

Figure 2.10: Difference in precipitation (left) and evaporation (right): (a, b) FM1 minus FM2, (c, d) FM1 minus HadCM3, and (e, f) FM2 minus HadCM3. FAMOUS data are the annual climate means calculated from the first 100 years of the simulations. HadCM3 data are the 240 year annual climatology. Hatched areas show the approximate locations of the simulated Northern Hemisphere deep water formation regions, which are in good agreement with observed deep and intermediate water formation regions in the Nordic Seas and North Pacific Ocean, respectively. Note that FAMOUS does not simulate deep water formation in the Labrador Sea.

in the Pacific Ocean (Figure 2.11b; Zweng et al., 2013). The SSS biases are therefore more complex when comparing FAMOUS directly to observations, although the North Pacific deep water formation region remains too saline in both generations of the model.

Both versions of FAMOUS are also >2 °C warmer than HadCM3 in the northeast North Pacific Ocean, and >1 °C colder in the northwest North Pacific (Figure 2.12). However, HadCM3 has a prominent cold bias in the North Pacific Ocean (Figure 2.12b). Sea surface temperatures across the majority of the North Pacific are therefore too cold when comparing FAMOUS directly to observations (Figures 2.12d and 2.12f). Consequently, FAMOUS simulates too much sea ice in the northwest North Pacific (Figure 2.13), which is another known limitation of the model (Smith et al., 2008a). North of the Bering Strait, FAMOUS is >3 psu saltier and up to 3 °C warmer than both

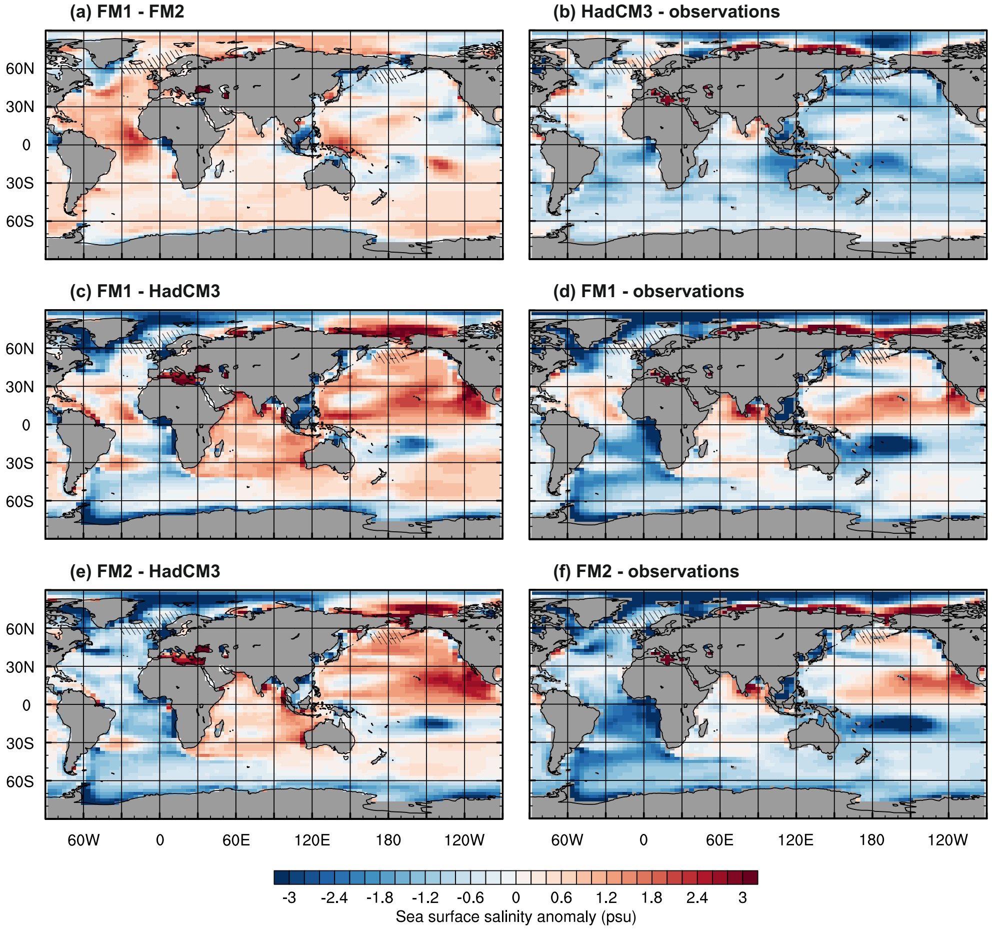

Figure 2.11: Difference in sea surface salinity: (a) FM1 minus FM2, (b) HadCM3 minus observations, (c) FM1 minus HadCM3, (d) FM1 minus observations, (e) FM2 minus HadCM3, and (f) FM2 minus observations. FAMOUS data are the annual climate means calculated from the first 100 years of the simulations. HadCM3 data are the 240 year annual climatology. Observations are the 1955 to 2012 surface climatology from the World Ocean Atlas 2013 version 2 (Zweng et al., 2013). Hatched areas show the approximate location of the simulated Northern Hemisphere deep water formation regions as per Figure 2.10.

HadCM3 and observations, with insufficient Arctic sea ice. We suggest that these biases occur because the closed seaway reduces high-latitude exchange, and they are more pronounced in FM2. Furthermore, FM2 is up to 4 °C warmer than FM1 in the Bering Sea (Figure 2.12a), which contributes towards the enhanced evaporation rates (Figure 2.10a) and increased SSS (Figure 2.11a) in this region. Although the simulated warming somewhat counteracts the influence of elevated SSSs on sea surface density in the Bering Sea in FM2, the effect of the elevated SSSs (increasing density) outweighs the effect of the elevated SSTs (reducing density). Consequently surface waters become less buoyant compared to FM1 and HadCM3, reducing water column stability and promoting deep water formation.

Both versions of FAMOUS simulate temperatures up to 9 °C cooler than HadCM3

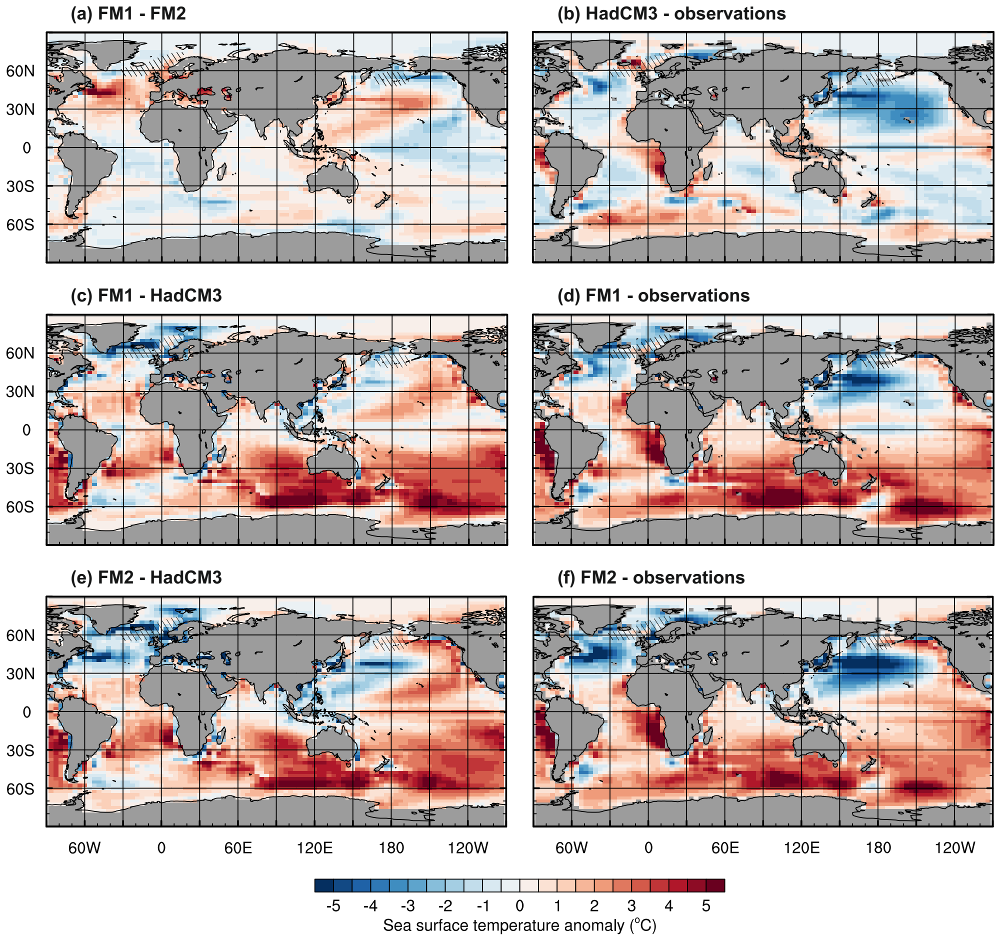

Figure 2.12: As for Figure 2.11, but for sea surface temperature. Observations are the 1955 to 2012 surface climatology from the World Ocean Atlas 2013 version 2 (Locarnini et al., 2013).

and observations around the coast of Greenland and Iceland (Figure 2.12), which is linked with expanded annual sea ice in the Nordic and Labrador Seas (Figure 2.13). FM1 simulates the lowest temperatures and the most sea ice in these regions, which creates denser surface waters (as poleward-bound water in the upper AMOC limb cools) and enhances deep water formation. With less brine rejection occurring in FM2, the North Atlantic sea surface is ≈1 psu fresher than in FM1 (Figure 2.11a). Consequently, the North Atlantic surface waters in FM2 are more buoyant, which inhibits convective mixing in the Nordic Seas.

Overall, FM2 is initially warmer and fresher than FM1 in the North Atlantic deep water formation regions. These biases increase the buoyancy of the surface waters in FM2 relative to FM1, inhibiting deep convection. In the Bering Sea, FM2 is initially warmer and drier (due to increased evaporation and reduced precipitation), which makes the sea surface more saline, and hence the net-effect is to increase the density of the Pacific surface waters. The subsequent reduction in AMOC strength and invigoration of the PMOC (as described in Section 2.3.2) act to amplify these biases. We therefore

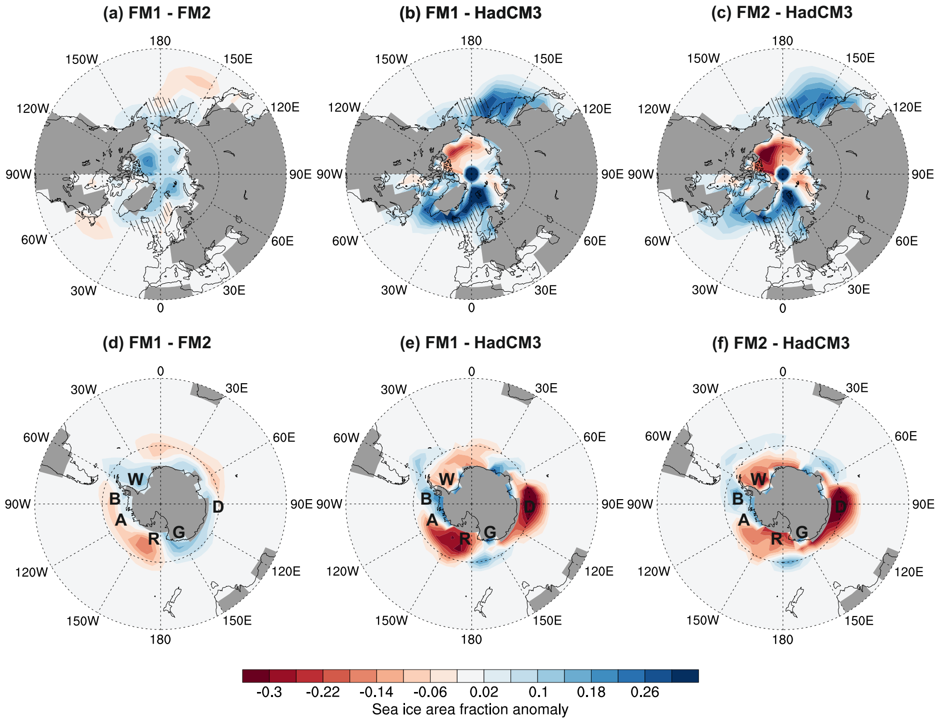

Figure 2.13: Difference in sea ice area fraction in the Northern Hemisphere (a – c) and the Southern Hemisphere (d – f). FAMOUS data are the annual climate means calculated from the first 100 years of the simulations. HadCM3 data are the 240 year annual climatology. Hatched areas show the approximate location of the simulated Northern Hemisphere deep water formation regions as per Figure 2.10. Text markers denote the location of the Amundsen Sea (A), the Bellingshausen Sea (B), the Davis Sea (D), George V Land (G), the Ross Sea (R), and the Weddell Sea (W).

propose that the salinity drift correction schemes (Section 2.2.2.1 and Section 2.3) only alter the timing of the MOC tendencies in FM2 and do not prevent them.

Observational estimates suggest that, in the modern oceans, approximately 0.8 Sv of freshwater is transported from the North Pacific Ocean into the Arctic Ocean via the Bering Strait (Coachman and Aagaard, 1988). Modelling studies have examined the impacts of an open versus closed Bering Strait on the strength of the AMOC, demonstrating that a closed Bering Strait increases the salinity of the Arctic and North Atlantic Oceans, which results in a stronger AMOC (e.g. Shaffer and Bendtsen, 1994; Goosse et al., 1997; Wadley and Bigg, 2002). In contrast, an open Bering Strait increases the freshwater input into the North Atlantic Ocean, which supresses the AMOC. The closed Bering Strait could therefore be contributing to the MOC problems in the FM2 simulations, because the salinity anomalies are being trapped in their respective basins. Opening this gateway could provide an important negative feedback mechanism for redistributing freshwater and prevent the build-up of salinity in the North Pacific in FM2. However, opening the Bering Strait is non-trivial and to-date has always caused the circulation in FAMOUS to become unstable.

2.4.3 Southern Ocean

Although the focus of this study has been on the Northern Hemisphere driven MOCs, we briefly note that there are also differences between the two generations of FAMOUS in the Southern Ocean. With no transport through the Bering Strait, all exchange between the Atlantic and Pacific basins goes through the Southern Ocean. Biases in this region are therefore important for Southern Hemisphere deep water formation, the accurate simulation of abyssal water mass properties, and the reinforcement of climatological trends in the Atlantic and Pacific basins. Southern Ocean SSTs in FAMOUS are initially 0.5 to 6 °C warmer than in HadCM3 (Figure 2.12), and there is less sea ice in the Ross, Weddell and Davis Seas (Figure 2.13). With less brine rejection occurring in FAMOUS, the surface of the Southern Ocean is >3 psu fresher than in HadCM3 (Figure 2.11), which will increase surface buoyancy and vertical stratification. FM2 has more sea ice than FM1 in the Bellingshausen, Amundsen and Ross Seas, where SSTs are up to 2 °C colder, and less sea ice in the Weddell Sea and off the coast of George V Land, where SSTs are up to 2.5 °C warmer. As previously discussed, surface biases impact the water column properties. In the Southern Ocean, the consequence is that FM2 is colder and fresher than FM1 in the top 200 m of the Southern Ocean, and warmer and more saline below this depth (Figure 2.14). Where they counteract, the effect of salinity tends to outweigh the effect of temperature on water buoyancy. FM1 is therefore denser in the uppermost kilometre of the ocean, whilst the FM2 water column is more stratified, which inhibits vertical convection and the formation of AABW.

Antarctic Bottom Water formation is well correlated with the strength of the Antarctic Circumpolar Current (ACC; Gent et al., 2001; Smith, 2012), which is the strongest current in the global oceans. The ACC extends between 56 and 62° S (Johnson and Bryden, 1989) and has measured strengths of 137±8 Sv in the Drake Passage (Cunningham et al., 2003). For comparison, the observed strength of the Gulf Stream in the Florida Straits is ≈32 Sv, increasing to 120 Sv off the coast of Newfoundland (Meinen and Luther, 2016). The mean transport of the East Australia Current at 30° S has been estimated at ≈22 Sv (Mata et al., 2000) and the total transport of the Agulhas Current between 27 and 40° S is ≈70 Sv (Bryden et al., 2005a). The ACC strength in FM1 (30 Sv) is weaker than range of values in the Intergovernmental Panel on Climate Change's Fourth Assessment Report (IPCC, 2007). However, it is stronger than the 15 to 20 Sv simulated in FM2 (Figure 2.15). Overall, the combination of an ACC that is operating at less than a quarter strength and weak AABW formation will further limit the amount of exchange that occurs between the major ocean basins, thereby reinforcing the Atlantic and Pacific trends. The effect is greater in FM2 because its ACC is approximately half the strength of the ACC in FM1.

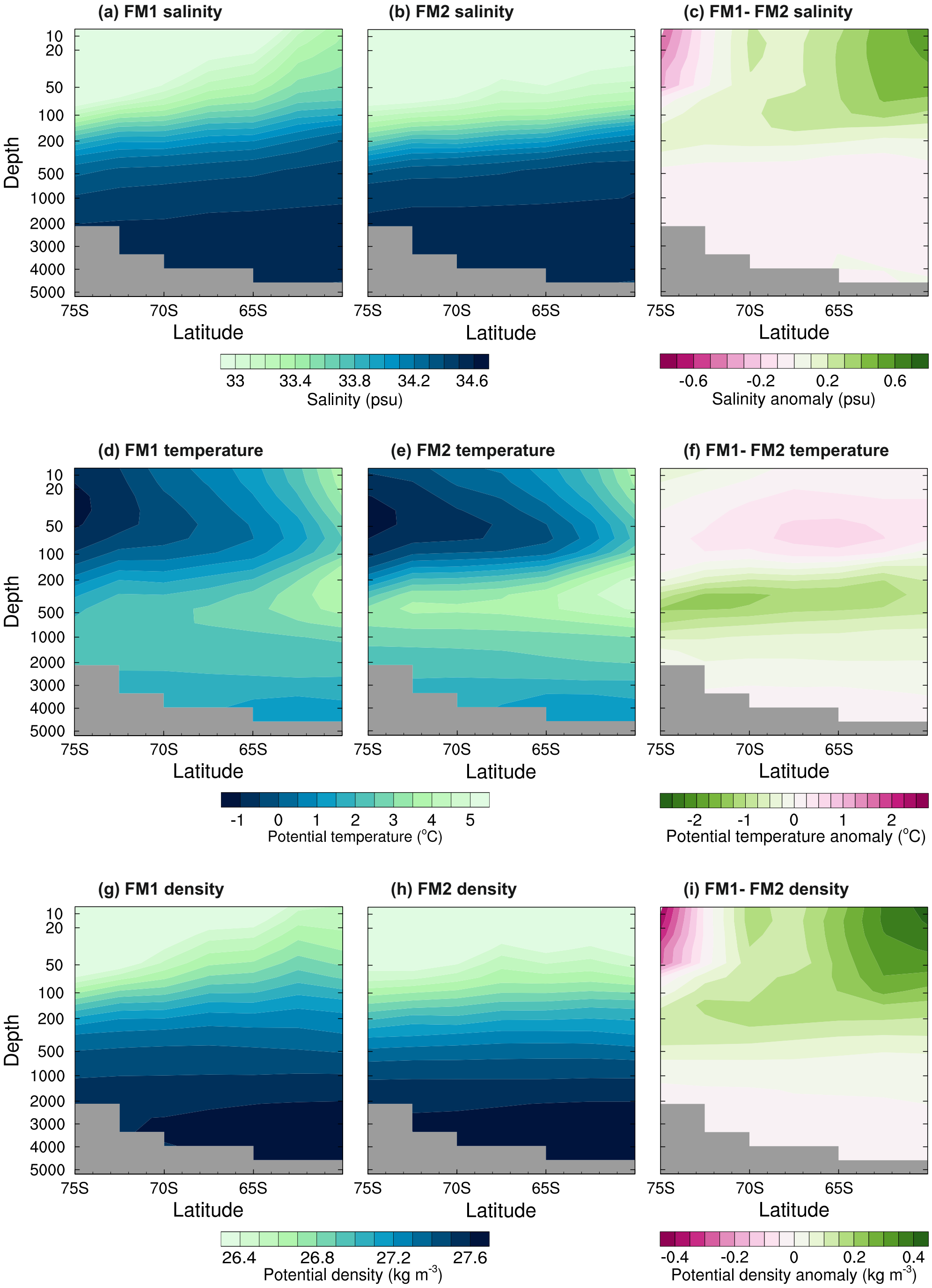

Figure 2.14: Southern Ocean stratification in FM1 (left) and FM2 (middle) as identified from salinity (a – c), potential temperature (d – f), and potential density (g – i). Data are the zonal annual climate means calculated from the first 100 years of the simulations. Note that depth is non-linear.

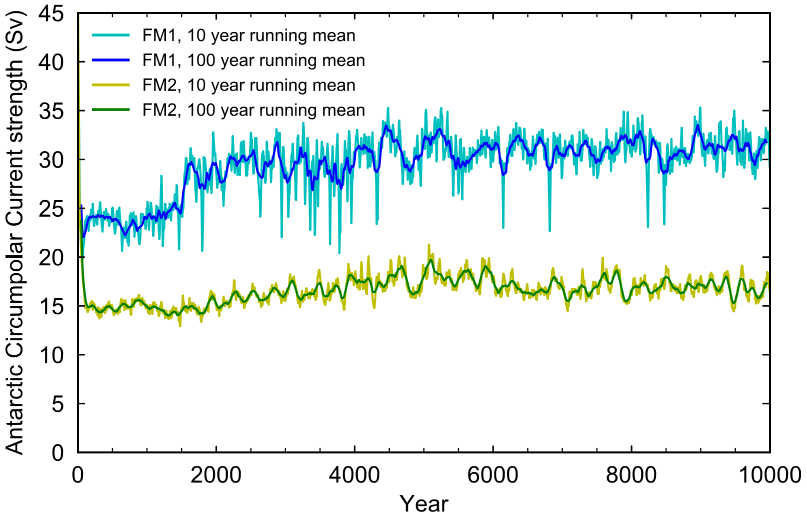

Figure 2.15: Maximum Antarctic Circumpolar Current strength in FM1 (blue) and FM2 (green), calculated as the integrated total ocean U-velocity across the Drake Passage.

2.5 Discussion and conclusion

As with many GCMs, the surface hydrological budget in FAMOUS is not fully closed, with imbalanced hydrology over inland seas and insufficient snowmelt leading to small salinity drifts. These drifts may accumulate over time; therefore they are particularly important in the long integrations for which FAMOUS was partially intended. Any drifts in surface salinity can eventually propagate in to the deep ocean, affecting the global MOC, and consequently, poleward heat transport, surface climate, the ocean carbon cycle, and ocean tracer distributions. Two different methods were employed to account for these imbalances and neutralise the salinity drifts in the most recent version of the model (FM2): the first (SFLUX) maintains the global volume-weighted mean salinity at 34.65 psu by applying a surface flux correction; the second (VFLUX) enforces zero drift by applying a small salinity tendency equally throughout the depth of the ocean to cancel out any net surface forcing. Both methods successfully maintained a steady global mean salinity. However, neither method prevented regional salinity drifts. Small but persistent increases in SSS were simulated in the northwest North Pacific Ocean, with concurrent freshening in the northeast North Atlantic. These changes stimulated positive feedback loops in the MOC and surface climate, leading to the development of a strong, deep PMOC and a collapsed AMOC after 6000 years. For example, in the Pacific basin, increasing SSS raised the sea surface density, which promoted sinking and an intensification of the PMOC. The stronger MOC enhanced poleward salt and heat transport thereby increasing regional SSS and SSTs. The warmer sea surface was more evaporative, which led to further increases in SSS. The opposite biases and feedbacks operate in the North Atlantic, therefore the net effect is a weakening of the AMOC. Both simulations exhibited a period of metastability before trending resumed, highlighting the risk of carrying out too short model integrations when studying deep ocean circulation and ocean biogeochemical cycles.

Comparing two different generations of the model (FM1 and FM2) suggests that these problems are endemic to multi-millennial simulations with FM2 (the latest generation of the model), and would occur regardless of the choice of salinity drift correction scheme. The sea surface in the North Atlantic deep water formation regions in FM2 is intrinsically too warm and fresh, which inhibits sinking, whilst the combination of too much evaporation and insufficient precipitation in the northwest North Pacific Ocean increases the SSS and initiates deep convection. Thus, we postulate that the AMOC in the latest generation of the model is primed to collapse in multi-millennial simulations, without the need for freshwater forcing. FM1 (the older generation of the model) does not suffer the same biases in the sea surface climatologies. Erroneous pre-industrial NPDW formation therefore does not occur in FM1, and AMOC remains strong (though over-deep). The over-deep NADW cell is also an important model bias that will have implications for the surface climate and ocean tracer distributions. It would therefore be valuable for future model development work to focus on increasing the strength of the ACC, shoaling the NADW cell, and maintaining an abyssal AABW cell in the deep Atlantic basin. Currently, the importance of the surface imbalances and MOC differences depend on the scientific questions for which the model is being used. However, where long integrations are required, FM1 is a more appropriate choice as it provides a better representation of the pre-industrial MOC than FM2.

The MOC abnormalities that occur in the FM2 simulations could potentially be resolved with tuning, which is a calibration process that attempts to find the optimal values of uncertain model parameters and minimise the discrepancy between observations and model output (Gregoire et al., 2011). FAMOUS has previously been tuned both systematically (Jones et al., 2005; Gregoire et al., 2011; Williams et al., 2013) and manually (Smith et al., 2008a), with the focus being on the tuneable parameters that have a high impact on the climate in HadCM3, such as the threshold of relative humidity for cloud formation and the conversion rate of cloud liquid water droplets to precipitation. Other physical parameters that have been tuned include the sea ice albedo, and the atmospheric and oceanic diffusion parameters (Gregoire et al., 2011). Variations in these parameters affect the model's P-E balance, and therefore the SSS, sea surface density, and MOC. For example, the simulation of clouds is crucial for the simulation of precipitation, and also planetary albedo, which influences surface temperatures, and consequently evaporation rates. Typically, perturbed parameter simulations have a centennial run length (e.g. Gregoire et al., 2011; Williams et al., 2013). There is therefore a risk that small errors in the optimised surface climatologies may not be identified during the calibration process. As demonstrated by this study, these become important on longer timescales when localised drifts occur. However, it is not feasible to conduct hundreds of multi-millennial perturbed parameter simulations with a model of this complexity and resolution. A more suitable methodology would be to conduct multi-millennial runs with a subset of high performing simulations from an ensemble of centennial integrations, offering a way forward for carrying out an improved tuning approach. In the process of choosing optimal parameter values for these extended simulations, we suggest that particular attention should be paid to the temperature and salinity balances in the surface ocean, particularly in the deep water formation regions.

Overall, this study demonstrates that small, regional biases in the sea surface climate are important for the accurate simulation of the MOC on multi-millennial timescales, because they can cause regional salinity drifts even when the global hydrological cycle has been forcibly closed. Currently, we have not identified any specific trends that occur well in advance of the final collapse of the AMOC, which would allow other model users to diagnose potential problems in the overturning circulation without the need to run for multiple millennia. However, we suggest that the northwest North Pacific Ocean (50 to 60° N; 165 to 195° E) and northeast North Atlantic Ocean (50 to 70° N; 0 to 30° W) are important areas that should be closely monitored for imbalances in the surface hydrology that may redistribute freshwater between sites of deep water formation.

CHAPTER 3

Simulating stable carbon isotopes in the ocean model of the FAMOUS GCM

Abstract

Isotopic ratios are often utilised as proxies for ocean circulation and the marine carbon cycle. However, interpreting these records is non-trivial because they reflect a complex interplay between physical and biogeochemical processes. By directly simulating multiple isotopic tracer fields within numerical models, we can improve our understanding of the processes that control large-scale isotope distributions and interpolate the spatiotemporal gaps in both modern and palaeo data sets. We have added the stable isotope ^{13}C to the ocean component of the FAMOUS coupled atmosphere-ocean General Circulation Model, which is a valuable tool for simulating complex feedbacks between different Earth system processes on decadal to multi-millennial timescales. We tested three different biological fractionation parameterisations to account for the uncertainty associated with equilibrium fractionation during photosynthesis and used sensitivity experiments to quantify the effects of fractionation during air-sea gas exchange and primary productivity on the simulated $\delta^{13}C_{DIC}$ distributions. Following a 10,000 year pre-industrial spin-up, we simulated the Suess effect (the isotopic imprint of anthropogenic fossil fuel burning) to assess the performance of the model in replicating modern observations. Our implementation captures the large-scale structure and range of $\delta^{13}C_{DIC}$ observations in the surface ocean, but the simulated values are too high at all depths, which we infer is due to biases in the biological pump. In the first instance, the new ^{13}C tracer will therefore be useful for recalibrating both the physical and biogeochemical components of FAMOUS.

3.1 Introduction

Carbon isotopes are often used as proxies for ocean circulation and the marine carbon cycle. There are three naturally occurring carbon isotopes: the stable isotopes ^{12}C (98.9 ‰) and ^{13}C (1.1 ‰), and the radioactive isotope ^{14}C (1.2×10^{-10} ‰), which is also known as radiocarbon (Key, 2001). The relative proportions of ^{12}C, ^{13}C and ^{14}C in a given oceanic pool (e.g. dissolved inorganic carbon, DIC, or particulate organic carbon, POC) are controlled by ocean circulation and mixing, and mass dependent fractionation during processes such as air-sea gas exchange (Lynch-Stieglitz et al., 1995; Zhang et al., 1995), photosynthesis (e.g. Sackett et al., 1965; Rau et al., 1989; Hollander and McKenzie, 1991; Keller and Morel, 1999), and calcium carbonate formation (Emrich et al., 1970; Turner, 1982; Ziveri et al., 2003). This is typically reported in delta (δ) notation, which is the heavy to light isotope ratio (R) of a sample relative to a standard in per mil (‰) units ($(\mathrm{R_{sample}}/\mathrm{R_{standard}} - 1) \times 1000$; Stuiver and Polach, 1977). In this study we focus on δ^{13}C, which is primarily used to track individual water masses (Curry and Oppo, 2005), study past changes in the carbon cycle (e.g. de la Fuente et al., 2015) and investigate changes in ocean circulation on glacial-interglacial timescales (e.g. Spero and Lea, 2002; Campos et al., 2017). It has also been used to constrain air-sea gas exchange rates (Gruber and Keeling, 2001) and to estimate the uptake of anthropogenic carbon by the global oceans (e.g. Quay et al., 1992, 2003).

Oceanographic surveys conducted since the 1970s, such as the World Ocean Circulation Experiment (WOCE; Orsi and Whitworth III, 2005; Talley, 2007; Koltermann et al., 2011; Talley, 2013), and synthesis projects such as Carbon dioxide in the Atlantic Ocean (CARINA; Key et al., 2010), Pacific Ocean Interior Carbon (PACIFICA; Suzuki et al., 2013), and the Global Ocean Data Analysis Project (GLODAP; Key et al., 2004, 2015; Olsen et al., 2016), provide an indication of large-scale carbon isotope distributions in the modern oceans. The two main drawbacks of these surveys are that they include relatively few measurements from the sub-surface ocean and that there were only a limited number of repeat measurements at fixed locations, which were often taken decades apart. These data sets are therefore insufficient for studying transient changes in carbon isotope distributions at sub-decadal resolution.

Geological archives such as corals (e.g. Guilderson et al., 2013) and sediment cores (e.g. Oliver et al., 2010) are used to extend the $\delta^{13}\mathrm{C_{DIC}}$ record further back in time. However, interpreting isotopic ratios in geological archives is non-trivial because they result from a complex interplay between physical processes and biogeochemical processes, both in the water column itself and during biomineralisation, which can be difficult to disentangle.

By including carbon isotopes in climate models, we can fill in the spatiotemporal gaps in both modern and palaeo data sets, and improve our understanding of the processes that control their large-scale distributions (Tagliabue and Bopp, 2008; Schmittner et al., 2013; Menviel et al., 2017). The Ocean Carbon-Cycle Modelling Intercomparison Project (OCMIP) was initiated in 1995 with the aim of evaluating the major differences between global ocean carbon cycle models and advancing our understanding of the ocean as a long-term CO_2 reservoir (Orr, 1999). Carbon isotopes are not routinely incorporated into climate models because of the computational expense associated with the long equilibration between the deep ocean and the atmosphere (Bardin et al., 2014). However, since OCMIP produced a legacy of standard input fields (Orr, 1999; Orr et al., 2000, 2017), carbon isotopes have increasingly been implemented into models of varying complexities to validate physical and biogeochemical schemes, to investigate the spatiotemporal variability in isotope distributions, and to reconcile the interpretation of ocean proxy data. As outlined in Table 3.1, the community of ^{13}C-enabled models currently includes: HAMOCC3.1 (Hofmann et al., 2000), the GFDL modular ocean model (MOM; Murnane and Sarmiento, 2000), CLIMBER-2 (Brovkin et al., 2002), MoBidiC (Crucifix, 2005), PISCES (Tagliabue and Bopp, 2008), Bern3D+C (Tschumi et al., 2011), the UVic Earth system model (ESM; Schmittner et al., 2013), iLOVECLIM (Bouttes et al., 2015), CESM (Jahn et al., 2015), and CSIRO Mk3L-COAL (Buchanan et al., 2019). Most of these are low resolution (3° to 5°), intermediate complexity models that are valuable tools for studying changes in ocean biogeochemistry on multi-millennial timescales. However, these models do not provide sufficient complexity in the ocean circulation, vertical mixing and atmosphere-ocean interactions to study more abrupt (decadal-to-centennial) changes. The more complex models (e.g. PISCES and CESM) provide a more sophisticated representation of physical and biogeochemical processes because of increased spatial resolution and/or the inclusion of more carbon pools. However, these models are computationally expensive. For example, at the time of their study, a 6010 year spin-up simulation with CESM took over 7 months to run (Jahn et al., 2015). Without employing offline or accelerated spin-up techniques (e.g. Lindsay, 2017), the higher complexity models are therefore less practical for running the long simulations required to fully spin-up the components of the Earth system that evolve on millennial timescales, such as deep ocean circulation (England, 1995) and ocean biogeochemical cycles (Falkowski et al., 2000; Key et al., 2004).

Here, we describe the implementation of ^{13}C in the ocean component of the FAMOUS General Circulation Model (GCM). FAMOUS is well suited to studying complex interactions between different components of the Earth system on decadal to multi-millennial timescales, owing to its reduced spatial resolution and increased timestep relative to the latest generation of state-of-the-art GCMs (Section 3.2.1). We use sensitivity experiments to quantify the effects of fractionation during air-sea gas exchange and primary productivity on the simulated $\delta^{13}C_{DIC}$ distributions (Section 3.2.3.3 and Section 3.3.1), and test three different parameterisations for photosynthetic fractionation to account for the uncertainty associated with the relative influence of ambient conditions, physiological effects and transport mechanism on the fractionation of carbon isotopes during

Table 3.1: Overview of existing ^{13}C-enabled models.

Model	**Resolution**	**Levels**	**Tracers**	**$\alpha_{\mathrm{POC}\leftarrow\mathrm{aq}}$ parameterisation**
HAMOCC3.1	3.5° × 3.5°	15	ALK[1], $CaCO_3$, DIC, $\delta^{13}C_{\mathrm{DIC}}$, DOC[2], POC, $\delta^{13}C_{\mathrm{POC}}$, phytoplankton, zooplankton, PO_4^{3-}, H_4SiO_4, O_2	Maier-Reimer (1993); Popp et al. (1989); Rau et al. (1996)
GFDL MOM	4° × 4°	12	ALK, DIC, $DI^{13}C$, DOC, $DO^{13}C$, PO_4^{3-}	Freeman and Hayes (1992)
CLIMBER-2	2.5° × 3 basins	20	ALK, DIC, $DI^{13}C$, $DI^{14}C$, fast and slow DOC, $DO^{13}C$, $DO^{14}C$, PO_4^{3-}, O_2	Rau et al. (1989)
MoBidiC	5° × 3 basins	19	ALK ,DIC, $DI^{13}C$, ^{14}C, DOC, $DO^{13}C$, PO_4^{3-}, O_2	Mook (1986))
PISCES	2° × 2°*	30	$CaCO_3$, CO_3^{2-}, DIC, ^{13}C (in the 3 dissolved and 7 particulate carbon pools), DOC, nanophytoplankon, diatoms, mesozooplankton, microzooplankton, 2 detrital classes, PO_4^{3-}, NO_3, H_4SiO_4, Fe	Laws et al. (1995)
Bern3D+C	36 cells × 36 cells	32	ALK, DIC, ^{13}C, ^{14}C, PO_4^{3-}, DOP[3], O_2, SiO_2, Fe	Freeman and Hayes (1992)
UVic	1.8° × 3.6°	19	ALK, DIC, ^{13}C (in the 5 carbon pools), phytoplankton (nitrogen fixers and other phytoplankton), zooplankton, detritus, PO_4^{3-}, NO_3, O_2	Popp et al. (1989)
iLOVECLIM	3° × 3°	20	ALK, $CaCO_3$, DIC, $\Delta^{14}C$, $\delta^{13}C$, DOC, slow DOC, POC, phytoplankton, zooplankton, PO_4^{3-}, NO_3, O_2	Freeman and Hayes (1992)
CESM	3° × 3°†	60	ALK, $CaCO_3$, DIC, abiotic ^{14}C (in the 7 carbon pools), biotic ^{14}C (in the 7 carbon pools), ^{13}C (in the 7 carbon pools), DOC, diazatrophs, diatoms, small phytoplankton, zooplankton, H_4SiO_4	Rau et al. (1989); Laws et al. (1995); Keller and Morel (1999)
CSIRO Mk3L-COAL	1.6° × 2.8°	21	ALK, DIC, $DI^{13}C$, ^{14}C, general phytoplankton diazotrophs, calcifiers, PO_4^{3-}, Fe, NO_3, $^{15}NO_3$, N_2O, O_2, abiotic O_2	Constant

* Mean resolution (enhanced meridional resolution at the equator)

† 3° × 3° for model development, 1° × 1° for scientific application

[1] ALK = Alkalinity, [2] DOC = Dissolved Organic Carbon, [3] DOP = Dissolved Organic Phosphate

photosynthetic CO_2 fixation (Section 3.2.2.2 and Section 3.3.3). We evaluate the overall performance of the model in simulating large-scale $\delta^{13}C_{DIC}$ distributions by comparing to modern observations (Section 3.3.2) and discuss the potential of the new ^{13}C tracer as a tuning target for future recalibration work (Section 3.3.4).

3.2 Methods

3.2.1 Model description

FAMOUS is a coupled ocean-atmosphere GCM based on the higher resolution HadCM3 (Gordon et al., 2000; Pope et al., 2000), a configuration of the UM version 4.5 (Jones et al., 2005; Smith et al., 2008a; Smith, 2012; Williams et al., 2013). The atmospheric model has a horizontal resolution of 5° × 7.5°, 11 vertical levels on a hybrid sigma-pressure coordinate system, and a 1 h timestep. The rigid-lid ocean model has a 12 h timestep, a horizontal resolution of 2.5° × 3.75°, and 20 vertical levels that vary in thickness from 10 m at the surface to more than 600 m at depth. The maximum depth of the ocean is 5500 m. The ocean and atmosphere are coupled once per model day. At the time of this study, FAMOUS is capable of simulating 400 to 500 model years per wallclock day on Tier 2 (regional) and Tier 3 (local) High Performance Computers at the University of Leeds, which makes it ideal for running multi-millennial simulations (Smith and Gregory, 2012; Gregoire et al., 2012, 2015) or large ensembles (Gregoire et al., 2011; Sagoo et al., 2013). The model currently includes oxygen (Williams et al., 2014) and chlorofluorocarbons (Pope et al., 2000) as optional tracers. Further technical documentation can be found in an ongoing special issue in Geoscientific Model Development (`http://www.geosci-model-dev.net/special_issue15.html`).

We added ^{13}C as an optional passive tracer into the ocean component of FAMOUS, using the Met Office Surface Exchange Scheme (MOSES) version 1 (Cox et al., 1999) generation of the model to evaluate our scheme. Although a newer version of the land surface model exists, which includes the terrestrial carbon cycle and interactive vegetation (MOSES2.2; Essery et al., 2001, 2003; Williams et al., 2013; Valdes et al., 2017), problems have been identified with its representation of Meridional Overturning Circulation (MOC) in multi-millennial simulations with constant pre-industrial boundary conditions (Dentith et al., 2019). Specifically, FAMOUS-MOSES2.2 simulates a collapsed Atlantic MOC (AMOC) and a strong, deep Pacific MOC when the run length exceeds 6000 years, resulting in spurious ocean tracer distributions. However, our code is directly transferable between the different generations of the model, meaning that the isotope system can be extended into the terrestrial carbon cycle following additional tuning to improve the physical ocean circulation in FAMOUS-MOSES2.2.

3.2.1.1 Hadley Centre Ocean Carbon Cycle Model (HadOCC)

The marine carbon cycle in FAMOUS is modelled by HadOCC, a coupled physical-biogeochemical model that simulates air-sea gas exchange, the circulation of DIC, and the cycling of carbon by marine biota (Palmer, 1998; Palmer and Totterdell, 2001). The ecosystem model provides a simplified representation of the ocean biological system, with a single (nitrogenous) nutrient, a single class of phytoplankton, a single class of (non-migrating) zooplankton, and detritus. Changes in the size of these pools are calculated through a series of coupled differential equations that describe primary production, respiration, mortality, grazing, excretion, and the sinking and remineralisation of detritus. The system is nitrogen limited and carbon flows are coupled to the nitrogen flows by stoichiometric ratios that are fixed for each pool of organic matter. In addition to the four biological components, HadOCC also explicitly simulates DIC and alkalinity. Modelled DIC concentrations depend upon phytoplankton growth and biological breakdown. Alkalinity is similarly affected by biological processes and is used to calculate the proportion of DIC that is in the form of CO_2 in the surface waters, and consequently the air-sea CO_2 flux. All six tracers are advected, diffused, and mixed across all levels, although phytoplankton and zooplankton concentrations are negligible below the euphotic zone (approximately the uppermost 100 m of the ocean). Detritus is the only biological tracer that is subject to sinking, which is parameterised at a constant rate of $10\,\mathrm{m\,d^{-1}}$. However, there is no representation of sediments: any detrital material that reaches the ocean floor is therefore immediately refluxed back to the top layer of the ocean to conserve carbon and nitrogen. Calcium carbonate ($CaCO_3$) production is represented as an instantaneous redistribution of DIC and alkalinity below the lysocline, the depth of which is spatially and temporally constant ($\approx$2500 m below sea level).

HadOCC accurately simulates low primary production in the sub-tropical gyres and high production in the regions with the greatest nutrient supply: the sub-polar North Pacific and North Atlantic Oceans, and around the Antarctic Convergence Zone (Figure 3.1). However, primary production is higher than observed in the eastern equatorial Pacific, which is attributed to excessive upwelling in the model (Palmer and Totterdell, 2001). Production is lower than observed northwards of 50° N in the Atlantic and Pacific basins because sea ice formation and melt do not affect salinity distributions. Consequently, stably stratified, low salinity layers of meltwater, which promote phytoplankton growth, are not represented in the model (Palmer and Totterdell, 2001). Furthermore, the simulated production in coastal regions is lower than observed. There are three main reasons for this: (1) HadOCC does not simulate riverine input of nutrients, which are a significant source of coastal nutrients; (2) most of the coastlines in FAMOUS are directly adjacent to ocean grid points that are more than 1 km deep, which dilutes near-surface nutrient concentrations; and (3) upwelling is spread out over several grid points, which causes production to be more diffuse than observed (Palmer and Totterdell, 2001).

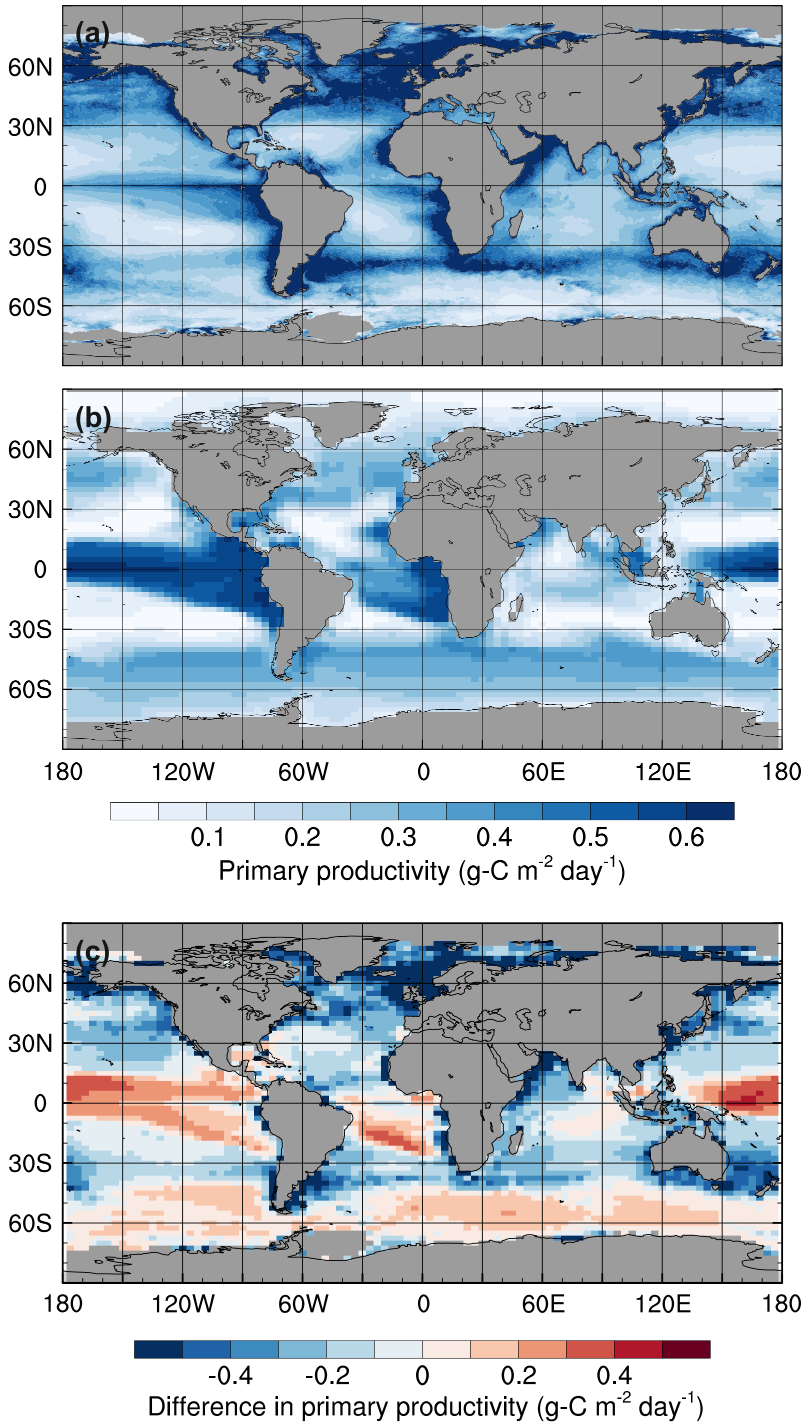

Figure 3.1: Mean annual surface primary productivity: (a) observations estimated from surface chlorophyll concentrations using the Vertically Generalised Production Model (Behrenfeld and Falkowski, 1997), (b) the *std* simulation in the 1990s, and (c) simulated minus observed. Monthly mean primary productivity data were obtained from the Oregon State University Ocean Productivity website (`http://www.science.oregonstate.edu/ocean.productivity`).

The level of representation of ecosystem processes in HadOCC is of intermediate complexity, making it computationally faster than more sophisticated ecosystem models that include additional POC species and/or multiple nutrients (e.g. PISCES). Errors in biogeochemical simulations are largely driven by biases in the physical ocean circulation (i.e. inaccuracies in the climate or ocean model to which the ecosystem model has been coupled; Doney, 1999; Doney et al., 2004; Najjar et al., 2007). Thus, simulating carbon isotopes in a more complex ecosystem model would not necessarily yield substantially better results.

3.2.2 Carbon isotope implementation

We added ^{13}C to the four carbon pools in HadOCC: DIC, phytoplankton, zooplankton, and detritus (Figure 3.2). We assume that modelled DIC is ^{12}C and carry ^{13}C as a ratio ($\mathrm{DI^{13}C/DI^{12}C}$), therefore virtual fluxes are not required to account for the dilution or concentration effects of surface freshwater fluxes (Appendix B.1). We also use model units to minimise the error associated with carrying small numbers:

$$\text{Model units} = \frac{\mathrm{DI^{13}C}}{\mathrm{DI^{12}C}} \times \frac{100}{\frac{^{13}\mathrm{C}}{^{12}\mathrm{C}}_{\mathrm{std}}} \tag{3.1}$$

where $^{13}\mathrm{C}/^{12}\mathrm{C}_{\mathrm{std}} = 1.123\,72 \times 10^{-2}$ (Craig, 1957). We account for isotopic fractionation during air-sea gas exchange (Section 3.2.2.1 and Appendix B.2) and photosynthesis (Section 3.2.2.2 and Appendix B.3). Observational estimates suggest that isotopic fractionation during $CaCO_3$ formation is between 3 ‰ and −2 ‰ (Ziveri et al., 2003), which is small compared to the other fractionation effects (Turner, 1982). Previous ^{13}C isotope implementation studies have therefore assumed either no isotopic fractionation during $CaCO_3$ production (Schmittner et al., 2013) or prescribed constant values, for example, 1 ‰ (Tagliabue and Bopp, 2008) or 2 ‰ (Jahn et al., 2015). We conducted sensitivity tests where fractionation during $CaCO_3$ formation was included at constant rates of −2 ‰, 0 ‰ and 2 ‰, respectively. After 10,000 years, there was 0.001 ‰ difference in both the mean surface ocean $\delta^{13}C_{\mathrm{DIC}}$ values and the surface standard deviations between all three simulations, and 0.02 ‰ difference between the three global volume-weighted integrals. Since these differences are small, we proceeded with the equivalent of no fractionation during $CaCO_3$ production ($\alpha_{\mathrm{CaCO3}} = 1.0$).

3.2.2.1 Air-sea gas exchange

The air-sea gas flux of $\mathrm{DI^{12}C}$ (F) is calculated as:

$$F = PV \times (C_{\mathrm{sat}} - C_{\mathrm{surf}}) \tag{3.2}$$

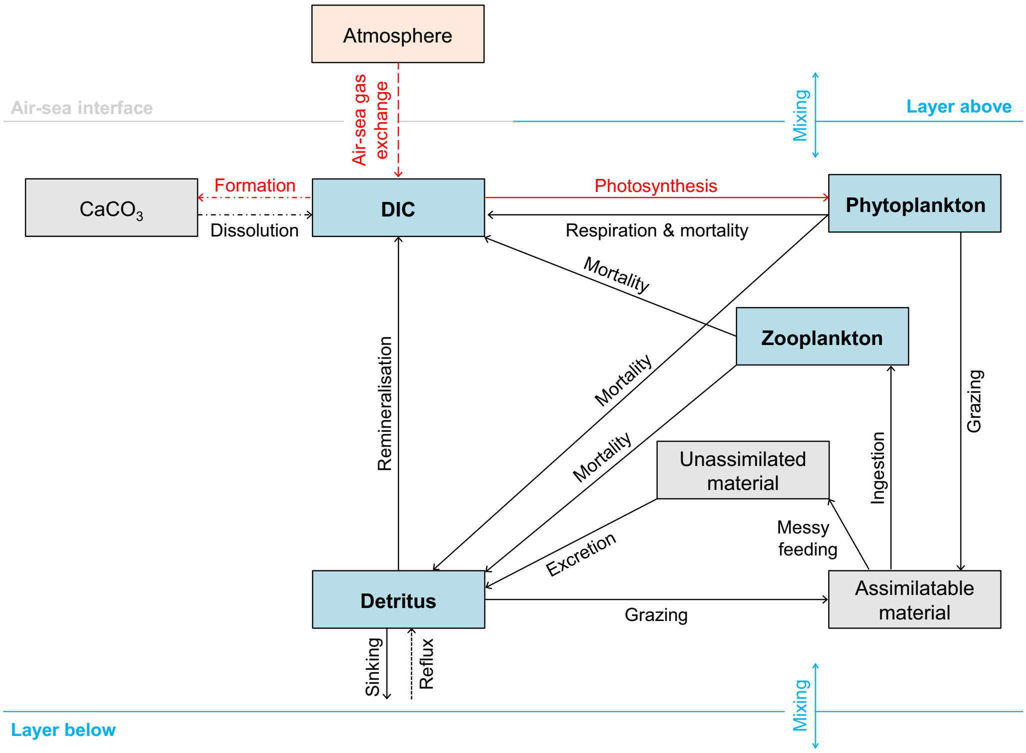

Figure 3.2: Schematic overview of the ^{13}C implementation in HadOCC. Blue boxes represent permanent carbon pools. Grey boxes represent temporary carbon pools. The orange box represents the prescribed atmospheric carbon pool. The dashed line represents fluxes of ^{13}C/^{12}C. Solid lines represent fluxes of ^{13}C. Dot-dashed lines represent processes that occur below the lysocline (≈2500 m below sea level). The dotted line represents the reflux of detrital material from the seafloor to the surface layer. Red lines represent fractionation effects. Note that all simulations presented in this study were run without fractionation during calcium carbonate formation ($\alpha_{\mathrm{CaCO3}} = 1.0$).

where C_{sat} is the saturation concentration of atmospheric CO_2 (in $\text{mol}\,\text{m}^{-3}$), C_{surf} is the surface aqueous CO_2 concentration (in $\text{mol}\,\text{m}^{-3}$), and PV is the piston velocity (in $\text{cm}\,\text{h}^{-1}$), which is calculated as:

$$PV = a \times u^2 \times (1 - a_{\text{ice}}) \times \left(\frac{Sc}{660}\right)^{-0.5} \tag{3.3}$$

where a is a tuneable coefficient, u is the wind speed (in $\text{m}\,\text{s}^{-1}$), a_{ice} is the fractional ice cover and Sc is the Schmidt number for CO_2, calculated as a function of sea surface temperature (SST, in °C):

$$Sc = 2073.1 - 125.62 \times SST + 3.6276 \times SST^2 - 0.043219 \times SST^3. \tag{3.4}$$

The air-sea gas flux of $\text{DI}^{13}\text{C}/\text{DI}^{12}\text{C}$ ($F_{13/12}$) is calculated as:

$$\begin{aligned} F_{\frac{13}{12}} = \frac{1}{{}^{12}C} \times PV \times \Bigg[\alpha_{\text{k}} \times \alpha_{\text{aq}\leftarrow\text{g}} \times \left(C_{\text{sat}} \times \frac{{}^{13}A}{{}^{12}A} - \frac{C_{\text{surf}} - \frac{{}^{13}C}{{}^{12}C}}{\alpha_{\text{DIC}\leftarrow\text{g}}}\right) \\ - \left(\frac{{}^{13}C}{{}^{12}C} \times [C_{\text{sat}} - C_{\text{surf}}]\right)\Bigg] \end{aligned} \tag{3.5}$$

where ${}^{13}A/{}^{12}A$ and ${}^{13}C/{}^{12}C$ are the ${}^{13}\text{C}/{}^{12}\text{C}$ ratios of the atmosphere and DIC, respectively, α_{k} is the constant kinetic fractionation factor (0.99919), $\alpha_{\text{aq}\leftarrow\text{g}}$ is the temperature-dependent fractionation during gas dissolution:

$$\alpha_{\text{aq}\leftarrow\text{g}} = 0.9986 - (4.9 \times 10^{-6}) \times SST, \tag{3.6}$$

and $\alpha_{\text{DIC}\leftarrow\text{g}}$ is the temperature-dependent fractionation between aqueous CO_2 and DIC:

$$\alpha_{\text{DIC}\leftarrow\text{g}} = 1.01051 - (1.05 \times 10^{-4}) \times SST. \tag{3.7}$$

All three fractionation factors are based on the equations of Zhang et al. (1995). However, following Schmittner et al. (2013), we neglect the effect that the carbonate fraction ($f CO_3$) has on $\alpha_{\text{DIC}\leftarrow\text{g}}$ because this is much smaller (0.05 ‰) than the temperature effect (3 ‰). Currently, atmospheric CO_2 and δ^{13}C concentrations can either be held constant or prescribed from a file that contains a single global weighted-average value per year.

3.2.2.2 Photosynthesis

Isotopic fractionation during photosynthesis ($\alpha_{\text{POC}\leftarrow\text{DIC}}$, herein α_{p}) is calculated as:

$$\alpha_{\text{p}} = \frac{\alpha_{\text{aq}\leftarrow\text{g}}}{\alpha_{\text{DIC}\leftarrow\text{g}}} \times \alpha_{\text{POC}\leftarrow\text{aq}} \tag{3.8}$$

where $\alpha_{\mathrm{POC}\leftarrow\mathrm{aq}}$ is the equilibrium fractionation factor between aqueous CO_2 and particulate organic carbon (POC).

Empirical relationships for the different biogeochemical fractionation effects ($\alpha_{\mathrm{aq}\leftarrow\mathrm{g}}$, $\alpha_{\mathrm{DIC}\leftarrow\mathrm{g}}$, and $\alpha_{\mathrm{POC}\leftarrow\mathrm{aq}}$) have been established from laboratory experiments, modern oceans and lakes, and the sedimentary record. However, there are still uncertainties associated with the parameterisation of $\alpha_{\mathrm{POC}\leftarrow\mathrm{aq}}$. Early studies investigated a potential temperature dependence of the carbon isotope composition of marine phytoplankton. For example, Sackett et al. (1965) proposed that photosynthetic fractionation is higher at lower temperatures (0.23 ‰ per °C) after observing that phytoplankton in the Drake Passage had more negative δ^{13}C values than those in the tropics. Wong and Sackett (1978) also recorded small temperature effects (-0.13 to 0.36 ‰ per °C) in 17 species of marine phytoplankton; however, the authors concluded that the 15 ‰ range observed in their samples was primarily related to different metabolic pathways within the organisms. Numerous studies have suggested that the fractionation of carbon isotopes during photosynthetic CO_2 fixation relates to aqueous CO_2 concentrations (CO_2^*) in the ambient environment (Popp et al., 1989; Rau et al., 1989; Jasper and Hayes, 1990; Hollander and McKenzie, 1991; Freeman and Hayes, 1992). However, these studies assumed that CO_2 only enters the phytoplankton by passive diffusion and neglected physiological effects, such as phytoplankton growth rate, cell size and geometry, and cell membrane permeability. Taking into consideration that physiological factors may modify, weaken, or eliminate the relationship between CO_2^* and photosynthetic fractionation, Rau et al. (1996) proposed a model that accounted for the isotopic composition of the ambient aqueous CO_2, isotopic fractionation associated with diffusive transport into the cell, and isotopic fractionation associated with enzymatic, intracellular fixation. Laws et al. (1995) identified a linear relationship between phytoplankton growth rate, CO_2^* and isotopic fractionation during photosynthesis, under the assumption that the growth rate is proportional to the net transport of CO_2 into the cell. A later study by Laws et al. (1997), which analysed the same species of marine diatom over a larger range of CO_2^*, revised this to a non-linear relationship. Burkhardt et al. (1999) and Keller and Morel (1999) additionally included active bicarbonate transport in their calculations, recognising that aqueous CO_2 is not the only substrate for photosynthetic fixation and that processes other than diffusion can contribute to inorganic carbon acquisition. This has been a relatively inactive research area in the last 20 years, but there remains no single accepted model for fractionation during photosynthesis.

Consequently, previous carbon isotope implementation studies have used a number of different parameterisations for biological fractionation (Table 3.1), with the choice of scheme largely reflecting the complexity of the simulated biogeochemical and ecosystem processes. It is difficult to compare the success of the different parameterisations used by individual modelling groups because inter-model differences in the simulated isotopic distributions predominantly relate to resolution, complexity, and biases in the physical ocean circulation and ocean biogeochemistry, as opposed to the choice of fractionation scheme. However, Hofmann et al. (2000) tested three different fractionation schemes within a single model. In their study, the oversimplified assumption of constant biological fractionation, taken from Maier-Reimer (1993), failed to reproduce the observed latitudinal gradients in $\delta^{13}C_{POC}$. Calculating the fractionation as a function of CO_2^*, as per Popp et al. (1989), successfully replicated the interhemispheric asymmetry in $\delta^{13}C_{POC}$, but a growth rate dependent fractionation (e.g. Rau et al., 1996) was required to additionally capture the seasonal variations. Jahn et al. (2015) also demonstrated differences between three different fractionation schemes within a single model. In their study, the simple scheme of Rau et al. (1989) produced lower $\delta^{13}C_{DIC}$ values in the surface ocean and higher $\delta^{13}C_{DIC}$ values below 150 m compared to the more complex parameterisations of Laws et al. (1995) and Keller and Morel (1999). The differences between the intermediate complexity formulation (Laws et al., 1995) and the most complex formulation (Keller and Morel, 1999) were small, and the Laws et al. (1995) equation was chosen as the default scheme.

To account for the uncertainty associated with biological fractionation in FAMOUS, we tested three different parameterisations for $\alpha_{POC \leftarrow aq}$. In the standard simulation (*std*), we calculated $\alpha_{POC \leftarrow aq}$ according to Popp et al. (1989):

$$\alpha_{POC \leftarrow aq} = -0.017 log(CO_2^*) + 1.0034 \tag{3.9}$$

where CO_2^* is the aqueous CO_2 concentration (in $\mu mol\,l^{-1}$). Both of the alternative parameterisations calculated $\alpha_{POC \leftarrow aq}$ as a function of the phytoplankton specific growth rate (μ) and CO_2^*, representing an increase in complexity relative to the standard scheme. The first was a linear relationship derived from the experimental results of Laws et al. (1995):

$$\alpha_{POC \leftarrow aq} = \frac{-15}{\left(\frac{\mu}{CO_2^*}\right) - 15.371}. \tag{3.10}$$

The second was a non-linear relationship derived from the experimental results of Laws et al. (1997):

$$\alpha_{POC \leftarrow aq} = \frac{1 + \left(\frac{\mu}{0.225 CO_2^*}\right)}{1.0268 + 1.005\left(\frac{\mu}{0.225 CO_2^*}\right)}. \tag{3.11}$$

Because HadOCC is a relatively simple ecological model, with only a single representation of phytoplankton, we did not test more complex schemes, such as those that use phytoplankton type-specific cell parameters (e.g. Burkhardt et al., 1999; Keller and Morel, 1999).

3.2.2.3 Advection

The default advection scheme in FAMOUS is Quadratic Upstream Interpolation for Convective Kinematics (QUICK) with flux limiter (Leonard, 1993). This scheme is used to compute the transport of tracers such as temperature, salinity, nutrients, and DIC throughout the ocean. For consistency, we use the same advection scheme to calculate ^{13}C concentrations in the ocean interior. For greater numerical stability, $\delta^{13}C_{DIC}$ is fixed at 0 ‰ in the Hudson Bay and Baltic Sea. With the model's standard pre-industrial land-sea mask, these inland bodies of water are isolated from the global oceans, therefore their isotope concentrations will not affect large-scale tracer distributions.

3.2.3 Simulations

3.2.3.1 Spin-up simulation

Carbon isotope simulations must be spun-up over multiple millennia (5000 to 15,000 years; Orr et al., 2000) to reach steady state because of the long timescale of deep ocean ventilation (Bardin et al., 2014). We therefore ran our spin-up simulation for 10,000 years with constant pre-industrial boundary conditions, where $\delta^{13}C_{atm}$ was fixed at -6.5 ‰ (Francey et al., 1999) and $\delta^{13}C_{ocn}$ was initialised at a globally uniform value of 0 ‰. The global volume-weighted integral of $\delta^{13}C_{DIC}$ started to stabilise after 7000 years, and at the end of the spin-up simulation, the drift was less than 0.001 ‰ yr^{-1} (Figure C.1).

3.2.3.2 Historical simulation

A transient simulation for the period 1765 to 2000 CE was initialised from the end of the spin-up simulation to generate model output that is directly comparable to modern observations (Figure 3.3). Atmospheric CO_2 concentrations were prescribed from the OCMIP-2 files (Orr et al., 2000) and $\delta^{13}C_{atm}$ was prescribed from the Law Dome and South Pole ice core records (Rubino et al., 2013). The decrease in $\delta^{13}C_{atm}$ from -6.5 ‰ in 1750 to approximately -8.0 ‰ in 2000 is due to the Suess effect. First observed in tree ring records of atmospheric composition, the Suess effect refers to the dilution of ^{13}C in any carbon pool due to fossil fuel burning (Suess, 1955; Keeling, 1979). Fossil fuels formed millions of years ago from organic matter, which is relatively ^{13}C-depleted due to isotopic fractionation during photosynthesis. Their isotopic signature is therefore approximately 20 ‰ lower than that of the ambient atmosphere (Andres et al., 1994, 1996). To act as a control, the spin-up simulation was continued for an additional 235 years with constant CO_2 and $\delta^{13}C_{atm}$.

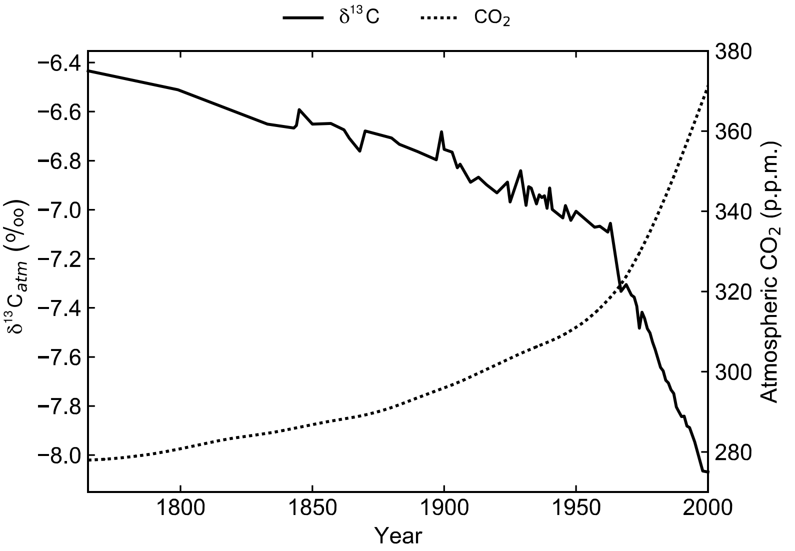

Figure 3.3: Prescribed atmospheric δ^{13}C values (solid) from the Law Dome and South Pole ice core records (Rubino et al., 2013) and prescribed atmospheric CO_2 values (dashed) from the OCMIP-2 files (Orr et al., 2000).

3.2.3.3 Sensitivity experiments

Five further simulations were conducted to quantify the effects of fractionation during air-sea gas exchange and primary productivity on the simulated $\delta^{13}C_{DIC}$ distributions. All five simulations were run for 10,000 years with constant pre-industrial boundary conditions. In each of the simulations, $\delta^{13}C_{atm}$ was fixed at −6.5 ‰ and $\delta^{13}C_{ocn}$ was initialised at 0 ‰. At the end of each of the spin-up simulations, the global volume-weighted $\delta^{13}C_{DIC}$ integral was drifting by less than 0.001 ‰ yr^{-1}.

Three of the simulations were designed to quantify the effects of the individual processes outlined in Section 3.2.2 (Table 3.2). In the *ki-fract-only* simulation, $\alpha_{aq\leftarrow g}$, $\alpha_{DIC\leftarrow g}$, and α_p were all set to 1, therefore only kinetic fractionation effects were calculated. In the *no-asgx-fract* simulation, α_k, $\alpha_{aq\leftarrow g}$, and $\alpha_{DIC\leftarrow g}$ were all set to 1 to eliminate the effect of fractionation during air-sea gas exchange. Fractionation during photosynthesis continued to be calculated using the *std* biological fractionation scheme, as per Eq. (3.8 - 3.9). In the *no-bio-fract* simulation, α_p was set to 1 to remove the effect of fractionation during photosynthesis, but fractionation during air-sea gas exchange continued to be calculated as per Eq. (3.5 - 3.7).

The other two simulations were designed to assess the sensitivity of the simulated $\delta^{13}C_{DIC}$ distributions to the choice of biological fractionation scheme (Section 3.2.2.2). In the *L95* simulation, $\alpha_{POC\leftarrow aq}$ was calculated using Eq. (3.10), whilst in the *L97* simulation, $\alpha_{POC\leftarrow aq}$ was calculated using Eq. (3.11). As with the *std* simulation, we initialised a 235 year transient simulation (with the ^{13}C-Suess effect) from the end of both of these spin-ups to allow the output from all three photosynthetic fractionation schemes to be compared directly to observations.

Table 3.2: Overview of the fractionation factors used in the sensitivity experiments.

Simulation	$\alpha_{\mathbf{k}}$	$\alpha_{\mathbf{aq\leftarrow g}}$, $\alpha_{\mathbf{DIC\leftarrow g}}$	$\alpha_{\mathbf{p}}$
std	Standard[1]	Variable[2]	Variable[3]
ki-fract-only	Standard	1	1
no-asgx-fract	1	1	Variable
no-bio-fract	Standard	Variable	1

[1] 0.99919

[2] Calculated as per Eq. (3.6 – 3.7)

[3] With $\alpha_{\mathrm{POC}\leftarrow \mathrm{aq}}$ calculated as per Eq. (3.9)

3.3 Results and discussion

3.3.1 Validating the isotope scheme

Isolating the different fractionation effects allows us to assess the relative contribution of air-sea gas exchange and biology to the simulated $\delta^{13}\mathrm{C}_{\mathrm{DIC}}$ distributions, and validate that the new isotope scheme is responding to physical and biogeochemical processes as expected. If there is no fractionation during either air-sea gas exchange or photosynthesis, the ocean equilibrates at a uniform value of −6.5 ‰, in line with the atmosphere. Kinetic fractionation has only a minor effect on surface ocean $\delta^{13}\mathrm{C}_{\mathrm{DIC}}$ distributions, with simulated $\delta^{13}\mathrm{C}_{\mathrm{DIC}}$ values in the *ki-fract-only* simulation ranging between −6.57 ‰ in the Labrador Sea and −6.42 ‰ in the eastern equatorial Pacific (Figure 3.4a). This represents a −0.07 ‰ to 0.08 ‰ shift relative to no isotopic fractionation. Specifically, there is $^{13}\mathrm{C}$ depletion (low $\delta^{13}\mathrm{C}_{\mathrm{DIC}}$) in areas of net CO_2 invasion, such as the extra-tropics and high latitudes, and $^{13}\mathrm{C}$ enrichment (high $\delta^{13}\mathrm{C}_{\mathrm{DIC}}$) in the equatorial upwelling zones and the deep water formation regions where CO_2 is being outgassed. Kinetic fractionation has a negligible effect on the $\delta^{13}\mathrm{C}_{\mathrm{DIC}}$ depth profile, with globally averaged $\delta^{13}\mathrm{C}_{\mathrm{DIC}}$ values of −6.4955 ‰ in the surface ocean and −6.5011 ‰ in the abyssal ocean (Figure 3.5).

When both the equilibrium and kinetic fractionation effects are included during air-sea gas exchange (*no-bio-fract*), the large-scale $\delta^{13}\mathrm{C}_{\mathrm{DIC}}$ distributions are closely related to the SST patterns because of the temperature dependence of $\alpha_{\mathrm{aq}\leftarrow \mathrm{g}}$ and $\alpha_{\mathrm{DIC}\leftarrow \mathrm{g}}$ (Figure 3.4b). Relatively high $\delta^{13}\mathrm{C}_{\mathrm{DIC}}$ values (>2.5 ‰) are simulated in the Southern Ocean due to combined effect of CO_2 outgassing and low SSTs, both of which cause $^{13}\mathrm{C}$ enrichment. The $\delta^{13}\mathrm{C}_{\mathrm{DIC}}$ values in the Arctic Ocean are comparably low because the model has more extensive sea ice in the Northern Hemisphere than in the Southern Hemisphere, which inhibits air-sea gas exchange. The highest values (3.00 ‰) are simulated in the eastern equatorial Pacific where there are high rates of net CO_2 outgassing and Antarctic Bottom Water (AABW), which has a high $\delta^{13}\mathrm{C}_{\mathrm{DIC}}$ signature, is upwelled. Low $\delta^{13}\mathrm{C}_{\mathrm{DIC}}$ values are simulated in the Indian Ocean, with the lowest values (1.1 ‰) in South East Asia, because the sea surface is warmer than at the equivalent latitudes in the Atlantic and Pacific

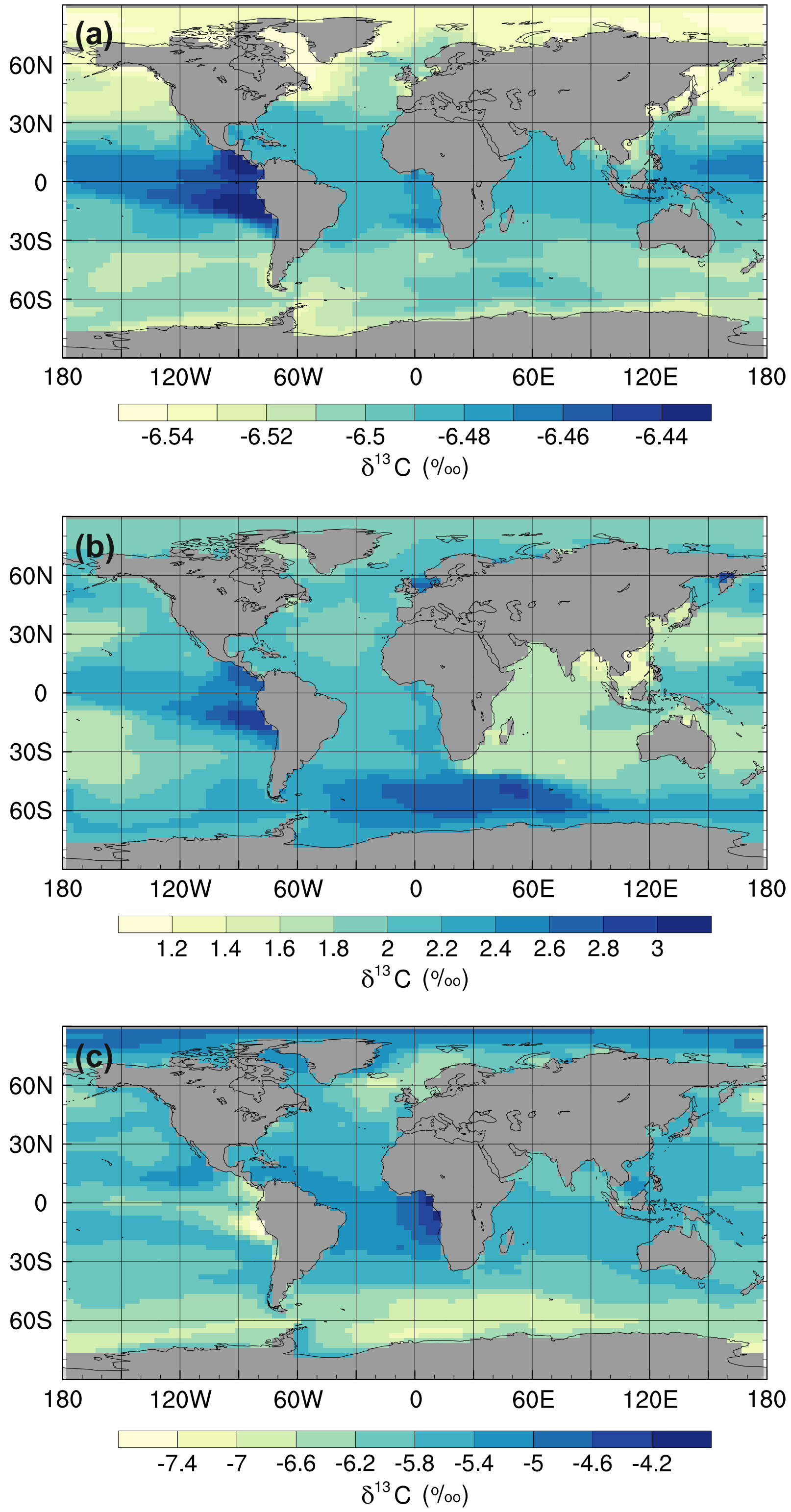

Figure 3.4: Mean annual surface $\delta^{13}C_{\mathrm{DIC}}$ values at the end of the sensitivity experiment spin-up simulations (years 9900 to 10,000): (a) *ki-fract-only*, (b) *no-bio-fract*, and (c) *no-asgx-fract*.

Oceans. The globally averaged $\delta^{13}C_{DIC}$ values in this simulation range between 2.03 ‰ in the surface ocean and 2.16 ‰ in the deep ocean, with a minimum value of 2.00 ‰ at a depth of approximately 200 m (Figure 3.5). Below approximately 1500 m, the globally averaged $\delta^{13}C_{DIC}$ is near constant with depth, matching the simulated temperature profile.

In the *no-asgx-fract* simulation, $\delta^{13}C_{DIC}$ values in the surface ocean range between −7.65 ‰ in the eastern equatorial Pacific and −3.89 ‰ in the eastern equatorial Atlantic (Figure 3.4c), representing a shift of −1.15 ‰ to 2.61 ‰ relative to no isotopic fractionation. The asymmetry between these two upwelling zones occurs because the waters that are being upwelled from the deep Pacific Ocean are approximately 600 years older than the equivalent waters in the Atlantic Ocean. They therefore contain a higher percentage of remineralised organic matter, which is enriched in ^{12}C. Relatively low $\delta^{13}C_{DIC}$ values are also simulated in the Southern Ocean and northeast North Atlantic Ocean where older water is mixed upwards from the abyssal ocean to the surface ocean at sites of deep water formation. The globally averaged $\delta^{13}C_{DIC}$ values in this simulation range between −5.85 ‰ in the productive surface ocean and −7.56 ‰ in the abyssal ocean, with a minimum value of −7.86 ‰ at a depth of approximately 1000 m, which corresponds to the depth of maximum remineralisation in the model (Figure 3.5). The values change from greater than −6.5 ‰ (enriched in ^{13}C relative to no fractionation) to less than −6.5 ‰ (depleted in ^{13}C relative to no fractionation) at a depth of approximately 100 m, which corresponds to the photic zone.

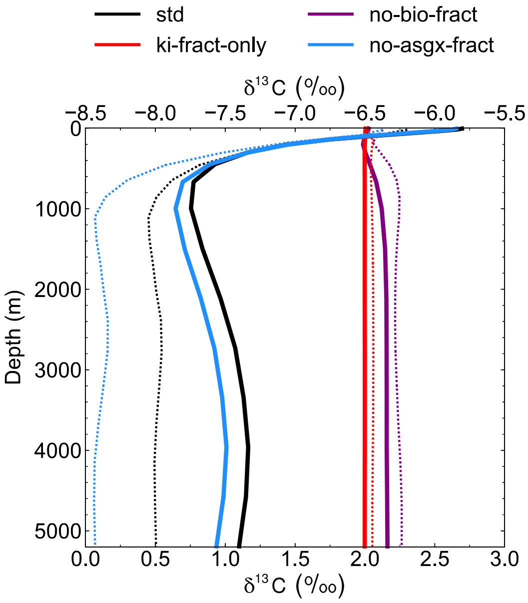

Figure 3.5: Depth profiles of globally averaged $\delta^{13}C_{DIC}$ at the end of the sensitivity experiment spin-up simulations (years 9900 to 10,000). The *std* (black) and *no-bio-fract* (purple) simulations use the bottom axis, whilst the *ki-fract-only* (red) and *no-asgx-fract* (blue) simulations use the top axis. The dotted lines are the equivalent simulations conducted by Schmittner et al. (2013) with the UVic ESM: *std* (black) and *no-bio* (purple) on the bottom axis; *ki-only* (red) and *const-gasx* (blue) on the top axis.

The spatial patterns in the *std* simulation and the *no-asgx-fract* simulation are closely matched, both in the surface ocean (Figure 3.6) and at depth (Figure 3.5), demonstrating the importance of biology to the large-scale $\delta^{13}C_{DIC}$ distributions. However, in the surface layer, air-sea gas exchange partly compensates for the biological effects in the Southern Ocean, the Northern Hemisphere deep water formation region, and the equatorial upwelling zones, as inferred from the peak surface zonal mean $\delta^{13}C_{DIC}$ values at 60° S, 55° N and 0° in the *no-bio-fract* simulation, which correspond with reduced amplitude troughs in the *std* simulation relative to the *no-asgx-fract* simulation. Similar results pertaining to the relative influence of air-sea gas exchange and biology were presented by Schmittner et al. (2013), who concluded that air-sea gas exchange and temperature-dependent fractionation reduce the spatial $\delta^{13}C_{DIC}$ gradients created by biology. Earlier work by Murnane and Sarmiento (2000) and Schmittner et al. (2013) also supports the notion that biology is the dominant factor controlling $\delta^{13}C_{DIC}$ distributions in the interior ocean. Overall, the sensitivity experiments demonstrate that the new carbon isotope scheme is accurately responding to physical and biogeochemical processes in the model, such as temperature, air-sea gas exchange, and the biological pump.

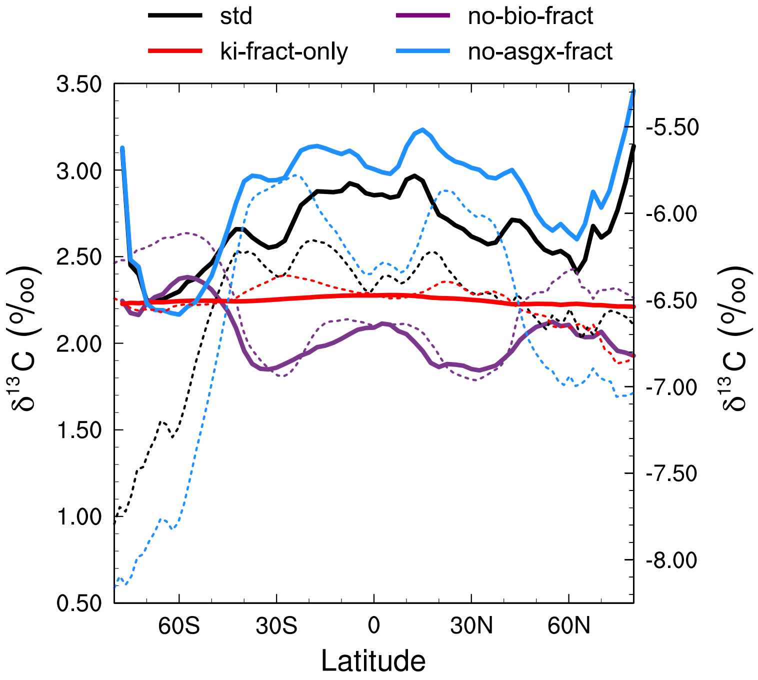

Figure 3.6: Zonally averaged mean annual surface $\delta^{13}C_{DIC}$ at the end of the sensitivity experiment spin-up simulations (years 9900 to 10,000). The *std* (black) and *no-bio-fract* (purple) simulations use the left-hand axis, whilst the *ki-fract-only* (red) and *no-asgx-fract* (blue) simulations use the right-hand axis. The dotted lines are the equivalent simulations conducted by Schmittner et al. (2013) with the UVic ESM: *std* (black) and *no-bio* (purple) on the left-hand axis; *ki-only* (red) and *const-gasx* (blue) on the right-hand axis.

3.3.2 Comparison to observations

To assess the model performance in representing large-scale ^{13}C distributions, we compare the simulated mean $\delta^{13}C_{DIC}$ values for the 1990s with observations from GLODAP version 2 (v2; Key et al., 2015; Olsen et al., 2016) and the gridded global ocean climatology of Eide et al. (2017). The $\delta^{13}C_{DIC}$ values in the *std* simulation are, on average, 0.97 ‰ higher than the GLODAPv2 observations in the surface ocean (Figure 3.7) and 0.64 ‰ higher globally, with root mean square error (RMSE) values of 1.03 ‰ and 0.91 ‰, respectively. However, the simulated range in the surface ocean (3.2 ‰) is in excellent agreement with the observed range (3.3 ‰). Specifically, the simulated surface $\delta^{13}C_{DIC}$ values are between 1.4 ‰ and 4.6 ‰, with a mean value of 2.6 ‰, whilst the observed surface $\delta^{13}C_{DIC}$ values range between −0.3 ‰ and 3.0 ‰, with a mean value of 1.5 ‰.

Re-examining the results of the sensitivity experiments allows us to ascertain the underlying causes of the model-data discrepancy. Schmittner et al. (2013, herein *S13*) conducted a similar set of simulations with the UVic ESM to elucidate the relative influence of biology and air-sea gas exchange on the distribution of oceanic $\delta^{13}C_{DIC}$ (see Table 1 in *S13*). Overall, there is good agreement between our *ki-fract-only* and *no-bio-fract* simulations and the equivalent simulations in *S13* (*ki-fract* and *no-bio*, respectively), both in the surface ocean (Figure 3.6) and at depth (Figure 3.5). However, there is a clear difference between the results of our *no-asgx-fract* simulation and the equivalent simulation in *S13* (*const-gasx*). Specifically, the surface ocean zonal mean $\delta^{13}C_{DIC}$ values in our *no-asgx-fract* simulation range between −6.6 ‰ at 60° S and −5.5 ‰ in the sub-tropics, with a local minimum of −5.8 ‰ at the equator (solid blue line in Figure 3.6). For comparison, the surface ocean zonal mean values in *const-gasx* range between −8.0 ‰ in the Southern Ocean and −5.75 ‰ in the Southern Hemisphere sub-tropics, with a localised minimum of −6.25 ‰ at the equator (dotted blue line in Figure 3.6). Similarly, whilst the globally averaged deep ocean $\delta^{13}C_{DIC}$ values in our *no-asgx-fract* simulation have a comparable range (2.01 ‰) to the deep ocean values in *const-gasx*, there is an offset of approximately 1 ‰, with *S13* simulating $\delta^{13}C_{DIC}$ values of −6.4 ‰ in the surface ocean, −8.4 ‰ in the deep ocean, and near constant values below 1000 m (blue lines in Figure 3.5). Overall, the $\delta^{13}C_{DIC}$ values in the standard simulation with the UVic ESM are in good agreement with observations, with a global linear regression r^2 value of 0.91 and a global RMSE of 0.33 ‰ (Schmittner et al., 2013; Buchanan et al., 2019). We therefore postulate that the $\delta^{13}C_{DIC}$ biases in FAMOUS relate to biases in the biological carbon cycle.

Elucidating the exact cause of $\delta^{13}C_{DIC}$ model-data discrepancy is difficult. There are a number of fluxes in to and out of the DI^{13}C pool (Figure 3.2), each of which could have biases that are compounding or reducing the overall $\delta^{13}C_{DIC}$ bias. For example, if any of the rates of phytoplankton respiration, phytoplankton mortality or zooplankton

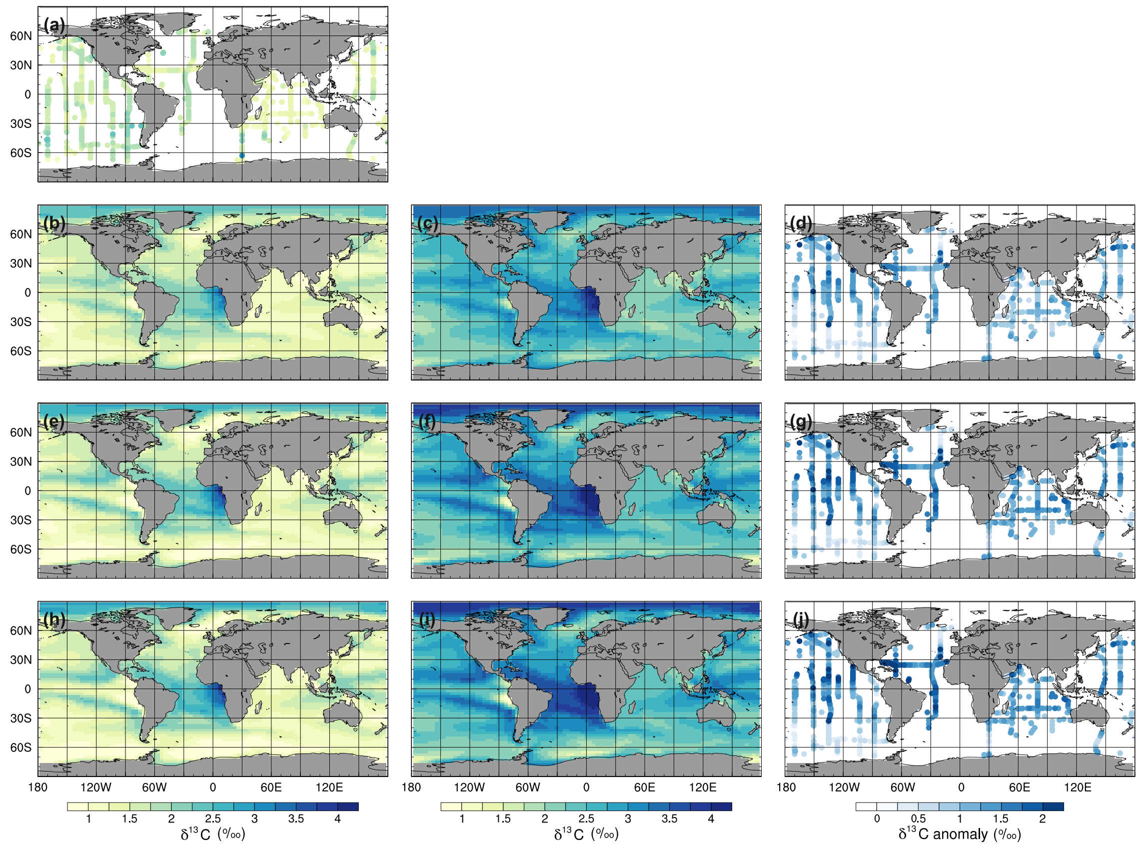

Figure 3.7: Mean annual surface $\delta^{13}C_{DIC}$ during the 1990s: (a) observations from GLODAPv2 (Key et al., 2015; Olsen et al., 2016), (b) the *std* simulation corrected for the mean surface bias (0.97 ‰), which is calculated as Σ(simulated-observed)/number of observations, (c) the *std* simulation, (d) *std* minus GLODAPv2, (e) the *L95* simulation corrected for the mean surface bias (1.13 ‰), (f) the *L95* simulation, (g) *L95* minus GLODAPv2, (h) the *L97* simulation corrected for the mean surface bias (1.15 ‰), (i) the *L97* simulation, and (j) *L97* minus GLODAPv2.

mortality are too low, the input of ^{12}C-enriched material back into the DIC pool would be insufficient. Similarly, if the model is not simulating enough remineralisation, either as a direct consequence of the parameterised remineralisation rate or as a result of insufficient POC export, the input of ^{12}C-enriched material back into the DIC pool would again be too low.

Primary producers preferentially take up ^{12}C during photosynthesis, therefore higher than observed rates of net primary production in the photic zone would increase $\delta^{13}C_{DIC}$. However, if the $\delta^{13}C_{DIC}$ discrepancy in FAMOUS was a simple function of the biases in net primary production, $\delta^{13}C_{DIC}$ would be lower than observed in the sub-tropical gyres, the Indian Ocean, and the northern North Atlantic and North Pacific Oceans, and higher than observed in the equatorial upwelling zones and the Southern Ocean (Figure 3.1). Thus, whilst the differences in net primary production could be contributing towards the $\delta^{13}C_{DIC}$ bias, particularly in the equatorial upwelling zones, they alone cannot explain the unidirectional offset.

Alternatively, the fractionation during photosynthesis could be too strong as a result of imbalances in the carbonate chemistry (Figure C.2). The global mean alkalinity in FAMOUS is 81 μmol kg^{-1} higher than observed and the mean alkalinity in the uppermost 50 m of the ocean is 107 μmol kg^{-1} too high (Key et al., 2004; Sarmiento and Gruber, 2006). In addition, the simulated global mean DIC concentration is 54 μmol kg^{-1} higher than observed and the mean DIC concentration in the uppermost 50 m of the ocean is 96 μmol kg^{-1} too high (Key et al., 2004; Sarmiento and Gruber, 2006). Furthermore, the mean ocean temperatures in FAMOUS are warmer than observed, both globally (2.2 °C) and in the uppermost 50 m of the ocean (1 °C; Sarmiento and Gruber, 2006; Locarnini et al., 2013). Increasing alkalinity increases CO_2^*, whilst increasing the temperature and DIC concentrations decreases CO_2^*. Hence, the overall effect of the carbonate chemistry biases in FAMOUS result in the global mean CO_2^* being 3.03 μmol l^{-1} too low and the mean CO_2^* in the uppermost 50 m of the ocean being 0.58 μmol l^{-1} too high. In the photic zone, this translates to a simulated α_p of 0.97378 compared to an observed α_p of 0.97415 using the *std* fractionation parameterisation. Thus, we postulate that imbalances in the carbonate chemistry, and the consequent differences in α_p, are contributing towards the $\delta^{13}C_{DIC}$ bias, but the overall effect is likely to be small.

The smallest model-data discrepancies in the surface layer are in the Southern Ocean and the northeast North Atlantic Ocean where deep convection mixes ^{12}C-enriched waters upwards into the surface ocean (Figure 3.7). In contrast, in the equatorial upwelling zones, the effect of higher than observed primary productivity (increasing $\delta^{13}C_{DIC}$) outweighs the effect of vertical mixing (reducing $\delta^{13}C_{DIC}$), therefore the overall model-data biases are higher in these regions. Despite the global offset, the model accurately simulates lower $\delta^{13}C_{DIC}$ values in the Indian Ocean compared to the Atlantic and Pacific Oceans, because the Indian Ocean is relatively nutrient poor, both in the model and reality (Figure

C.3), which limits primary productivity (Figure 3.1). Similar to previous ^{13}C modelling studies (e.g. Hofmann et al., 2000; Tagliabue and Bopp, 2008; Schmittner et al., 2013), FAMOUS also accurately simulates the observed latitudinal gradient in mixed layer $\delta^{13}C_{POC}$, with relatively high values (≈20 ‰) in the low latitudes and relatively low values (≈27 ‰) at high latitudes (Figure 3.8).

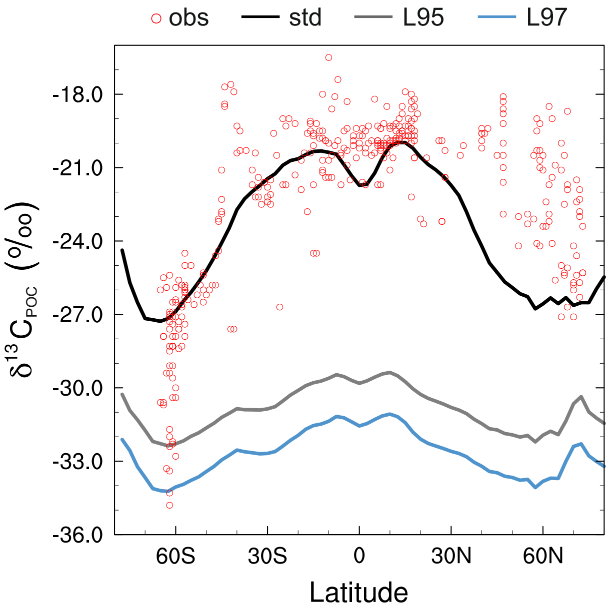

Figure 3.8: Zonally averaged mixed layer $\delta^{13}C_{POC}$ during the 1990s: observations (Goericke and Fry, 1994, red), the *std* simulation (black), the *L95* simulation (grey), and the *L97* simulation (blue).

As observed, $\delta^{13}C_{DIC}$ decreases with depth in all basins due to the remineralisation of isotopically light organic matter (Figure 3.9). The maximum remineralisation depth in the model is approximately 1000 m, which is 200 m to 500 m shallower than observed. In the deep ocean, the highest $\delta^{13}C_{DIC}$ values are in the Atlantic basin, with intermediate values in the Indian basin, and the lowest values in the Pacific basin, where the waters are older and therefore contain more remineralised organic material (enriched in ^{12}C). However, there are notable structural differences in the zonal means (Figure 3.10), which arise due to inaccuracies in the physical ocean circulation in FAMOUS. Specifically, FAMOUS does not capture the observed structure in the Atlantic basin because, in this generation of the model, the AMOC is characterised by an over-deep North Atlantic Deep Water (NADW) cell and insufficient AABW formation (Dentith et al., 2019). FAMOUS also simulates weak (less than 3 Sv) ventilation to depths of 2000 m in the North Pacific Ocean (Dentith et al., 2019), which prevents the accumulation of old, ^{12}C-enriched (low $\delta^{13}C_{DIC}$) waters at intermediate depths in the Northern Hemisphere. Instead, the oldest carbon in the model is in the eastern equatorial Pacific. In addition, the surface winds in the model are weaker than observed (Kalnay et al., 1996), resulting in a relatively shallow mixed layer.

This promotes the excessive accumulation of high $\delta^{13}C_{DIC}$ values in the surface ocean, which is particularly notable in the Southern Hemisphere sub-tropical gyres. These physical model biases are also clearly visible in the zonal mean profiles of other tracers, such as nutrients (Figure C.4) and DIC (Figure C.5). The overall shape of the simulated depth profile reaffirms the notion that there are both physical and biogeochemical biases in the model. Below approximately 1000 m, the simulated $\delta^{13}C_{DIC}$ values increase with depth in each ocean basin, whilst the observed basin averages are near constant with depth. The offset between the simulated and observed values is greatest in the deep Atlantic Ocean, where too much ^{13}C-enriched water from the shallow ocean is being circulated into the abyssal ocean. However, the trend towards increasing $\delta^{13}C_{DIC}$ with depth could also be in-part explained by insufficient remineralisation in the model. This is supported by lower than observed nutrient concentrations in the deep ocean (Figure C.4). HadOCC's global export ratio at 2000 m is within the observed range, but a lack of spatial variation means that the geographic distributions are partially incorrect (Palmer and Totterdell, 2001). Hence, we postulate that localised inaccuracies in the export ratio, together with deficiencies in the parameterisation of the remineralisation rate, are contributing towards the $\delta^{13}C_{DIC}$ offset. The basin-averaged model bias is smallest in the Pacific Ocean, where the waters are old and therefore have had more time to remineralise, thereby partially compensating for the biogeochemical biases. Indeed, the shape of the simulated and observed basin-averaged depth profiles are in good agreement below approximately 2000 m in the Pacific Ocean, despite the structural differences in the zonal mean.

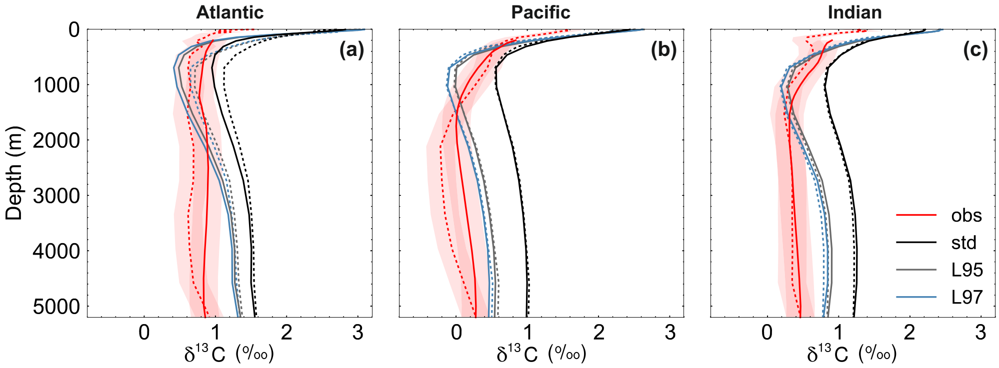

Figure 3.9: Depth profiles of $\delta^{13}C_{DIC}$ during the 1990s: (a) Atlantic Ocean, (b) Pacific Ocean, and (c) Indian Ocean. The $\delta^{13}C_{DIC}$ values in the *std* (black), *L95* (grey) and *L97* (blue) simulations are compared to observations (red). Solid lines are used for the global data set, with observations from the gridded climatology produced by Eide et al. (2017). The simulated values have also been sub-sampled at the locations where there is a corresponding observation in the GLODAPv2 data set (Key et al., 2015; Olsen et al., 2016, dashed). The red shading shows the estimated uncertainty in $\delta^{13}C_{DIC}$ observations due to unresolved inter-calibration issues between different laboratories (±0.2 ‰; Schmittner et al., 2013; Eide et al., 2017).

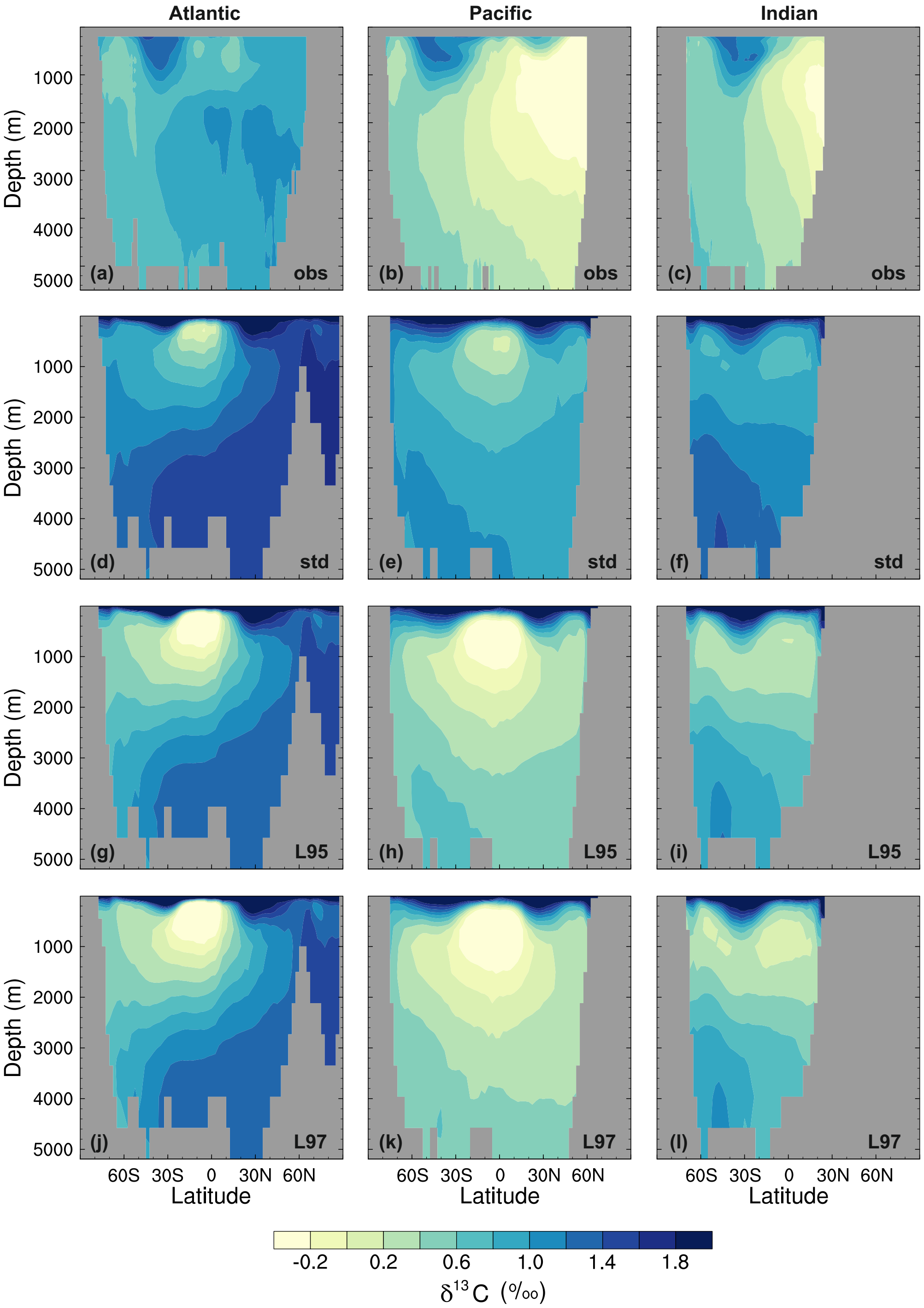

Figure 3.10: Zonal mean $\delta^{13}C_{\mathrm{DIC}}$ during the 1990s in the Atlantic Ocean (left), Pacific Ocean (centre) and Indian Ocean (right): (a – c) gridded observations (Eide et al., 2017), (d – f) the *std* simulation, (g – i) the *L95* simulation, and (j – l) the *L97* simulation.

As outlined in Section 3.3.1, our carbon isotope implementation is sensitive to physical and biogeochemical processes in the model. Thus, whilst biases in the overturning circulation and the biological pump are currently limiting the model's ability to accurately represent modern large-scale ^{13}C distributions, the model-data agreement could be improved if the physical and ecological components of the model were recalibrated. This will be discussed further in Section 3.3.4.

3.3.3 Biological fractionation parameterisations

Given the uncertainty associated with biological fractionation (Section 3.2.2.2), we tested three different parameterisations for equilibrium fractionation during photosynthesis. For all three parameterisations, the total fractionation during photosynthesis is greatest in the high latitudes (where SSTs are relatively low and CO_2^* is relatively high) and lowest in the equatorial regions (where SSTs are relatively high and CO_2^* is relatively low; Figure 3.11). The *std* parameterisation produces the largest range of α_p values (between approximately 0.97 and 0.98), whilst the *L95* parameterisation produces the smallest range (between approximately 0.964 and 0.970). The total fractionation during photosynthesis increases with the complexity of the parameterisation, with *L97* producing the largest overall effect (with a minimum α_p of 0.9635). For all three parameterisations, α_p decreases (i.e. the strength of fractionation increases) with depth in the photic zone, with the largest gradient produced by the *std* parameterisation (Figure C.6).

The large-scale $\delta^{13}C_\mathrm{DIC}$ patterns are very similar for all three photosynthetic fractionation schemes, but taking into account the phytoplankton growth rate increases the surface ocean $\delta^{13}C_\mathrm{DIC}$ values everywhere except in the Southern Ocean, the Nordic Seas, and the eastern equatorial regions, where older ^{13}C-depleted waters are mixed upwards from the abyssal ocean during deep water formation and upwelling (Figure 3.7). The differences are amplified when using the *L97* parameterisation (RMSE = 1.24 ‰, bias = 1.15 ‰), which specifies a non-linear relationship between μ and CO_2^*, compared to the *L95* parameterisation (RMSE = 1.21 ‰, bias = 1.13 ‰), which specifies a linear relationship (Figure C.7). Conversely, the alterative parameterisations decrease $\delta^{13}C_\mathrm{DIC}$ at depth compared to the *std* simulation, bringing the simulated values closer to the observations (Figure 3.9). Below approximately 500 m depth, the $\delta^{13}C_\mathrm{DIC}$ values are consistently lower when using the *L97* parameterisation compared to the *L95* parameterisation. This is due to the preconditioning of $\delta^{13}C_\mathrm{DIC}$ and $\delta^{13}C_\mathrm{POC}$ as a result of fractionation during photosynthesis in the photic zone. In the *L95* and *L97* simulations, $\delta^{13}C_\mathrm{POC}$ is lower than in the *std* simulation due to increased uptake of ^{12}C during primary production (lower α_p). The latitudinal $\delta^{13}C_\mathrm{POC}$ gradients in the mixed layer in these simulations are lower than observed, with zonal mean values ranging between approximately −30 ‰ at the equator and −33 ‰ at 60° N/S (Figure 3.8). When the POC is remineralised, a relatively low δ^{13}C signal is therefore being released back into the DIC pool, which causes the $\delta^{13}C_\mathrm{DIC}$

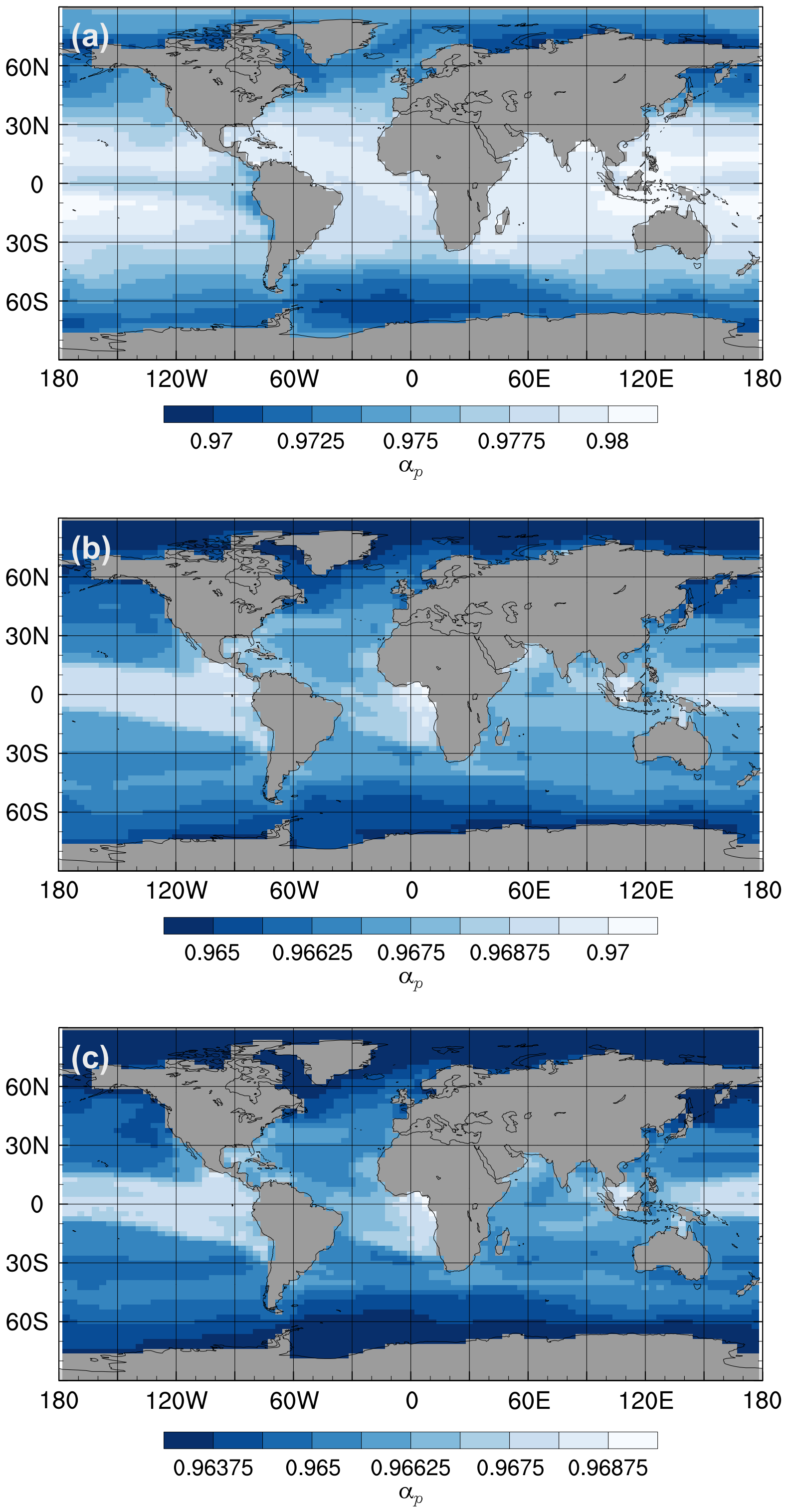

Figure 3.11: Mean annual isotopic fractionation during photosynthesis (α_p) in the surface ocean at the end of the spin-up simulations (years 9900 to 10,000): (a) the *std* simulation, (b) the *L95* simulation, and (c) the *L97* simulation.

in the deep ocean to be lower than in the *std* simulation. Thus, although the rates of biological exchange and overturning circulation are the same in all three simulations, the preconditioning of $\delta^{13}C_{DIC}$ and $\delta^{13}C_{POC}$ in the photic zone creates differences between the three simulations at depth. Whilst the global RMSE compared to the GLODAPv2 data set is lower in the *L95* and *L97* simulations (0.86 ‰ and 0.87 ‰, respectively), it is still almost double the RMSE in other models (Buchanan et al., 2019). Overall, increasing the complexity of the fractionation scheme does not significantly improve the model-data agreement because of the aforementioned physical and biogeochemical biases.

3.3.4 A new tuning target

In this study, we have demonstrated that the new carbon isotope scheme in FAMOUS is sensitive to both physical and biogeochemical processes. The simulated $\delta^{13}C_{DIC}$ distributions therefore reflect known physical inaccuracies (such as over-deep NADW and weak convection in the sub-polar North Pacific Ocean) and have allowed us to identify previously undisclosed biogeochemical biases (e.g. in the representation of remineralisation). The new tracer therefore offers excellent potential as a holistic tuning target for recalibrating FAMOUS in the future.

FAMOUS has previously been tuned both systematically (Jones et al., 2005; Gregoire et al., 2011; Williams et al., 2013) and manually (Smith et al., 2008a). Most recently, Williams et al. (2013) tuned the 20 structural parameters in HadOCC (coupled to FAMOUS-MOSES2.2) using an objective hypercube technique. Specifically, the parameter set included the C:N ratios for the different carbon pools, phytoplankton-specific parameters (e.g. maximum rate of photosynthesis), zooplankton-specific parameters (e.g. linear and quadratic zooplankton mortality rates), detritus-specific parameters (e.g. shallow and deep remineralisation rates), and carbonate-specific parameters (e.g. calcite export ratio). The main diagnostics used to evaluate the performance of the ensemble members were December-January-February and June-July-August surface air temperatures, annual mean total precipitation rate, annual mean nitrate concentrations, and primary productivity. Crucially, this study only ran each perturbed parameter simulation for 200 years and neglected to evaluate the strength and structure of the AMOC. The optimal parameter set therefore had small but important imbalances in the surface climate, which caused the AMOC to collapse over longer (multi-millennial) timescales (Dentith et al., 2019).

HadOCC has not yet been tuned for the configuration of the model used in our study (FAMOUS-MOSES1). Simultaneously recalibrating HadOCC and the physical ocean circulation in this generation of the model could therefore improve the simulated $\delta^{13}C_{DIC}$ distributions. We propose that the addition of $\delta^{13}C$ as a tuning target would improve the work of Williams et al. (2013) because it is an objective and straightforward way of assessing whether the balance between all of the ecological processes in the model is correct. We also suggest that implementing the radioactive isotope (^{14}C) into FAMOUS would be beneficial for future recalibration work (as well as subsequent scientific application of the isotope-enabled model) because it is more sensitive to overturning circulation and air-sea gas exchange, and less sensitive to the biological pump, than ^{13}C.

3.4 Summary

We have added the stable isotope ^{13}C to the ocean component of the FAMOUS GCM, using the MOSES1 generation of the model to validate our scheme. We account for fractionation during air-sea gas exchange and photosynthesis, and have tested three different parameterisations for the latter. The model captures the range of observed $\delta^{13}C_{\mathrm{DIC}}$ values in the surface ocean, but the simulated values are approximately 1 ‰ too high at all depths. The differences between the three fractionation schemes are relatively minor, but when fractionation during photosynthesis accounts for phytoplankton growth rates as opposed to just aqueous CO_2 concentrations the discrepancies between the model and observations are further increased in the surface ocean and reduced at depth. The sensitivity experiments suggest that the simulated values are too high because of underlying biases in the biological carbon cycle, therefore retuning HadOCC could improve the model-data agreement. Biases in the large-scale ocean circulation also inhibit the model's ability to accurately simulate the large-scale distribution of carbon isotopes in the deep ocean. Retuning the ocean circulation to improve the representation of the AMOC, in particular, would further reduce the model-data discrepancies. Thus, our results emphasise the utility of implementing carbon isotopes in GCMs; the simulated isotope distributions provide an additional measure against which the physical and biogeochemical model performance can be evaluated and offer an extra tuning metric for prospective development work. In the future, we intend to implement ^{14}C following the same framework, before using the isotope-enabled model to study ocean circulation and the marine carbon cycle in both a modern and palaeo context, for example, at the Last Glacial Maximum (21,000 years ago) and during the last deglaciation (21,000 to 11,000 years ago).

CHAPTER 4

Simulating oceanic radiocarbon with the FAMOUS GCM: implications for its use as a proxy for ventilation and carbon uptake

Abstract

Constraining ocean circulation and its temporal variability is crucial for understanding changes in surface climate and the carbon cycle. Radiocarbon (^{14}C) is often used as a geochemical tracer of ocean circulation, but interpreting Δ^{14}C in geological archives is complex. Isotope-enabled models enable us to directly compare simulated Δ^{14}C values to Δ^{14}C measurements and investigate plausible mechanisms for the observed signals. We have added three new tracers (water age, abiotic ^{14}C, and biotic ^{14}C) to the ocean component of the FAMOUS General Circulation Model to study large-scale ocean circulation and the marine carbon cycle. Following a 10,000 year spin-up, we prescribed the Suess effect (the isotopic imprint of anthropogenic fossil fuel burning) and the bomb pulse (the isotopic imprint of thermonuclear weapons testing) in a transient simulation spanning 1765 to 2000 CE. To validate the new isotope scheme, we compare the model output to direct Δ^{14}C observations in the surface ocean (pre-bomb and post-bomb) and at depth (post-bomb only). We also compare the timing, shape and amplitude of the simulated marine bomb spike to Δ^{14}C in geological archives from shallow-to-intermediate water depths across the North Atlantic. The model captures the large-scale structure and range of Δ^{14}C values (both spatially and temporally) suggesting that, on the whole, the uptake and transport of ^{14}C are well represented in FAMOUS. Differences between the simulated and observed values arise due to physical model biases (such as weak surface winds and over-deep North Atlantic Deep Water), demonstrating the potential of the ^{14}C tracer as a sensitive, independent tuning diagnostic. We also examine the influence of the biological pump on deep ocean ^{14}C concentrations and assess the extent to which ^{14}C can be interpreted as a ventilation tracer. Comparing the simulated biotic

and abiotic δ^{14}C values, we infer that biology has a spatially heterogeneous influence on ^{14}C distributions in the surface ocean (between 18 and 30 ‰), but a near constant influence at depth (≈20 ‰). Nevertheless, the decoupling between the simulated water ages and the simulated ^{14}C ages in FAMOUS demonstrates that interpreting proxy Δ^{14}C measurements in terms of ventilation alone could lead to erroneous conclusions about palaeocean circulation. Specifically, our results suggest that Δ^{14}C is only a faithful proxy for water age in regions with strong convection; elsewhere, the temperature dependence of the solubility of CO_2 in seawater complicates the signal.

4.1 Introduction

Understanding ocean circulation, how it has changed in the past, and how it might change in the future is crucial for understanding changes in surface climate and the carbon cycle (Rhein et al., 2013), but constraining ocean circulation is challenging due to the large range of spatiotemporal scales over which it operates (Talley, 2011). Modern methods for measuring ocean currents include moored arrays, drifting buoys, gliders, Acoustic Doppler Current Profilers, Argo floats, and satellite measurements (Dohan et al., 2010). Physical oceanographers also commonly infer ocean circulation from density distributions (Blanckenburg, 1999; Lynch-Stieglitz, 2001). Together, these techniques provide extensive spatiotemporal coverage in shallow and intermediate waters. However, historical and deep ocean measurements are much sparser (Rhein et al., 2013). The slowest ocean currents operate on centennial-to-millennial timescales (Talley, 2011), but there are no direct measurements of temperature and salinity, from which density is derived, or advection itself, beyond the instrumental record (i.e. prior to the late 1950s; Rhein et al., 2013). Instead, to determine past changes in ocean circulation, palaeoceanographers rely on indirect ("proxy") measurements (e.g. carbon isotopes) in geological archives such as sediment cores and corals (Blanckenburg, 1999; Rahmstorf, 2002; Lynch-Stieglitz, 2003).

There are three naturally occurring carbon isotopes: the stable isotopes ^{12}C (98.9 %) and ^{13}C (1.1 %), and the radioactive isotope ^{14}C (1.2×10^{-10} %), which is also known as radiocarbon (Key, 2001). Natural ^{14}C is produced in the atmosphere by the cosmic spallation of nitrogen and enters the oceans via air-sea gas exchange. Once in the oceans, ^{14}C is transported via large-scale ocean circulation and decays with a known half-life of 5730 years (Key, 2001). As there is no additional production of ^{14}C in the interior ocean, the ^{14}C content of deeper waters provides an indication of the time elapsed since the water was last in contact with the atmosphere (also termed the "water age" or “ventilation age”). Oceanic ^{14}C distributions are also affected to a lesser extent by changes in atmospheric production (on multi-millennial timescales; Damon et al., 1978) and mass dependent fractionation during carbon cycle processes: air-sea gas exchange (e.g. Zhang et al., 1995), photosynthesis (e.g. Popp et al., 1989), and calcium carbonate formation (e.g.

Emrich et al., 1970). Oceanographic ^{14}C data are typically reported as Δ^{14}C in per mil (‰) units (Stuiver and Polach, 1977), which is the ^{14}C/^{12}C ratio of a sample relative to a standard, with corrections applied to account for fractionation effects and to normalise all samples relative to the mean value of terrestrial wood in 1950 CE (Broecker and Walton, 1959; Key, 2001).

Between 1945 and 1963, thermonuclear weapons testing approximately doubled the amount of ^{14}C in the atmosphere (Mahadevan, 2001). This artificial ("bomb") ^{14}C spike has since been cycled through natural systems and can be utilised as a physical and biogeochemical tracer in terrestrial and marine settings (Scourse et al., 2012). For example, the flux, distribution and inventory of bomb ^{14}C in the oceans can be used to constrain rates of air-sea gas exchange (Sweeney et al., 2007) and exchange between the shallow and deep ocean (Graven et al., 2012a). This is particularly valuable as both of these processes are important controls of oceanic CO_2 uptake (Graven et al., 2012a). The oceans are estimated to have absorbed approximately one third of anthropogenic CO_2 emissions, with an uncertainty of ±20 % (Khatiwala et al., 2013). More precise quantification of the size of the oceanic carbon sink from observations is hindered by a lack of data from the sub-surface ocean, and the temporal duration and resolution of hydrographic measurements (Khatiwala et al., 2013).

A number of oceanographic surveys have been conducted since the early 1970s, providing an indication of large-scale carbon isotope distributions in the modern oceans that can be used to estimate the bomb ^{14}C inventory and anthropogenic carbon uptake. These include: the Geochemical Ocean Sections Study (GEOSECS; 1972 to 1978; Östlund et al., 1988), Transient Tracers in the Ocean (TTO; 1981 to 1983; Brewer et al., 1985, 1986; Östlund and Grall, 1987), the South Atlantic Ventilation Experiment (SAVE; 1987 to 1989; Scripps Institute of Oceanography, 1992a,b), Indien Gaz Ocean (INDIGO; 1985 to 1987; Sepanski, 1991), and the World Ocean Circulation Experiment (WOCE; 1990 to 1998; Orsi and Whitworth III, 2005; Talley, 2007; Koltermann et al., 2011; Talley, 2013). Although they provide a wealth of important data, one of the main shortcomings of these surveys is their low sampling frequency, with repeat measurements typically taken decades apart (Hood, 2009). They are therefore unable to capture the precise timing and amplitude of the bomb pulse. An additional limitation is that there are very few baseline (i.e. pre-bomb) measurements (especially in intermediate and deep waters) to contextualise anthropogenic changes relative to natural variability.

Isotopic ratios in geological archives (e.g. corals and bivalves) can complement direct oceanographic ^{14}C measurements (e.g. Sherwood et al., 2008; Scourse et al., 2012) and extend the record further back in time (e.g. Robinson et al., 2005; Burke and Robinson, 2012; Chen et al., 2015). Corals grow at a large range of depths (ranging from near-surface to more than 3000 m; Etnoyer and Morgan, 2005; Roark et al., 2009) for hundreds to thousands of years (Adkins et al., 2004; Roark et al., 2009), with their carbonate skeletons recording the ^{14}C content of the seawater in which they formed (Druffel, 1980; Adkins et al., 2002; Farmer et al., 2015). Typically, warm-water corals grow in regions where the water temperature is between 23 °C and 29 °C (i.e. within 30° latitude of the equator and at <100 m depth; Spalding and Brown, 2015). Cold-water corals are found at shallow-to-intermediate depths (50 to 1000 m) in the high latitudes and at depths of up to 4000 m in the low latitudes, where the water temperature is between 4 °C and 12 °C (Roberts et al., 2006). Certain cold-water species (e.g. bamboo corals) possess a two-part skeleton that can be used to simultaneously reconstruct both the surface and deep water ^{14}C signature. The proteinaceous nodes are formed from recently exported particulate organic matter, which reflects the isotopic signature of the surface ocean, whilst the calcite skeleton is derived from ambient dissolved inorganic carbon (Sherwood et al., 2008; Farmer et al., 2015). In contrast, most marine bivalve species are relatively short lived (<20 years) and have a narrow geographical range, which limits their utility for providing similarly long-term reconstructions (Weidman, 1995). However, "long-lived" species such as *Arctica islandica* have been widely used for generating more recent (i.e. 20th century) data sets (Scourse et al., 2012). *A. islandica* inhabit the continental shelves and slopes of the North Atlantic (between 10 and 200 m water depth and between 35° N and 70° N; Weidman, 1995). They commonly live for around 100 years and deposit carbonate shells with annual periodicity (Weidman, 1995).

Interpreting the ^{14}C signal in proxy records in terms ocean circulation and marine biogeochemistry is complex. However, by simulating ^{14}C in numerical climate models we can directly compare the model output to $\Delta^{14}C$ measurements and provide plausible mechanisms for the observed signals. Radiocarbon is not routinely incorporated into climate models because of the computational expense associated with fully spinning up the deep ocean and marine carbon cycle (Bardin et al., 2014). However, since the Ocean Carbon-Cycle Model Intercomparison Project (OCMIP) produced a legacy of standard input fields and simulations (Orr et al., 2000), ^{14}C has been implemented into models of varying complexities, including: the UVic Earth system model (Meissner et al., 2003; Koeve et al., 2015), the Hamburg LSG ocean circulation model (Butzin et al., 2005), MoBidiC (Crucifix, 2005), CM2Mc (Galbraith et al., 2011), CCSM (Graven et al., 2012a), and CESM (Jahn et al., 2015). It is valuable to add another model, the FAMOUS General Circulation Model (GCM), to this list, not only to increase the Earth system capabilities of the model itself, but also because examining the inter-model differences in $\Delta^{14}C$ distributions can help us to better understand the underlying processes. Within the list of ^{14}C-enabled models, FAMOUS has the unique capability of being computationally efficient enough to fully spin-up the deep ocean circulation and the marine carbon cycle in a timely manner (without the need for offline or accelerated spin-up techniques), whilst still being able to maintain sufficient detail in the representation of the feedbacks between Earth system processes to study changes on decadal-to-centennial timescales. An additional benefit of adding ^{14}C to numerical climate models is that it can be used to diagnose model biases. Temperature and salinity are commonly tuned to observations (Williamson et al., 2017), but ^{14}C provides an independent constraint against which the simulated ocean circulation and marine carbon cycle can be evaluated.

Here, we describe the implementation of three new tracers in the ocean component of the FAMOUS GCM: water age, abiotic ^{14}C, and biotic ^{14}C (Section 4.2). The two representations of ^{14}C differ in that the abiotic tracer is only affected by air-sea gas exchange, advection, and radioactive decay, whilst the biotic tracer is additionally cycled through the biological pump and is subject to isotopic fractionation during air-sea gas exchange and photosynthesis. We evaluate the performance of the model in simulating pre- and post-bomb Δ^{14}C values by comparing the biotic tracer to observations (Sections 4.3.1 and 4.3.2, respectively). Specifically, the pre-bomb surface ocean Δ^{14}C and post-bomb deep ocean Δ^{14}C (i.e. natural ^{14}C distributions) are used to validate the model's large-scale ocean circulation and air-sea gas exchange scheme. The post-bomb surface ocean Δ^{14}C (i.e. anthropogenic ^{14}C) is used to further test the accuracy of the air-sea gas exchange, as well as vertical mixing in the shallow-to-intermediate water column. We also examine the transient bomb signal in natural archives (corals and bivalves) and in the model (Section 4.3.3). We compare the timing, magnitude, and shape of the ^{14}C peak in different locations and at different water depths across the North Atlantic, and consider the implications for anthropogenic carbon uptake. Lastly, we assess the extent to which ^{14}C can be interpreted as a ventilation tracer. We consider the importance of the biological pump for deep water ^{14}C concentrations by comparing the simulated biotic and abiotic δ^{14}C distributions (Section 4.3.4). In this study, we use the term "biological pump" to refer to dissolved inorganic carbon (DIC) being converted into particulate organic carbon (POC) during photosynthesis, the transport of the POC from the shallow ocean into the abyssal ocean via gravitational settling, and its consequent remineralisation at depth, which is analogous to the "soft-tissue pump" outlined by Volk and Hoffert (1985). We then assess how well the simulated biotic ^{14}C ages compare to idealised water ages, which directly count the length of time since a water parcel was last in the uppermost layer of the ocean, and consider the implications for interpreting Δ^{14}C proxy records from different regions (Section 4.3.5).

4.2 Methods

4.2.1 Model description

We have added three new tracers (water age, abiotic ^{14}C, and biotic ^{14}C) to the ocean component of the FAMOUS atmosphere-ocean GCM (Jones et al., 2005; Smith et al., 2008a; Smith, 2012; Williams et al., 2013), which is a low resolution model derived from HadCM3 (Gordon et al., 2000; Pope et al., 2000). Briefly, the primitive equation atmospheric model has a horizontal resolution of 5° × 7.5° and 11 vertical levels on a hybrid sigma-pressure grid. The rigid-lid ocean is $2.5° \times 3.75°$ with 20 vertical levels that vary in thickness from 10 m at the surface to more than 600 m at depth. The atmosphere operates on a 1 h timestep, the ocean has a 12 h timestep, and the two components are coupled every 24 h. At the time of this study, and with a full suite of oceanic tracer fields enabled, FAMOUS is capable of simulating approximately 400 model years per wallclock day on 16 core processors at the University of Leeds. It is therefore well suited to running the multi-millennial length simulations that are required to spin-up deep ocean circulation and the marine carbon cycle.

In this study, we used the Met Office Surface Exchange Scheme (MOSES) version 1 (Cox et al., 1999) generation of the model. Although the MOSES2.2 generation of the model offers increased and more dynamic Earth system capabilities (Essery et al., 2001, 2003; Williams et al., 2013; Valdes et al., 2017), the published setup does not accurately simulate the Meridional Overturning Circulation in multi-millennial simulations with constant pre-industrial boundary conditions (Dentith et al., 2019). At present, FAMOUS-MOSES1 is therefore a more appropriate tool for studying oceanic tracers. Nevertheless, our code is directly transferable between the different generations of FAMOUS and the parent model. The new carbon isotope scheme can therefore be implemented into FAMOUS-MOSES2.2 once the large-scale ocean circulation has been recalibrated, or into HadCM3 for higher resolution scientific application.

The Hadley Centre Ocean Carbon Cycle (HadOCC) model is embedded within the ocean component of FAMOUS. In brief, HadOCC simulates air-sea gas exchange, the circulation of DIC, and the cycling of carbon by marine biota (Palmer, 1998; Palmer and Totterdell, 2001). Nutrients, phytoplankton, zooplankton, detritus, DIC, and alkalinity are simulated explicitly. The four biological components are considered in terms of their nitrogen contents, with the carbon contents and fluxes calculated using fixed stoichiometric ratios. All six model tracers are advected, diffused and mixed across all levels, although phytoplankton and zooplankton concentrations are negligible outside of the uppermost 100 m of the ocean. The primary mechanism for vertical carbon export is via detrital sinking, however, there is no representation of sediments. The small flux of detrital material that reaches the seafloor is therefore immediately refluxed back into the surface layer to conserve nitrogen and carbon. A more detailed description of HadOCC is provided in Chapter 3.

4.2.2 Tracer implementation

4.2.2.1 Water age tracer

Carbon isotope ratios in oceanic geological archives, and $\Delta^{14}C$ in particular, are often interpreted in terms of water age (e.g. Stuiver et al., 1983; Broecker et al., 1990). To test this interpretation, we included a simple water age tracer in the model, which counts the number of timesteps since the water in a single grid cell was last in contact with the atmosphere:

$$\mathrm{Age}_{(t+\Delta t)} = \mathrm{Age}_{(t)} + \Delta t \tag{4.1}$$

where t is the current timestep.

The water age is instantly reset to zero in the surface layer, regardless of surface water residence times and whether or not air-sea gas exchange occurs (e.g. due to the presence of sea ice). This is therefore a highly idealised calculation, based purely on physical ocean circulation, which can be used as a first-order comparative tool to understand the processes that influence ^{14}C age (such as air-sea gas exchange and ocean carbon cycle interactions) and how to interpret carbon isotope records of past ocean circulation.

4.2.2.2 Abiotic ^{14}C

Abiotic ^{14}C (i.e. ^{14}C that is not affected by biological activity or isotopic fractionation) has previously been implemented into the ocean component of FAMOUS (Palmer, 1998). However, as the model has been further developed, this legacy code had not been maintained. At the outset of this study, initial tests revealed numerical instabilities (with Δ^{14}C values in excess of $\pm 1 \times 10^6$ ‰ developing during the first hundred years of the simulation), which eventually caused the model to crash. We therefore implemented an upper bound on the oceanic CO_2 flux (capping pCO$_2$ values at 1000 p.p.m. and the CO_2 flux at 30 mol m^{-2} yr^{-1}). As a reference for future studies, we provide full documentation of the abiotic ^{14}C implementation, which follows the OCMIP-2 protocol (Orr et al., 2000) with the following differences:

- We assume that modelled DIC is ^{12}C and carry ^{14}C as a ratio ($\mathrm{DI^{14}C}/\mathrm{DI^{12}C}$), therefore virtual fluxes are not required to account for the dilution or concentration effects of surface freshwater fluxes (Appendix B.1).
- We carry ^{14}C in model units to minimise the error associated with carrying small numbers:

  $$\text{Model units} = \frac{\mathrm{DI^{14}C}}{\mathrm{DI^{12}C}} \times \frac{100}{\frac{^{14}\mathrm{C}}{^{12}\mathrm{C}}_{\mathrm{std}}} \tag{4.2}$$

  where $^{14}\mathrm{C}/^{12}\mathrm{C}_{\mathrm{std}} = 1.176 \times 10^{-12}$ (Karlen et al., 1965).
- In the calculation of the partial pressure of CO_2, we do not scale the mean ocean alkalinity with sea surface salinity. Instead we continue to calculate the sea surface alkalinity using the standard equations in HadOCC, which consider the nutrient fluxes between the different organic pools and the rate of $CaCO_3$ production.
- In the calculation of aqueous CO_2, we use the carbonic acid constants of Roy et al. (1993) as opposed to Millero (1995) because this is consistent with the formulation of CO_2 solubility used in other areas of the model.

- In the calculation of the piston velocity, we use a coefficient of 0.31 $\mathrm{cm\,h^{-1}}$ (Wanninkhof, 1992) instead of the 0.337 $\mathrm{cm\,h^{-1}}$ specified in the protocol. We also use the squared 10 m wind speed from the coupled atmospheric model as opposed to the climatology of the squared monthly average of the instantaneous Special Sensor Microwave Imager (SSMI) velocity plus its variance. This is consistent with the gas transfer formulation used in other areas of the model and previous carbon isotope implementations in coupled atmosphere-ocean models (e.g. Jahn et al., 2015).

As outlined in Chapter 3, the air-sea gas flux of $\mathrm{DI^{12}C}$ (F) is calculated as:

$$F = PV \times (C_{\mathrm{sat}} - C_{\mathrm{surf}}) \tag{4.3}$$

where C_{sat} is the saturation concentration of atmospheric CO_2 (in $\mathrm{mol\,m^{-3}}$), C_{surf} is the surface aqueous CO_2 concentration (in $\mathrm{mol\,m^{-3}}$), and PV is the piston velocity (in $\mathrm{cm\,h^{-1}}$), which is calculated as:

$$PV = a \times u^2 \times (1 - a_{\mathrm{ice}}) \times \left(\frac{Sc}{660}\right)^{-0.5} \tag{4.4}$$

where a is a tuneable coefficient, u is the wind speed (in $\mathrm{m\,s^{-1}}$), a_{ice} is the fractional ice cover and Sc is the Schmidt number for CO_2, calculated as a function of sea surface temperature (SST, in °C):

$$Sc = 2073.1 - 125.62 \times SST + 3.6276 \times SST^2 - 0.043219 \times SST^3 \tag{4.5}$$

The air–sea gas flux of $\mathrm{DI^{14}C/DI^{12}C}$ ($F_{14/12}$) is therefore calculated as:

$$\frac{d\left(\frac{^{14}C}{^{12}C}\right)}{dt} = \frac{1}{^{12}C} \times PV \times C_{\mathrm{sat}} \times \left(\frac{^{14}A}{^{12}A} - \frac{^{14}C}{^{12}C}\right) \tag{4.6}$$

where $^{14}A/^{12}A$ and $^{14}C/^{12}C$ are the $\mathrm{^{14}C/^{12}C}$ ratios of the atmosphere and DIC, respectively (Appendix D.1). Atmospheric CO_2 and $\Delta^{14}C$ concentrations can either be held constant or prescribed from a file that contains a single global weighted-average value per year.

4.2.2.3 Biotic ^{14}C

We implemented biotic ^{14}C following the same methodology used for ^{13}C (Chapter 3). We account for kinetic and equilibrium fractionation during air-sea gas exchange (Appendix D.2) based on the equations of Zhang et al. (1995), and calculate fractionation during photosynthesis as a function of aqueous CO_2 concentration (CO_2^*) using the parameterisation of Popp et al. (1989). We do not account for fractionation during calcium carbonate formation because its inclusion has a negligible effect on the isotope distributions (Chapter 3, Section 3.2.2). For all processes, the isotopic enrichment factor (ε) for ^{14}C is twice that of ^{13}C ($\varepsilon 14 = 2 \times \varepsilon 13$; Craig, 1954), with

$$\varepsilon = (\alpha - 1) \times 1000. \tag{4.7}$$

Biotic ^{14}C is also subject to radioactive decay in all four carbon pools, whereas ^{13}C is not.

4.2.2.4 Isotopic fractionation correction

To compare the simulated biotic ^{14}C values to observations, we apply the isotopic fractionation correction of Stuiver and Polach (1977):

$$\Delta^{14}C = \delta^{14}C - 2 \times \left(\delta^{13}C + 25\right) \times \left(1 + \frac{\delta^{14}C}{1000}\right) \tag{4.8}$$

where

$$\delta^{X}C = \left(\frac{\frac{^{X}C}{^{12}C}\text{sample}}{\frac{^{X}C}{^{12}C}\text{standard}} - 1 \right) \times 1000. \tag{4.9}$$

The “2” accounts for the mass dependency of isotopic fractionation and the “25” normalises all samples to the mean value of terrestrial wood in 1950 CE (Key, 2001). As δ^{13}C is close to zero, the Δ^{14}C values are reduced by a near-constant value of −50 ‰ relative to the δ^{14}C values.

Other modelling studies typically compare their abiotic δ^{14}C values directly to Δ^{14}C observations because, without isotopic fractionation effects, $\Delta^{14}\text{C} = \delta^{14}\text{C}$ (e.g. Toggweiler et al., 1989a). In the absence of a biotic implementation, abiotic δ^{14}C is a useful first-order representation of the processes that are important for the distribution of oceanic Δ^{14}C (air-sea gas exchange, advection, and radioactive decay). When both an abiotic and a biotic formulation are included in the same model, however, the value of comparing the two tracers is to examine the differences between the simulated fields to improve our understanding of the processes that are important for the distribution of oceanic ^{14}C. If the biotic Δ^{14}C values are compared to the abiotic Δ^{14}C values, the relationship between the two tracers is artificially reversed because the magnitude of the biotic fractionation correction (≈50 ‰) is larger than the uncorrected difference between the two tracers (which, as will be discussed in Section 4.3.4, is approximately 20 ‰). Consequently, we only compare the biotic Δ^{14}C values to observations (Sections 4.3.1, 4.3.2, and 4.3.3) because they are a more complete representation of reality than the abiotic values. To assess the importance of the biological pump to the vertical profile of ^{14}C, both in the global ocean and regionally, we compare the biotic and the abiotic tracers as uncorrected δ^{14}C (Section 4.3.4).

In Section 4.3.5, the simulated biotic ^{14}C concentrations (‰) are converted to ^{14}C ages (relative to 1950 CE) as per Stuiver and Polach (1977):

$$^{14}C_{\text{age}} = -\frac{5730}{ln(2)} \times ln\left(1 + \frac{\Delta^{14}C}{1000}\right). \tag{4.10}$$

4.2.2.5 Advection

Radiocarbon concentrations in the ocean interior are calculated as a function of 3-dimensional tracer transport and radioactive decay:

$$\frac{d\left(\frac{DI^{14}C}{DI^{12}C}\right)}{dt} = L\left(\left[\frac{DI^{14}C}{DI^{12}C}\right]\right) - \beta \times \frac{DI^{14}C}{DI^{12}C} \tag{4.11}$$

where β is the radioactive decay constant ($3.889\,15 \times 10^{-12}$ s^{-1}), which is based on a half-life of 5730 years (Godwin, 1962), and L is the advection term. Flux-limited Quadratic Upstream Interpolation for Convective Kinematics (QUICK) advection (Leonard, 1993) is the default transport scheme in FAMOUS because it is positivity preserving and offers a better balance between numerical stability and diffusion compared to the standard alternatives (upstream differencing and centred differencing). It is used to transport all of the existing oceanic tracers (including temperature, salinity, and nutrients) and, for consistency, we have selected the same option for all three of our new tracers (water age, abiotic ^{14}C, and biotic ^{14}C).

4.2.3 Simulations

4.2.3.1 Spin-up simulation

We ran a 10,000 year spin-up simulation with constant pre-industrial boundary conditions to allow the deep ocean circulation and ocean carbon cycle to reach steady state. $\Delta^{14}C_{\text{atm}}$ was fixed at 0 ‰, $\delta^{14}C_{\text{ocn}}$ was initialised at a globally uniform value of 0 ‰ (i.e. biotic $\Delta^{14}C_{\text{ocn}}$ was initialised at −50 ‰), and the water age was initialised at a globally uniform value of 0 years. The global volume-weighted integral of Δ^{14}C started to stabilise after 6000 years and the water age stabilised after 8000 years (Figure E.1). At the end of the spin-up simulation, the Δ^{14}C drift was less than 0.001 ‰ yr^{-1} (equivalent to a change in ^{14}C age of 8.27 years per millennia), satisfying the OCMIP-2 criterion for steady state (Orr et al., 2000).

4.2.3.2 Historical simulation

We initialised a transient simulation for the period 1765 to 2000 CE from the end of the spin-up simulation to generate model output that is directly comparable to modern observations. Again, we followed the OCMIP-2 protocol with minor adjustments where necessary. The OCMIP-2 files contain biannual atmospheric CO_2 values and annual $\Delta^{14}C_{atm}$ values that are separated into three latitude bands (90 to 20° N, 20° N to 20° S, and 20 to 90° S; Orr et al., 2000). However, as FAMOUS currently only allows a single atmospheric CO_2 value to be prescribed per model year, we calculated annual average atmospheric CO_2 values from the OCMIP-2 data. At present, our isotope implementation also does not allow for latitudinal variability in $\Delta^{14}C_{atm}$. We therefore prescribed weighted global mean $\Delta^{14}C_{atm}$ values, which only differ from the regional values between 1956 and 1969 (Figure 1). The depletion of $\Delta^{14}C_{atm}$ to negative values during the early half of the 20th century is due to the input of ^{14}C-free CO_2 into the atmosphere from the burning of fossil fuels, known as the Suess effect (Suess, 1955; Keeling, 1979). Nuclear weapons testing commenced in 1945, and intensified between 1955 and 1963, rapidly enriching the atmosphere in ^{14}C (Mahadevan, 2001). The subsequent $\Delta^{14}C_{atm}$ decline primarily reflects the penetration of $^{14}CO_2$ into the oceans and the terrestrial biosphere (e.g. Graven et al., 2012a). To act as a control, the spin-up simulation was continued for an additional 235 years with constant atmospheric CO_2 and $\Delta^{14}C$.

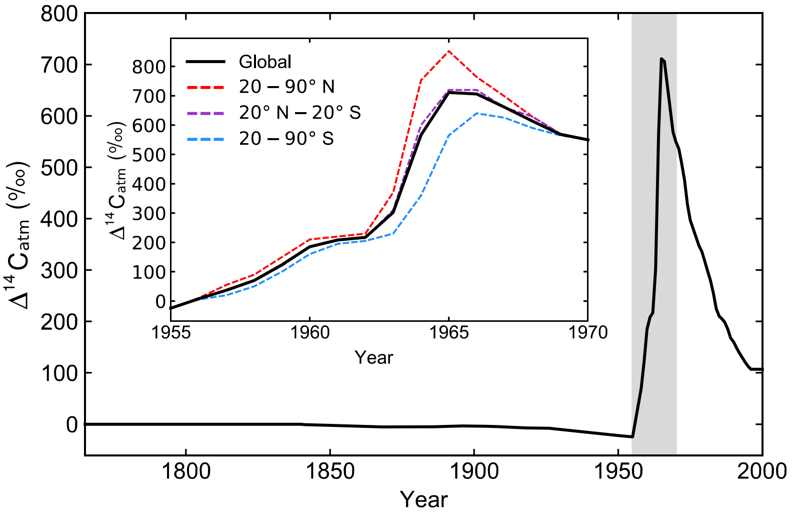

Figure 4.1: Prescribed atmospheric $\Delta^{14}C$ values (1765 to 2000 CE). Inset (1955 to 1970 CE, shaded): Weighted global mean (black, prescribed) compared to the three latitude bands outlined in the OCMIP-2 files (Orr et al., 2000); Northern Hemisphere (90 to 20° N, red), tropics (20° N to 20° S, purple), and Southern Hemisphere (20 to 90° S, blue).

4.3 Results and discussion

4.3.1 Pre-bomb surface ocean $\Delta^{14}C$ distributions

To assess the model performance in simulating natural (pre-bomb) $\Delta^{14}C$ distributions, we compare the simulated mean surface ocean $\Delta^{14}C$ values for the period 1955 to 1959 CE with historical surface measurements compiled by Graven et al. (2012b). We define this period as pre-bomb because, although atmospheric nuclear weapons testing intensified from 1955 onwards, the timescale for isotopic equilibration between the surface ocean and the atmosphere is 5 to 10 years (Toggweiler et al., 1989a; Lynch-Stieglitz, 2003; Sarmiento and Gruber, 2006). The signature of bomb ^{14}C at the sea surface should therefore be minimal in the 5 year period immediately following its injection into the atmosphere. For example, Broecker and Walton (1959) estimated that the concentration of tropospheric $^{14}CO_2$ in the Northern Hemisphere increased by approximately 5 % per year between March 1955 and March 1958, but that only 10 % of the bomb ^{14}C produced in this period had entered the oceans at the time of their study. Their calculations suggested that if this bomb ^{14}C was concentrated in the uppermost 100 m of the ocean, the average surface ocean Δ^{14}C value in 1959 would be 12 to 32 ‰ higher than in 1955. In agreement with these calculations, between 1955 and 1960, the prescribed change in $\Delta^{14}C_{atm}$ is 210 ‰, but the simulated change in the globally averaged Δ^{14}C in the upper 100 m of the ocean is just 17 ‰. For comparison, the total simulated change (pre-bomb to peak bomb) in the upper 100 m of the ocean is 170 ‰. Therefore, whilst neither the simulated nor the observed values for this period represent entirely natural ^{14}C, these data provide a good indication of pre-bomb Δ^{14}C distributions in the absence of earlier (pre-1955) ship measurements. We focus our analysis on the surface ocean (0 to 10 m) because direct measurements of pre-bomb Δ^{14}C in the intermediate and deep ocean are scarce. There are 67 data points from the air-sea interface in the compilation of Graven et al. (2012b), however, there are only a further 125 data points at depths of 10 m and below (which accounts for more than 99.5 % of the global ocean volume). Binning the data according to the vertical levels in the model demonstrates that very few of these data points are at comparable depths (Table E.1) and there are only a handful of locations that have multiple measurements throughout the entire water column. These data are therefore insufficient for providing a coherent picture of natural Δ^{14}C distributions in the deep ocean.

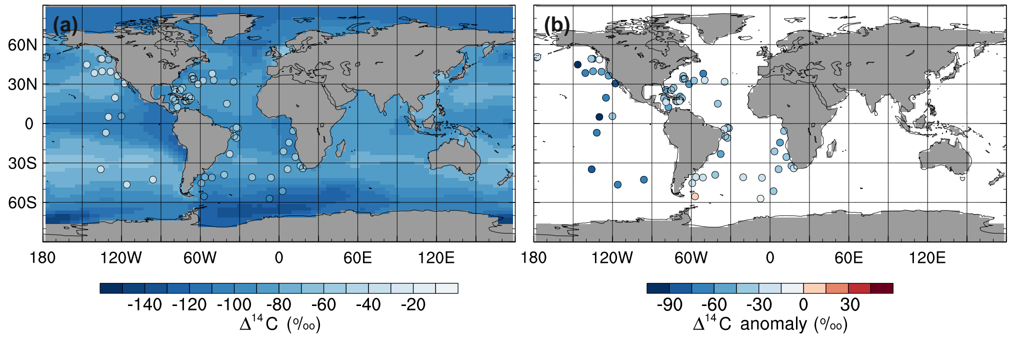

Figure 4.2: (a) Mean surface ocean Δ^{14}C (1955 to 1959 CE; coloured contours) overlain with historical surface measurements (filled dots) for the same period (compiled by Graven et al., 2012b) and (b) simulated minus observed Δ^{14}C.

The model captures the overall structure of the observations in the surface ocean (Figure 4.2a). The highest values (≈ -52 ‰) are in the sub-tropical gyres where surface water residence times are relatively long, allowing for greater equilibration with the atmosphere. Equatorial regions have intermediate $\Delta^{14}C$ values due to the combined effect of older (^{14}C-depleted) waters from the deep ocean upwelling back to the sea surface and weaker winds than in the sub-tropics reducing the input of ^{14}C from the atmosphere. The lowest values (≈ -150 ‰) are in the high latitudes because (1) sea ice inhibits air-sea gas exchange, (2) surface water residence times are relatively short, and (3) older water is mixed upwards from the abyssal ocean to the surface ocean at sites of deep water formation. In absolute terms, the simulated values are, on average, 60 ‰ lower than observed in the Pacific Ocean and 33 ‰ lower than observed in the Atlantic Ocean (Figure 4.2b). The discrepancy may be partly reconciled by the envelope of uncertainty on the pre-bomb observations (5 to 36 ‰; Graven et al., 2012b), which encompasses much of the offset between the simulated and observed $\Delta^{14}C$ values in the Atlantic basin. However, this does not account for the larger bias in the Pacific basin, which is better explained by the atmospheric forcing, specifically the timing and geographical distribution of early nuclear weapons testing. Approximately 70 atmospheric nuclear weapons tests were conducted by the U.S.A., U.S.S.R. and U.K. between 1945 and 1955 in Kazakhstan, Nevada, and the Pacific Ocean (Yang et al., 2003). The Pacific observations could therefore include a small bomb signal from the preliminary testing that took place on the Bikini and Enewetak Atolls. The model does not capture this early period of nuclear activity because we prescribed a globally uniform bomb signal beginning in 1955 (Section 4.2.3.2).

4.3.2 Post-bomb $\Delta^{14}C$ distributions

To assess the model performance in the post-bomb era, we compare the simulated mean $\Delta^{14}C$ values for the 1990s with data from version 1 of the Global Data Analysis Project (GLODAP; Key et al., 2004), which is a compilation of 3-dimensional measurements from approximately 12,000 hydrographic stations. Overall, the model shows good agreement with the observations, with a global linear regression r^2 value of 0.75 and a root mean square error (RMSE) of 55 ‰ (Figure 4.3). The best agreement is in the Pacific Ocean (where the r^2 value is 0.86 and the RMSE is 57 ‰) and the worst agreement is in the Southern Ocean (where the r^2 value is 0.52 and the RMSE is 52 ‰).

At the sea surface, the model successfully replicates the large-scale distribution of $\Delta^{14}C$ with the highest values in the sub-tropics, intermediate values in the tropics, and the lowest values in the polar regions (Figure 4.4 and Figure 4.5). This demonstrates that, to the first order, the processes that control the uptake and transport of ^{14}C (air-sea gas exchange, biological activity, and ocean circulation) are well represented in the model. By investigating the reasons for some of the differences between the simulated

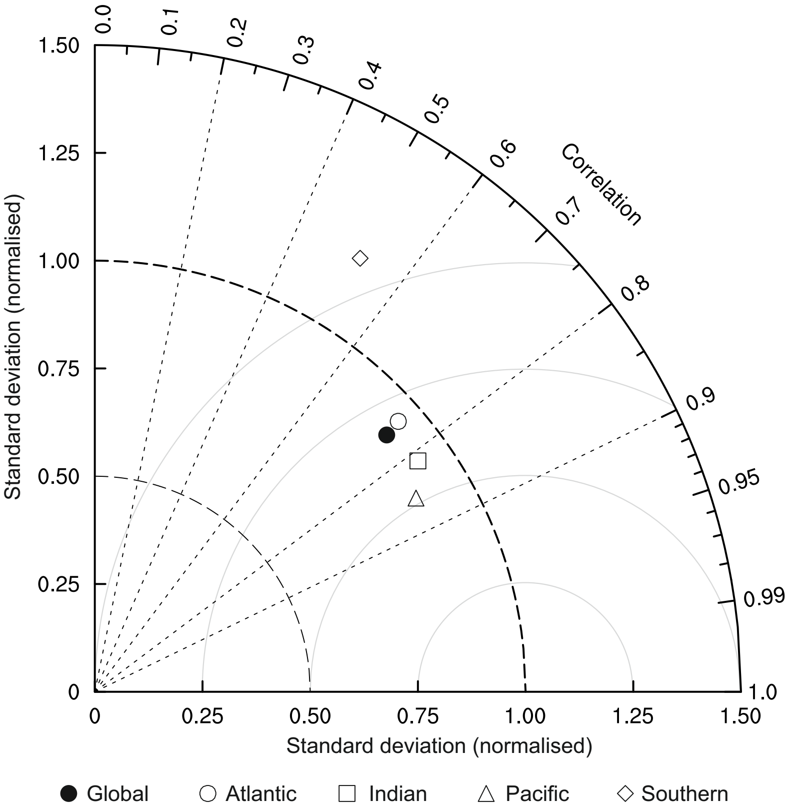

Figure 4.3: Taylor plot of simulated $\Delta^{14}C$ relative to the ungridded GLODAP observations from the 1990s (Key et al., 2004) separated by major ocean basin: global (filled circled), Atlantic (hollow circle), Indian (square), Pacific (triangle), and Southern (diamond). A perfect simulation would have a correlation coefficient of 1 and a normalised standard deviation (simulated standard deviation/observed standard deviation) of 1.

and observed values in more detail, we can assess the relative importance of each of these processes in controlling the $\Delta^{14}C$ distributions and establish how well the isotope scheme captures the behaviour of the model. For example, the simulated values are too high southwards of ≈30° S due to a combination of technical simulation set-up and model biases. Specifically, prescribing latitudinally-uniform atmospheric $\Delta^{14}C$ (Section 4.2.3.2) means that the input value is between 2 and 206 ‰ too high in the Southern Hemisphere between 1956 and 1969 (Figure 4.1). Consequently, the influx of ^{14}C into the surface ocean in this region is too large. This is accentuated by insufficient sea ice being simulated in the Southern Ocean, promoting excessive air-sea gas exchange. Furthermore, the simulated surface winds are weaker than observed (e.g. Kalnay et al., 1996). Although this reduces the input of ^{14}C from the atmosphere into the surface ocean (opposing the effects of the high input value and insufficient sea ice), it also results in a relatively shallow mixed layer. Reduced vertical mixing of the surface signal therefore leads to an accumulation of ^{14}C in the uppermost layers of the ocean. Conversely, but for similar reasons, the simulated values are lower than observed in the Northern Hemisphere sub-tropical gyres, largely because the input of ^{14}C is between 2 and 187 ‰

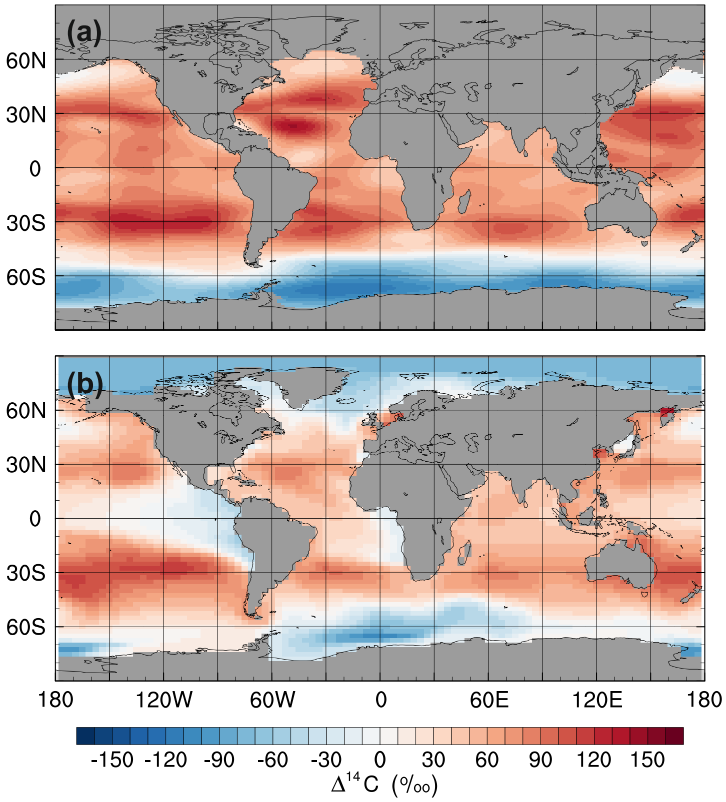

Figure 4.4: Mean surface ocean $\Delta^{14}C$ during the 1990s: (a) the gridded GLODAP data (Key et al., 2004) and (b) the simulated values.

too low northwards of 20° N (Figure 4.1). The simulated values are also lower than observed in the eastern equatorial regions due to the excessive upwelling of ^{14}C-depleted waters from the deep ocean (Palmer and Totterdell, 2001).

At depth, the highest $\Delta^{14}C$ values (youngest waters) are simulated in the Atlantic Ocean, with intermediate values in the Indian Ocean, and the lowest values (oldest waters) in the Pacific Ocean, in agreement with observations (Figure 4.6 and Figure E.2). The bomb signal (positive $\Delta^{14}C$ values) and newly formed deep waters (higher $\Delta^{14}C$ values) are clearly identifiable in the zonal means (Figure 4.6). However, the penetration of the bomb signal (white and red colours in Figure 4.6) is a few hundred metres too shallow in the model. This is due to the aforementioned insufficient convective mixing, which results in a relatively shallow mixed layer and excessive pooling of ^{14}C in the upper ocean. The simulated $\Delta^{14}C$ values also indicate that the abyssal Atlantic waters are too well ventilated as a result of over-deep North Atlantic Deep Water (NADW) formation and insufficient Atlantic-sector Antarctic Bottom Water (AABW) formation, which are known limitations of the FAMOUS GCM (Smith, 2012; Dentith et al., 2019). Across the whole ocean, the observed minimum $\Delta^{14}C$ value is -240 ‰, which occurs in the northeast North Pacific Ocean, at a depth of approximately 2500 m. In the model, there is weak (<1 Sv) convection to around 3 km depth in the sub-polar North Pacific, which

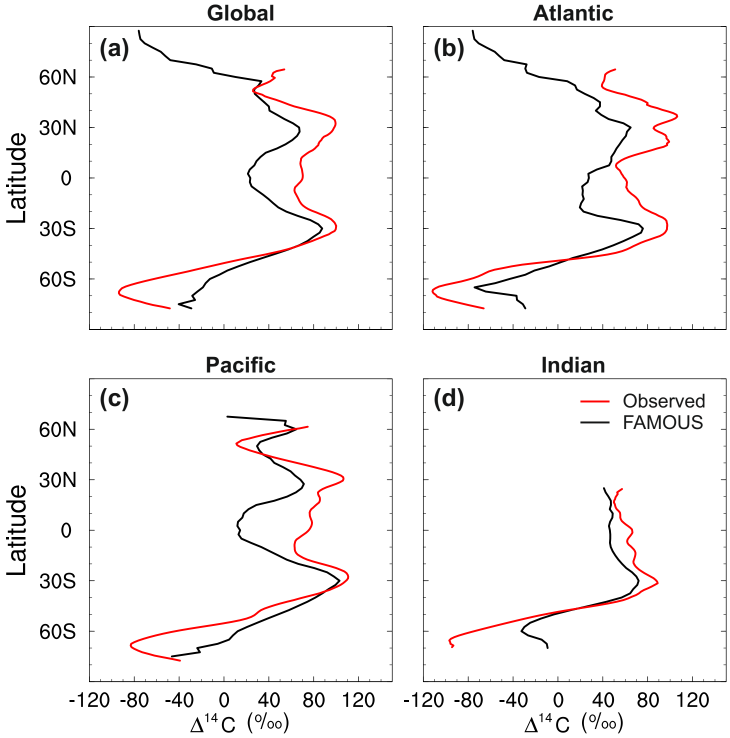

Figure 4.5: Zonal mean surface ocean Δ^{14}C during the 1990s: (a) global ocean, (b) Atlantic Ocean, (c) Pacific Ocean, (d) Indian Ocean.

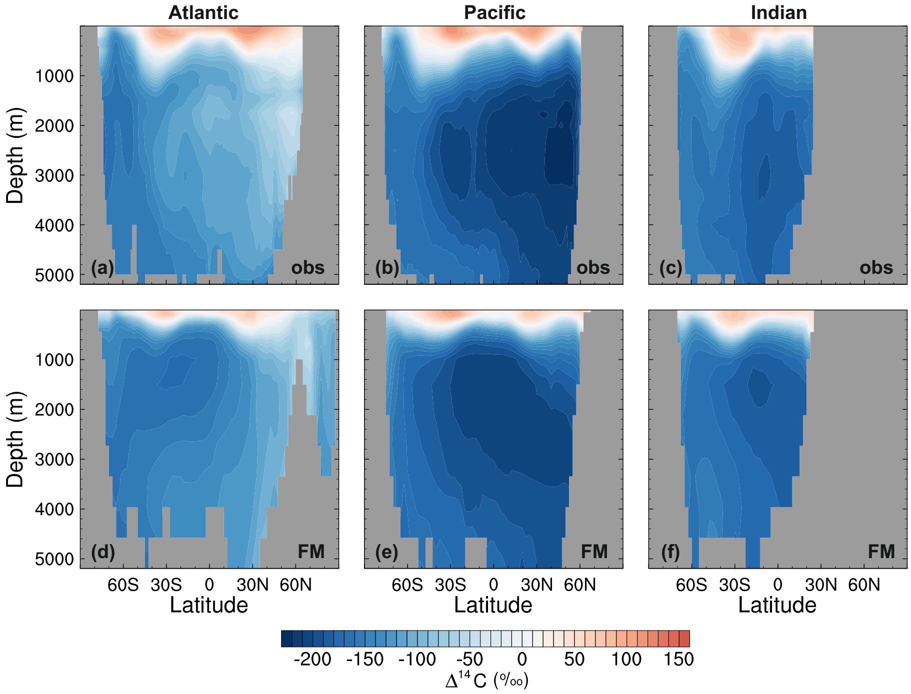

Figure 4.6: Zonal mean Δ^{14}C during the 1990s in the Atlantic Ocean (left), Pacific Ocean (centre) and Indian Ocean (right): the gridded GLODAP data (Key et al., 2004, top) and the simulated values (bottom).

prevents the accumulation of old, ^{12}C-enriched (low Δ^{14}C) waters (Figure 2.9). Instead, the simulated Δ^{14}C minimum (-215 ‰) is in the eastern equatorial Pacific at a depth of approximately 1500 m. Thus, the discrepancies between the simulated and observed Δ^{14}C distributions demonstrate that the ^{14}C isotope scheme is capturing the physical behaviour of the model well.

To examine the model performance in more detail, we have sub-divided the global ocean into 14 regions of interest, which include the sub-tropical gyres, deep water formation regions (simulated and/or observed), upwelling zones, and common coral locations (Figure 4.7). The simulated and observed depth profiles are well-matched, both regionally and globally (Figure 4.8), further supporting the notion that (on the whole) the uptake and transport of ^{14}C are well represented in the model. The globally averaged simulated Δ^{14}C values are a near-perfect match to the observed values at depths below 2500 m and, interestingly, there is excellent agreement between the simulated and observed Δ^{14}C values in the Southern Hemisphere deep water formation region (SH_DWF) and the Southern Ocean upwelling zone (SO_UP). We therefore infer that, although the Antarctic Circumpolar Current in FAMOUS is weak compared to observations (Dentith et al., 2019), it is still strong enough to homogenize the water column.

As previously discussed, and similar to other ^{14}C-enabled models (e.g. Jahn et al., 2015), many of the differences between the simulated and observed Δ^{14}C distributions can be explained by known physical biases. For example, the simulated Δ^{14}C gradient between the surface ocean and approximately 1000 m depth is shallower than observed

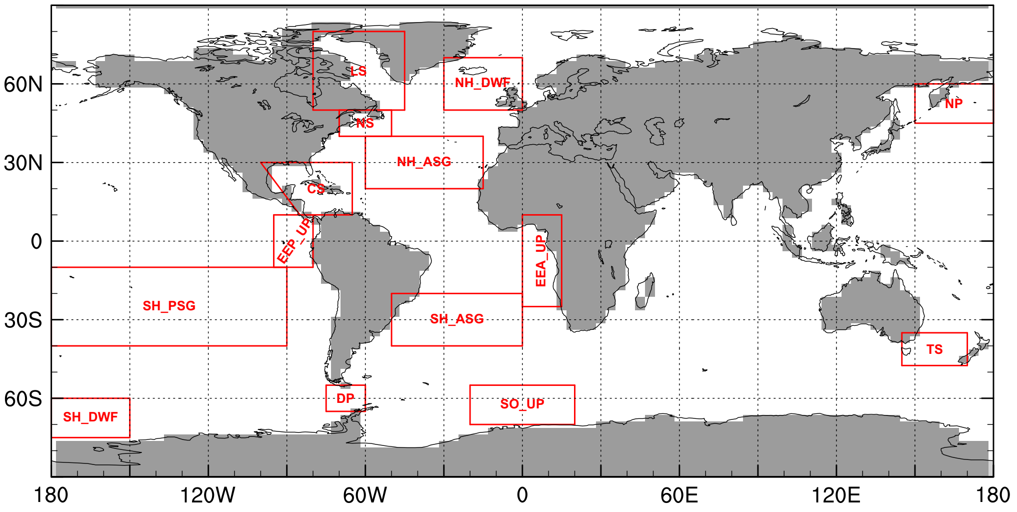

Figure 4.7: Location map of the regions of interest: Caribbean Sea (CS), Drake Passage (DP), eastern equatorial Atlantic upwelling zone (EEA_UP), eastern equatorial Pacific upwelling zone (EEP_UP), Labrador Sea (LS), Northern Hemisphere Atlantic sub-tropical gyre (NH_ASG), Northern Hemisphere deep water formation region (NH_DWF), North Pacific (NP), Nova Scotia (NS), Southern Hemisphere Atlantic sub-tropical gyre (SH_ASG), Southern Hemisphere deep water formation region (SH_DWF), Southern Hemisphere Pacific sub-tropical gyre (SH_PSG), Southern Ocean upwelling zone (SO_UP), and Tasman Sea (TS).

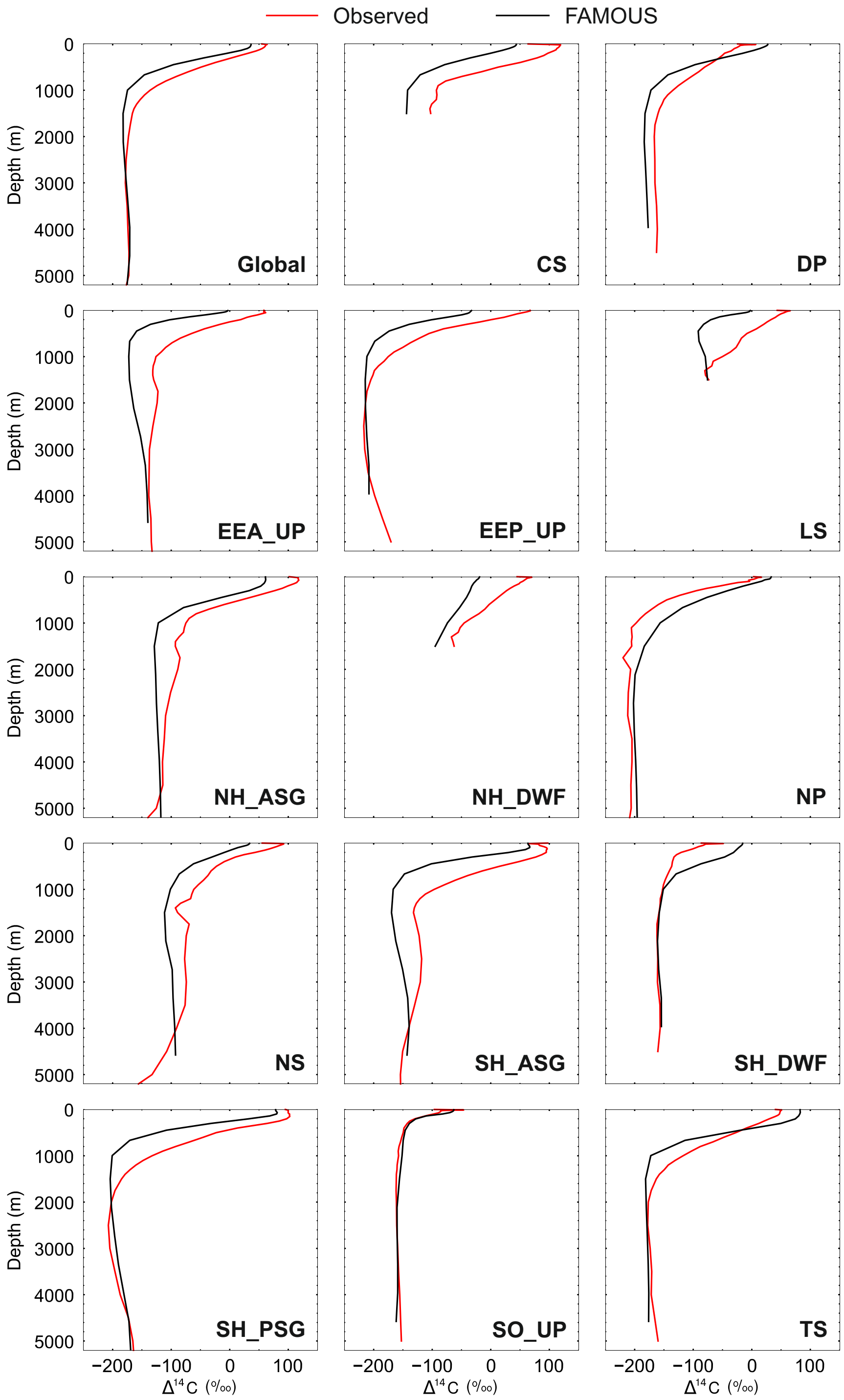

Figure 4.8: Global and regional depth profiles of simulated (black) and observed (red) Δ^{14}C during the 1990s. The regions are outlined in Figure 4.7: Caribbean Sea (CS), Drake Passage (DP), eastern equatorial Atlantic upwelling zone (EEA_UP), eastern equatorial Pacific upwelling zone (EEP_UP), Labrador Sea (LS), Northern Hemisphere Atlantic sub-tropical gyre (NH_ASG), Northern Hemisphere deep water formation region (NH_DWF), North Pacific (NP), Nova Scotia (NS), Southern Hemisphere Atlantic sub-tropical gyre (SH_ASG), Southern Hemisphere deep water formation region (SH_DWF), Southern Hemisphere Pacific sub-tropical gyre (SH_PSG), Southern Ocean upwelling zone (SO_UP), and Tasman Sea (TS).

because of insufficient convective mixing. This is visible in all regions, except the Northern Hemisphere deep water formation region (NH_DWF) and the North Pacific (NP), where convection in the model is deeper than it should be (Figure 2.9), thereby actively mixing the bomb signal into the sub-surface waters. In the modern oceans, NADW is formed in the Labrador and Nordic Seas (Kuhlbrodt et al., 2007); therefore, the observed depth profiles in these regions (LS and NH_DWF, respectively) are very similar. However, FAMOUS does not simulate deep water formation in the Labrador Sea, so the model has a much shallower $\Delta^{14}C$ profile here. In each of the observed Northern Hemisphere profiles (LS, NH_ASG, NH_DWF, NP, and NS), there is a negative $\Delta^{14}C$ excursion from ^{14}C-depleted Antarctic Intermediate Water between 1000 and 1500 m depth. This water mass is not represented in FAMOUS, so the simulated depth profiles are relatively smooth. Similarly, in the Southern Hemisphere Atlantic sub-tropical gyre (SH_ASG), the positive excursion in the $\Delta^{14}C$ measurements between 1500 m and 3000 m reflects the influx of ^{14}C-enriched NADW. In FAMOUS, the positive excursion extends below 4000 m because, as previously discussed, the modelled NADW cell has a greater vertical range than observed. The model accurately replicates the deep ocean values in the equatorial upwelling zones (EEA_UP and EEP_UP), which means that the waters being mixed upwards from the abyssal ocean towards the sea surface have approximately the correct isotopic signature. However, the strong upwelling rates in FAMOUS (Palmer and Totterdell, 2001) create an offset between the simulated values and the $\Delta^{14}C$ measurements in the shallow and intermediate waters. The masking in the GLODAP data set also contributes towards some of the offset between the model and the observations. For example, we include the relatively low Arctic Ocean values in our global, Northern Hemisphere deep water formation region (NH_DWF) and Labrador Sea (LS) profiles, but these latitudes are masked out in GLODAP due to the sparsity of data (Figure 4.4a). Overall, the regional depth profiles corroborate the skill of the biotic ^{14}C scheme in correctly capturing the physical behaviour of the model and demonstrate the potential of the new tracer for providing an independent constraint for future recalibration work (e.g. to improve the representation of the Atlantic Meridional Overturning Circulation in FAMOUS).

4.3.3 Comparison to natural archives

To better understand the penetration of the bomb signal into the ocean, we compare the transient surface and shallow-to-intermediate water $\Delta^{14}C$ values in our model with coral and bivalve records from 12 sites across the North Atlantic (Figure 4.9). Collectively, these archives span the period between the late 1800s and the early 2000s, thereby providing a record of pre-bomb $\Delta^{14}C$, the timing and magnitude of peak $\Delta^{14}C$ values, and the subsequent rate of decline. We present 16 published records in total (Table 4.1). The 7 bivalve records (as presented in the compilation of Scourse et al., 2012) are all from the uppermost 100 m of the water column. Five of the corals are from intermediate

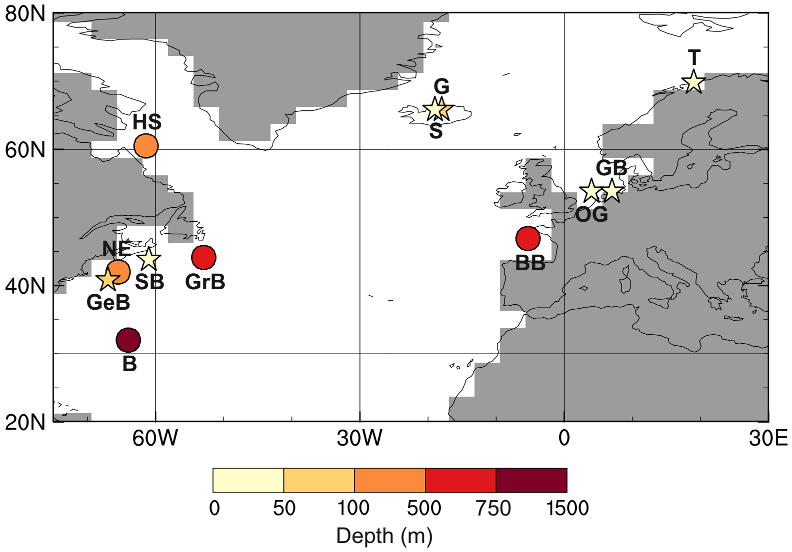

Figure 4.9: Location map of the North Atlantic coral (circles) and bivalve (stars) data used in this study: Bermuda (B), Bay of Biscay (BB), Grimsey (G), German Bight (GB), Georges Bank (GeB), Grand Banks (GrB), Hudson Strait (HS), Northeast Channel (NE), Oyster Ground (OG), Siglufjörður (S), Sable Bank (SB), and Tromsø (T). The depth of the archive is denoted by the marker colour.

depths (between 362.5 m and 1410.0 m). Three of these corals are bamboo corals, which simultaneously record the surface and ambient Δ^{14}C (Section 4.1). We have also included a surface coral record from Bermuda to complement the deep-sea record from this site.

Bomb ^{14}C is observed in all 16 published records and in the corresponding model output (Figure 4.10). The peak oceanic values are consistently lower than the peak atmospheric values (Figure 4.1) because of the relative sizes of the two carbon pools (Ciais et al., 2013). In general, the model captures both the relative timing and the overall shape of the observed profiles very well. This reaffirms the skill of FAMOUS in representing carbon uptake and transport. It also suggests that large-scale processes (such as air-sea gas exchange and vertical mixing) are more important for determining the manifestation of the marine bomb pulse than local processes (such as riverine input and exchange between coastal basins and the open ocean), which are not represented as accurately in the model.

In the shallow ocean (0 to 100 m), the ambient Δ^{14}C profiles (both simulated and observed) closely resemble the simulated surface Δ^{14}C profiles (Figure 4.10), demonstrating how efficiently the bomb signal is transferred throughout the mixed layer. Bomb ^{14}C is detected at all sites almost immediately following its injection into the atmosphere, with the simulated Δ^{14}C values starting to increase as early as 1956 and 1957. At every site the rate of increase from pre-bomb to peak Δ^{14}C values is faster than the rate of decline, indicating that air-sea gas exchange is more efficient than vertical mixing between shallow and intermediate waters. By the year 2000, all sites still have elevated Δ^{14}C relative to the natural levels.

Table 4.1: Coral and bivalve locations, record lengths, and original references.

Identifier	Location	Latitude (° N)	Longitude (° E)	Depth (m)	Archive	Length of record	Number of measurements	Reference
B	Bermuda	32	-64	0	Coral	1950 to 1983	35	Druffel (1989)
B	Bermuda	32	-64	1410	Coral	≈1400[1] to 2001	26[2]	Lee et al. (2017)
BB	Bay of Biscay	46.9	-5	691	Coral	1950 to 1985	19	Montero-Serrano et al. (2013)
G	Grimsey	66	-18	82	Bivalve	1935 to 2005	16	Scourse et al. (2012)
GB	German Bight	54	7	37	Bivalve	1948 to 1990	20	Weidman (1995)
GeB	Georges Bank	41	-67	76	Bivalve	1939 to 1989	13	Weidman and Jones (1993)
GrB	Grand Banks	44.13	-52.93	0	Coral	1884 to 1991	12	Sherwood et al. (2008)
GrB	Grand Banks	44.13	-52.93	713	Coral	1879 to 2001	12	Sherwood et al. (2008)
HS	Hudson Strait	60.5	-61.4	0	Coral	1925 to 2000	18	Sherwood et al. (2008)
HS	Hudson Strait	60.5	-61.4	414	Coral	1941 to 1994	3	Sherwood et al. (2008)
NE	Northeast Channel	42	-65.5	0	Coral	1924 to 2002	26	Sherwood et al. (2008)
NE	Northeast Channel	42	-65.5	362.5[3]	Coral	1890 to 1983	14	Sherwood et al. (2008)
OG	Oyster Ground	54	4	40	Bivalve	1928 to 1986	30	Witbaard et al. (1994)
S	Siglufjörður	66	-19	22	Bivalve	1874 to 1991	17	Weidman (1995)
SB	Sable Bank	44	-61	35	Bivalve	1956 to 1981	15	Kilada et al. (2007)
T	Tromsø	70	-19	3	Bivalve	1940 to 1993	14	Weidman (1995)

[1] 1441 based on the coral's higher vertical extension rate and 1373 based on the coral's lower vertical extension rate.

[2] 19 of which are between ≈1880 and 2001 and 7 of which are between ≈1400 and ≈1700.

[3] Between 275 m and 450 m.

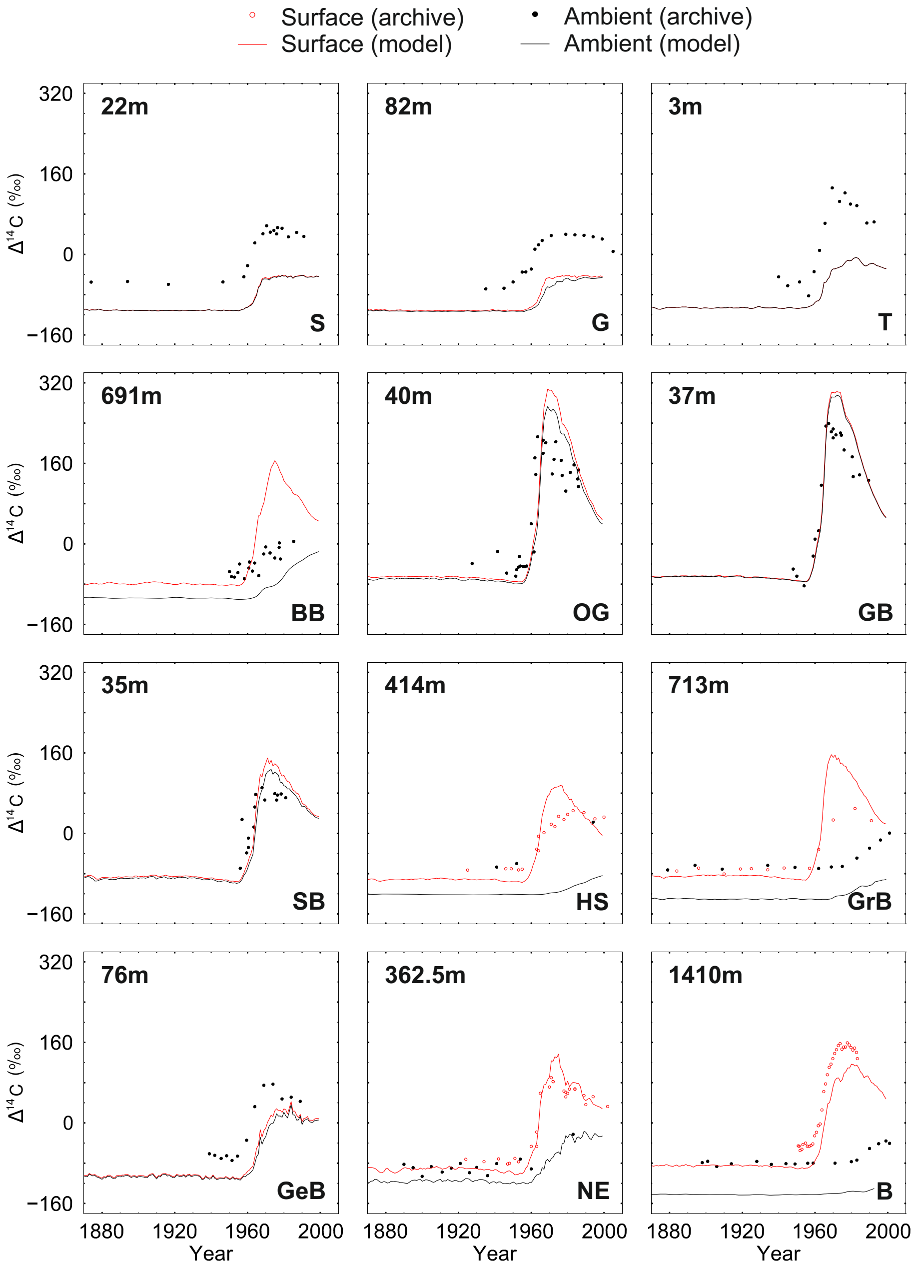

Figure 4.10: Simulated (lines) and observed (markers) surface (red) and ambient (black) $\Delta^{14}C$ at the coral and bivalve locations (outlined in Figure 4.9): Bermuda (B), Bay of Biscay (BB), Grimsey (G), German Bight (GB), Georges Bank (GeB), Grand Banks (GrB), Hudson Strait (HS), Northeast Channel (NE), Oyster Ground (OG), Siglufjörður (S), Sable Bank (SB), and Tromsø (T). Note that only the bamboo corals (GrB, HS, and NE) and Bermuda (B) have surface observations. Additionally, the simulated surface and ambient $\Delta^{14}C$ values are the same for Tromsø (T) because the surface layer in the model is 10 m deep.

Examining the similarities and differences between the simulated and observed timeseries, and between the simulated timeseries in different locations, can also help to improve our understanding of the important processes controlling the expression of the marine bomb spike, both in the model and in reality. As noted by Scourse et al. (2012), the hydrographic setting of each site influences the time taken for ^{14}C to be detected, the overall strength of the signal, and its residence time. The surface timeseries therefore fall into three categories: high amplitude-early peaks, low amplitude-late peaks, and intermediate amplitude peaks (Figure 4.10). In agreement with observations, the highest $\Delta\Delta^{14}$C (peak Δ^{14}C minus pre-bomb Δ^{14}C) values are simulated at Oyster Ground (OG; ≈370 ‰) and German Bight (GB; ≈365 ‰), with peak values attained in 1972 and 1969, respectively. These are both shallow, coastal sites that have small carbon reservoirs (Figure 4.9 and Figure 4.11), therefore they are strongly influenced by air-sea gas exchange. Conversely, the lowest $\Delta\Delta^{14}$C values are simulated at Siglufjörður (S; 70.0 ‰) and Grimsey (G; 70.0 ‰), where the Δ^{14}C values plateau between 1970 and 2000. These sites are in the NADW formation region where the water column is well mixed, with ^{14}C-depleted waters being upwelled from the abyssal ocean and ^{14}C-enriched surface waters being quickly transported to depth (Figure 4.11). The simulated timeseries have higher variability at sites where convection is less persistent (GeB and NE; Figure 4.10), and similar variability is captured by the Oyster Ground (OG) bivalve, which is subject to increased stratification in the summer months (Scourse et al., 2012). The Tromsø (T) bivalve is located in a fjord that is strongly influenced by the North Atlantic Current and the Norwegian Coastal current (Scourse et al., 2012), but this unique hydrographic setting is not captured by FAMOUS. Instead, Tromsø is within the model's Northern Hemisphere deep water formation region. The model therefore simulates an attenuated bomb peak relative to the observations (Figure 4.10), which is comparable to the simulated timeseries at other sites that are affected by persistent deep convection, such as Grimsey (G) and Siglufjörður (S). The observed surface ocean profiles from the Hudson Strait (HS) and Grand Banks (GrB) corals are very similar (Figure 4.10) because both sites are influenced by the Labrador Current, which has a one year transit time from HS in the northwest to GrB in the southeast (Sherwood et al., 2008). FAMOUS does not simulate deep water formation in the Labrador Sea and coastal currents in this semi-enclosed region are not well resolved by the model. The simulated surface peaks at these sites are therefore of a higher amplitude than observed, more so at Grand Banks (GrB), which is less affected by seasonal sea ice than the Hudson Strait (HS). It is interesting to note that, in the model, similar bomb profiles are simulated in very different hydrographic settings, for example in the Hudson Strait (HS) and Bermuda (B). The Hudson Strait (HS) is a semi-enclosed setting that is characterised by weak surface currents although, as previously discussed, it should also be influenced by deep convection (but is not in the model). In contrast, Bermuda (the furthest site from the coast included in this study) is influenced by strong horizontal advection (sub-tropical gyre circulation) and weak vertical mixing. In general, both of the simulated profiles adequately capture the shape and timing of the observed surface timeseries, however, the two observed profiles differ in that the Hudson Strait (HS) could be classed as having a low-to-medium amplitude peak whilst Bermuda (B) has a medium-to-high amplitude peak.

As expected, in the intermediate ocean (362.5 m to 1410.0 m), the bomb signal is lagged and damped relative to the surface ocean (Figure 4.10). For example, in the Northeast Channel (NE), bomb ^{14}C is detected in the ambient Δ^{14}C signal in 1961 (5 years later than in the surface ocean), with peak values simulated in 1989 (14 years later than in the surface ocean). The simulated $\Delta\Delta^{14}$C at depth is $\approx$100 ‰ compared to $\approx$140 ‰ in the surface ocean, and by the year 2000, the ambient values had only decreased by $\approx$10 ‰ compared to $\approx$110 ‰ in the surface layer. Given the temporal resolution of the coral records, it is unclear whether the Δ^{14}C values in the intermediate ocean have peaked at the end of the timeseries, but we can use the isotope-enabled model to predict the depth to which the bomb ^{14}C has penetrated (Figure 4.11) and thus infer ongoing trends. For example, the relatively high resolution Grand Banks (GrB) record still appears to be on an upward trajectory in the year 2000, which is corroborated by the model output (Figure 4.10). However, the 1410 m Bermuda (B) coral records a $\approx$5 ‰ decrease in Δ^{14}C between 1999 and 2001 (Figure 4.10). Additional measurements would be needed to confirm whether this is natural variability or a permanent reversal, but because the model accurately captures the observed signal at this site, we infer that the Δ^{14}C values at $\approx$1400 m have not peaked by the year 2000 (Figure 4.10 and Figure 4.11). We can also use the isotope-enabled model to fill in the gaps when there is a lack of ambient data. For example, there are only three data points from intermediate water depths in the Hudson Strait (HS), each of which is within 15 ‰ of the nearest dated surface measurement (Figure 4.10). From these data alone, it is therefore unclear whether the Δ^{14}C values at intermediate depths peak at a similar time to the surface ocean or whether the intermediate ocean responds more slowly. Again, however, we use the model to infer that peak ^{14}C values have not been attained at $\approx$400 m depth by the year 2000. In fact, the model suggests that, by the year 2000, the Δ^{14}C values have only peaked at the shallowest of the intermediate ocean sites included in this study, the Northeast Channel (NE; Figure 4.10 and Figure 4.11).

The difference between the surface and ambient Δ^{14}C can be used to infer the extent of vertical mixing in the water column (Sherwood et al., 2008). In both the Hudson Strait (HS) and Grand Banks (GrB) coral records, the intermediate water values are similar to the surface ocean values in the pre-bomb era, demonstrating that the water column is well mixed to depths of at least 400 m and 700 m, respectively. In the Northeast Channel (NE), the average difference between the observed surface and ambient values in the pre-bomb era is approximately 15 ‰, suggesting that the water column is more stratified off the coast of Nova Scotia than it is further to the north (in the Labrador Sea) and east (off the coast of Newfoundland). The model simulates a larger difference (approximately 10 to

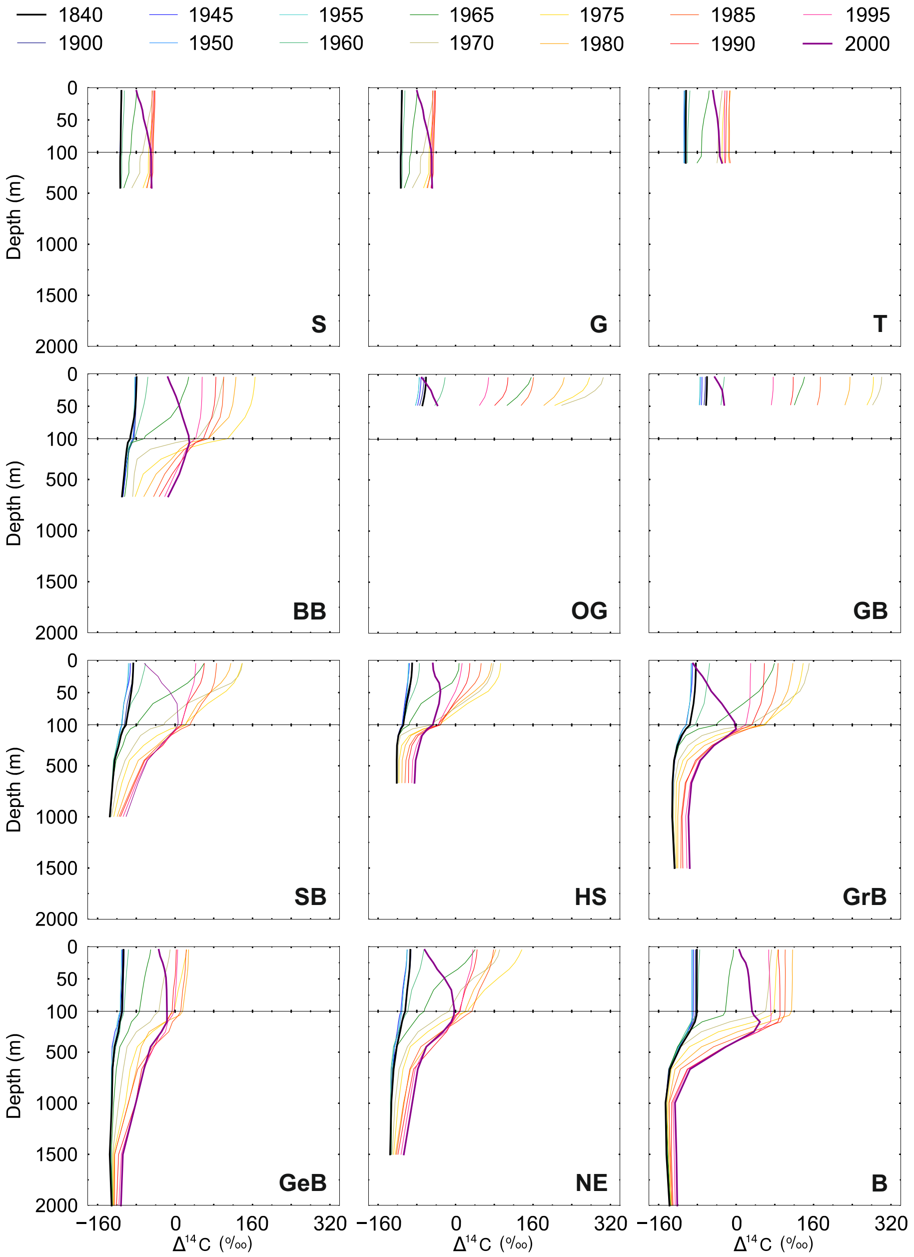

Figure 4.11: Transient depth profiles of simulated Δ^{14}C at the coral and bivalve locations (outlined in Figure 4.9): Bermuda (B), Bay of Biscay (BB), Grimsey (G), German Bight (GB), Georges Bank (GeB), Grand Banks (GrB), Hudson Strait (HS), Northeast Channel (NE), Oyster Ground (OG), Siglufjörður (S), Sable Bank (SB), and Tromsø (T). Note that the vertical scale has been expanded for the uppermost 100 m of the water column.

30 ‰) between the surface and ambient signal at all four of the sites where the natural archives cover multiple depths (HS, GrB, NE, and B), which corroborates our earlier interpretation that the water column in FAMOUS is less well ventilated than observed.

Overall, this comparison demonstrates the utility of the isotope-enabled model for providing plausible data to fill in spatiotemporal gaps in proxy records and for corroborating suggestions from observational studies about the processes controlling the transfer of carbon from the atmosphere to shallow and intermediate water depths in different hydrographic settings. It also underlines the skill of the isotope scheme in highlighting physical model biases (e.g. insufficient convection in the Labrador Sea), which could be improved by retuning the model.

4.3.4 Influence of the biological pump

To analyse the influence of biology on the ^{14}C distributions in FAMOUS, it is useful to compare the simulated biotic and abiotic δ^{14}C values (Eq. (4.9)) in the surface ocean and at depth. As outlined in Sections 4.2.2.3 and 4.2.2.2, respectively, the biotic tracer is cycled through the biological pump and is subject to isotopic fractionation, whereas the abiotic tracer is only affected by air-sea gas exchange, advection, and radioactive decay.

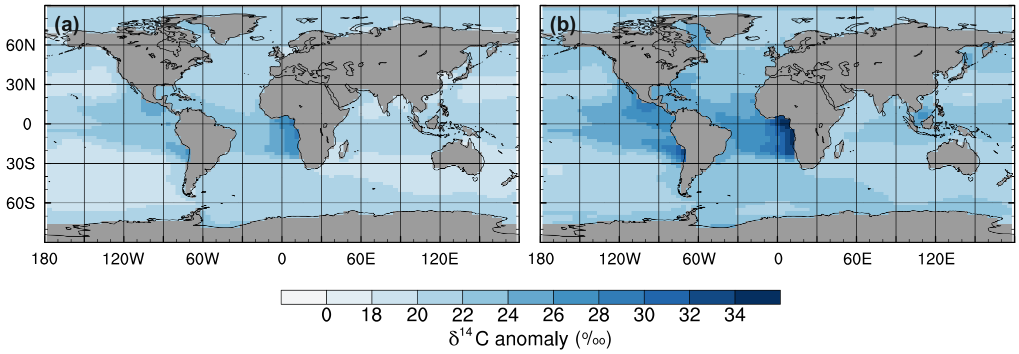

Figure 4.12: Biotic minus abiotic surface ocean δ^{14}C: (a) the end of the spin-up simulation (years 9900 to 10,000) and (b) the 1990s. Note that Figure E.4 presents the equivalent figures in the Δ^{14}C reference frame.

As expected, the simulated biotic δ^{14}C values are higher than the corresponding abiotic δ^{14}C values everywhere in the global surface ocean (Figure 4.12). This is because the biotic tracer accounts for the preferential uptake of ^{12}C during primary productivity, which leaves the DIC pool relatively enriched in ^{14}C, whereas the abiotic tracer is not affected by biological fractionation. In the pre-industrial ocean, the offset between the two tracers ranges between 17.6 ‰ in the Southern Hemisphere Pacific sub-tropical gyre and 28.6 ‰ in the equatorial upwelling zones, with a mean difference of 20.8 ‰. In the post-bomb era, the offset ranges between 19.8 ‰ and 35.2 ‰, with a mean difference of 22.6 ‰. Notably, in both cases, the anomaly is larger in the eastern equatorial Atlantic

Ocean than the eastern equatorial Pacific Ocean, even though the Pacific region has higher simulated primary productivity. We propose that this asymmetry relates to the age of the waters that are being upwelled in each basin. The upwelling Pacific waters are approximately 600 years older than water that is being upwelled from the deep Atlantic basin (Figure E.3). The deep Pacific waters will therefore have a relatively lower δ^{14}C signature as a result of radioactive decay. However, both the abiotic and biotic schemes account for this effect. Instead, we suggest that the primary cause of the asymmetrical difference between the biotic and abiotic tracers is that the older Pacific waters contain a larger proportion of remineralised organic matter, which is enriched in ^{12}C in the biotic scheme, reinforcing the lower δ^{14}C signal that is being mixed upwards into the surface waters.

We also assess the importance of the biological pump for transporting ^{14}C into the deep ocean (Figures E.6 to E.11). We have focussed our analysis on the same 14 regions of interest outlined in Section 4.3.2 and Figure 4.7. In both the pre-industrial and the post-bomb ocean, the globally averaged difference between the biotic and abiotic δ^{14}C in the deep ocean is approximately 19.7 ‰ (Figure 4.13). This is lower than the mean difference between the two tracers in the surface ocean because the remineralisation of ^{12}C-enriched particulate organic carbon reduces the biotic δ^{14}C at depth, but the abiotic δ^{14}C is unaffected by this process. The δ^{14}C difference in the eastern equatorial Pacific upwelling zone (EEP_UP) is 0.6 ‰ higher than the global mean difference in the pre-industrial ocean, and 0.75 ‰ higher in the post-bomb ocean. In each of the 13 other regions of interest, the deep ocean difference between the abiotic and biotic tracers is close to the global mean difference in both timeslices. Δ^{14}C measurements from proxy records are typically reported to 1 decimal place (e.g. Sherwood et al., 2008; Scourse et al., 2012) and the error in the coral and bivalve data presented in Section 4.3.3 ranges between 2.1 ‰ and 22.0 ‰, with an average error of approximately 5.5 ‰. The offset between the δ^{14}C difference in the eastern equatorial Pacific upwelling zone (EEP_UP) and the global mean difference (which is the largest spatial disparity; Figure 4.13) is therefore of the same order of magnitude as the precision of ^{14}C measurements and is well within the analytical error. Thus, we infer that, from an analytical perspective, the biological pump has a spatially constant influence on deep ocean ^{14}C concentrations, which could be accounted for with a global correction of approximately 20 ‰. Simulations performed with other ^{14}C-enabled models (Table 1.2) would be needed to verify how model-dependent our suggested correction is. Furthermore, sensitivity experiments would be required to verify whether the same conclusion (and correction) holds true for palaeo studies, for example, at the Last Glacial Maximum, when there is evidence that the spatial distribution and overall levels of primary productivity were different from present (although there is no overall consensus as to whether the biological pump was weaker or stronger; Shemesh et al., 1993; Kumar et al., 1995; Anderson et al., 1998).

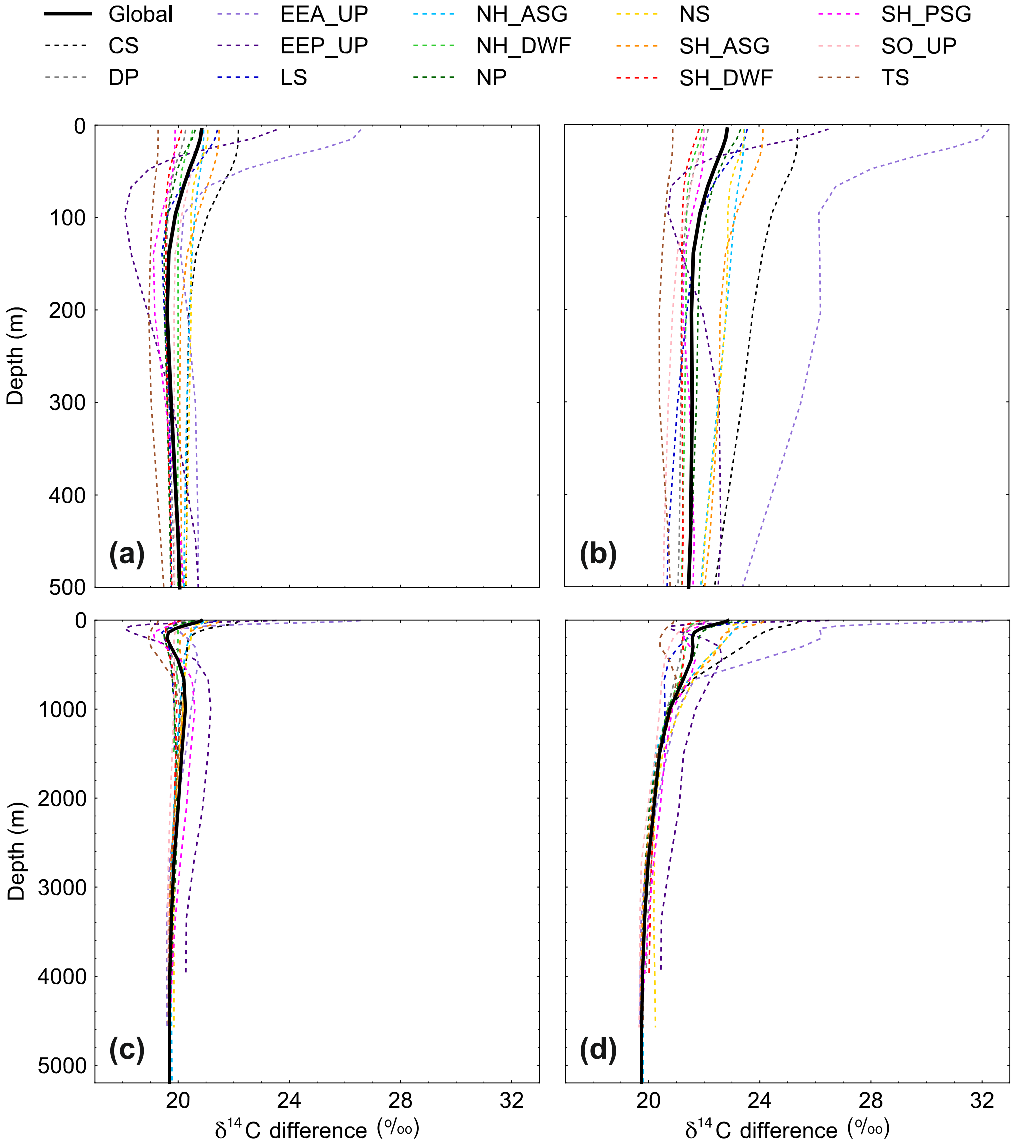

Figure 4.13: Global (solid black) and regional (dotted) depth profiles of biotic minus abiotic δ^{14}C: (a, c) the end of the spin-up simulation (years 9900 to 10,000) and (b, d) the 1990s; (a, b) the uppermost 500 m of the ocean and (c, d) the whole water column. The regions are outlined in Figure 4.7: Caribbean Sea (CS), Drake Passage (DP), eastern equatorial Atlantic upwelling zone (EEA_UP), eastern equatorial Pacific upwelling zone (EEP_UP), Labrador Sea (LS), Northern Hemisphere Atlantic sub-tropical gyre (NH_ASG), Northern Hemisphere deep water formation region (NH_DWF), North Pacific (NP), Nova Scotia (NS), Southern Hemisphere Atlantic sub-tropical gyre (SH_ASG), Southern Hemisphere deep water formation region (SH_DWF), Southern Hemisphere Pacific sub-tropical gyre (SH_PSG), Southern Ocean upwelling zone (SO_UP), and Tasman Sea (TS). Note that Figure E.5 presents the equivalent figures in the Δ^{14}C reference frame.

4.3.5 Comparison to water age

Radiocarbon ages are commonly used as a proxy for the length of time since a water parcel was last in contact with the atmosphere (e.g. Stuiver et al., 1983; Broecker et al., 1990). To assess the validity of this interpretation, we compare the simulated ^{14}C ages (Eq. (4.10)) with the idealised water ages at the end of the 10,000 year spin-up simulation. By subsetting the data in two different ways, we are able to identify specific regions where the water ages are well represented by ^{14}C ages, as well as regions where the relationship breaks down. Firstly, we consider the major ocean basins and divide the water column into shallow (0 to 550 m), intermediate (550 to 2500 m) and deep (2500 to 5500 m) water based on the components of overturning circulation described by Talley (1999). We also compare the water age and ^{14}C age depth profiles in the 14 regions of interest outlined in Figure 4.7.

As expected, the simulated ^{14}C ages are consistently older than the simulated water ages in the surface ocean, where the water age is preconditioned to be zero. The ^{14}C reservoir effect ranges between approximately 450 years in the sub-tropical gyres and 1300 years in the Southern Ocean (Figure 4.14a), reflecting the 5 to 10 year timescale required for isotopic equilibration between the ocean and the atmosphere (Toggweiler et al., 1989a; Lynch-Stieglitz, 2003; Sarmiento and Gruber, 2006), which is significantly longer than surface water residence times (e.g. 2 years for Antarctic Surface Waters; Lynch-Stieglitz et al., 1995). Consequently, in the shallow ocean (0 to 550 m; red shapes in Figure 4.15), the lowest r^2 values are in the Southern Ocean because sea ice and short surface water residence times limit air-sea gas exchange, which increases the ^{14}C reservoir ages (Figure 4.14b and Figure 4.14c). The convective mixing of ^{14}C-depleted waters from the abyssal ocean into the shallow ocean at sites of deep water formation further increases the reservoir effect. The highest shallow ocean r^2 values are in the Indian Ocean where relatively long surface water residence times in the sub-tropical gyre allow the surface ocean to come closer to equilibrium with the atmosphere (reducing the ^{14}C reservoir effect) and, in contrast to the Atlantic and Pacific basins, there is no significant upwelling of older (^{14}C -depleted) waters from the deep ocean.

The regional depth profiles demonstrate that, where there is convective mixing (i.e. in the near-surface ocean), the ^{14}C ages and water ages follow similar patterns, with an offset due to the aforementioned incomplete air-sea gas exchange (Figure 4.16 and Figure E.12). Considering the water column as a whole, the water ages generally increase with depth because they are a simple function of advection. In contrast, the ^{14}C ages typically decrease or remain near constant with depth below approximately 1000 m, as per the DIC concentrations. In Section 4.3.4, we concluded that the biological pump has a spatially constant influence on deep ocean ^{14}C concentrations. We therefore infer that the shapes of the regional ^{14}C age profiles are largely controlled by the solubility pump, which we can separate into two components: the physical component (i.e. ocean circulation) and

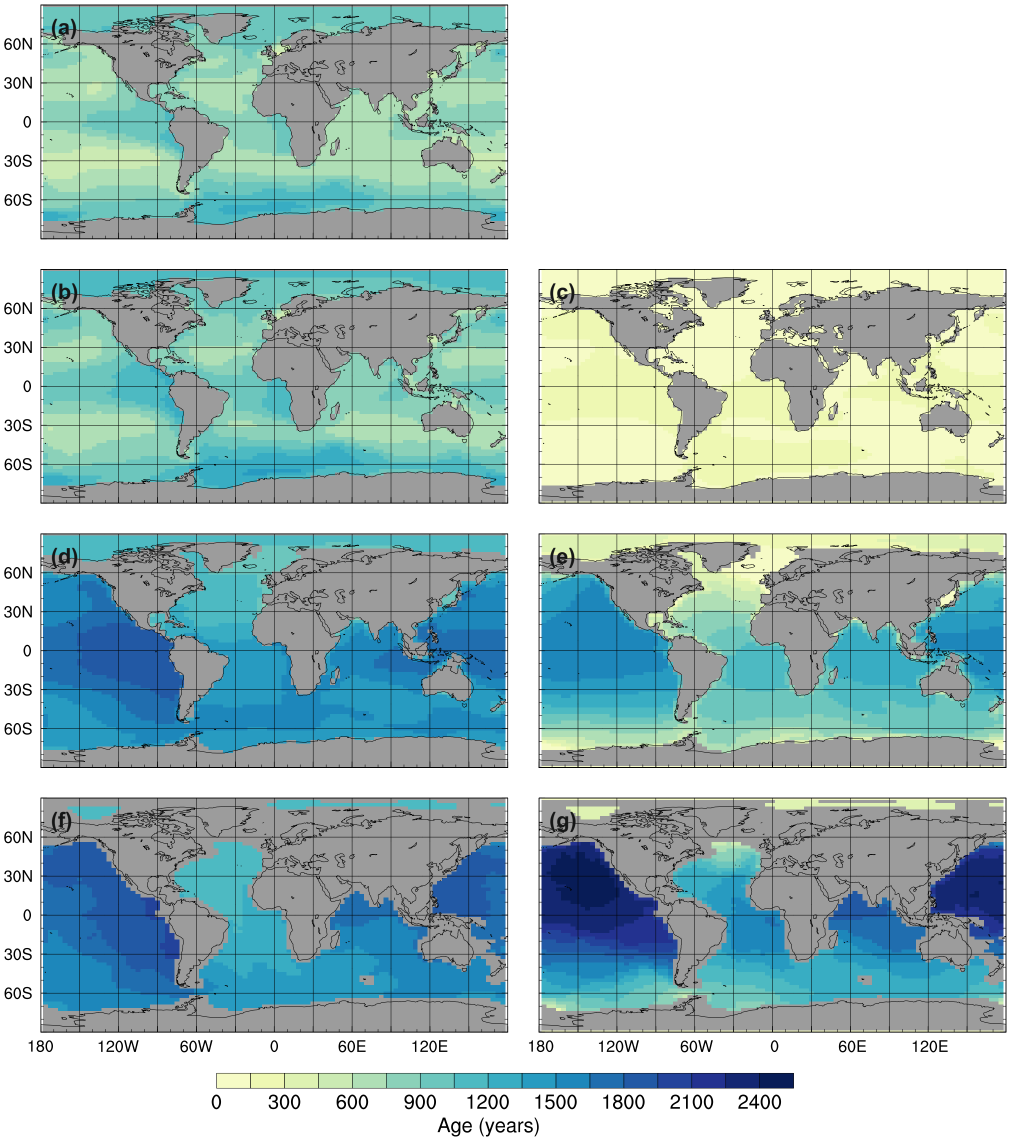

Figure 4.14: ^{14}C ages (left) and water ages (right) at the end of the spin-up simulation (years 9900 to 10,000): (a) the surface ocean (0 to 10 m), (b – c) the shallow ocean (0 to 550 m), (d – e) the intermediate ocean (550 to 2500 m), and (f – g) the deep ocean (2500 to 5500 m).

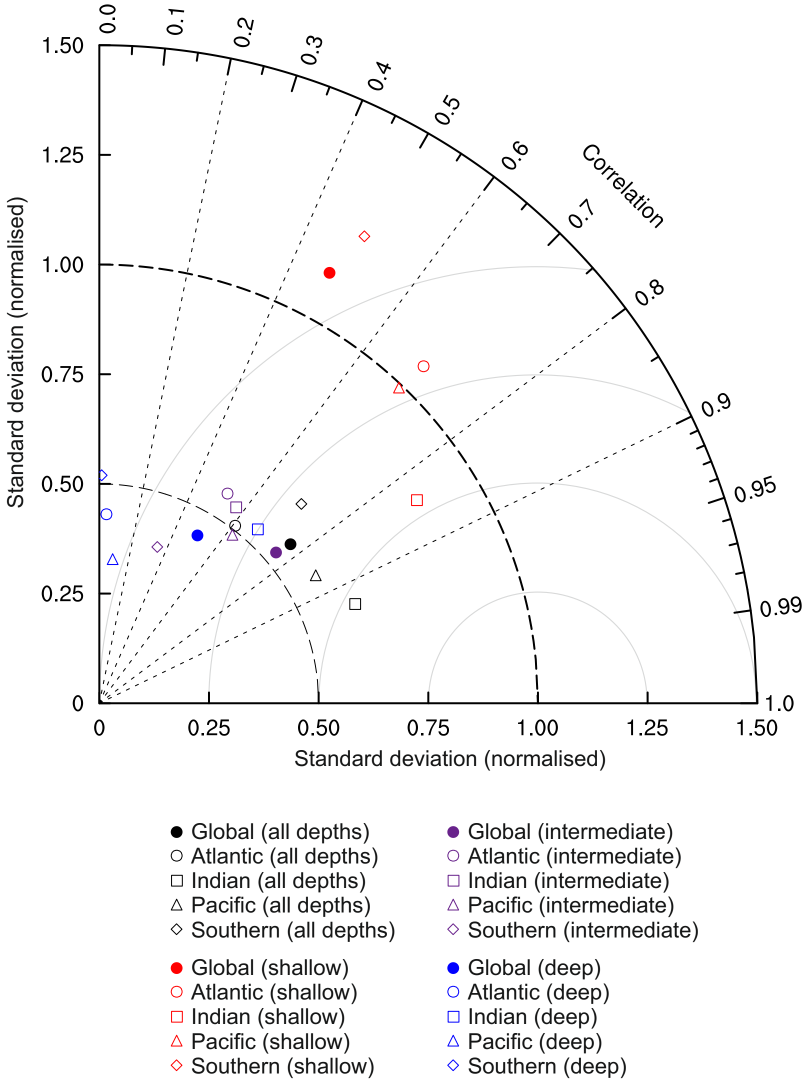

Figure 4.15: Taylor plot of ^{14}C age relative to the idealised water age at the end of the spin-up simulation (years 9900 to 10,000). The data are separated by basin (shapes) and water depth (colours): shallow (0 to 550 m), intermediate (550 to 2500 m), and deep (2500 to 5500 m). A perfect simulation would have a correlation coefficient of 1 and a normalised standard deviation (simulated standard deviation/observed standard deviation) of 1.

the chemical component (i.e. the temperature dependence of the solubility of CO_2 in seawater, with increased solubility in cold – high latitude and deep ocean – waters relative to warm – low latitude and surface ocean – waters). Our simulations demonstrate that ^{14}C is a good tracer for water age in regions where the physical component is more dominant (i.e. in well mixed regions such as the Drake Passage, DP, the Northern Hemisphere deep water formation region, NH_DWF, and the Tasman Sea, TS; and in shallow marginal seas, such as the Caribbean Sea, CS, and the Labrador Sea, LS), and that elsewhere, where the chemical component is more dominant, the relationship between water age and ^{14}C age breaks down

In the deep ocean (2500 to 5550 m; blue shapes in Figure 4.15), the r^2 values in the Atlantic, Pacific and Southern Oceans are all less than 0.1, demonstrating that, at basin-scale, the water age distributions at these depths are not well represented by the ^{14}C ages (Figure 4.14f and Figure 4.14g). In contrast, the r^2 value in the deep Indian Ocean is 0.67. We propose two main reasons as to why the correlation between the water ages and the ^{14}C ages in the deep Indian Ocean is higher than elsewhere. Firstly, there is no deep water formation in this basin, which mixes young water with a relatively high ^{14}C age into the abyssal Atlantic and Southern Oceans. Secondly, the average surface ocean temperature is between 4.5 °C and 18 °C higher than in the other basins, which means that the chemical component of the solubility pump is weaker.

Previous studies have also identified problems with using ^{14}C to infer deep ocean ventilation rates. For example, Campin et al. (1999) implemented a water age tracer and abiotic ^{14}C into a $3^\circ \times 3^\circ$ ocean-only GCM. In their model, the simulated ^{14}C ages of NADW and AABW were systematically older than the water ages, which the authors attributed to incomplete air-sea equilibration as a result of short surface water residence times with respect to air-sea gas exchange rates and interference from sea ice. The ^{14}C ages of NADW and AABW in FAMOUS are >700 years and >1000 years older than the water ages, respectively (Figure 4.14). In agreement with Campin et al. (1999), we propose that this is largely due to the ^{14}C surface reservoir effect. However, Campin et al. (1999) did not account for isotopic fractionation in their study, nor was their ^{14}C tracer cycled through the marine biological pump. Based on the results of our abiotic-biotic $\delta^{14}C$ comparison (Section 4.3.4), we suggest that the biological pump reduces the ^{14}C reservoir effect (more so in the surface ocean than at depth) because it enriches the DIC pool in the heavier isotope (Figure 4.13).

Overall, we have demonstrated that the simulated ^{14}C distributions are sensitive to a mixture of physical and biogeochemical processes, therefore, in agreement with Campin et al. (1999), we suggest that interpreting ^{14}C ages in terms of ventilation alone may lead to erroneous conclusions about palaeocean circulation. Proxy data from the deep ocean are important for understanding how physical ocean circulation may have changed in the past, but our model results suggest that, to be interpreted in terms of water age, the

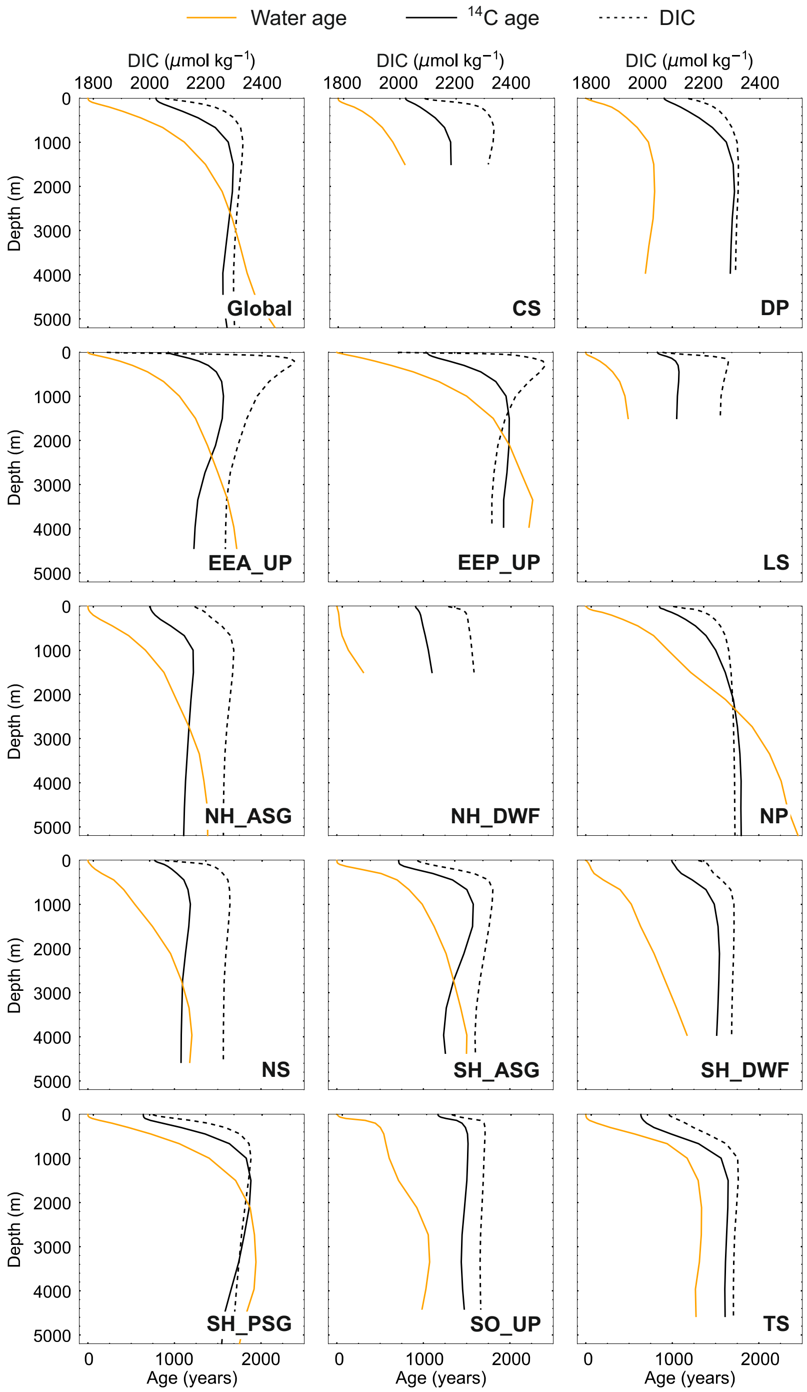

Figure 4.16: Global and regional depth profiles of water age (orange), ^{14}C age (solid black), and DIC concentration (dotted black) at the end of the spin-up simulation (years 9900 to 10,000). The water ages and ^{14}C ages use the bottom axis, and the DIC concentrations use the top axis. The regions are outlined in Figure 4.7: Caribbean Sea (CS), Drake Passage (DP), eastern equatorial Atlantic upwelling zone (EEA_UP), eastern equatorial Pacific upwelling zone (EEP_UP), Labrador Sea (LS), Northern Hemisphere Atlantic sub-tropical gyre (NH_ASG), Northern Hemisphere deep water formation region (NH_DWF), North Pacific (NP), Nova Scotia (NS), Southern Hemisphere Atlantic sub-tropical gyre (SH_ASG), Southern Hemisphere deep water formation region (SH_DWF), Southern Hemisphere Pacific sub-tropical gyre (SH_PSG), Southern Ocean upwelling zone (SO_UP), and Tasman Sea (TS).

records must be carefully selected from well mixed regions, and should be interpreted as a local not a basin-wide signal. The isotope-enabled model is therefore a useful tool for identifying plausible convective regions in the geological past (for example under glacial boundary conditions), which could provide valuable data for improving our understanding of how circulation has changed through time.

4.4 Summary

We have added three new tracers (water age, abiotic ^{14}C, and biotic ^{14}C) to the ocean component of the FAMOUS GCM to study ocean circulation and the marine carbon cycle. The model accurately simulates large-scale Δ^{14}C distributions both spatially (in the surface ocean and at depth) and temporally (in the pre-bomb era and the post-bomb era), and is able to capture the timing, shape, and amplitude of the marine bomb pulse at various locations across the North Atlantic Ocean. This therefore suggests that, on the whole, the uptake and transport of ^{14}C are well represented in FAMOUS. Differences between the simulated and observed values arise due to model biases, including weak surface winds, over-deep NADW, insufficient Atlantic-sector AABW formation, and an absence of deep convection in the Labrador Sea. This therefore demonstrates that the new Δ^{14}C tracer is accurately capturing the physical behaviour of the model and will be a useful tuning metric for recalibrating FAMOUS in the future, for example, to improve the representation of the Atlantic Meridional Overturning Circulation.

Radiocarbon ages in geological archives are typically interpreted in terms of ventilation. To assess the validity of this interpretation, we first examined the importance of the biological pump to deep ocean ^{14}C concentrations by comparing the simulated biotic and abiotic δ^{14}C values. The biotic δ^{14}C values are higher than the abiotic values at all depths because the biotic tracer accounts for the preferential uptake of ^{12}C during primary productivity (whereas the abiotic tracer is not affected by biological fractionation) and remineralisation in the deep ocean occurs without further fractionation. In the surface ocean, the difference between the two tracers reflects the large-scale patterns of primary productivity, but the difference is near constant at depth (both vertically and regionally). We therefore propose that this could be accounted for with a global correction of approximately 20 ‰. Secondly, we compared the simulated ^{14}C ages with the idealised water ages. We conclude that, in our model, the water ages are not well represented by the ^{14}C ages at global- or basin-scale, but ^{14}C is a good tracer for water age in well-mixed regions, where the physical component of the solubility pump is a more dominant control of DIC distributions than the chemical component. Due consideration of the balance between physical and biogeochemical processes should therefore be exercised when interpreting Δ^{14}C in proxy records to avoid drawing erroneous conclusions about palaeocean circulation.

CHAPTER 5

Discussion and conclusion

5.1 Summary

The aim of this thesis was to use carbon isotopes to investigate ocean circulation and the marine carbon cycle in a full complexity General Circulation Model (GCM). In Chapter 1, this was broken down into three main research questions:

- How important are small salinity drifts and biases in sea surface climate in multi-millennial climate simulations?
- How accurately can modern carbon isotopes distributions be simulated in a low resolution coupled atmosphere-ocean GCM?
- To what extent can ^{14}C be used as a ventilation tracer?

The work in Chapters 2, 3 and 4 addressed these research questions using the FAMOUS GCM, a configuration of the UK Met Office Unified Model version 4.5 (UM4.5). Specifically, Chapter 2 investigated the importance of small salinity drifts in multi-millennial climate simulations, which are required to fully spin-up deep ocean circulation and the marine carbon cycle. Chapters 3 and 4 examined the accuracy with which FAMOUS simulates modern ^{13}C and ^{14}C distributions, respectively. Chapter 4 also assessed the importance of biological activity for deep water ^{14}C concentrations, and thus the extent to which ^{14}C can be used as a ventilation tracer.

In this chapter, I summarise how the previous chapters link together, discuss how they answer the original research questions and address the overall aim of the thesis, explore the wider implications of the results, outline the limitations of the work, and suggest possible directions for future studies. As each of the three results chapters had self-contained discussions, only the key points pertaining to each of the aforementioned research questions will be discussed further here.

5.2 Answering the research questions

5.2.1 How important are small salinity drifts and biases in sea surface climate in multi-millennial simulations?

Multi-millennial (10,000 year) simulations are a pre-requisite for any oceanic carbon isotope implementation because both the deep ocean circulation and the marine carbon cycle must be fully spun-up for the isotope signals to be interpreted with confidence. Previous studies have speculated that slowly evolving (centennial-to-millennial timescale) drifts that originate from imbalances in the surface climate can cause large shifts in the ocean circulation regime, even under constant pre-industrial boundary conditions (Bryan, 1998; Covey et al., 2006), but no modelling group had run a long enough simulation to observe these changes.

At the outset of the study, it was intended that carbon isotopes would be implemented into FAMOUS-MOSES2.2 (FM2), the most recent generation of the model, which provides increased and more dynamic Earth System capabilities relative to FAMOUS-MOSES1 (FM1). Specifically, FM2 includes a terrestrial carbon cycle and interactive vegetation (Williams et al., 2013; Valdes et al., 2017), and both the terrestrial and marine carbon cycles have been tuned (Williams et al., 2013). However, initial testing with the standard version of FM2 demonstrated that the global volume-weighted mean salinity drift in a 10,000 year pre-industrial simulation is $0.25\,\mathrm{psu\,kyr^{-1}}$, which ultimately leads to a collapsed Atlantic Meridional Overturning Circulation (AMOC) and invigorated Pacific Meridional Overturning Circulation (PMOC). Notably, this drift is significantly larger than the global volume-weighted salinity drifts reported by Covey et al. (2006) for HadCM3 ($\approx 6.25 \times 10^{-3}\,\mathrm{psu\,kyr^{-1}}$) and CCSM2 ($\approx 1 \times 10^{-3}\,\mathrm{psu\,kyr^{-1}}$). It is also around 50 % larger than the volume-averaged salinity drift in the North Atlantic Ocean in HadCM3 ($\approx 0.16\,\mathrm{psu\,kyr^{-1}}$; Pardaens et al., 2003). However, it is approximately 85 % smaller than the shallow ocean (≈ 260 m below sea level) drift and around a third smaller than the deep ocean (≈ 3500 m below sea level) drift in CSM1 ($\approx 1.6\,\mathrm{psu\,kyr^{-1}}$ and $\approx 0.4\,\mathrm{psu\,kyr^{-1}}$, respectively; Bryan, 1998). Most modelling studies do not publish details of their salinity drifts, but (whilst larger than the drift in some models) the drift in FAMOUS is not the most extreme to have been reported. Thus, CSM1 and other models with salinity drifts that are of a similar magnitude to or larger than the drift in FM2 could also be susceptible to AMOC collapses if they were run for long enough to allow their deep oceans to reach equilibrium (i.e. multiple millennia).

Two different methods for neutralising the unforced salinity drift in FM2 were tested: surface flux correction (SFLUX) and volumetric flux correction (VFLUX). Both methods successfully maintained a steady global mean salinity, but neither scheme prevented the redistribution of salt from the Atlantic Ocean into the Pacific Ocean. The resultant positive feedback loop in the Meridional Overturning Circulation (MOC) and the surface climate caused the AMOC to collapse to a maximum strength of 4 to 5 Sv (compared to an initial strength of 14 to 15 Sv, which is broadly consistent with observations; Talley et al., 2003). In brief, freshening in the Nordic Seas increased the buoyancy of the surface waters, which reduced the overturning rates. The subsequent reduction in poleward salt and heat transport decreased the regional sea surface temperature (SST) and salinity (SSS). The cooler sea surface was less evaporative, which further enhanced the salinity imbalances. In the Bering Sea, the opposite biases and feedbacks invigorated a deep PMOC with a maximum strength of 14.5 to 15.5 Sv (compared to shallow overturning with a maximum strength of 6 Sv at the start of the simulation). Thus, in answer to the original research question, small salinity drifts and biases in the surface climate are very important in multi-millennial climate simulations because they can cause significant changes in the circulation regime, even under constant pre-industrial boundary conditions and when the global hydrological budget has been forcibly closed.

FM1 has previously been run for 12,000 years without encountering the aforementioned MOC problems (Smith et al., 2008a). It was therefore pertinent to examine the hydrological differences between the two generations of the model to establish why the AMOC in FM1 is more stable than in FM2. The global volume-weighted mean salinity drift in a 10,000 year pre-industrial simulation with the standard version of FM1 is 0.02 psu kyr^{-1}, an order of magnitude smaller than in the drift in FM2. Consequently, after 10,000 years, the maximum AMOC strength in FM1 was 20 Sv (compared to an initial strength of 16.5 Sv) and the shallow Pacific overturning cell had a maximum strength of 4.5 Sv (i.e. negligible PMOC). In terms of the surface climate, FM2 was initially warmer and fresher than FM1 in the Nordic Seas. These biases reduced the density of the surface waters in FM2 relative to FM1 and inhibited deep convection. In the Bering Sea, FM2 was initially warmer and more saline than FM1 (as a result of higher evaporation rates and lower precipitation rates). In the model, the effect of the elevated SSSs (increasing density) outweighed the effect of the elevated SSTs (reducing density), therefore the surface waters in FM2 were less buoyant than in FM1, which ultimately resulted in deep convection. Thus, following the example in Chapters 3 and 4 of this thesis, future studies that require long integrations should use the FM1 generation of the model until the large-scale ocean circulation in FM2 has been retuned.

5.2.2 How accurately can modern carbon isotope distributions be simulated in a low resolution coupled atmosphere-ocean GCM?

Previous carbon isotope implementation studies have attributed their model-data discrepancies to inaccuracies in the representation of physical and/or biogeochemical processes. This research question was therefore addressed in two parts: firstly, how well do the new tracers represent the processes to which carbon isotope distributions are known to be sensitive (large-scale ocean circulation, air-sea gas exchange, and biological activity);

secondly, how well do the simulated carbon isotope distributions match observations, both spatially and temporally?

The on-off sensitivity experiments in Chapter 3 demonstrated the success of the new ^{13}C scheme in representing the physical and biogeochemical processes in FAMOUS. For example, when only kinetic fractionation effects were included (*ki-fract-only*), the lowest surface ocean $\delta^{13}C_{DIC}$ values (-6.55 ‰) were simulated in areas of net CO_2 invasion (the extra-tropics and the high latitudes) and the highest surface ocean $\delta^{13}C_{DIC}$ values (-6.45 ‰) were simulated in areas of net outgassing (the equatorial upwelling zones and the deep water formation regions). When both equilibrium and kinetic fractionation effects were included (*no-bio-fract*), the large-scale $\delta^{13}C_{DIC}$ distributions were closely related to the SST patterns because of the temperature dependence of $\alpha_{aq\leftarrow g}$ and $\alpha_{DIC\leftarrow g}$. Relatively high surface ocean $\delta^{13}C_{DIC}$ values (>2.5 ‰) were simulated in the eastern equatorial Pacific, where there are high rates of net CO_2 outgassing and cold Antarctic Bottom Water (AABW) is upwelled, and relatively low $\delta^{13}C_{DIC}$ values (<1.8 ‰) were simulated in the Indian surface ocean, which is warmer than the other major ocean basins. When only biological effects were included (*no-asgx-fract*), relatively low surface ocean $\delta^{13}C_{DIC}$ values (<-6.5 ‰) were simulated in the eastern equatorial Pacific, the Southern Ocean, and the northeast North Atlantic Ocean, where ^{12}C-enriched waters from the abyssal ocean are brought to the surface via upwelling and deep convective mixing. The highest $\delta^{13}C_{DIC}$ values (>-5 ‰) were simulated in the eastern equatorial Atlantic surface ocean, where primary productivity is high and the upwelling waters are relatively young (therefore not as enriched in ^{12}C as at comparable latitudes in the Pacific basin).

Consequently, the model accurately captured the large-scale structure of sea surface ^{13}C observations, simulating lower $\delta^{13}C_{DIC}$ values in the nutrient-poor Indian Ocean than in the more productive Atlantic and Pacific Oceans, relatively high $\delta^{13}C_{POC}$ in the low latitudes (-20 ‰), and relatively low $\delta^{13}C_{POC}$ in the high latitudes (-27 ‰). The simulated $\delta^{13}C_{DIC}$ range (3.2 ‰) was also in excellent agreement with the observed range (3.3 ‰). However, the absolute $\delta^{13}C_{DIC}$ values were approximately 1 ‰ too high at all depths, largely due to biases in the biological pump (Chapter 3, Section 3.3.2).

In the process of validating the recent ^{13}C implementation in CSIRO Mk3L, Buchanan et al. (2019) presented a multi-model comparison of the skill of the UVic ESM, LOVECLIM, PISCES, and the low resolution configuration of CESM in reproducing large-scale pre-industrial $\delta^{13}C_{DIC}$ distributions. All of the models had strengths and weaknesses, as demonstrated by their respective linear regression r^2 values and root mean square errors (RMSEs). For example, LOVECLIM captured the mean $\delta^{13}C_{DIC}$ values, both globally and regionally, but the spatial distributions were biased similarly to those in FAMOUS (with an accumulation of ^{12}C-enriched material at shallow-to-intermediate depths in the equatorial Atlantic and Pacific Oceans). In contrast, UVic accurately reproduced the observed spatial structures, but consistently overestimated the $\delta^{13}C_{DIC}$ values by 0.2 ‰.

CSIRO Mk3L had a positive bias in the upper 200 to 500 m of the ocean, and had RMSEs between 0.43 ‰ in the Southern Ocean and 0.99 ‰ in the Indian Ocean, whilst CESM and PISCES were the best performing models, with relatively high global and regional r^2 values and relatively low RMSEs. In general, the Earth System Models of Intermediate Complexity (EMICs; UVic and LOVECLIM) perform better than FAMOUS because they have fewer degrees of predictive freedom, whilst the strong performance of PISCES and CESM can be attributed to their more skilful representation of ocean dynamics (as a result of finer vertical resolution and more complex horizontal grid structures; Table 1.2). However, as outlined in Chapter 1 (Sections 1.1.3 and 1.2.1), the advantage low resolution GCMs, such as FAMOUS and CSIRO Mk3L, is that they are computationally efficient enough to fully spin-up the deep ocean circulation and the marine carbon cycle (without the need for offline or accelerated spin-up techniques), whilst still maintaining sufficient detail in the representation of Earth System processes to study abrupt (decadal-to-centennial) changes in the climate system. In terms of scientific application, they therefore provide a middle ground to the speed of the EMICs and the complexity of the higher resolution GCMs. At present, the overall performance of FAMOUS is not as good as in CSIRO Mk3L (as demonstrated by the global RMSEs of 0.91 ‰ and 0.44 ‰ compared to modern and pre-industrial observations, respectively). However, because the new isotope scheme in FAMOUS is accurately representing the physical and biogeochemical processes (capturing the over-deep North Atlantic Deep Water, and the local inaccuracies in the export ratio and remineralisation rate), the overall performance of the model could be improved by a straightforward retuning exercise, following the approach of Gregoire et al. (2011) and Williams et al. (2013). This will be discussed further in Section 5.4.1.

FAMOUS also accurately captured the spatial and temporal $\Delta^{14}C$ distributions (Chapter 4), demonstrating that, to the first order, the processes that control the uptake and transport of ^{14}C (air-sea gas exchange, biological activity, and ocean circulation) are well represented in FAMOUS. In both the pre- and post-bomb snapshots, the highest $\Delta^{14}C$ values were simulated in the sub-tropical surface ocean, where long surface water residence times allow for greater equilibration with the atmosphere. Intermediate values were simulated in the equatorial surface ocean, where old (^{14}C-depleted) waters are upwelled from the abyssal ocean and relatively weak winds reduce the input of ^{14}C from the atmosphere. Relatively low $\Delta^{14}C$ values were simulated in the high latitude surface ocean, where sea ice inhibits air-sea gas exchange, surface residence times are short, and old (^{14}C-depleted) waters are mixed upwards from the abyssal ocean at sites of deep water formation. At depth, the highest $\Delta^{14}C$ values were simulated in the Atlantic Ocean, with intermediate values in the Indian Ocean, and low values in the Pacific Ocean, in agreement with observations and the notion of a global ocean conveyor (Figure 1.1). Comparing the simulated post-bomb values to the ungridded Global Data Analysis Project (GLODAP) data set (Key et al., 2004), the global linear regression r^2 value was

0.75 and the root mean square error (RMSE) was 55 ‰. Offsets in the absolute values were related to physical model biases such as insufficient sea ice in the Southern Ocean, weaker than observed surface winds, an over-deep North Atlantic Deep Water (NADW) cell, and weak convection in the sub-polar North Pacific Ocean. In this sense, the discrepancies between the simulated and observed Δ^{14}C distributions further demonstrate the success of the isotope scheme in capturing the physical model behaviour. Overall, FAMOUS performs well compared to other ^{14}C-enabled models (Table 1.2) and provides a better representation of Δ^{14}C at depth than CESM and LOVECLIM, which have biases as large as −100 ‰ in the deep North Pacific Ocean as a result of sluggish large-scale ocean circulation and insufficient mixing, respectively (Bouttes et al., 2015; Jahn et al., 2015).

To better understand the penetration of the bomb signal into the ocean, transient surface and shallow-to-intermediate water Δ^{14}C values from the model were compared with coral and bivalve records from 12 sites across the North Atlantic (Chapter 4, Section 4.3.3). Collectively, these archives recorded pre-bomb Δ^{14}C, the timing and magnitude of peak Δ^{14}C values, and the subsequent rate of decline. FAMOUS accurately captured the local expression of the bomb signal in the near-surface ocean, with high amplitude-early peaks in shallow coastal locations and low amplitude-later peaks in the NADW formation region. This suggested that large-scale processes (such as air-sea gas exchange and vertical mixing) are more important for controlling the uptake and transport of carbon by the oceans than local processes (such as riverine input and exchange between coastal basins and the open ocean), which are not as accurately represented in the model. At all sites, the simulated bomb signal was detected in the surface ocean 1 to 2 years after the original perturbation; peak values were attained between the late 1960s and mid 1980s; and the rate of decline was slower than the rate of increase. In the intermediate ocean, the signal was damped and lagged relative to the near-surface waters. Collectively, these responses demonstrated that air-sea gas exchange is a more efficient transport mechanism than vertical mixing. The coral records from intermediate water depths were lower resolution than the shallow ocean records. However, because the model was accurately capturing the correct rate and timing of change, it could be used to interpolate between the gaps in the observations (if due consideration was given to the current offset between the absolute values). Overall, this unique comparison corroborated suggestions from observational studies about the processes controlling the transfer of carbon from shallow to intermediate water depths in different hydrographic settings and further demonstrated the skill of the model in representing the carbon uptake.

Thus, in answer to the original research question, the new isotope scheme accurately reflects the physical and biogeochemical processes in this low resolution coupled atmosphere-ocean GCM. The differences between the simulated and observed values can largely be explained by model biases, therefore simultaneously recalibrating the ecosystem model (HadOCC) and the large-scale ocean circulation in FAMOUS could improve the model-data agreement for δ^{13}C and Δ^{14}C, as well as for existing oceanic tracers such as DIC, alkalinity, and nutrients.

5.2.3 To what extent can ^{14}C be interpreted as a ventilation tracer?

Radiocarbon ages are commonly used as a proxy for the length of time since a water parcel was last in contact with the atmosphere (Stuiver et al., 1983; Broecker et al., 1990), however, atmospheric production rates (Damon et al., 1978), air-sea equilibration times (Campin et al., 1999), and the transport of ^{14}C from the surface ocean to depth via the sinking of particular organic matter (Jain et al., 1997) can all complicate the signal. Campin et al. (1999) identified problems with using ^{14}C as a ventilation tracer because of incomplete air-sea gas exchange, but to-date, no study had assessed the extent to which the biological pump interferes with this interpretation. This research question was therefore addressed in two parts: firstly, the new biotic ^{14}C scheme was compared to the existing abiotic ^{14}C scheme (as uncorrected δ^{14}C (Eq. (4.9)) as opposed to Δ^{14}C (Eq. (4.8)) to examine the importance of the biological pump for surface and deep water ^{14}C concentrations; secondly, the biotic ^{14}C ages (Eq. (4.10)) were compared to the absolute water ages across a range of locations and water depths.

The biotic δ^{14}C values were higher than the corresponding abiotic values at all depths because the biotic tracer accounts for the preferential uptake of ^{12}C during primary productivity in the photic zone, whereas the abiotic tracer does not. Specifically, biological activity had a spatially variable influence in the surface ocean, with the distribution of δ^{14}C anomalies (biotic minus abiotic) broadly reflecting the pattern of primary productivity. The largest δ^{14}C anomalies ($\approx$30 ‰) were in the eastern equatorial Pacific upwelling zone, where the simulated surface primary productivity was 0.58 gC m^{-2} d^{-1} (compared to an observed value of 0.62 gC m^{-2} d^{-1}), and the smallest δ^{14}C anomalies ($\approx$18 ‰) were in the Southern Hemisphere Pacific sub-tropical gyre, where the simulated surface primary productivity was 0.16 gC m^{-2} d^{-1} (compared to 0.22 gC m^{-2} d^{-1} in the observations). From an analytical perspective, the difference between the two tracers at depth (below approximately 1000 m) was near-constant both vertically and regionally, and could therefore be accounted for with a correction of $\approx$20 ‰. The spatial distribution and overall levels of primary productivity may have been different in the geological past (e.g. Shemesh et al., 1993; Kumar et al., 1995; Anderson et al., 1998), therefore sensitivity experiments (either under different boundary conditions or under pre-industrial boundary conditions but with different nutrient distributions) would be required to verify the temporal validity of this conclusion. Furthermore, to assess the model dependency of this result, the same analysis would need to be conducted in other ^{14}C-enabled models. At present, this would be limited to CESM, which is the only other model that has both a biotic and an abiotic ^{14}C tracer (Table 1.2).

Despite the biological pump having a near constant influence on deep ocean ^{14}C concentrations in FAMOUS, the simulated ^{14}C ages were decoupled from the idealised water ages. In the surface ocean, this decoupling was largely due to incomplete air-sea gas exchange. The surface reservoir effect ranged between 450 years in the sub-tropical gyres (where relatively long surface water residence times allow the surface ocean to come closer to isotopic equilibrium with the atmosphere) and 1300 years in the Southern Ocean (where sea ice and relatively short surface residence times interfere with air-sea equilibration). Considering the water column as a whole, the depth profiles of ^{14}C age and water age were only in agreement in well mixed regions (with an offset due to the aforementioned surface reservoir effect), where the physical component of the solubility pump is the dominant control on DIC concentrations. The relationship between ^{14}C age and water age broke down elsewhere because the ^{14}C concentrations were primarily controlled by the chemical component of the solubility pump. This therefore suggests that it is appropriate to interpret deep sea Δ^{14}C records from the Tasman Sea (e.g. Goldstein et al., 2001) and the Drake Passage (e.g. Goldstein et al., 2001; Robinson and van de Flierdt, 2009) in terms of ventilation, as long as due consideration is given to the surface reservoir effect and how it might have changed in the past (e.g. due to changes in sea ice). In other regions, such as the North Atlantic sub-tropical gyre (e.g. Adkins et al., 1998; Eltgroth et al., 2006), simple age interpretations could be misleading because the deep sea Δ^{14}C signal reflects both ventilation and the carbon cycle.

Thus, in answer to the original research question, ^{14}C is only a good tracer for water age in well mixed regions, where the physical component of the solubility pump is the dominant control on DIC concentrations. Elsewhere, Δ^{14}C concentrations reflect the local balance between physical and biogeochemical processes, therefore interpreting ^{14}C ages solely in terms of ventilation could lead to erroneous conclusions about palaeocean circulation.

5.3 Scientific advances and wider implications

By answering the three research questions outlined in Table 1.4 (and re-outlined in Section 5.1), this thesis has addressed the gaps in our technical and scientific knowledge of carbon isotopes and their inclusion in numerical climate models that were identified in Chapter 1 (Section 1.1.4).

1. Before now, no modelling group had explored whether small drifts affect the stability of the climate system in multi-millennial (e.g. 10,000 year) simulations, which are required to fully spin-up deep ocean circulation and the marine carbon cycle.

The work in Chapter 2 confirmed the conjecture from earlier studies (Bryan, 1998; Covey et al., 2006): small salinity drifts arising from regional biases in the surface climate can lead to a different ocean circulation regime (such as a collapsed AMOC and invigorated PMOC), even under constant pre-industrial boundary conditions. In modelling studies with pre-industrial setups, these MOCs have only previously been replicated by "hosing experiments" – simulations in which freshwater is systematically added to the ocean (e.g. Smith and Gregory, 2009; Jackson et al., 2016b). It was not possible to identify a specific precursor to the sudden shift in the circulation, but imbalances in the surface hydrology in key regions such as the northwest North Pacific Ocean (50 to 60° N; 165 to 195° E) and northeast North Atlantic Ocean (50 to 70° N; 0 to 30° W) should be closely monitored.

Additional scientific advances arising from Chapter 2 relate to the stability and structure of the AMOC in numerical climate models. Specifically, the centennial-to-millennial period of metastability that was simulated with FM2 highlights the risk of carrying out too short model integrations and demonstrates the requirement for a minimum run time of 5000 years to reach near steady state. Potential issues with periods of metastability have previously been discussed in the context of shorter (<5000 year) simulations (e.g. Brandefelt and Otto-Bliesner, 2009; Zhang et al., 2013; Marzocchi and Jansen, 2017). For example, Brandefelt and Otto-Bliesner (2009) conducted an ≈1800 year simulation under glacial boundary conditions with CCSM3. The global mean annual surface air temperature reached a period of metastability (lasting 150 years) only 100 years into the integration before the climate continued to cool. A new equilibrium, which differed substantially from the original quasi steady state (with a 1.1 °C cooler global mean surface air temperature and a 30 % reduction in AMOC strength) was reached 800 years after the start of the simulation. Similarly, Marzocchi and Jansen (2017) demonstrated the inadequacy of diagnosing deep ocean equilibrium from short (e.g. 100 year) timeslices. In their 2100 year glacial simulation with CCSM4, the AMOC appeared to be stable between model years 1500 and 1600. However, examining the last 900 years of the simulation as a whole showed that the temperature and salinity of the deep ocean were drifting, leading to a doubling in stratification and a reduction in the strength and depth of the AMOC (by >10 Sv and ≈400 m, respectively). This trend was masked by internal variability over shorter timescales, but was showing no signs of abating at the end of the simulation. This thesis is the first study in which periods of metastability lasting >1000 years have been reported. Similar behaviour in other models, in combination with insufficient run times, could therefore lead to inaccurate conclusions about the strength and structure of the AMOC in inter-model and model-data comparisons. Furthermore, although the maximum strength of the AMOC in FM1 is in good agreement with observations, the overall structure (over-deep NADW and an absence of AABW) demonstrates why single number metrics should not be used as comprehensive measures of the MOC. Instead, a trifold assessment of the strength of maximum overturning, and the latitude and depth at which this occurs, would be more appropriate.

FAMOUS has previously been tuned both systematically (Jones et al., 2005; Gregoire et al., 2011; Williams et al., 2013) and manually (Smith et al., 2008a), however, by simulating a reversal in the MOCs a couple of millennia into a 10,000 year pre-industrial spin-up simulation, this study has highlighted a significant flaw with the current approach of selecting an optimal parameter set based on centennial-length simulations. Williams et al. (2013) used an objective hypercube tuning technique to optimise both the terrestrial and marine carbon cycles in FAMOUS and, outwardly, the resultant surface climate was an improvement relative to previous published versions of the model. However, considering that FAMOUS is intended for multi-millennial simulations, as assessment of the strength and/or structure of the AMOC (such as the aforementioned trifold metric) was an important omission from the cost function. This, in combination with the fact that the 100 member ensemble was only spun-up for 200 years, meant that the resultant MOC tendencies were not identified sooner. Whilst it may not be currently feasible to conduct hundreds of multi-millennial perturbed parameter simulations with a model of this complexity and resolution, this study has highlighted the need to extend the run-length of a subset of high performing simulations from an initial ensemble of centennial integrations. It has also underlined that the choice of inputs into the cost function can alter the optimal solution and be central to their failings.

2. Carbon isotopes had yet to be implemented into a numerical climate model that was computationally efficient enough to fully spin-up the deep ocean circulation and marine carbon cycle in a timely manner (without the need for offline or accelerated spin-up techniques), whilst still maintaining sufficient detail in the representation of the feedbacks between Earth System processes to study changes on decadal-to-centennial timescales.

This study has presented and validated the first implementation of ^{13}C and biotic ^{14}C in the FAMOUS GCM, a fully coupled atmosphere-ocean GCM that simulates approximately 400 years per day (when run with a full suite of oceanic tracers), and therefore completes a 10,000 year spin-up simulation in approximately one month. This implementation bridges the gap between previous carbon isotope implementations in faster, but less complex models (such as the UVic ESM and LOVECLIM) and those in more complex, but slower models (such as PISCES and CESM). Overall, there are two main benefits to this implementation: firstly, it has increased the Earth System capabilities of FAMOUS itself; secondly, it has provided another tool for examining the inter-model differences in simulated carbon isotope distributions, which can help us to better understand the underlying processes.

Notably, this study has presented the most comprehensive validation of ^{14}C in a numerical climate model to-date. Previous ^{14}C implementations have typically been evaluated by comparing the spatial Δ^{14}C distributions in either a pre-industrial (i.e. natural) or historical (i.e. bomb) simulation to cruise data (Table 5.1). Before now, only Toggweiler et al. (1989a,b) and Guilderson et al. (2000) had examined both natural and bomb Δ^{14}C distributions in a single model. Furthermore, only Guilderson et al. (2000)

Table 5.1: Examples of the analysis and data sets used to validate the ^{14}C scheme in other numerical climate models.

Reference	**Model**	**Simulation**	**Data set(s)**	**Analysis**
Toggweiler et al. (1989a)	GFDL	PI*	Surface corals GEOSECS*	Surface maps (global) Depth profiles (globally averaged) Cross-sections (longitude versus depth)
Toggweiler et al. (1989b)	GFDL	Bomb	GEOSECS TTO$^+$ INDIGO$^\mp$	Surface maps (global) Zonal means (surface ocean) Cross-sections (latitude versus depth) Bomb inventory
Guilderson et al. (2000)	GFDL MOM	Bomb	Biological archives WOCE†	Surface maps (global pre-bomb) Time evolution at three sites in the Pacific Ocean (surface only) Cross sections (latitude versus depth)
Meissner et al. (2003)	UVic ESM	Bomb	GEOSECS	Zonal means (Atlantic Ocean)
Butzin et al. (2005)	Hamburg LSG OGCM	PI	GLODAP$^{\ddagger 1}$	Zonal means (Atlantic and Pacific Oceans)
Crucifix (2005)	MoBidiC	Bomb	GEOSECS	Zonal means (Atlantic and Pacific Oceans)
Galbraith et al. (2011)	GFDL CM2Mc	PI	GLODAP^1	Surface maps (global) Zonal means (Atlantic and Pacific Oceans)
Bouttes et al. (2015)	iLOVECLIM	PI	GLODAP	Zonal means (Atlantic and Pacific Oceans)
Jahn et al. (2015)	CESM	Bomb	GLODAP	Surface maps (global) Zonal means (Atlantic, Pacific and Indian Oceans) Depth profiles (globally averaged plus Atlantic, Pacific and Indian Oceans) Bomb inventory

* Pre-industrial, * Geochemical Ocean Sections Study (1970s), $^+$ Transient Tracers in the Ocean (early 1980s), $^\mp$ Indian Gaz Ocean (mid 1970s), † World Ocean Circulation Experiment (1990s), ‡ Global Data Analysis Project (1990s), ^{1} Natural Δ^{14}C only had investigated the time evolution of simulated Δ^{14}C to ascertain whether their model captured the timing, magnitude, and shape of the ^{14}C peak in different locations. Even then, the analysis was limited to three sites in the Pacific surface ocean. This study has therefore expanded the scope of previous work by examining how accurately FAMOUS reproduces regional Δ^{14}C depth profiles. Furthermore, the comparison between the transient simulated and observed values at 12 sites across the North Atlantic is novel because it is the first time that the time evolution of simulated Δ^{14}C has been studied (1) outside of the surface ocean and (2) at multiple depths in a single location. Overall, these additional assessments give greater confidence to the success of both the model and the new isotope scheme.

3. To-date, no modelling group had used an independent age tracer to assess the importance of the biological pump for deep water ^{14}C concentrations, and thus the extent to which ^{14}C ages reflect the ventilation timescale of the oceans.

This study has presented the first model assessment of how biological activity affects the spatial distribution of ^{14}C, both in the surface ocean and at depth. The comparison between the biotic and abiotic ^{14}C tracers demonstrated that particulate export increases δ^{14}C in the deep ocean by approximately 20 ‰, regardless of primary productivity in the surface ocean. This effect could therefore be corrected for when interpreting ^{14}C ages in terms of the length of time since a water parcel was last in contact with the atmosphere. However, the subsequent comparison between the simulated ^{14}C ages and the idealised water ages demonstrated that ^{14}C distributions are sensitive to physical and biogeochemical processes, and that the local balance between these processes ultimately determines the extent to which ^{14}C can be interpreted in terms of ventilation. Specifically, only proxy data from well mixed regions are a faithful representation of water age; even then, the ^{14}C age must be interpreted relative to the local surface reservoir age.

Going forwards the isotope-enabled version of FAMOUS will be useful for identifying potential locations where it would be appropriate to interpret palaeo Δ^{14}C records in terms of ventilation. In particular, the model can be used to generate plausible suggestions of the location of convective regions in the past and provide an indication of what the surface reservoir effect was in those regions. The isotope-enabled model is also a useful tool for revisiting the interpretation of existing Δ^{14}C data sets from non-convective regions and providing a better understanding of how the local balance between physical and biogeochemical processes is expressed in these records. For example, Eltgroth et al. (2006) inferred rapid reorganisations of water masses in the intermediate/deep ocean during the Younger Dryas from North Atlantic deep sea coral Δ^{14}C records (taken from between 1000 and 2400 m below sea level). However, the corals analysed by Eltgroth et al. (2006) all lie close to or within the Northern Hemisphere Atlantic sub-tropical gyre, where the simulated ^{14}C ages were decoupled from the idealised water ages below approximately 600 m depth. It would therefore be pertinent to simulate this time period with the isotope-enabled version of FAMOUS and, if the model is able to reproduce the observed Δ^{14}C signal, explore the underlying mechanisms in more detail. This would either allow the original interpretation to be verified or a plausible alternative to be suggested.

5.4 Limitations and future work

5.4.1 Biases and retuning

A recurring theme throughout this thesis has been that of biases (both physical and biogeochemical), which influenced the generation of FAMOUS that the carbon isotopes were implemented into and the isotope distributions themselves. As discussed in Section 5.2.1, at the outset of the study, it was intended that carbon isotopes would be implemented into FM2, the most recent generation of the model, which includes a terrestrial carbon cycle and interactive vegetation (Williams et al., 2013; Valdes et al., 2017). However, imbalances in the surface climate in this generation of the model ultimately lead to an unrealistic MOC configuration that is not conducive for studying pre-industrial ocean tracers. FM1 is not susceptible to the same problems, therefore the new code was tested with the earlier generation of the model.

FM1 itself has known physical biases, such as an over-deep AMOC and insufficient AABW formation (Smith, 2012), that clearly influence the distributions of both new (δ^{13}C and Δ^{14}C) and existing (nutrient and DIC) tracers. For example, the most ^{12}C- and nutrient-enriched waters in the global ocean are simulated at intermediate depths in the eastern equatorial Pacific instead of at high northern latitudes (as observed) because the model has weak ($<$1 Sv) convection to approximately 3 km depth in the sub-polar North Pacific. Furthermore, the ocean carbon cycle has been tuned in FM2 (Williams et al., 2013), but not yet in FM1. Biases in the biological pump therefore cause the simulated globally averaged DIC and alkalinity values to be higher than observed at all depths. The simulated δ^{13}C values are also higher than observed at most depths.

The new isotope schemes are able to capture the physical and biogeochemical behaviour of the model well (Section 5.2.2), and in this sense, they offer excellent utility as diagnostic targets in future retuning efforts, which are recommended before further scientific application (Section 5.4.4). As outlined in Chapter 2 (Section 2.5), tuning is a calibration process that attempts to find the optimal values of uncertain model parameters and minimise the discrepancy between observations and model output (Gregoire et al., 2011). Previous efforts to tune the physical components of FAMOUS have focussed on the parameters that have a high impact on the surface climate in HadCM3 (Table 5.2). These remain appropriate parameters to co-vary in the recalibration of FAMOUS because they affect the balance of precipitation minus evaporation (P-E) in the model. They are therefore important for SSS distributions, and ultimately, the representation of

Table 5.2: Physical and biogeochemical parameters of interest for the systematic retuning of the large-scale ocean circulation and the marine carbon cycle in FAMOUS (from Gregoire et al. (2011) and Williams et al. (2013), respectively).

Physical parameters	Biogeochemical parameters
Atmosphere	**C:N ratios**
Threshold of relative humidity for cloud formation (RHCRIT)	Phytoplankton (c2n_p) Zooplankton (c2n_z)
Conversion rate of cloud liquid water droplets to precipitation (CT)	Detritus (c2n_d)
Threshold of cloud liquid water for the formation of precipitation over land (CW_LAND) and sea (CW_SEA)	**Phytoplankton-specific** Initial slope of photosynthesis (alpha) Maximum rate of photosynthesis (psmax)
Roughness length for free convective heat and moisture transport over the sea (Z0FSEA)	Increase in phytoplankton growth rate for a 10 °C temperature increase (Q10H) Half-saturation constant for phytoplankton mortality (mort_sat)
Surface drag coefficient for neutral conditions (CDN)	Maximum phytoplankton mortality expressed as the fraction of biomass lost per day (pmort_max)
Bulk transfer coefficient for heat/moisture under neutral conditions (CHN)	Rate of phytoplankton respiration expressed as the fraction of biomass lost per day (resp_rate)
Ocean	
Vertical diffusivity at the surface (KAPPA0_SI)	
Coefficients for isopycnal diffusivity (AHI1_SI , AHI2_SI)	**Zooplankton-specific** Maximum specific rate of zooplankton grazing (graze_max)
Sea ice	Half-saturation constant for zooplankton grazing (graze_sat)
Albedo of sea ice (or snow on sea ice) at melting point (ALPHAM)	Threshold for zooplankton grazing (graze_threshold)
	Assimilation efficiency for zooplankton feeding on phytoplankton (beta_p)
	Assimilation efficiency for zooplankton feeding on detritus (beta_d)
	Linear zooplankton mortality (z_mort_1)
	Quadratic zooplankton mortality (z_mort_2)
	Detritus-specific
	Shallow remineralisation rate (remin_rate_shallow)
	Deep remineralisation rates (remin_date_deep)
	Sinking rate for detritus (sink_rate_dt)
	Calcium carbonate
	Carbon (calcite) export as a proportion of primary production (rain_ratio)

the MOC. The biogeochemical tuning of Williams et al. (2013) focussed on the twenty structural parameters in HadOCC, which were sub-divided into five categories (Table 5.2). Equally, these remain the most appropriate parameters to use in the future because they directly affect the sensitivity of the biological pump.

As outlined in Section 5.3, the current (centennial) run length of perturbed parameter simulations mean that small errors in the optimised solutions might not be identified during the calibration process. When the model is retuned, a subset of high performing simulations from an initial ensemble of centennial integrations should therefore be continued for multiple millennia (e.g. 5000 years) to ensure that the final parameter set provides a realistic and stable climate in the long simulations for which FAMOUS is intended. Both Gregoire et al. (2011) and Williams et al. (2013) evaluated the performance of their optimised parameter sets by comparing the resultant surface air temperature and precipitation patterns to observations. Whilst these remain important diagnostics against which the physical model performance should be assessed, this study has highlighted the need for more specific targets in the future (Table 5.3). In particular, greater precedence should be given to the surface climate in the deep water formation regions, where small imbalances can have significant ramifications. Furthermore, to assess the accuracy of the AMOC, a trifold appraisal of the strength, depth, and latitude of maximum overturning is required.

Table 5.3: Physical and biogeochemical diagnostics to be used as targets in the retuning of FAMOUS.

Diagnostics previously used to tune FAMOUS	**Additional diagnostics recommended by this study**
Atmosphere	**Atmosphere**
Surface air temperature*†	Precipitation*† minus evaporation (P-E)
Ocean	**Ocean**
Sea surface temperature*	Sea surface salinity
Nitrate concentration†	Maximum AMOC strength
	Latitude of maximum AMOC
Sea ice	Depth of maximum AMOC
Sea ice concentration *	Dissolved inorganic carbon
	Alkalinity
	Carbon isotopes (Δ^{14}C and δ^{13}C)

* Used by Gregoire et al. (2011)
† Used by Williams et al. (2013)

5.4.2 Closing the carbon (isotope) budget

Currently the model has prescribed atmospheric CO_2 and carbon isotope concentrations (Sections 3.2 and 4.2). Although three isotopologues of CO_2 ($^{12}CO_2$, $^{13}CO_2$ and $^{14}CO_2$)

are outgassed from the surface ocean during air-sea gas exchange, they do not alter the atmospheric concentrations. This approach allows greater control in model development work and is consistent with previous carbon isotope implementation studies. Scientifically, simulations with a prescribed atmosphere are sufficient for examining changes in oceanic carbon isotope distributions under different (e.g. glacial or deglacial) circulation regimes, and for studying the rate and geographical distribution of carbon uptake by the oceans.

There are two main benefits to adding carbon isotopes to the atmospheric carbon pool in the future. Firstly, if both the simulated oceanic and atmospheric isotopic ratios agree with observations in a fully interactive system, it gives more confidence in the accuracy of the isotope scheme itself, our understanding of the underlying physical and biogeochemical processes, and their representation within the model. Secondly, a fully coupled system would allow changes in sources and sinks of carbon to be investigated more thoroughly over a range of timescales (both anthropogenic and palaeo).

Similarly, the MOSES2.2 generation of the model was preferred at the outset of this study because of its inclusion of a terrestrial carbon cycle and interactive vegetation (Williams et al., 2013; Valdes et al., 2017). Future efforts to extend the isotope scheme into the terrestrial carbon cycle, which currently has three representations of carbon (soil, vegetation, and litter), would therefore allow the partitioning of CO_2 between the land and the oceans to be examined in both an anthropogenic and a palaeo context.

To extend the isotopes into the atmosphere and the land surface scheme, a fully interactive carbon cycle would be required. Although FAMOUS does not currently have interactive carbon (Smith et al., 2008a; Williams et al., 2013), there are versions of the UM4.5 family that do (e.g. HadCM3L; Cox et al., 2000, 2004).

Without a fully interactive system, shorter simulations (for example the transient bomb simulation presented in Chapter 4) would benefit from having increased spatiotemporal resolution in the prescribed atmospheric values. Currently the model only allows a single global atmospheric value per year for CO_2 and the carbon isotopes, but prescribing multiple latitude bands would allow the north-south gradient in fossil fuel emissions and the location of atmospheric nuclear weapons testing to be better represented. Similarly, prescribing more than one atmospheric value per year would allow seasonal cycles to be investigated more rigorously.

5.4.3 Transferring the carbon isotope code into the parent model (HadCM3)

As outlined in Chapter 1 (Section 1.2.1), FAMOUS was an excellent tool for validating the new oceanic carbon isotope scheme in the UM4.5 family because it takes approximately 1 month to complete a 10,000 year simulation, which is required to fully spin-up the deep ocean circulation and the marine carbon cycle, compared to approximately 5 months with HadCM3 (Table 1.3). Now that the isotope code is fully functioning and has demonstrated accurate sensitivity to both physical and biogeochemical processes (Section 5.2.2), it would be beneficial to implement the new tracers (^{13}C and ^{14}C) into the parent model, which operates at a higher spatiotemporal resolution and provides a better representation of the structure of the AMOC than FAMOUS (Valdes et al., 2017). In its current (ocean-only) format, the carbon isotope code is directly transferable into HadCM3. In the first instance, the new tracers could therefore be used to validate the accuracy of the physical ocean circulation and the marine biogeochemistry in the parent model and, if required, provide a sensitive diagnostic for recalibration. Additionally, implementing the same code into a different configuration of the UM4.5 would allow an assessment to be made regarding the influence that model resolution has on the simulated δ^{13}C and Δ^{14}C distributions.

HadCM3 was one of the major models used in the Third and Fourth Assessments by the Intergovernmental Panel on Climate Change (IPCC, 2001, 2007) and it has been extensively used in palaeoclimate studies (e.g. Haywood and Valdes, 2004; Holloway et al., 2016; Ivanovic et al., 2017). Although no longer considered state-of-the-art, it continues to perform well compared to the latest generation of models, at least in terms of its mean climate (Valdes et al., 2017). Furthermore, oxygen isotopes have already been included throughout its entire hydrological cycle (Tindall et al., 2009). Oxygen isotopes are typically used to make inferences about temperature, precipitation, and circulation patterns (e.g. Clark et al., 2012), therefore, the existing tracers could be used in conjunction with the new oceanic tracers to provide a more holistic assessment of past changes in large-scale ocean circulation, the carbon cycle, and the surface climate. Thus, implementing the new carbon isotope scheme into multiple generations of the UM4.5 family would offer greater flexibility for future scientific application, depending on the required resolution, complexity, and run speed.

5.4.4 Scientific applications of the isotope-enabled model

The first scientific application of the isotope-enabled model was presented in Chapter 4: assessing the extent to which ^{14}C can be interpreted as a ventilation tracer. As one of the main reasons why low resolution GCMs such as FAMOUS were developed was to study palaeoclimate, two possible palaeoclimatic applications of the isotope-enabled model are discussed briefly. These suggestions are intended to illustrate the potential of the isotope-enabled model for reconciling our interpretation of proxy records and improving our understanding of palaeoclimatic transitions, as opposed to being an exhaustive list.

5.4.4.1 Simulating the Atlantic Meridional Overturning Circulation at the Last Glacial Maximum

As outlined in Chapter 1 (Section 1.1.3), there is no consensus on the strength and structure of the AMOC at the Last Glacial Maximum (LGM; 21,000 years ago). Some proxy reconstructions suggest that the NADW cell was weaker and shallower than modern (termed "Glacial North Atlantic Intermediate Water", GNAIW), with southern-sourced waters occupying a larger volume of the deep Atlantic than modern AABW (Duplessy et al., 1988; Marchitto et al., 2002; Curry and Oppo, 2005). Other reconstructions suggest that glacial overturning occurred at a similar or higher rate than today (Yu et al., 1996). More recently, Keigwin and Swift (2017) presented novel carbon isotope data that suggested that southern-sourced waters centred at 4200 m may have been sandwiched between GNAIW and a northern-sourced deep water mass. This interpretation is dissimilar from previous inferences, which all have a water mass analogous to modem AABW filling the deep ocean. Gebbie (2014) used a matrix transport model to find a steady state solution for glacial overturning that was consistent with δ^{13}C, Cd/Ca and δ^{18}O observations, and their respective uncertainties. The most plausible solution from this combined model-data approach was that the core (i.e. maximum stream function) of Glacial North Atlantic Water shoaled by approximately 1000 m, but that the vertical range of the water mass was similar to modern NADW. The author therefore concluded that the current generation of LGM proxy observations do not necessitate the renaming of NADW to GNAIW. Numerical climate models also produce a range of different glacial AMOCs (shallower and weaker, no significant changes from modern, and stronger and deeper), despite having comparable circulation states in present day simulations (Otto-Bliesner et al., 2007).

One approach for determining which, if any, of these interpretations best reconciles both the physical and biogeochemical structure of the oceans at the LGM would be to run an ensemble of isotope-enabled simulations under glacial boundary conditions (orbital parameters, land-sea mask, and atmospheric composition). A range of different overturning strengths and structures could be produced by changing the physical model parameters in Table 5.2, and the resultant surface climatologies and isotope distributions could be directly compared to proxy records.

5.4.4.2 Simulating the Atlantic Meridional Overturning Circulation during the last deglaciation

Major climatic and oceanic changes occurred during the last deglaciation (21,000 to 11,000 years ago) as the Earth transitioned from the relatively cold state of the LGM to the relatively warm state of the Holocene. Several abrupt (decadal-to-centennial) climatic fluctuations were superimposed on the gradual warming trend (Clark et al., 2012): Heinrich Stadial 1 (17,500 to 14,500 years ago), the Bølling Warming (approximately 14,500 years ago), and the Younger Dryas (12,700 to 11,500 years ago). As outlined in Chapter 1 (Section 1.1.1), reconstructing the precise chain of events surrounding these periods of rapid warming and cooling remains a challenge, but improving our understanding of the interplay between surface climate, the MOC, and the carbon cycle during these intervals can provide insights into how the Earth System might respond to anthropogenic forcing.

Transient simulations of the last deglaciation have been performed with fully coupled atmosphere-ocean GCMs (Liu et al., 2009; Gregoire et al., 2012) and with isotope-enabled EMICs (Roche et al., 2011; Menviel et al., 2017), but to-date, this period has not been studied with a full complexity GCM that includes isotopic tracers. It would therefore be pertinent to run a transient simulation of the deglaciation (prescribing changes in greenhouse gases, insolation, and freshwater fluxes) with the isotope-enabled version of FAMOUS. Interesting questions to consider include: is the model able to reproduce the major features of the deglacial surface climate (as inferred from proxy records); how well do the simulated and observed oceanic carbon isotope signals agree during the aforementioned periods of interest; what are the mechanisms that underpin these events and how well do these agree with the ideas that have been proposed by other models or data-based studies?

References

Adkins, J. F., Cheng, H., Boyle, E. A., Druffel, E. R. M., and Edwards, R. L. (1998). Deep-Sea Coral Evidence for Rapid Change in Ventilation of the Deep North Atlantic 15,400 Years Ago. *Science*, 280(5364):725–728.

Adkins, J. F., Griffin, S., Kashgarian, M., Cheng, H., Druffel, E. R. M., Boyle, E. A., Lawrence Edwards, R., and Shen, C.-C. (2002). Radiocarbon Dating of Deep-Sea Corals. *Radiocarbon*, 44(02):567–580.

Adkins, J. F., Henderson, G. M., Wang, S. L., O'Shea, S., and Mokadem, F. (2004). Growth rates of the deep-sea scleractinia Desmophyllum cristagalli and Enallopsammia rostrata. *Earth and Planetary Science Letters*, 227(3):481–490.

Alley, R. B. (2007). Wally Was Right: Predictive Ability of the North Atlantic "Conveyor Belt" Hypothesis for Abrupt Climate Change.

Anderson, R. F., Kumar, N., Mortlock, R. A., Froelich, P. N., Kubik, P., Dittrich-Hannen, B., and Suter, M. (1998). Late-Quaternary changes in productivity of the Southern Ocean. *Journal of Marine Systems*, 17(1):497–514.

Andres, R., Boden, T., and Marland, G. (1996). Annual Fossil-Fuel CO_2 Emissions: Global Stable Carbon Isotopic Signature. CDIAC. doi:10.3334/CDIAC/FFE.DB1013.2017.

Andres, R. J., Marland, G., Boden, T., and Bischof, S. (1994). Carbon dioxide emissions from fossil fuel consumption and cement manufacture, 1751-1991; and an estimate of their isotopic composition and latitudinal distribution. Technical Report CONF-9307181-4, Oak Ridge National Lab., TN (United States); Oak Ridge Inst. for Science and Education, TN (United States).

Bardin, A., Primeau, F., and Lindsay, K. (2014). An offline implicit solver for simulating prebomb radiocarbon. *Ocean Modelling*, 73:45–58.

Behrenfeld, M. J. and Falkowski, P. G. (1997). Photosynthetic rates derived from satellite-based chlorophyll concentration. *Limnology and Oceanography*, 42(1):1–20.

Blanckenburg, F. v. (1999). Tracing Past Ocean Circulation? *Science*, 286(5446):1862–1863.

Bostock, H. C., Opdyke, B. N., Gagan, M. K., and Fifield, L. K. (2004). Carbon isotope evidence for changes in Antarctic Intermediate Water circulation and ocean ventilation in the southwest Pacific during the last deglaciation. *Paleoceanography*, 19(4).

Bouttes, N., Roche, D. M., Mariotti, V., and Bopp, L. (2015). Including an ocean carbon cycle model into iLOVECLIM (v1.0). *Geoscientific Model Development*, 8(5):1563–1576.

Bradtmiller, L. I., McManus, J. F., and Robinson, L. F. (2014). ^{231}Pa/^{230}Th evidence for a weakened but persistent Atlantic meridional overturning circulation during Heinrich Stadial 1. *Nature Communications*, 5(1):5817.

Brandefelt, J. and Otto-Bliesner, B. L. (2009). Equilibration and variability in a Last Glacial Maximum climate simulation with CCSM3. *Geophysical Research Letters*, 36(19):L19712.

Brewer, P., Sarmiento, J. L., and Smethie, W. (1985). The Transient Tracers in the Ocean (TTO) program: The North Atlantic Study, 1981; The Tropical Atlantic Study, 1983. *Journal of Geophysical Research: Oceans*, 90(C4):6903–6905.

Brewer, P. G., Takahashi, T., and Williams, R. T. (1986). Transient tracers in the oceans (TTO) - Hydrographic data and carbon dioxide systems with revised carbon chemistry data. Technical report, Oak Ridge National Laboratory, Tennessee.

Broecker, W., Barker, S., Clark, E., Hajdas, I., Bonani, G., and Stott, L. (2004). Ventilation of the Glacial Deep Pacific Ocean. *Science*, 306(5699):1169–1172.

Broecker, W. S. (1987). The biggest chill. In *Global Climate Change Linkages; Acid Rain, Air Quality, and Stratospheric Ozone*, pages 13–22. Elsevier New York.

Broecker, W. S., Gerard, R., Ewing, M., and Heezen, B. C. (1960). Natural radiocarbon in the Atlantic Ocean. *Journal of Geophysical Research*, 65(9):2903–2931.

Broecker, W. S., Kennett, J. P., Flower, B. P., Teller, J. T., Trumbore, S., Bonani, G., and Wolfli, W. (1989). Routing of meltwater from the Laurentide Ice Sheet during the Younger Dryas cold episode. *Nature*, 341(6240):318.

Broecker, W. S., Peng, T.-H., Trumbore, S., Bonani, G., and Wolfli, W. (1990). The distribution of radiocarbon in the glacial ocean. *Global Biogeochemical Cycles*, 4(1):103–117.

Broecker, W. S. and Walton, A. (1959). Radiocarbon from Nuclear Tests. *Science*, 130(3371):309–314.

Brovkin, V., Bendtsen, J., Claussen, M., Ganopolski, A., Kubatzki, C., Petoukhov, V., and Andreev, A. (2002). Carbon cycle, vegetation, and climate dynamics in the Holocene: Experiments with the CLIMBER-2 model. *Global Biogeochemical Cycles*, 16(4).

Bryan, F. O. (1998). Climate Drift in a Multicentury Integration of the NCAR Climate System Model. *Journal of Climate*, 11(6):1455–1471.

Bryden, H. L., Beal, L. M., and Duncan, L. M. (2005a). Structure and Transport of the Agulhas Current and Its Temporal Variability. *Journal of Oceanography*, 66:479–492.

Bryden, H. L., Longworth, H. R., and Cunningham, S. A. (2005b). Slowing of the Atlantic meridional overturning circulation at 25° N. *Nature*, 438(7068):655–657.

Buchanan, P. J., Matear, R. J., Chase, Z., Phipps, S. J., and Bindoff, N. L. (2019). Ocean carbon and nitrogen isotopes in CSIRO Mk3l-COAL version 1.0: a tool for palaeoceanographic research. *Geoscientific Model Development*, 12(4):1491–1523.

Burke, A. and Robinson, L. F. (2012). The Southern Ocean's Role in Carbon Exchange During the Last Deglaciation. *Science*, 335(6068):557–561.

Burkhardt, S., Riebesell, U., and Zondervan, I. (1999). Effects of growth rate, CO_2 concentration, and cell size on the stable carbon isotope fractionation in marine phytoplankton. *Geochimica et Cosmochimica Acta*, 63(22):3729–3741.

Butzin, M., Prange, M., and Lohmann, G. (2005). Radiocarbon simulations for the glacial ocean: The effects of wind stress, Southern Ocean sea ice and Heinrich events. *Earth and Planetary Science Letters*, 235(1–2):45–61.

Campin, J.-M., Fichefet, T., and Duplessy, J.-C. (1999). Problems with using radiocarbon to infer ocean ventilation rates for past and present climates. *Earth and Planetary Science Letters*, 165(1):17–24.

Campos, M. C., Chiessi, C. M., Voigt, I., Piola, A. R., Kuhnert, H., and Mulitza, S. (2017). δ^{13}C decreases in the upper western South Atlantic during Heinrich Stadials 3 and 2. *Climate of the Past*, 13(4):345–358.

Chen, T., Robinson, L. F., Burke, A., Southon, J., Spooner, P., Morris, P. J., and Ng, H. C. (2015). Synchronous centennial abrupt events in the ocean and atmosphere during the last deglaciation. *Science*, 349(6255):1537–1541.

Chikamoto, M. O., Menviel, L., Abe-Ouchi, A., Ohgaito, R., Timmermann, A., Okazaki, Y., Harada, N., Oka, A., and Mouchet, A. (2012). Variability in North Pacific intermediate and deep water ventilation during Heinrich events in two coupled climate models. *Deep Sea Research Part II: Topical Studies in Oceanography*, 61–64:114–126.

Ciais, P., Sabine, C., Bala, G., Bopp, L., Brovkin, V., Canadell, J., Chhabra, A., DeFries, R., Galloway, J., Heimann, M., Jones, C., Le Quéré, C., Myneni, R., Piao, S., and Thornton (2013). Carbon and Other Biogeochemical Cycles. In *Climate Change 2013: The Physical Science Basis. Contribution of Working Group I to the Fifth Assessment Report of the Intergovernmental Panel on Climate Change [Stocker, T.F., D. Qin, G.-K. Plattner, M. Tignor, S.K. Allen, J. Boschung, A. Nauels, Y. Xia, V. Bex and P.M. Midgley (eds.)].*, pages 465–570. Cambridge University Press, Cambridge, United Kingdom and New York, NY, USA,.

Clark, P. U., Shakun, J. D., Baker, P. A., Bartlein, P. J., Brewer, S., Brook, E., Carlson, A. E., Cheng, H., Kaufman, D. S., Liu, Z., Marchitto, T. M., Mix, A. C., Morrill, C., Otto-Bliesner, B. L., Pahnke, K., Russell, J. M., Whitlock, C., Adkins, J. F., Blois, J. L., Clark, J., Colman, S. M., Curry, W. B., Flower, B. P., He, F., Johnson, T. C., Lynch-Stieglitz, J., Markgraf, V., McManus, J., Mitrovica, J. X., Moreno, P. I., and Williams, J. W. (2012). Global climate evolution during the last deglaciation. *Proceedings of the National Academy of Sciences*, 109(19):E1134–E1142.

Coachman, L. K. and Aagaard, K. (1988). Transports through Bering Strait: Annual and interannual variability. *Journal of Geophysical Research: Oceans*, 93(C12):15535–15539.

Collins, M., Knutti, R., Arblaster, J., Dufresne, J.-L., Fichefet, T., Friedlingstein, P., Gao, X., Gutowski, W., Johns, T., Krinner, G., Shongwe, M., Tebaldi, C., Weaver, A. J., and Wehner, M. (2013). Long-term Climate Change: Projections, Commitments and Irreversibility. In *Climate Change 2013: The Physical Science Basis. Contribution of Working Group I to the Fifth Assessment Report of the Intergovernmental Panel on Climate Change [Stocker, T.F., D. Qin, G.-K. Plattner, M. Tignor, S.K. Allen, J. Boschung, A. Nauels, Y. Xia, V. Bex and P.M. Midgley (eds.)]*, pages 1029–1136. Cambridge University Press, Cambridge, United Kingdom and New York, NY, USA.

Collins, W. J., Bellouin, N., Doutriaux-Boucher, M., Gedney, N., Halloran, P., Hinton, T., Hughes, J., Jones, C. D., Joshi, M., Liddicoat, S., Martin, G., O'Connor, F., Rae, J., Senior, C., Sitch, S., Totterdell, I., Wiltshire, A., and Woodward, S. (2011). Development and evaluation of an Earth-System model – HadGEM2. *Geoscientific Model Development*, 4(4):1051–1075.

Condron, A. and Winsor, P. (2012). Meltwater routing and the Younger Dryas. *Proceedings of the National Academy of Sciences*, 109(49):19928–19933.

Covey, C., Gleckler, P. J., Phillips, T. J., and Bader, D. C. (2006). Secular trends and climate drift in coupled ocean-atmosphere general circulation models. *Journal of Geophysical Research: Atmospheres*, 111(D3):D03107.

Cox, P. M., Betts, R. A., Bunton, C. B., Essery, R. L. H., Rowntree, P. R., and Smith, J. (1999). The impact of new land surface physics on the GCM simulation of climate and climate sensitivity. *Climate Dynamics*, 15(3):183–203.

Cox, P. M., Betts, R. A., Collins, M., Harris, P. P., Huntingford, C., and Jones, C. D. (2004). Amazonian forest dieback under climate-carbon cycle projections for the 21st century. *Theoretical and Applied Climatology*, 78(1-3).

Cox, P. M., Betts, R. A., Jones, C. D., Spall, S. A., and Totterdell, I. J. (2000). Acceleration of global warming due to carbon-cycle feedbacks in a coupled climate model. *Nature*, 408(6809):184–187.

Craig, H. (1954). Carbon 13 in Plants and the Relationships between Carbon 13 and Carbon 14 Variations in Nature. *The Journal of Geology*, 62(2):115–149.

Craig, H. (1957). Isotopic standards for carbon and oxygen and correction factors for mass-spectrometric analysis of carbon dioxide. *Geochimica et Cosmochimica Acta*, 12:133–149.

Crucifix, M. (2005). Distribution of carbon isotopes in the glacial ocean: A model study. *Paleoceanography*, 20(4):PA4020.

Cunningham, S. A., Alderson, S. G., King, B. A., and Brandon, M. A. (2003). Transport and variability of the Antarctic Circumpolar Current in Drake Passage. *Journal of Geophysical Research: Oceans*, 108(C5):8084.

Cunningham, S. A., Kanzow, T., Rayner, D., Baringer, M. O., Johns, W. E., Marotzke, J., Longworth, H. R., Grant, E. M., Hirschi, J. J.-M., Beal, L. M., Meinen, C. S., and Bryden, H. L. (2007). Temporal Variability of the Atlantic Meridional Overturning Circulation at 26 5° N. *Science*, 317(5840):935–938.

Curry, W. B. and Oppo, D. W. (2005). Glacial water mass geometry and the distribution of δ^{13}C of ΣCO_2 in the western Atlantic Ocean. *Paleoceanography*, 20(1).

Damon, P. E., Lerman, J. C., and Long, A. (1978). Temporal Fluctuations of Atmospheric ^{14}C: Causal Factors and Implications. *Annual Review of Earth and Planetary Sciences*, 6(1):457–494.

de la Fuente, M., Calvo, E., Skinner, L., Pelejero, C., Evans, D., Müller, W., Povea, P., and Cacho, I. (2017). The Evolution of Deep Ocean Chemistry and Respired Carbon in the Eastern Equatorial Pacific Over the Last Deglaciation. *Paleoceanography*, 32(12):2017PA003155.

de la Fuente, M., Skinner, L., Calvo, E., Pelejero, C., and Cacho, I. (2015). Increased reservoir ages and poorly ventilated deep waters inferred in the glacial Eastern Equatorial Pacific. *Nature Communications*, 6:7420.

Delworth, T. L. and Dixon, K. W. (2006). Have anthropogenic aerosols delayed a greenhouse gas-induced weakening of the North Atlantic thermohaline circulation? *Geophysical Research Letters*, 33(2).

Dentith, J. E., Ivanovic, R. F., Gregoire, L. J., Tindall, J. C., and Smith, R. S. (2019). Ocean circulation drifts in multi-millennial climate simulations: the role of salinity corrections and climate feedbacks. *Climate Dynamics*, 52(3):1761–1781.

Dixon, K. W., Delworth, T. L., Knutson, T. R., Spelman, M. J., and Stouffer, R. J. (2003). A comparison of climate change simulations produced by two GFDL coupled climate models. *Global and Planetary Change*, 37(1–2):81–102.

Dohan, K., Bonjean, F., Centurioni, L., Cronin, M., Lagerloef, G., Lee, D.-K., Lumpkin, R., Maximenko, N. A., Niiler, P. P., and Uchida, H. (2010). Measuring the global ocean surface circulation with satellite and in situ observations. In *Proceedings of OceanObs'09: Sustained Ocean Observations and Information for Society (Vol. 2)*, Venice, Italy, 21-25 September 2009. Hall, J., Harrison, D.E. & Stammer, D., Eds., European Space Agency, ESA Publication WPP-306.

Doney, S. C. (1999). Major challenges confronting marine biogeochemical modeling. *Global Biogeochemical Cycles*, 13(3):705–714.

Doney, S. C., Lindsay, K., Caldeira, K., Campin, J.-M., Drange, H., Dutay, J.-C., Follows, M., Gao, Y., Gnanadesikan, A., Gruber, N., Ishida, A., Joos, F., Madec, G., Maier-Reimer, E., Marshall, J. C., Matear, R. J., Monfray, P., Mouchet, A., Najjar, R., Orr, J. C., Plattner, G.-K., Sarmiento, J., Schlitzer, R., Slater, R., Totterdell, I. J., Weirig, M.-F., Yamanaka, Y., and Yool, A. (2004). Evaluating global ocean carbon models: The importance of realistic physics. *Global Biogeochemical Cycles*, 18(3):GB3017.

Druffel, E. M. (1980). Radiocarbon in Annual Coral Rings of Belize and Florida. *Radiocarbon*, 22(02):363–371.

Druffel, E. R. M. (1989). Decade time scale variability of ventilation in the North Atlantic: High-precision measurements of bomb radiocarbon in banded corals. *Journal of Geophysical Research: Oceans*, 94(C3):3271–3285.

Duplessy, J. C., Shackleton, N. J., Fairbanks, R. G., Labeyrie, L., Oppo, D., and Kallel, N. (1988). Deepwater source variations during the last climatic cycle and their impact on the global deepwater circulation. *Paleoceanography*, 3(3):343–360.

Eide, M., Olsen, A., Ninnemann, U. S., and Johannessen, T. (2017). A global ocean climatology of preindustrial and modern ocean δ^{13}C. *Global Biogeochemical Cycles*, 31(3):515–534.

Eltgroth, S. F., Adkins, J. F., Robinson, L. F., Southon, J., and Kashgarian, M. (2006). A deep-sea coral record of North Atlantic radiocarbon through the Younger Dryas: Evidence for intermediate water/deepwater reorganization. *Paleoceanography*, 21(4).

Emrich, K., Ehhalt, D. H., and Vogel, J. C. (1970). Carbon isotope fractionation during the precipitation of calcium carbonate. *Earth and Planetary Science Letters*, 8(5):363–371.

England, M. H. (1995). The Age of Water and Ventilation Timescales in a Global Ocean Model. *Journal of Physical Oceanography*, 25(11):2756–2777.

England, M. H. and Rahmstorf, S. (1999). Sensitivity of Ventilation Rates and Radiocarbon Uptake to Subgrid-Scale Mixing in Ocean Models. *Journal of Physical Oceanography*, 29(11):2802–2828.

Essery, R. L. H., Best, M. J., Betts, R. A., Cox, P. M., and Taylor, C. M. (2003). Explicit Representation of Subgrid Heterogeneity in a GCM Land Surface Scheme. *Journal of Hydrometeorology*, 4(3):530–543.

Essery, R. L. H., Best, M. J., and Cox, P. M. (2001). MOSES2.2 Technical Documentation. Hadley Centre Tech. Note 30, Met Office, Bracknell, United Kingdom, 30 pp.

Etnoyer, P. and Morgan, L. E. (2005). Habitat-forming deep-sea corals in the Northeast Pacific Ocean. In Freiwald, A. and Roberts, J. M., editors, *Cold-Water Corals and Ecosystems*, Erlangen Earth Conference Series, pages 331–343. Springer Berlin Heidelberg, Berlin, Heidelberg.

Falkowski, P., Scholes, R. J., Boyle, E., Canadell, J., Canfield, D., Elser, J., Gruber, N., Hibbard, K., Högberg, P., Linder, S., Mackenzie, F. T., Iii, B. M., Pedersen, T., Rosenthal, Y., Seitzinger, S., Smetacek, V., and Steffen, W. (2000). The Global Carbon Cycle: A Test of Our Knowledge of Earth as a System. *Science*, 290(5490):291–296.

Farmer, J. R., Robinson, L. F., and Hönisch, B. (2015). Growth rate determinations from radiocarbon in bamboo corals (genus Keratoisis). *Deep Sea Research Part I: Oceanographic Research Papers*, 105:26–40.

Ferreira, D., Cessi, P., Coxall, H. K., Boer, A. d., Dijkstra, H. A., Drijfhout, S. S., Eldevik, T., Harnik, N., McManus, J. F., Marshall, D. P., Nilsson, J., Roquet, F., Schneider, T., and Wills, R. C. (2018). Atlantic-Pacific Asymmetry in Deep-Water Formation. *Annual Review of Earth and Planetary Sciences*, 46(1).

Flato, G., Marotzke, J., Abiodun, B., Braconnot, P., Chou, S. C., Collins, W. J., Cox, P., Driouech, F., Emori, S., Eyring, V., Forest, C., Gleckler, P., Guilyardi, E., Jakob, C., Kattsov, V., Reason, C., and Rummukaines, M. (2013). Evaluation of Climate Models.

In: Climate Change 2013: The Physical Science Basis. Contribution of Working Group I to the Fifth Assessment Report of the Intergovernmental Panel on Climate Change. In *Climate Change 2013*, volume 5, pages 741–866. Cambridge University Press.

Francey, R. J., Allison, C. E., Etheridge, D. M., Trudinger, C. M., Enting, I. G., Leuenberger, M., Langenfelds, R. L., Michel, E., and Steele, L. P. (1999). A 1000-year high precision record of δ^{13}C in atmospheric CO_2. *Tellus B*, 51(2):170–193.

Freeland, H. J. and Cummins, P. F. (2005). Argo: A new tool for environmental monitoring and assessment of the world's oceans, an example from the N.E. Pacific. *Progress in Oceanography*, 64(1):31–44.

Freeman, K. H. and Hayes, J. M. (1992). Fractionation of carbon isotopes by phytoplankton and estimates of ancient CO_2 levels. *Global Biogeochemical Cycles*, 6(2):185–198.

Galbraith, E. D., Kwon, E. Y., Gnanadesikan, A., Rodgers, K. B., Griffies, S. M., Bianchi, D., Sarmiento, J. L., Dunne, J. P., Simeon, J., Slater, R. D., Wittenberg, A. T., and Held, I. M. (2011). Climate Variability and Radiocarbon in the CM2Mc Earth System Model. *Journal of Climate*, 24(16):4230–4254.

Garcia, H., Locarnini, R., Boyer, T., Antonov, J., Baranova, O., Zweng, M., Reagan, J., and Johnson, D. (2014). *World Ocean Atlas 2013, Volume 4: Dissolved Inorganic Nutrients (phosphate, nitrate, silicate).* S. Levitus, Ed., A. Mishonov Technical Ed.; NOAA Atlas NESDIS 76.

Gebbie, G. (2014). How much did Glacial North Atlantic Water shoal? *Paleoceanography*, 29(3):190–209.

Gent, P. R., Danabasoglu, G., Donner, L. J., Holland, M. M., Hunke, E. C., Jayne, S. R., Lawrence, D. M., Neale, R. B., Rasch, P. J., Vertenstein, M., Worley, P. H., Yang, Z.-L., and Zhang, M. (2011). The Community Climate System Model Version 4. *Journal of Climate*, 24(19):4973–4991.

Gent, P. R., Large, W. G., and Bryan, F. O. (2001). What sets the mean transport through Drake Passage? *Journal of Geophysical Research: Oceans*, 106(C2):2693–2712.

Gherardi, J. M., Labeyrie, L., McManus, J. F., Francois, R., Skinner, L. C., and Cortijo, E. (2005). Evidence from the Northeastern Atlantic basin for variability in the rate of the meridional overturning circulation through the last deglaciation. *Earth and Planetary Science Letters*, 240(3):710–723.

Godwin, H. (1962). Half-life of Radiocarbon. *Nature*, 195(4845):984.

Goericke, R. and Fry, B. (1994). Variations of marine plankton δ^{13}C with latitude, temperature, and dissolved CO_2 in the world ocean. *Global Biogeochemical Cycles*, 8(1):85–90.

Goldstein, S. J., Lea, D. W., Chakraborty, S., Kashgarian, M., and Murrell, M. T. (2001). Uranium-series and radiocarbon geochronology of deep-sea corals: implications for Southern Ocean ventilation rates and the oceanic carbon cycle. *Earth and Planetary Science Letters*, 193(1):167–182.

Goosse, H., Brovkin, V., Fichefet, T., Haarsma, R., Huybrechts, P., Jongma, J., Mouchet, A., Selten, F., Barriat, P.-Y., Campin, J.-M., Deleersnijder, E., Driesschaert, E., Goelzer, H., Janssens, I., Loutre, M.-F., Morales Maqueda, M. A., Opsteegh, T., Mathieu, P.-P., Munhoven, G., Pettersson, E. J., Renssen, H., Roche, D. M., Schaeffer, M., Tartinville, B., Timmermann, A., and Weber, S. L. (2010). Description of the Earth system model of intermediate complexity LOVECLIM version 1.2. *Geoscientific Model Development*, 3(2):603–633.

Goosse, H., Campin, J. M., Fichefet, T., and Deleersnijder, E. (1997). Sensitivity of a global ice–ocean model to the Bering Strait throughflow. *Climate Dynamics*, 13(5):349–358.

Gordon, C., Cooper, C., Senior, C. A., Banks, H., Gregory, J. M., Johns, T. C., Mitchell, J. F. B., and Wood, R. A. (2000). The simulation of SST, sea ice extents and ocean heat transports in a version of the Hadley Centre coupled model without flux adjustments. *Climate Dynamics*, 16(2-3):147–168.

Graven, H. D., Gruber, N., Key, R., Khatiwala, S., and Giraud, X. (2012a). Changing controls on oceanic radiocarbon: New insights on shallow-to-deep ocean exchange and anthropogenic CO_2 uptake. *Journal of Geophysical Research: Oceans*, 117(C10):C10005.

Graven, H. D., Kozyr, A., and Key, R. M. (2012b). Historical observations of oceanic radiocarbon conducted prior to GEOSECS. http://cdiac.ornl.gov/ftp/oceans/Historical_c14_obs/. Carbon Dioxide Information Analysis Center, Oak Ridge National Laboratory, US Department of Energy, Oak Ridge, Tennessee. doi: 10.3334/CDIAC/OTG.HIST_c14_obs.

Gregoire, L. J., Otto-Bliesner, B., Valdes, P. J., and Ivanovic, R. (2016). Abrupt Bølling warming and ice saddle collapse contributions to the Meltwater Pulse 1a rapid sea level rise. *Geophysical Research Letters*, 43(17):2016GL070356.

Gregoire, L. J., Payne, A. J., and Valdes, P. J. (2012). Deglacial rapid sea level rises caused by ice-sheet saddle collapses. *Nature*, 487(7406):219–222.

Gregoire, L. J., Valdes, P. J., and Payne, A. J. (2015). The relative contribution of orbital forcing and greenhouse gases to the North American deglaciation. *Geophysical Research Letters*, 42(22):2015GL066005.

Gregoire, L. J., Valdes, P. J., Payne, A. J., and Kahana, R. (2011). Optimal tuning of a GCM using modern and glacial constraints. *Climate Dynamics*, 37(3-4):705–719.

Gregory, J. M., Browne, O. J. H., Payne, A. J., Ridley, J. K., and Rutt, I. C. (2012). Modelling large-scale ice-sheet–climate interactions following glacial inception. *Climate of the Past*, 8(5):1565–1580.

Gregory, J. M., Dixon, K. W., Stouffer, R. J., Weaver, A. J., Driesschaert, E., Eby, M., Fichefet, T., Hasumi, H., Hu, A., Jungclaus, J. H., Kamenkovich, I. V., Levermann, A., Montoya, M., Murakami, S., Nawrath, S., Oka, A., Sokolov, A. P., and Thorpe, R. B. (2005). A model intercomparison of changes in the Atlantic thermohaline circulation in response to increasing atmospheric CO_2 concentration. *Geophysical Research Letters*, 32(12):L12703.

Gruber, N. and Keeling, C. D. (2001). An improved estimate of the isotopic air-sea disequilibrium of CO_2: Implications for the oceanic uptake of anthropogenic CO_2. *Geophysical Research Letters*, 28(3):555–558.

Guilderson, T. P., Caldeira, K., and Duffy, P. B. (2000). Radiocarbon as a diagnostic tracer in ocean and carbon cycle modeling. *Global Biogeochemical Cycles*, 14(3):887–902.

Guilderson, T. P., McCarthy, M. D., Dunbar, R. B., Englebrecht, A., and Roark, E. B. (2013). Late Holocene variations in Pacific surface circulation and biogeochemistry inferred from proteinaceous deep-sea corals. *Biogeosciences*, 10(9):6019–6028.

Gupta, A. S., Muir, L. C., Brown, J. N., Phipps, S. J., Durack, P. J., Monselesan, D., and Wijffels, S. E. (2012). Climate Drift in the CMIP3 Models. *Journal of Climate*, 25(13):4621–4640.

Hardiman, S. C., Butchart, N., O'Connor, F. M., and Rumbold, S. T. (2017). The Met Office HadGEM3-ES chemistry–climate model: evaluation of stratospheric dynamics and its impact on ozone. *Geoscientific Model Development*, 10(3):1209–1232.

Hawkins, E., Smith, R. S., Allison, L. C., Gregory, J. M., Woollings, T. J., Pohlmann, H., and de Cuevas, B. (2011). Bistability of the Atlantic overturning circulation in a global climate model and links to ocean freshwater transport. *Geophysical Research Letters*, 38(10):L10605.

Haywood, A. M. and Valdes, P. J. (2004). Modelling Pliocene warmth: contribution of atmosphere, oceans and cryosphere. *Earth and Planetary Science Letters*, 218(3):363–377.

Hazeleger, W., Wang, X., Severijns, C., Ştefănescu, S., Bintanja, R., Sterl, A., Wyser, K., Semmler, T., Yang, S., Hurk, B. v. d., Noije, T. v., Linden, E. v. d., and Wiel, K. v. d.

(2012). EC-Earth V2.2: description and validation of a new seamless earth system prediction model. *Climate Dynamics*, 39(11):2611–2629.

Henry, L. G., McManus, J. F., Curry, W. B., Roberts, N. L., Piotrowski, A. M., and Keigwin, L. D. (2016). North Atlantic ocean circulation and abrupt climate change during the last glaciation. *Science*, 353(6298):470–474.

Hodell, D. A. and Venz-Curtis, K. A. (2006). Late Neogene history of deepwater ventilation in the Southern Ocean. *Geochemistry, Geophysics, Geosystems*, 7(9).

Hofmann, M., Broecker, W. S., and Lynch-Stieglitz, J. (1999). Influence of a [$CO_{2(aq)}$] dependent biological C-isotope fractionation on glacial $^{13}C/^{12}C$ ratios in the ocean. *Global Biogeochemical Cycles*, 13(4):873–883.

Hofmann, M., Wolf-Gladrow, D. A., Takahashi, T., Sutherland, S. C., Six, K. D., and Maier-Reimer, E. (2000). Stable carbon isotope distribution of particulate organic matter in the ocean: a model study. *Marine Chemistry*, 72(2–4):131–150.

Hollander, D. J. and McKenzie, J. A. (1991). CO_2 control on carbon-isotope fractionation during aqueous photosynthesis: A paleo-pCO_2 barometer. *Geology*, 19(9):929–932.

Holloway, M. D., Sime, L. C., Singarayer, J. S., Tindall, J. C., and Valdes, P. J. (2016). Reconstructing paleosalinity from $\delta^{18}O$: Coupled model simulations of the Last Glacial Maximum, Last Interglacial and Late Holocene. *Quaternary Science Reviews*, 131:350–364.

Hood, M. (2009). Ship-based Repeat Hydrography: a Strategy for a Sustained Global Programme. A Community White Paper developed by the Global Ocean Ship-based Repeat Hydrographic Investigations Panel for the OceanObs '09 Conference, Venice, Italy, 21–25 September 2009. Report, UNESCO.

Hopcroft, P. O., Valdes, P. J., and Beerling, D. J. (2011). Simulating idealized Dansgaard-Oeschger events and their potential impacts on the global methane cycle. *Quaternary Science Reviews*, 30(23):3258–3268.

Hurrell, J. W., Holland, M. M., Gent, P. R., Ghan, S., Kay, J. E., Kushner, P. J., Lamarque, J.-F., Large, W. G., Lawrence, D., Lindsay, K., Lipscomb, W. H., Long, M. C., Mahowald, N., Marsh, D. R., Neale, R. B., Rasch, P., Vavrus, S., Vertenstein, M., Bader, D., Collins, W. D., Hack, J. J., Kiehl, J., and Marshall, S. (2013). The Community Earth System Model: A Framework for Collaborative Research. *Bulletin of the American Meteorological Society*, 94(9):1339–1360.

Huybrechts, P., Goelzer, H., Janssens, I., Driesschaert, E., Fichefet, T., Goosse, H., and Loutre, M.-F. (2011). Response of the Greenland and Antarctic Ice Sheets to

Multi-Millennial Greenhouse Warming in the Earth System Model of Intermediate Complexity LOVECLIM. *Surveys in Geophysics*, 32(4):397–416.

IPCC (2001). *Climate Change 2001: The Scientific Basis. Contribution of Working Group I to the Third Assessment Report of the Intergovernmental Panel on Climate Change*. Cambridge University Press, Cambridge, UK, New York, NY, USA.

IPCC (2007). *Climate Change 2007: The Physical Science Basis. Contribution of Working Group I to the Fourth Assessment Report of the Intergovernmental Panel on Climate Change.* Cambridge University Press, Cambridge, UK, New York, NY, USA.

Ito, T. and Follows, M. J. (2003). Upper ocean control on the solubility pump of CO_2. *Journal of Marine Research*, 61(4):465–489.

Ivanovic, R. F., Gregoire, L. J., Burke, A., Wickert, A. D., Valdes, P. J., Ng, H. C., Robinson, L. F., McManus, J. F., Mitrovica, J. X., Lee, L., and Dentith, J. E. (2018). Acceleration of Northern Ice Sheet Melt Induces AMOC Slowdown and Northern Cooling in Simulations of the Early Last Deglaciation. *Paleoceanography and Paleoclimatology*, 33(7):807–824.

Ivanovic, R. F., Gregoire, L. J., Kageyama, M., Roche, D. M., Valdes, P. J., Burke, A., Drummond, R., Peltier, W. R., and Tarasov, L. (2016). Transient climate simulations of the deglaciation 21–9 thousand years before present (version 1) – PMIP4 Core experiment design and boundary conditions. *Geoscientific Model Development*, 9(7):2563–2587.

Ivanovic, R. F., Gregoire, L. J., Wickert, A. D., Valdes, P. J., and Burke, A. (2017). Collapse of the North American ice saddle 14,500 years ago caused widespread cooling and reduced ocean overturning circulation. *Geophysical Research Letters*, 44(1):2016GL071849.

Jackson, L. and Vellinga, M. (2012). Multidecadal to Centennial Variability of the AMOC: HadCM3 and a Perturbed Physics Ensemble. *Journal of Climate*, 26(7):2390–2407.

Jackson, L. C., Peterson, K. A., Roberts, C. D., and Wood, R. A. (2016a). Recent slowing of Atlantic overturning circulation as a recovery from earlier strengthening. *Nature Geoscience*, 9(7):518–522.

Jackson, L. C., Smith, R. S., and Wood, R. A. (2016b). Ocean and atmosphere feedbacks affecting AMOC hysteresis in a GCM. *Climate Dynamics*, pages 1–19.

Jahn, A., Lindsay, K., Giraud, X., Gruber, N., Otto-Bliesner, B. L., Liu, Z., and Brady, E. C. (2015). Carbon isotopes in the ocean model of the Community Earth System Model (CESM1). *Geoscientific Model Development*, 8(8):2419–2434.

Jain, A. K., Kheshgi, H. S., and Wuebbles, D. J. (1997). Is there an imbalance in the global budget of bomb-produced radiocarbon? *Journal of Geophysical Research: Atmospheres*, 102(D1):1327–1333.

Jasper, J. and Hayes, J. M. (1990). A carbon isotope record of CO_2 levels during the late Quaternary. *Nature*, 347:462–464.

Jin, J., Zeng, Q., Wu, L., Liu, H., and Zhang, M. (2017). Formulation of a new ocean salinity boundary condition and impact on the simulated climate of an oceanic general circulation model. *Science China Earth Sciences*, 60(3):491–500.

Johns, T. C., Durman, C. F., Banks, H. T., Roberts, M. J., McLaren, A. J., Ridley, J. K., Senior, C. A., Williams, K. D., Jones, A., Rickard, G. J., Cusack, S., Ingram, W. J., Crucifix, M., Sexton, D. M. H., Joshi, M. M., Dong, B.-W., Spencer, H., Hill, R. S. R., Gregory, J. M., Keen, A. B., Pardaens, A. K., Lowe, J. A., Bodas-Salcedo, A., Stark, S., and Searl, Y. (2006). The New Hadley Centre Climate Model (HadGEM1): Evaluation of Coupled Simulations. *Journal of Climate*, 19(7):1327–1353.

Johnson, G. and Bryden, H. (1989). On the size of the Antarctic Circumpolar Current. *Deep Sea Research*, 36(1):39–53.

Jones, C., Gregory, J., Thorpe, R., Cox, P., Murphy, J., Sexton, D., and Valdes, P. (2005). Systematic optimisation and climate simulation of FAMOUS, a fast version of HadCM3. *Climate Dynamics*, 25(2-3):189–204.

Kalnay, E., Kanamitsu, M., Kistler, R., Collins, W., Deaven, D., Gandin, L., Iredell, M., Saha, S., White, G., Woollen, J., Zhu, Y., Chelliah, M., Ebisuzaki, W., Higgins, W., Janowiak, J., Mo, K., Ropelewski, C., Wang, J., Leetmaa, A., Reynolds, R., Jenne, R., and Joseph, D. (1996). The NCEP/NCAR 40-Year Reanalyis Project. *Bulletin of the American Meteorological Society*, 77:437–470.

Kanzow, T., Cunningham, S. A., Johns, W. E., Hirschi, J. J.-M., Marotzke, J., Baringer, M., Meinen, C. S., Chidichimo, M. P., Atkinson, C., Beal, L. M., Bryden, H. L., and Collins, J. (2010). Seasonal Variability of the Atlantic Meridional Overturning Circulation at 26 5° N. *Journal of Climate*, 23:5678–5698.

Karlen, I., Olsson, I. U., Kallberg, P., and Kilicci, S. (1965). Absolute determination of the activity of two C-14 dating standards. *Arkiv Geofysik*, 4.

Keeling, C. D. (1979). The Suess effect: ^{13}Carbon-^{14}Carbon interrelations. *Environment International*, 2(4):229–300.

Keigwin, L. D., Jones, G. A., Lehman, S. J., and Boyle, E. A. (1991). Deglacial meltwater discharge, North Atlantic Deep Circulation, and abrupt climate change. *Journal of Geophysical Research: Oceans*, 96(C9):16811–16826.

Keigwin, L. D. and Swift, S. A. (2017). Carbon isotope evidence for a northern source of deep water in the glacial western North Atlantic. *Proceedings of the National Academy of Sciences*, 114(11):2831–2835.

Keller, K. and Morel, F. M. M. (1999). A model of carbon isotopic fractionation and active carbon uptake in phytoplankton. *Marine Ecology Progress Series*, 182:295–298.

Key, R., Olsen, A., Van Heuven, S., Lauvset, S., Velo, A., Lin, X., Schirnick, C., Kozyr, A., Tanhua, T., Hoppema, M., Jutterstrom, S., Steinfeldt, R., Jeansson, E., Ishi, M., Perez, F., and Suzuki, T. (2015). Global Ocean Data Analysis Project, Version 2 (GLODAPv2), ORNL/CDIAC-162, ND-P093.

Key, R. M. (2001). Radiocarbon. *Encyclopedia of Ocean Sciences. Academic Press.*

Key, R. M., Kozyr, A., Sabine, C. L., Lee, K., Wanninkhof, R., Bullister, J. L., Feely, R. A., Millero, F. J., Mordy, C., and Peng, T.-H. (2004). A global ocean carbon climatology: Results from Global Data Analysis Project (GLODAP). *Global Biogeochemical Cycles*, 18(4):GB4031.

Key, R. M., Tanhua, T., Olsen, A., Hoppema, M., Jutterström, S., Schirnick, C., van Heuven, S., Lin, X., Wallace, D. W. R., and Mintrop, L. (2010). The CARINA data synthesis project: Introduction and overview. *Earth System Science Data*, 2:105–121.

Khatiwala, S., Tanhua, T., Mikaloff Fletcher, S., Gerber, M., Doney, S. C., Graven, H. D., Gruber, N., McKinley, G. A., Murata, A., Ríos, A. F., and Sabine, C. L. (2013). Global ocean storage of anthropogenic carbon. *Biogeosciences*, 10(4):2169–2191.

Kilada, R. W., Campana, S. E., and Roddick, D. (2007). Validated age, growth, and mortality estimates of the ocean quahog (Arctica islandica) in the western Atlantic. *ICES Journal of Marine Science*, 64(1):31–38.

Koeve, W., Wagner, H., Kähler, P., and Oschlies, A. (2015). ^{14}C-age tracers in global ocean circulation models. *Geoscientific Model Development*, 8:2079–2094.

Koltermann, K. P., Gouretski, V., and Jancke, K. (2011). *Hydrographic Atlas of the World Ocean Circulation Experiment (WOCE): volume 3: Atlantic Ocean*. National Oceanography Centre.

Kuhlbrodt, T., Griesel, A., Montoya, M., Levermann, A., Hofmann, M., and Rahmstorf, S. (2007). On the driving processes of the Atlantic meridional overturning circulation. *Reviews of Geophysics*, 45(2):RG2001.

Kumar, N., Anderson, R. F., Mortlock, R. A., Froelich, P. N., Kubik, P., Dittrich-Hannen, B., and Suter, M. (1995). Increased biological productivity and export production in the glacial Southern Ocean. *Nature*, 378(6558):675–680.

Lavender, K. L., Davis, R. E., and Owens, W. B. (2002). Observations of Open-Ocean Deep Convection in the Labrador Sea from Subsurface Floats. *Journal of Physical Oceanography*, 32(2):511–526.

Laws, E. A., Bidigare, R. R., and Popp, B. N. (1997). Effect of growth rate and CO_2 concentration on carbon isotopic fractionation by the marine diatom Phaeodactylum tricornutum. *Limnology and Oceanography*, 42(7).

Laws, E. A., Popp, B. N., Bidigare, R. R., Kennicutt, M. C., and Macko, S. A. (1995). Dependence of phytoplankton carbon isotopic composition on growth rate and $[CO_2]_{aq}$: Theoretical considerations and experimental results. *Geochimica et Cosmochimica Acta*, 59(6):1131–1138.

Ledbetter, M. T. and Johnson, D. A. (1976). Increased Transport of Antarctic Bottom Water in the Vema Channel During the Last Ice Age. *Science*, 194(4267):837–839.

Lee, J.-M., Eltgroth, S. F., Boyle, E. A., and Adkins, J. F. (2017). The transfer of bomb radiocarbon and anthropogenic lead to the deep North Atlantic Ocean observed from a deep sea coral. *Earth and Planetary Science Letters*, 458:223–232.

Leonard, B. P. (1979). A stable and accurate convective modelling procedure based on quadratic upstream interpolation. *Computer Methods in Applied Mechanics and Engineering*, 19(1):59–98.

Leonard, B. P. M. (1993). Positivity-preserving numerical schemes for multidimensional advection. Technical report.

Lindsay, K. (2017). A Newton–Krylov solver for fast spin-up of online ocean tracers. *Ocean Modelling*, 109:33–43.

Liu, Z., Otto-Bliesner, B. L., He, F., Brady, E. C., Tomas, R., Clark, P. U., Carlson, A. E., Lynch-Stieglitz, J., Curry, W., Brook, E., Erickson, D., Jacob, R., Kutzbach, J., and Cheng, J. (2009). Transient Simulation of Last Deglaciation with a New Mechanism for Bølling-Allerød Warming. *Science*, 325(5938):310–314.

Locarnini, R., Mishonov, A., Antonov, J., Boyer, T., Garcia, H., Baranova, O., Zweng, M., Reagan, J., Johnson, D., Hamilton, M., and Seidov, D. (2013). *World Ocean Atlas 2013, Volume 1: Temperature*. S. Levitus, Ed., A. Mishonov Technical Ed.; NOAA Atlas NESDIS 73.

Lynch-Stieglitz, J. (2001). Using ocean margin density to constrain ocean circulation and surface wind strength in the past. *Geochemistry, Geophysics, Geosystems*, 2(12).

Lynch-Stieglitz, J. (2003). Tracers of Past Ocean Circulation. *Treatise on Geochemistry*, 6:625.

Lynch-Stieglitz, J., Curry, W. B., and Slowey, N. (1999a). A geostrophic transport estimate for the Florida Current from the oxygen isotope composition of benthic foraminifera. *Paleoceanography*, 14(3):360–373.

Lynch-Stieglitz, J., Curry, W. B., and Slowey, N. (1999b). Weaker Gulf Stream in the Florida Straits during the Last Glacial Maximum. *Nature*, 402(6762):644.

Lynch-Stieglitz, J., Stocker, T. F., Broecker, W. S., and Fairbanks, R. G. (1995). The influence of air-sea exchange on the isotopic composition of oceanic carbon: Observations and modeling. *Global Biogeochemical Cycles*, 9(4):653–665.

Mahadevan, A. (2001). An analysis of bomb radiocarbon trends in the Pacific. *Marine Chemistry*, 73(3-4):273–290.

Maier-Reimer, E. (1993). Geochemical cycles in an ocean general circulation model. Preindustrial tracer distributions. *Global Biogeochemical Cycles*, 7(3):645–677.

Marchal, O., François, R., Stocker, T. F., and Joos, F. (2000). Ocean thermohaline circulation and sedimentary ^{231}Pa/^{230}Th ratio. *Paleoceanography*, 15(6):625–641.

Marchitto, T. M. and Broecker, W. S. (2006). Deep water mass geometry in the glacial Atlantic Ocean: A review of constraints from the paleonutrient proxy Cd/Ca. *Geochemistry, Geophysics, Geosystems*, 7(12).

Marchitto, T. M., Oppo, D. W., and Curry, W. B. (2002). Paired benthic foraminiferal Cd/Ca and Zn/Ca evidence for a greatly increased presence of Southern Ocean Water in the glacial North Atlantic. *Paleoceanography*, 17(3):10–1–10–18.

Martin, G., Bellouin, N., Collins, W. J., Culverwell, I. D., Halloran, P. R., Hardiman, S. C., Hinton, T. J., Jones, C. D., McDonald, R. E., McLaren, A. J., O'Connor, F. M., Roberts, M. J., Rodriguez, J. M., Woodward, S., Best, M. J., Brooks, M. E., Brown, A. R., Butchart, N., Dearden, C., Derbyshire, S. H., Dharssi, I., Doutriaux-Boucher, M., Edwards, J. M., Falloon, P. D., Gedney, N., Gray, L. J., Hewitt, H. T., Hobson, M., Huddleston, M. R., Hughes, J., Ineson, S., Ingram, W. J., James, P. M., Johns, T. C., Johnson, C. E., Jones, A., Jones, C. P., Joshi, M. M., Keen, A. B., Liddicoat, S., Lock, A. P., Maidens, A. V., Manners, J. C., Milton, S. F., Rae, J. G. L., Ridley, J. K., Sellar, A., Senior, C. A., Totterdell, I. J., Verhoef, A., Vidale, P. L., and Wiltshire, A. (2011). The HadGEM2 family of Met Office Unified Model climate configurations. *Geoscientific Model Development*, 4(3):723–757.

Marzocchi, A. and Jansen, M. F. (2017). Connecting Antarctic sea ice to deep-ocean circulation in modern and glacial climate simulations. *Geophysical Research Letters*, 44(12):6286–6295.

Mata, M. M., Tomczak, M., Wijffels, S., and Church, J. A. (2000). East Australian Current volume transports at 30° S: Estimates from the World Ocean Circulation Experiment hydrographic sections PR11/P6 and the PCM3 current meter array. *Journal of Geophysical Research: Oceans*, 105(C12):28509–28526.

Matsumoto, K., Sarmiento, J. L., Key, R. M., Aumont, O., Bullister, J. L., Caldeira, K., Campin, J.-M., Doney, S. C., Drange, H., Dutay, J.-C., Follows, M., Gao, Y., Gnanadesikan, A., Gruber, N., Ishida, A., Joos, F., Lindsay, K., Maier-Reimer, E., Marshall, J. C., Matear, R. J., Monfray, P., Mouchet, A., Najjar, R., Plattner, G.-K., Schlitzer, R., Slater, R., Swathi, P. S., Totterdell, I. J., Weirig, M.-F., Yamanaka, Y., Yool, A., and Orr, J. C. (2004). Evaluation of ocean carbon cycle models with data-based metrics. *Geophysical Research Letters*, 31(7):L07303.

McCave, I. N., Manighetti, B., and Robinson, S. G. (1995). Sortable silt and fine sediment size/composition slicing: Parameters for palaeocurrent speed and palaeoceanography. *Paleoceanography*, 10(3):593–610.

McManus, J. F., Francois, R., Gherardi, J.-M., Keigwin, L. D., and Brown-Leger, S. (2004). Collapse and rapid resumption of Atlantic meridional circulation linked to deglacial climate changes. *Nature*, 428(6985):834–837.

Meinen, C. S. and Luther, D. S. (2016). Structure, transport, and vertical coherence of the Gulf Stream from the Straits of Florida to the Southeast Newfoundland Ridge. *Deep Sea Research Part I: Oceanographic Research Papers*, 112:137–154.

Meissner, K. J., Schmittner, A., Weaver, A. J., and Adkins, J. F. (2003). Ventilation of the North Atlantic Ocean during the Last Glacial Maximum: A comparison between simulated and observed radiocarbon ages. *Paleoceanography*, 18(2):1023.

Menary, M. B., Kuhlbrodt, T., Ridley, J., Andrews, M. B., Dimdore-Miles, O. B., Deshayes, J., Eade, R., Gray, L., Ineson, S., Mignot, J., Roberts, C. D., Robson, J., Wood, R. A., and Xavier, P. (2018). Preindustrial Control Simulations With HadGEM3-GC3.1 for CMIP6. *Journal of Advances in Modeling Earth Systems*, 10(12):3049–3075.

Menviel, L., Timmermann, A., Elison Timm, O., Mouchet, A., Abe-Ouchi, A., Chikamoto, M. O., Harada, N., Ohgaito, R., and Okazaki, Y. (2012). Removing the North Pacific halocline: Effects on global climate, ocean circulation and the carbon cycle. *Deep Sea Research Part II: Topical Studies in Oceanography*, 61–64:106–113.

Menviel, L., Timmermann, A., Timm, O. E., and Mouchet, A. (2011). Deconstructing the Last Glacial termination: the role of millennial and orbital-scale forcings. *Quaternary Science Reviews*, 30(9–10):1155–1172.

Menviel, L., Yu, J., Joos, F., Mouchet, A., Meissner, K. J., and England, M. H. (2017). Poorly ventilated deep ocean at the Last Glacial Maximum inferred from carbon isotopes: A data-model comparison study. *Paleoceanography*, 32(1):2–17.

Millero, F. J. (1995). Thermodynamics of the carbon dioxide system in the oceans. *Geochimica et Cosmochimica Acta*, 59(4):661–677.

Montero-Serrano, J.-C., Frank, N., Tisnérat-Laborde, N., Colin, C., Wu, C.-C., Lin, K., Shen, C.-C., Copard, K., Orejas, C., Gori, A., De Mol, L., Van Rooij, D., Reverdin, G., and Douville, E. (2013). Decadal changes in the mid-depth water mass dynamic of the Northeastern Atlantic margin (Bay of Biscay). *Earth and Planetary Science Letters*, 364:134–144.

Mook, W. G. (1986). ^{13}C in atmospheric CO$_2$. *Netherlands Journal of Sea Research*, 20(2):211–223.

Murnane, R. J. and Sarmiento, J. L. (2000). Roles of biology and gas exchange in determining the δ^{13}C distribution in the ocean and the preindustrial gradient in atmospheric δ^{13}C. *Global Biogeochemical Cycles*, 14(1):389–405.

Najjar, R. G., Jin, X., Louanchi, F., Aumont, O., Caldeira, K., Doney, S. C., Dutay, J.-C., Follows, M., Gruber, N., Joos, F., Lindsay, K., Maier-Reimer, E., Matear, R. J., Matsumoto, K., Monfray, P., Mouchet, A., Orr, J. C., Plattner, G.-K., Sarmiento, J. L., Schlitzer, R., Slater, R. D., Weirig, M.-F., Yamanaka, Y., and Yool, A. (2007). Impact of circulation on export production, dissolved organic matter, and dissolved oxygen in the ocean: Results from Phase II of the Ocean Carbon-cycle Model Intercomparison Project (OCMIP-2). *Global Biogeochemical Cycles*, 21(3):GB3007.

Okazaki, Y., Timmermann, A., Menviel, L., Harada, N., Abe-Ouchi, A., Chikamoto, M. O., Mouchet, A., and Asahi, H. (2010). Deepwater Formation in the North Pacific During the Last Glacial Termination. *Science*, 329(5988):200–204.

Oliver, K. I. C., Hoogakker, B. A. A., Crowhurst, S., Henderson, G. M., Rickaby, R. E. M., Edwards, N. R., and Elderfield, H. (2010). A synthesis of marine sediment core δ^{13}C data over the last 150 000 years. *Climate of the Past*, 6(5):645–673.

Olsen, A., Key, R. M., van Heuven, S., Lauvset, S. K., Velo, A., Lin, X., Schirnick, C., Kozyr, A., Tanhua, T., Hoppema, M., Jutterström, S., Steinfeldt, R., Jeansson, E., Ishii, M., Pérez, F. F., and Suzuki, T. (2016). The Global Ocean Data Analysis Project version 2 (GLODAPv2) – an internally consistent data product for the world ocean. *Earth System Science Data*, 8(2):297–323.

Orr, J., Najjar, R., Sabine, C. L., and Joos, F. (2000). Abiotic-HOWTO. Technical report. Revision: 1.16.

Orr, J. C. (1999). Ocean Carbon-Cycle Model Intercomparison Project (OCMIP): Phase 1 (1995-1997). *GAIM Report 7*.

Orr, J. C., Najjar, R. G., Aumont, O., Bopp, L., Bullister, J. L., Danabasoglu, G., Doney, S. C., Dunne, J. P., Dutay, J.-C., Graven, H., Griffies, S. M., John, J. G., Joos, F., Levin, I., Lindsay, K., Matear, R. J., McKinley, G. A., Mouchet, A., Oschlies, A., Romanou, A., Schlitzer, R., Tagliabue, A., Tanhua, T., and Yool, A. (2017). Biogeochemical protocols and diagnostics for the CMIP6 Ocean Model Intercomparison Project (OMIP). *Geoscientific Model Development*, 10:2169–2199.

Orsi, A. H. and Whitworth III, T. (2005). *Hydrographic Atlas of the World Ocean Circulation Experiment (WOCE) Volume 1: Southern Ocean*.

Otto-Bliesner, B. L., Hewitt, C. D., Marchitto, T. M., Brady, E., Abe-Ouchi, A., Crucifix, M., Murakami, S., and Weber, S. L. (2007). Last Glacial Maximum ocean thermohaline circulation: PMIP2 model intercomparisons and data constraints. *Geophysical Research Letters*, 34(12):L12706.

Palmer, J. (1998). The Ocean Carbon Cycle in the Unified Model.

Palmer, J. R. and Totterdell, I. J. (2001). Production and export in a global ocean ecosystem model. *Deep Sea Research Part I: Oceanographic Research Papers*, 48(5):1169–1198.

Pardaens, A. K., Banks, H. T., Gregory, J. M., and Rowntree, P. R. (2003). Freshwater transports in HadCM3. *Climate Dynamics*, 21(2):177–195.

Phipps, S. J., Rotstayn, L., Gordon, H., Roberts, J. L., Hirst, A., and Budd, W. (2011). The CSIRO Mk3L climate system model version 1.0 – Part 1: Description and evaluation. *Geoscientific Model Development*, 4:483–509.

Piotrowski, A. M., Goldstein, S. L., Hemming, S. R., and Fairbanks, R. G. (2004). Intensification and variability of ocean thermohaline circulation through the last deglaciation. *Earth and Planetary Science Letters*, 225(1):205–220.

Pope, V. D., Gallani, M. L., Rowntree, P. R., and Stratton, R. A. (2000). The impact of new physical parametrizations in the Hadley Centre climate model: HadAM3. *Climate Dynamics*, 16(2-3):123–146.

Popp, B., Takigiku, R., Hayes, J., Louda, J., and Baker, E. (1989). The post-Paleozoic chronology and mechanism of ^{13}C depletion in primary marine organic matter. *American Journal of Science*, 289:436–454.

Quay, P., Sonnerup, R., Westby, T., Stutsman, J., and McNichol, A. (2003). Changes in the ^{13}C/^{12}C of dissolved inorganic carbon in the ocean as a tracer of anthropogenic CO_2 uptake. *Global Biogeochemical Cycles*, 17(1).

Quay, P. D., Tilbrook, B., and Wong, C. S. (1992). Oceanic Uptake of Fossil Fuel CO_2: Carbon-13 Evidence. *Science*, 256(5053):74–79.

Rae, J. W. B., Sarnthein, M., Foster, G. L., Ridgwell, A., Grootes, P. M., and Elliott, T. (2014). Deep water formation in the North Pacific and deglacial CO_2 rise. *Paleoceanography*, 29(6):2013PA002570.

Rahmstorf, S. (2002). Ocean circulation and climate during the past 120,000 years. *Nature*, 419(6903):207–214.

Rahmstorf, S., Box, J. E., Feulner, G., Mann, M. E., Robinson, A., Rutherford, S., and Schaffernicht, E. J. (2015). Exceptional twentieth-century slowdown in Atlantic Ocean overturning circulation. *Nature Climate Change*, 5(5):475–480.

Rau, G., Takahashi, T., and Des Marais, D. (1989). Latitudinal variations in plankton δ^{13}C: implications for CO_2 and productivity in past oceans. *Nature*, 341:516–518.

Rau, G. H., Riebesell, U., and Wolf-Gladrow, D. (1996). A model of photosynthetic 13 C fractionation by marine phytoplankton based on diffusive molecular CO 2 uptake. *Marine Ecology Progress Series*, 133:275–285.

Rayner, D., Hirschi, J. J. M., Kanzow, T., Johns, W. E., Wright, P. G., Frajka-Williams, E., Bryden, H. L., Meinen, C. S., Baringer, M. O., Marotzke, J., Beal, L. M., and Cunningham, S. A. (2011). Monitoring the Atlantic meridional overturning circulation. *Deep Sea Research Part II: Topical Studies in Oceanography*, 58(17):1744–1753.

Reimer, P. J., Baillie, M. G. L., Bard, E., Bayliss, A., Beck, J. W., Blackwell, P. G., Ramsey, C. B., Buck, C. E., Burr, G. S., Edwards, R. L., Friedrich, M., Grootes, P. M., Guilderson, T. P., Hajdas, I., Heaton, T. J., Hogg, A. G., Hughen, K. A., Kaiser, K. F., Kromer, B., McCormac, F. G., Manning, S. W., Reimer, R. W., Richards, D. A., Southon, J. R., Talamo, S., Turney, C. S. M., Plicht, J. v. d., and Weyhenmeyer, C. E. (2009). IntCal09 and Marine09 Radiocarbon Age Calibration Curves, 0–50,000 Years cal BP. *Radiocarbon*, 51(4):1111–1150.

Rhein, M., Rintoul, S., Aoki, S., Campos, E., Chambers, D., Feely, R. A., Gulev, S., Johnson, G., Josey, S., Kostianoy, A., Mauritzen, C., Roemmich, D., Talley, L., and Wang, F. (2013). Observations: Ocean. In *Climate Change 2013: The Physical Science Basis. Contribution of Working Group I to the Fifth Assessment Report of the Intergovernmental Panel on Climate Change [Stocker, T.F., D. Qin, G.-K. Plattner, M. Tignor, S.K. Allen, J. Boschung, A. Nauels, Y. Xia, V. Bex and P.M. Midgley (eds.)]*, pages 255–316. Cambridge University Press, Cambridge, United Kingdom and New York, NY, USA,.

Richardson, C. A. (2001). Molluscs as archives of environmental change. In *Oceanography and Marine Biology, An Annual Review*, volume 39, pages 103–164. CRC Press.

Ridgwell, A., Hargreaves, J. C., Edwards, N. R., Annan, J. D., Lenton, T. M., Marsh, R., Yool, A., and Watson, A. (2007). Marine geochemical data assimilation in an efficient Earth System Model of global biogeochemical cycling. *Biogeosciences*, 4(1):87–104.

Roark, E. B., Guilderson, T. P., Dunbar, R. B., Fallon, S. J., and Mucciarone, D. A. (2009). Extreme longevity in proteinaceous deep-sea corals. *Proceedings of the National Academy of Sciences*, 106(13):5204–5208.

Roberts, J. M., Wheeler, A., and Freiwald, A. (2006). Reefs of the Deep: The Biology and Geology of Cold-Water Coral Ecosystems. *Science*, 312(5773):543–547.

Robinson, L. F., Adkins, J. F., Keigwin, L. D., Southon, J., Fernandez, D. P., Wang, S.-L., and Scheirer, D. S. (2005). Radiocarbon Variability in the Western North Atlantic During the Last Deglaciation. *Science*, 310(5753):1469–1473.

Robinson, L. F. and van de Flierdt, T. (2009). Southern Ocean evidence for reduced export of North Atlantic Deep Water during Heinrich event 1. *Geology*, 37(3):195–198.

Roche, D. M., Paillard, D., Caley, T., and Waelbroeck, C. (2014). LGM hosing approach to Heinrich Event 1: results and perspectives from data–model integration using water isotopes. *Quaternary Science Reviews*, 106:247–261.

Roche, D. M., Renssen, H., Paillard, D., and Levavasseur, G. (2011). Deciphering the spatio-temporal complexity of climate change of the last deglaciation: a model analysis. *Climate of the Past*, 7(2):591–602.

Roy, R. N., Roy, L. N., Vogel, K. M., Porter-Moore, C., Pearson, T., Good, C. E., Millero, F. J., and Campbell, D. M. (1993). The dissociation constants of carbonic acid in seawater at salinities 5 to 45 and temperatures 0 to 45°C. *Marine Chemistry*, 44(2):249–267.

Rubino, M., Etheridge, D. M., Trudinger, C. M., Allison, C. E., Battle, M. O., Langenfelds, R. L., Steele, L. P., Curran, M., Bender, M., White, J. W. C., Jenk, T. M., Blunier, T., and Francey, R. J. (2013). A revised 1000 year atmospheric $\delta^{13}CO_2$ record from Law Dome and South Pole, Antarctica. *Journal of Geophysical Research: Atmospheres*, 118(15):8482–8499.

Rutberg, R. L., Hemming, S. R., and Goldstein, S. L. (2000). Reduced North Atlantic Deep Water flux to the glacial Southern Ocean inferred from neodymium isotope ratios. *Nature*, 405(6789):935–938.

Sabine, C. L., Feely, R. A., Gruber, N., Key, R. M., Lee, K., Bullister, J. L., Wanninkhof, R., Wong, C. S., Wallace, D. W. R., Tilbrook, B., Millero, F. J., Peng, T.-H., Kozyr, A., Ono, T., and Rios, A. F. (2004). The Oceanic Sink for Anthropogenic CO_2. *Science*, 305(5682):367–371.

Sackett, W. M., Eckelmann, W. R., Bender, M. L., and Bé, A. W. H. (1965). Temperature Dependence of Carbon Isotope Composition in Marine Plankton and Sediments. *Science*, 148(3667):235–237.

Saenko, O. A., Schmittner, A., and Weaver, A. J. (2004). The Atlantic–Pacific Seesaw. *Journal of Climate*, 17(11):2033–2038.

Sagoo, N., Valdes, P., Flecker, R., and Gregoire, L. J. (2013). The Early Eocene equable climate problem: can perturbations of climate model parameters identify possible solutions? *Philosophical Transactions. Series A, Mathematical, Physical, and Engineering Sciences*, 371(2001):20130123.

Sarmiento, J. and Gruber, N. (2006). *Ocean Biogeochemical Dynamics*. Princeton University Press.

Sarmiento, J. L. and Toggweiler, J. R. (1984). A new model for the role of the oceans in determining atmospheric pCO_2. *Nature*, 308(5960):621–624.

Sarnthein, M., Winn, K., Jung, S. J. A., Duplessy, J.-C., Labeyrie, L., Erlenkeuser, H., and Ganssen, G. (1994). Changes in East Atlantic Deepwater Circulation over the last 30,000 years: Eight time slice reconstructions. *Paleoceanography*, 9(2):209–267.

Schmittner, A. (2003). Southern Ocean sea ice and radiocarbon ages of glacial bottom waters. *Earth and Planetary Science Letters*, 213(1–2):53–62.

Schmittner, A. (2005). Decline of the marine ecosystem caused by a reduction in the Atlantic overturning circulation. *Nature*, 434(7033):628–633.

Schmittner, A., Brook, E. J., and Ahn, J. (2007). Impact of the ocean's Overturning circulation on atmospheric CO_2. In Schmittner, A., Chiang, J. C. H., and Hemming, S. R., editors, *Ocean Circulation: Mechanisms and Impacts—Past and Future Changes of Meridional Overturning*, pages 315–334. American Geophysical Union.

Schmittner, A., Gruber, N., Mix, A. C., Key, R. M., Tagliabue, A., and Westberry, T. K. (2013). Biology and air–sea gas exchange controls on the distribution of carbon isotope ratios (δ^{13}C) in the ocean. *Biogeosciences*, 10(9):5793–5816.

Scourse, J. D., Wanamaker, A. D., Weidman, C., Heinemeier, J., Reimer, P. J., Butler, P. G., Witbaard, R., and Richardson, C. A. (2012). The marine radiocarbon bomb pulse across the temperate north Atlantic: a compilation of δ^{14}C time histories from Arctica Islandica growth increments. *Radiocarbon*, 54(2):165–186.

Scripps Institute of Oceanography (1992a). *South Atlantic Ventilation Experiment (SAVE): Chemical, Physical, and CTD Data Reports, Legs 1-3. ODF publ 231, SIO refs 92-9*. Oceanographic Data Facility, University of California, San Diego.

Scripps Institute of Oceanography (1992b). *South Atlantic Ventilation Experiment (SAVE): Chemical, Physical, and CTD Data Reports, Legs 4-5. ODF publ 232, SIO refs 92-10*. Oceanographic Data Facility, University of California, San Diego.

Sepanski, R. J. (1991). Indian Ocean radiocarbon: Data from the INDIGO 1, 2, and 3 cruises. Technical Report ORNL/CDIAC-41; NDP-036, Oak Ridge National Lab., TN (USA).

Shackleton, N. J. (1977). Carbon 13 in Uvigerina: tropical rainforest history and the Equatorial Pacific carbonate dissolution cycles. *Marine science*.

Shaffer, G. and Bendtsen, J. (1994). Role of the Bering Strait in controlling North Atlantic ocean circulation and climate. *Nature*, 367(6461):354–357.

Shemesh, A., Macko, S. A., Charles, C. D., and Rau, G. H. (1993). Isotopic Evidence for Reduced Productivity in the Glacial Southern Ocean. *Science*, 262(5132):407–410.

Sherwood, O. A., Edinger, E. N., Guilderson, T. P., Ghaleb, B., Risk, M. J., and Scott, D. B. (2008). Late Holocene radiocarbon variability in Northwest Atlantic slope waters. *Earth and Planetary Science Letters*, 275(1-2):146–153.

Smeed, D. A., McCarthy, G. D., Cunningham, S. A., Frajka-Williams, E., Rayner, D., Johns, W. E., Meinen, C. S., Baringer, M. O., Moat, B. I., Duchez, A., and Bryden, H. L. (2014). Observed decline of the Atlantic meridional overturning circulation 2004-2012. *Ocean Science*, 10(1):29–38.

Smith, R. S. (2012). The FAMOUS climate model (versions XFXWB and XFHCC): description update to version XDBUA. *Geoscientific Model Development*, 5(1):269–276.

Smith, R. S., Dubois, C., and Marotzke, J. (2006). Global Climate and Ocean Circulation on an Aquaplanet Ocean–Atmosphere General Circulation Model. *Journal of Climate*, 19(18):4719–4737.

Smith, R. S. and Gregory, J. M. (2009). A study of the sensitivity of ocean overturning circulation and climate to freshwater input in different regions of the North Atlantic. *Geophysical Research Letters*, 36(15):L15701.

Smith, R. S. and Gregory, J. M. (2012). The last glacial cycle: transient simulations with an AOGCM. *Climate Dynamics*, 38(7-8):1545–1559.

Smith, R. S., Gregory, J. M., and Osprey, A. (2008a). A description of the FAMOUS (version XDBUA) climate model and control run. *Geoscientific Model Development*, 1(1):53–68.

Smith, R. S., Gregory, J. M., Thorpe, R., and Rodriguez, J. M. (2008b). Response of the MOC in a reverse world experiment. *EGU General Assembly, session CL26 poster; Ref. No.: EGU2008-A-06893*.

Spalding, M. D. and Brown, B. E. (2015). Warm-water coral reefs and climate change. *Science*, 350(6262):769–771.

Spero, H. and Lea, D. (2002). The Cause of Carbon Isotope Minimum Events on Glacial Terminations. *Science*, 296(5567):522–525.

Srokosz, M., Baringer, M., Bryden, H., Cunningham, S., Delworth, T., Lozier, S., Marotzke, J., and Sutton, R. (2012). Past, Present, and Future Changes in the Atlantic Meridional Overturning Circulation. *Bulletin of the American Meteorological Society*, 93(11):1663–1676.

Östlund, H. G. and Grall, C. (1987). *Transient tracers in the ocean: North and tropical Atlantic tritium and radiocarbon*. University of Miami, Rosenstiel School of Marine and Atmospheric Science.

Östlund, H. G., Stuiver, M., and Boden, T. A. (1988). *GEOSECS Atlantic, Pacific, Indian, and Mediterranean Radiocarbon Data*. Environmental Sciences Division, Oak Ridge National Laboratory.

Stuiver, M. and Polach, H. (1977). Discussion: Reporting of C-14 data. *Radiocarbon*, 19(3):355–363.

Stuiver, M., Quay, P. D., and Ostlund, H. G. (1983). Abyssal Water Carbon-14 Distribution and the Age of the World Oceans. *Science*, 219(4586):849–851.

Suess, H. E. (1955). Radiocarbon Concentration in Modern Wood. *Science*, 122(3166):415–417.

Suzuki, T., Ishii, M., Aoyama, M., Christian, J. R., Enyo, K., Kawano, T., Key, R. M., Kosugi, N., Kozyr, A., Miller, L., Murata, A., Nakano, T., Ono, T., Saino, T., Sasaki, K.-I., Sasano, D., Takatani, Y., Wakita, M., and Sabine, C. (2013). PACIFICA data synthesis project. Technical report, Carbon Dioxide Information Analysis Center, Oak Ridge National Laboratory, U.S. Department of Energy, Oak Ridge, Tennessee.

Sweeney, C., Gloor, E., Jacobson, A. R., Key, R. M., McKinley, G., Sarmiento, J. L., and Wanninkhof, R. (2007). Constraining global air-sea gas exchange for CO_2 with recent bomb ^{14}C measurements. *Global Biogeochemical Cycles*, 21(2).

Swingedouw, D., Braconnot, P., and Marti, O. (2006). Sensitivity of the Atlantic Meridional Overturning Circulation to the melting from northern glaciers in climate change experiments. *Geophysical Research Letters*, 33(7).

Tagliabue, A. and Bopp, L. (2008). Towards understanding global variability in ocean carbon-13. *Global Biogeochemical Cycles*, 22(1):GB1025.

Takahashi, T., Olafsson, J., Goddard, J. G., Chipman, D. W., and Sutherland, S. C. (1993). Seasonal variation of CO_2 and nutrients in the high-latitude surface oceans: A comparative study. *Global Biogeochemical Cycles*, 7(4):843–878.

Talley, L. D. (2007). *Hydrographic Atlas of the World Ocean Circulation Experiment (WOCE): Volume 2: Pacific Ocean*. WOCE International Project Office.

Talley, L. D. (2011). *Descriptive Physical Oceanography: An Introduction*. Academic Press.

Talley, L. D. (2013). *Hydrographic Atlas of the World Ocean Circulation Experiment (WOCE): Volume 4: Indian Ocean*. International WOCE Project Office.

Talley, L. D., Reid, J. L., and Robbins, P. E. (2003). Data-Based Meridional Overturning Streamfunctions for the Global Ocean. *Journal of Climate*, 16(19):3213–3226.

Tindall, J. C., Valdes, P. J., and Sime, L. C. (2009). Stable water isotopes in HadCM3: Isotopic signature of El Niño–Southern Oscillation and the tropical amount effect. *Journal of Geophysical Research: Atmospheres*, 114(D4).

Toggweiler, J. R., Dixon, K., and Bryan, K. (1989a). Simulations of radiocarbon in a coarse-resolution world ocean model: 1. Steady state prebomb distributions. *Journal of Geophysical Research: Oceans*, 94(C6):8217–8242.

Toggweiler, J. R., Dixon, K., and Bryan, K. (1989b). Simulations of radiocarbon in a coarse-resolution world ocean model: 2. Distributions of bomb-produced carbon 14. *Journal of Geophysical Research*, 94(C6):8243.

Tschumi, T., Joos, F., Gehlen, M., and Heinze, C. (2011). Deep ocean ventilation, carbon isotopes, marine sedimentation and the deglacial CO_2 rise. *Climate of the Past*, 7(3):771–800.

Turner, J. V. (1982). Kinetic fractionation of carbon-13 during calcium carbonate precipitation. *Geochimica et Cosmochimica Acta*, 46(7):1183–1191.

Valdes, P. J., Armstrong, E., Badger, M. P. S., Bradshaw, C. D., Bragg, F., Davies-Barnard, T., Day, J. J., Farnsworth, A., Hopcroft, P. O., Kennedy, A. T., Lord, N. S., Lunt, D. J., Marzocchi, A., Parry, L. M., Roberts, W. H. G., Stone, E. J., Tourte, G.

J. L., and Williams, J. H. T. (2017). The BRIDGE HadCM3 family of climate models: HadCM3@Bristol v1.0. *Geoscientific Model Development*, (10):3715–3743.

Valley, S., Lynch-Stieglitz, J., and Marchitto, T. M. (2017). Timing of Deglacial AMOC Variability From a High-Resolution Seawater Cadmium Reconstruction: Timing Deglacial Upper AMOC Variability. *Paleoceanography*, 32(11):1195–1203.

Volk, T. and Hoffert, M. I. (1985). Ocean Carbon Pumps: Analysis of Relative Strengths and Efficiencies in Ocean-Driven Atmospheric CO_2 Changes. In Sundquist, E. and Broecker, W., editors, *Geophysical Monograph Series*, pages 99–110. American Geophysical Union, Washington, D. C.

Wadley, M. R. and Bigg, G. R. (2002). Impact of flow through the Canadian Archipelago and Bering Strait on the North Atlantic and Arctic circulation: An ocean modelling study. *Quarterly Journal of the Royal Meteorological Society*, 128(585):2187–2203.

Wanninkhof, R. (1992). Relationship between wind speed and gas exchange over the ocean. *Journal of Geophysical Research: Oceans*, 97(C5):7373–7382.

Warren, B. A. (1983). Why is no deep water formed in the North Pacific? *Journal of Marine Research*, 41(2):327–347.

Weidman, C. R. (1995). Development and Application of the Mollusc Arctica Islandica as a Paleoceanographic Tool for the North Atlantic Ocean. unpublished PhD thesis, Massachusetts Institute of Technology/Woods Hole Oceanographic Institution, MT/WHOI 95–20.

Weidman, C. R. and Jones, G. A. (1993). A shell-derived time history of bomb ^{14}C on Georges Bank and its Labrador Sea implications. *Journal of Geophysical Research*, 98(C8):14577.

Williams, J. H. T., Smith, R. S., Valdes, P. J., Booth, B. B. B., and Osprey, A. (2013). Optimising the FAMOUS climate model: inclusion of global carbon cycling. *Geoscientific Model Development*, 6(1):141–160.

Williams, J. H. T., Totterdell, I. J., Halloran, P. R., and Valdes, P. J. (2014). Numerical simulations of oceanic oxygen cycling in the FAMOUS Earth-System model: FAMOUS-ES, version 1.0. *Geoscientific Model Development*, 7(4):1419–1431.

Williamson, D. B., Blaker, A. T., and Sinha, B. (2017). Tuning without over-tuning: parametric uncertainty quantification for the NEMO ocean model. *Geoscientific Model Development*, page 28.

Witbaard, R., Jenness, M., Van Der Borg, K., and Ganssen, G. (1994). Verification of annual growth increments in Arctica islandica L. from the North Sea by means of oxygen and carbon isotopes. *Netherlands Journal of Sea Research*, 33(1):91–101.

Wong, W. W. and Sackett, W. M. (1978). Fractionation of stable carbon isotopes by marine phytoplankton. *Geochimica et Cosmochimica Acta*, 42(12):1809–1815.

Yang, X., North, R., Romney, C., and Richards, P. G. (2003). Worldwide nuclear explosions. In *International Geophysics*, volume 81, pages 1595–1599. Elsevier.

Yeager, S. G., Shields, C. A., Large, W. G., and Hack, J. J. (2006). The Low-Resolution CCSM3. *Journal of Climate*, 19(11):2545–2566.

Yu, E.-F., Francois, R., and Bacon, M. P. (1996). Similar rates of modern and last-glacial ocean thermohaline circulation inferred from radiochemical data. *Nature*, 379(6567):689.

Zhang, J., Quay, P. D., and Wilbur, D. O. (1995). Carbon isotope fractionation during gas-water exchange and dissolution of CO_2. *Geochimica et Cosmochimica Acta*, 59(1):107–114.

Zhang, X., Lohmann, G., Knorr, G., and Xu, X. (2013). Different ocean states and transient characteristics in Last Glacial Maximum simulations and implications for deglaciation. *Climate of the Past*, 9(5):2319–2333.

Ziveri, P., Stoll, H., Probert, I., Klaas, C., Geisen, M., Ganssen, G., and Young, J. (2003). Stable isotope ‘vital effects’ in coccolith calcite. *Earth and Planetary Science Letters*, 210(1):137–149.

Zweng, M., Reagan, J., Antonov, J., Locarnini, R., Mishonov, A., Boyer, T., Garcia, H., Baranova, O., Johnson, D., Seidov, D., and Biddle, M. (2013). *World Ocean Atlas 2013, Volume 2: Salinity.* S. Levitus, Ed., A. Mishonov Technical Ed.; NOAA Atlas NESDIS 74.

APPENDIX A

Additional figures for Chapter 2

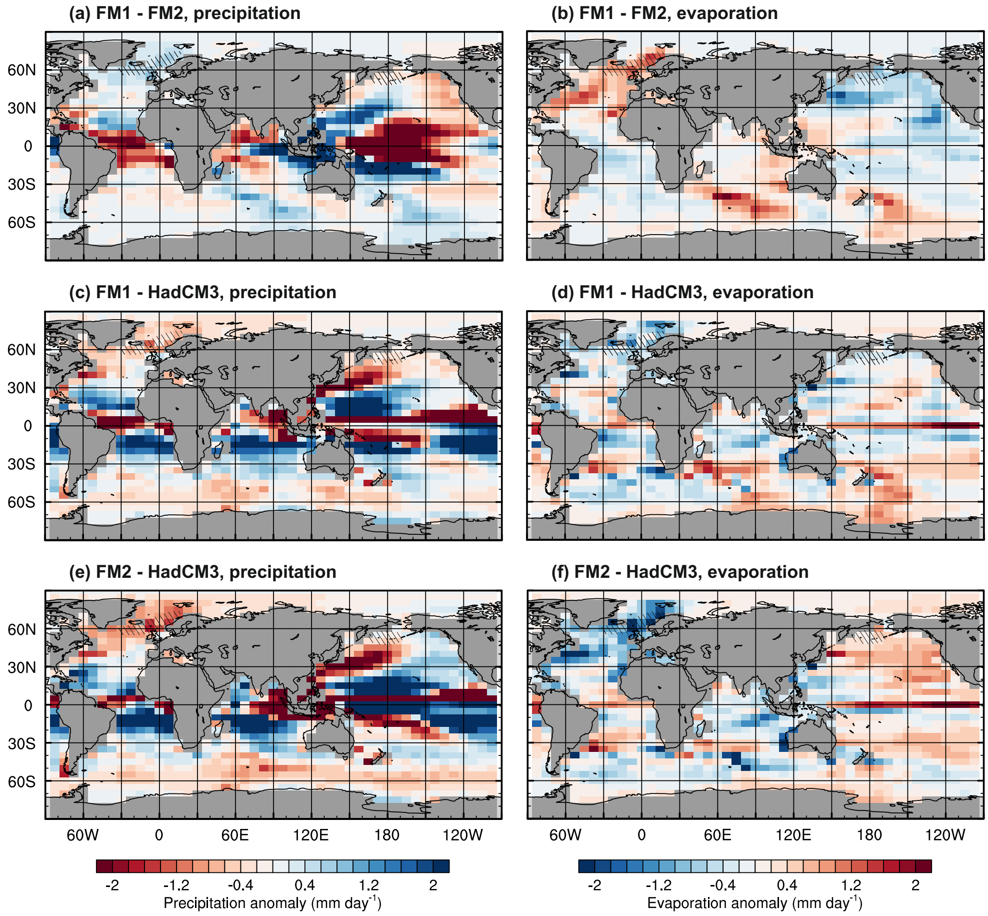

Figure A.1: Difference in precipitation (left) and evaporation (right): (a, b) FM1 minus FM2, (c, d) FM1 minus HadCM3, and (e, f) FM2 minus HadCM3. FAMOUS data are the annual climate means calculated from the final 100 years of the simulations. HadCM3 data are the 240 year annual climatology. Hatched areas show the approximate location of the simulated Northern Hemisphere deep water formation regions, which are in good agreement with observed deep and intermediate water formation regions in the Nordic Seas and North Pacific Ocean, respectively. Note that FAMOUS does not simulate deep water formation in the Labrador Sea.

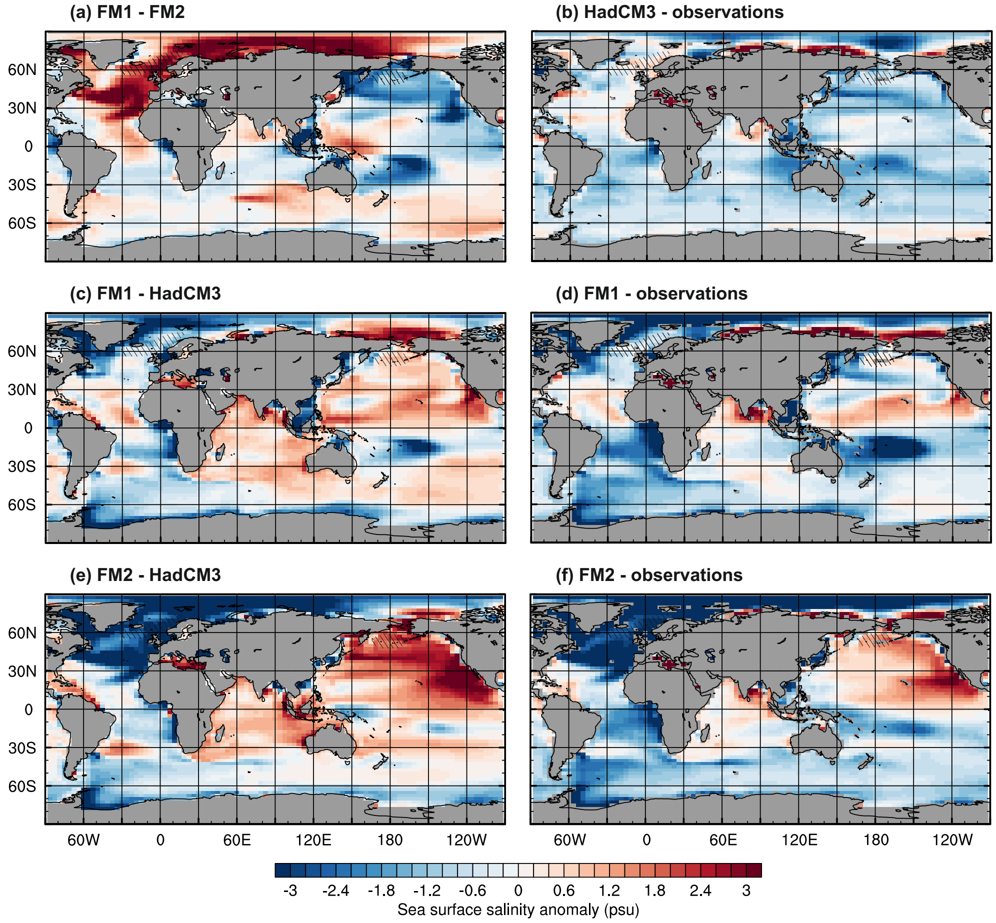

Figure A.2: Difference in sea surface salinity: (a) FM1 minus FM2, (b) HadCM3 minus observations, (c) FM1 minus HadCM3, (d) FM1 minus observations, (e) FM2 minus HadCM3, and (f) FM2 minus observations. FAMOUS data are the annual climate means calculated from the final 100 years of the simulations. HadCM3 data are the 240 year annual climatology. Observations are the 1955 to 2012 surface climatology from the World Ocean Atlas 2013 version 2 (Zweng et al., 2013). Hatched areas show the approximate location of the simulated Northern Hemisphere deep water formation regions.

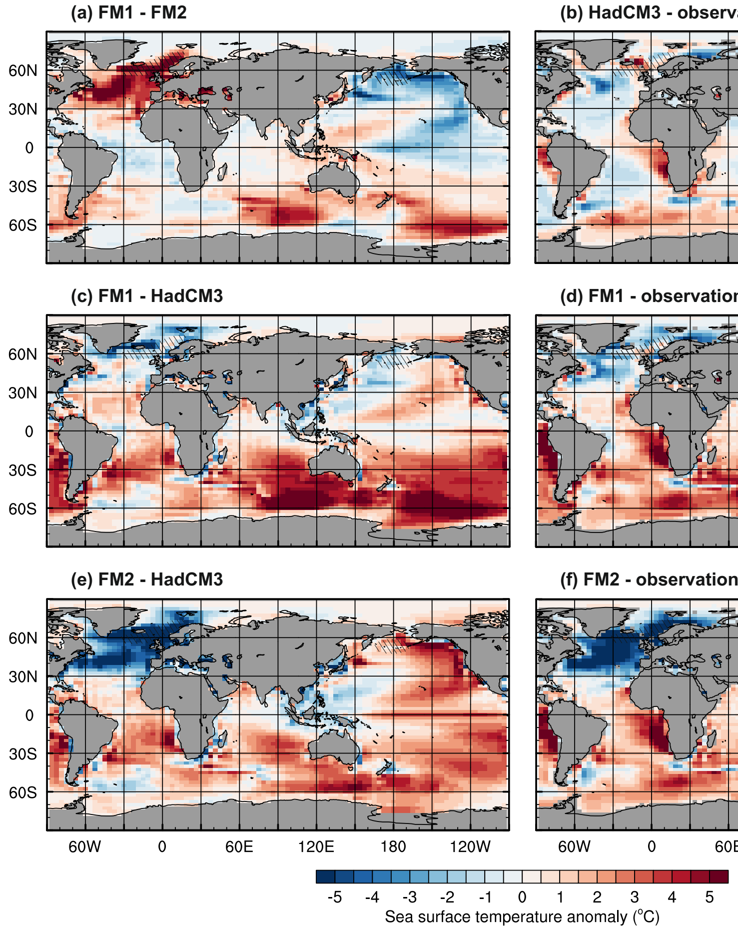

Figure A.3: As for Figure A.2, but for sea surface temperature. Observations are the 1955 to 2012 surface climatology from the World Ocean Atlas 2013 version 2 (Locarnini et al., 2013).

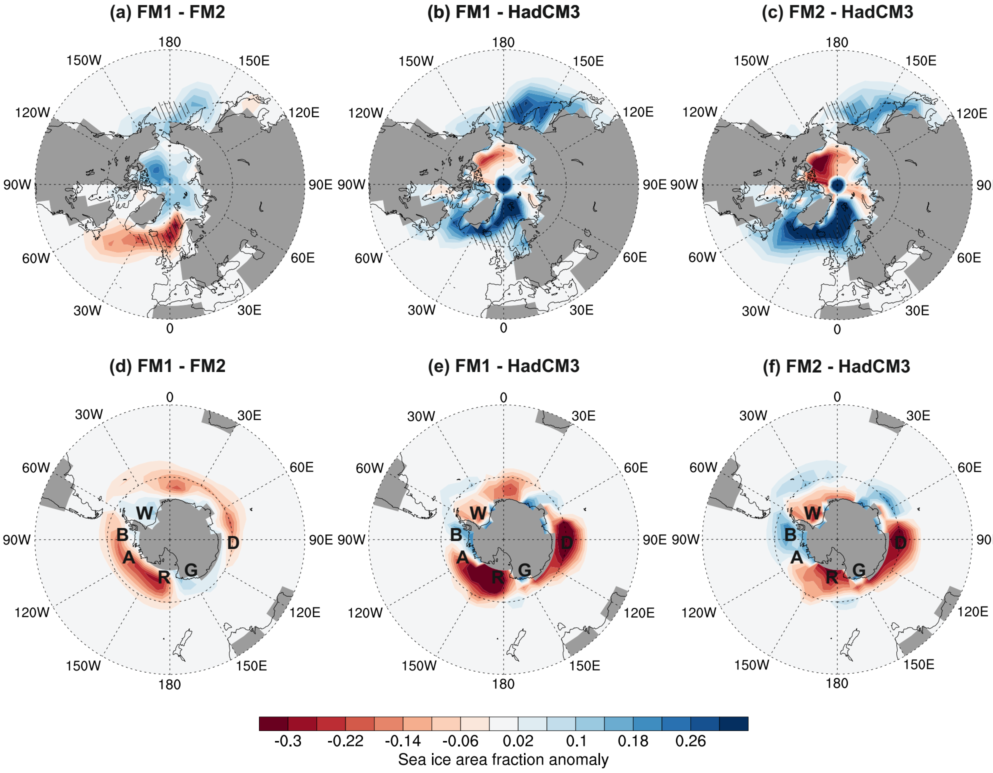

Figure A.4: Difference in sea ice area fraction in the Northern Hemisphere (a – c) and the Southern Hemisphere (d – f). FAMOUS data are the annual climate means calculated from the final 100 years of the simulations. HadCM3 data are the 240 year annual climatology. Hatched areas show the approximate location of the simulated Northern Hemisphere deep water formation regions. Text markers denote the location of the Amundsen Sea (A), the Bellingshausen Sea (B), the Davis Sea (D), George V Land (G), the Ross Sea (R), and the Weddell Sea (W).

APPENDIX B

Equations for Chapter 3

B.1 Virtual fluxes

The standard equation for calculating the virtual flux to account for the dilution or concentration effect of surface freshwater fluxes is:

$$\frac{d^{12}C}{dt} = {}^{12}C \times \frac{E - P}{dz} \tag{B.1}$$

where E is evaporation, P is precipitation, and dz is layer depth.

As we carry ^{13}C as a ratio (DI^{13}C/DI^{12}C), virtual fluxes are not required:

$$\frac{d\left(\frac{^{13}C}{^{12}C}\right)}{dt} = \frac{^{12}C \times \frac{d^{13}C}{dt} -^{13} C \times \frac{d^{12}C}{dt}}{(^{12}C)^2} \tag{B.2}$$

$$\frac{d\left(\frac{^{13}C}{^{12}C}\right)}{dt} = \frac{1}{^{12}C} \times \left[{}^{13}C \times \frac{(E - P)}{dz}\right] - \frac{^{13}C}{(^{12}C)^2} \times \left[{}^{12}C \times \frac{(E - P)}{dz}\right] \tag{B.3}$$

$$\frac{d\left(\frac{^{13}C}{^{12}C}\right)}{dt} = 0 \tag{B.4}$$

B.2 Air-sea gas exchange equations

The standard equation for calculating the change in DI^{13}C due to air-sea gas exchange is:

$$\frac{d^{13}C}{dt} = \alpha_{\mathrm{k}} \times \alpha_{\mathrm{aq}\leftarrow\mathrm{g}} \times PV \times \left(C_{\mathrm{sat}} \times \frac{^{13}A}{^{12}A} - \frac{C_{\mathrm{surf}} \times \frac{^{13}C}{^{12}C}}{\alpha_{\mathrm{DIC}\leftarrow\mathrm{g}}} \right) \tag{B.5}$$

where PV is the piston velocity in cm h^{-1} (Eq. (3.3)), C_{sat} is the saturation concentration of atmospheric CO$_2$ (in mol m^{-3}), C_{surf} is the surface aqueous CO$_2$ concentration (in mol m^{-3}), α_{k} is the constant kinetic fractionation factor, $\alpha_{\mathrm{aq}\leftarrow\mathrm{g}}$ is the temperature-dependent fractionation during gas dissolution (Eq. (3.6)), $\alpha_{\mathrm{DIC}\leftarrow\mathrm{g}}$ is the is the temperature-dependent fractionation between aqueous CO$_2$ and DIC (Eq. (3.7)), and $^{13}A/^{12}A$ and $^{13}C/^{12}C$ are the ^{13}C/^{12}C ratios of the atmosphere and DIC, respectively.

The equation for calculating the change in DI^{13}C/DI^{12}C due to air-sea gas exchange is:

$$\frac{d\left(\frac{^{13}C}{^{12}C}\right)}{dt} = \frac{^{12}C \times \frac{d^{13}C}{dt} -^{13} C \times \frac{d^{12}C}{dt}}{(^{12}C)^2} \tag{B.6}$$

$$\begin{aligned} \frac{d\left(\frac{^{13}C}{^{12}C}\right)}{dt} = \frac{1}{^{12}C} \times \left[\alpha_{\mathrm{k}} \times \alpha_{\mathrm{aq}\leftarrow\mathrm{g}} \times PV \times \left(C_{\mathrm{sat}} \times \frac{^{13}A}{^{12}A} - \frac{C_{\mathrm{surf}} \times \frac{^{13}C}{^{12}C}}{\alpha_{\mathrm{DIC}\leftarrow\mathrm{g}}} \right) \right] \\ - \frac{^{13}C}{\left(^{12}C\right)^2} \times \left[PV \times \left(C_{\mathrm{sat}} - C_{\mathrm{surf}} \right) \right] \end{aligned} \tag{B.7}$$

$$\begin{aligned} \frac{d\left(\frac{^{13}C}{^{12}C}\right)}{dt} = \frac{1}{^{12}C} \times PV \times \left[\alpha_{\mathrm{k}} \times \alpha_{\mathrm{aq}\leftarrow\mathrm{g}} \times \left(C_{\mathrm{sat}} \times \frac{^{13}A}{^{12}A} - \frac{C_{\mathrm{surf}} - \frac{^{13}C}{^{12}C}}{\alpha_{\mathrm{DIC}\leftarrow\mathrm{g}}} \right) \right. \\ \left. - \left(\frac{^{13}C}{^{12}C} \times \left[C_{\mathrm{sat}} - C_{\mathrm{surf}} \right] \right) \right] \end{aligned} \tag{B.8}$$

B.3 Biological equations

For consistency with the standard biological tracers, the ^{13}C contents of phytoplankton (^{13}P), zooplankton (^{13}Z) and detritus (^{13}D) are expressed in mmol-N m^{-3}. The DI^{13}C/DI^{12}C values are therefore converted from a ratio in model units (Eq. (3.1)) to normalised DI^{13}C concentrations before entering the soft tissue pump. The conversion is reversed at the end of each timestep.

B.3.1 Phytoplankton (P)

The standard equation for calculating the change in phytoplankton (^{12}P) is:

$$\frac{dP}{dt} = R_{\mathrm{P}} - G_{\mathrm{P}} - m_{\mathrm{P}} - \eta_{\mathrm{P}} \tag{B.9}$$

where R_{P} is the specific growth rate of phytoplankton, G_{P} represents grazing by zooplankton, m_{P} represents phytoplankton mortality due to overpopulation, and η_{P} represents phytoplankton respiration.

The equation for calculating the change in ^{13}P is:

$$\frac{d^{13}P}{dt} = R_{\mathrm{P}} \times \frac{^{13}C}{^{12}C} \times \alpha_{\mathrm{p}} - G_{\mathrm{P}} \times \frac{^{13}P}{^{12}P} - m_{\mathrm{P}} \times \frac{^{13}P}{^{12}P} - \eta_{\mathrm{P}} \times \frac{^{13}P}{^{12}P} \tag{B.10}$$

where α_{p} is the isotopic fractionation that occurs during photosynthesis (Eq. (3.8)), $^{13}C/^{12}C$ is the ^{13}C/^{12}C of DIC, and $^{13}P/^{12}P$ is the ^{13}C/^{12}C of phytoplankton.

The ^{13}P tracer is updated using the forward Euler method:

$$\begin{aligned} ^{13}P_{(t+\Delta t)} = {}^{13}P_{(t)} + \Delta t \times \Bigg(& R_{\mathrm{P}(t)} \times \frac{^{13}C}{^{12}C}_{(t)} \times \alpha_{\mathrm{p}(t)} - G_{\mathrm{P}(t)} \times \frac{^{13}P}{^{12}P}_{(t)} \\ & - m_{\mathrm{P}(t)} \times \frac{^{13}P}{^{12}P}_{(t)} - \eta_{\mathrm{P}(t)} \times \frac{^{13}P}{^{12}P}_{(t)} \Bigg) \end{aligned} \tag{B.11}$$

B.3.2 Zooplankton (Z)

The standard equation for calculating the change in zooplankton (^{12}Z) is:

$$\frac{dZ}{dt} = \beta_{\mathrm{P}} \times G_{\mathrm{P}} - \beta_{\mathrm{D}} \times G_{\mathrm{D}} - m_{\mathrm{Z}} \tag{B.12}$$

where β_{P} and β_{D} are the assimilation efficiencies associated with zooplankton grazing on phytoplankton (G_{P}) and detritus (G_{D}), respectively, and m_{Z} represents the zooplankton mortality due to predation and natural causes.

The equation for calculating the change in ^{13}Z is:

$$\frac{d^{13}Z}{dt} = \beta_{\mathrm{P}} \times G_{\mathrm{P}} \times \frac{^{13}P}{^{12}P} - \beta_{\mathrm{D}} \times G_{\mathrm{D}} \times \frac{^{13}D}{^{12}D} - m_{\mathrm{Z}} \times \frac{^{13}Z}{^{12}Z} \tag{B.13}$$

where $^{13}P/^{12}P$, $^{13}D/^{12}D$ and $^{13}Z/^{12}Z$ are the isotopic ratios of phytoplankton, detritus and zooplankton, respectively.

The ^{13}Z tracer is updated using the forward Euler method:

$$\begin{aligned} {}^{13}Z_{(t+\Delta t)} = {}^{13}Z_{(t)} + \Delta t \times \Bigg(& \beta_{\mathrm{P}(t)} \times G_{\mathrm{P}(t)} \times \frac{^{13}P}{^{12}P}_{(t)} + \beta_{\mathrm{D}(t)} \times G_{\mathrm{D}(t)} \times \frac{^{13}D}{^{12}D}_{(t)} \\ & - m_{\mathrm{Z}(t)} \times \frac{^{13}Z}{^{12}Z}_{(t)} \Bigg) \end{aligned} \tag{B.14}$$

B.3.3 Dissolved inorganic carbon (DIC, C)

The standard equation for calculating the change in DI^{12}C is:

$$\frac{dC}{dt} = -R_\mathrm{P} + \lambda_\mathrm{D} + (1 - \beta_\mathrm{P}) \times G_\mathrm{P} + (1 - \beta_\mathrm{D}) \times G_\mathrm{D} + m_\mathrm{Z} + m_\mathrm{P} + \eta_\mathrm{P} \tag{B.15}$$

where R_P is the specific growth rate of phytoplankton λ_D is detrital remineralisation, which is specified at a constant rate (0.1 d^{-1} in the uppermost 250 m of the ocean and 0.02 d^{-1} at all other depths), β_P and β_D are the assimilation efficiencies associated with zooplankton grazing on phytoplankton (G_P) and detritus (G_D), respectively, m_Z represents zooplankton mortality due to predation and natural causes, m_P represents phytoplankton mortality due to overpopulation, and η_P represents phytoplankton respiration.

The standard equation for calculating the change in DI^{13}C is:

$$\begin{aligned}\frac{d^{13}C}{dt} = &-R_\mathrm{P} \times \frac{^{13}C}{^{12}C} \times \alpha_\mathrm{p} + \lambda_\mathrm{D} \times \frac{^{13}D}{^{12}D} + (1 - \beta_\mathrm{P}) \times G_\mathrm{P} \times \frac{^{13}P}{^{12}P} \\ &+ (1 - \beta_\mathrm{D}) \times G_\mathrm{D} \times \frac{^{13}D}{^{12}D} + m_\mathrm{Z} \times \frac{^{13}Z}{^{12}Z} + m_\mathrm{P} \times \frac{^{13}P}{^{12}P} + \eta_\mathrm{P} \times \frac{^{13}P}{^{12}P}\end{aligned} \tag{B.16}$$

where α_p is the isotopic fractionation that occurs during photosynthesis (Eq. (3.8)) and $^{13}C/^{12}C$, $^{13}D/^{12}D$, $^{13}P/^{12}P$ and $^{13}Z/^{12}Z$ are the isotopic ratios of DIC, detritus, phytoplankton and zooplankton, respectively.

The DI^{13}C tracer is updated using the forward Euler method:

$$\begin{aligned}{}^{13}C_{(t+\Delta t)} = {}^{13}C_{(t)} + \Delta t \times \Bigg(&-R_{\mathrm{P}(t)} \times \frac{^{13}C}{^{12}C}_{(t)} \times \alpha_{\mathrm{p}(t)} + \lambda_{\mathrm{D}(t)} \times \frac{^{13}D}{^{12}D}_{(t)} \\ &+ (1 - \beta_\mathrm{P}) \times G_{\mathrm{P}(t)} \times \frac{^{13}P}{^{12}P}_{(t)} + (1 - \beta_\mathrm{D}) \times G_{\mathrm{D}(t)} \times \frac{^{13}D}{^{12}D}_{(t)} \\ &+ m_{\mathrm{Z}(t)} \times \frac{^{13}Z}{^{12}Z}_{(t)} + m_{\mathrm{P}(t)} \times \frac{^{13}P}{^{12}P}_{(t)} + \eta_{\mathrm{P}(t)} \times \frac{^{13}P}{^{12}P}_{(t)} \Bigg)\end{aligned} \tag{B.17}$$

B.3.4 Detritus (D)

Unlike the other biological tracers, the standard detritus tracer (^{12}D) is updated using a semi-implicit scheme:

$$\frac{D_{(t+\Delta t,k)} - D_{(t,k)}}{\Delta t} = \frac{dD}{dt}_{\text{bio}_{(t,k)}} + \frac{dD}{dt}_{\text{sink in}_{(t+\Delta t,k-1)}} - \frac{dD}{dt}_{\text{sink out}_{(t+\Delta t,k)}} \tag{B.18}$$

$$\begin{aligned} D_{(t+\Delta t,k)} - D_{(t,k)} = {} & \Delta t \times D_{\text{bio}(t,k)} + \Delta t \times \frac{\gamma}{dz/100} \times D_{(t+\Delta t,k-1)} \\ & - \Delta t \times \frac{\gamma}{dz/100} \times D_{(t+\Delta t,k)} \end{aligned} \tag{B.19}$$

$$\begin{aligned} D_{(t+\Delta t,k)} + \Delta t \times \frac{\gamma}{dz/100} \times D_{(t+\Delta t,k)} = {} & D_{(t,k)} + \Delta t \times D_{\text{bio}(t,k)} \\ & + \Delta t \times \frac{\gamma}{dz/100} \times D_{(t+\Delta t,k-1)} \end{aligned} \tag{B.20}$$

$$\begin{aligned} D_{(t+\Delta t,k)} \times \left(1 + \Delta t \times \frac{\gamma}{dz/100}\right) = {} & D_{(t,k)} + \Delta t \times D_{\text{bio}(t,k)} \\ & + \Delta t \times \frac{\gamma}{dz/100} \times D_{(t+\Delta t,k-1)} \end{aligned} \tag{B.21}$$

$$D_{(t+\Delta t,k)} = \frac{D_{(t,k)} + \Delta t \times D_{\text{bio}(t,k)} + \Delta t \times \frac{\gamma}{dz/100} \times D_{(t+\Delta t,k-1)}}{1 + \Delta t \times \frac{\gamma}{dz/100}} \tag{B.22}$$

$$D_{(t+\Delta t,k)} = D_{(t,k)} + \frac{dD}{dt}_{(t,k)} \tag{B.23}$$

$$\frac{dD}{dt}_{(t,k)} = D_{(t+\Delta t,k)} - D_{(t,k)} \tag{B.24}$$

$$\frac{dD}{dt}_{(t,k)} = \frac{D_{(t,k)} + \Delta t \times D_{\text{bio}(t,k)} + \Delta t \times \frac{\gamma}{dz/100} \times D_{(t+\Delta t,k-1)}}{1 + \Delta t \times \frac{\gamma}{dz/100}} - D_{(t,k)} \tag{B.25}$$

where t is the current timestep, k is the model level, ${}^{dD}/{}_{dt_{\text{bio}}}$ is the change in detritus due to biological effects (Eq. (B.27)), γ is the sinking rate, which is parameterised at $10\,\text{m}\,\text{d}^{-1}$, dz is the depth of the layer (in cm), and D is the detritus concentration.

Following the same principles, the ^{13}D tracer is updated using:

$$\frac{d^{13}D}{dt}_{(t,k)} = \frac{{}^{13}D_{(t,k)} + \Delta t \times {}^{13}D_{\text{bio}(t,k)} + \Delta t \times \frac{\gamma}{dz/100} \times {}^{13}D_{(t+\Delta t,k-1)}}{1 + \Delta t \times \frac{\gamma}{dz/100}} - {}^{13}D_{(t,k)} \tag{B.26}$$

B.3.4.1 Biological effects

The standard equation for calculating the change in detritus (^{12}D) due to biology is:

$$\frac{dD}{dt}_{\text{bio}} = m_{\mathrm{Z}} + m_{\mathrm{P}} - \lambda_{\mathrm{D}} - G_{\mathrm{D}} - (1 - \beta_{\mathrm{D}}) \times G_{\mathrm{D}} - (1 - \beta_{\mathrm{P}}) \times G_{\mathrm{P}} \tag{B.27}$$

where m_{Z} represents zooplankton mortality due to predation and natural causes, m_{P} represents phytoplankton mortality due to overpopulation, λ_{D} is detrital remineralisation, which is specified at a constant rate (0.1 d^{-1} in the uppermost 250 m of the ocean and 0.02 d^{-1} at all other depths), and β_{P} and β_{D} are the assimilation efficiencies associated with zooplankton grazing on phytoplankton (G_{P}) and detritus (G_{D}), respectively.

The equation for calculating the change in detritus (^{13}D) due to biology is:

$$\begin{aligned} \frac{d^{13}D}{dt}_{bio} = {} & m_{\mathrm{Z}} \times \frac{^{13}Z}{^{12}Z} + m_{\mathrm{P}} \times \frac{^{13}P}{^{12}P} - \lambda_{\mathrm{D}} \times \frac{^{13}D}{^{12}D} - G_{\mathrm{D}} \times \frac{^{13}D}{^{12}D} \\ & - G_{\mathrm{D}} \times \frac{^{13}D}{^{12}D} \times (1 - \beta_{\mathrm{D}}) - (1 - \beta_{\mathrm{P}}) \times G_{\mathrm{P}} \times \frac{^{13}P}{^{12}P} \end{aligned} \tag{B.28}$$

where $^{13}Z/^{12}Z$, $^{13}P/^{12}P$ and $^{13}D/^{12}D$ are the isotopic ratios of zooplankton, phytoplankton, and detritus, respectively.

B.3.4.2 Reflux

The small amount of detritus that reaches the ocean floor is immediately refluxed back to the surface layer to conserve nitrogen and carbon:

$$\frac{dD}{dt}_{\text{sink in}(k=1)} = \frac{\gamma}{dz/100} \times D_{(k=KMT)} \tag{B.29}$$

where k is the model level, γ is the sinking rate, which is parameterised at 10 m d^{-1}, dz is the depth of the layer (in cm), D is the detritus concentration, and KMT is the maximum depth of the ocean. The same equation applies for ^{13}D.

APPENDIX C

Additional figures for Chapter 3

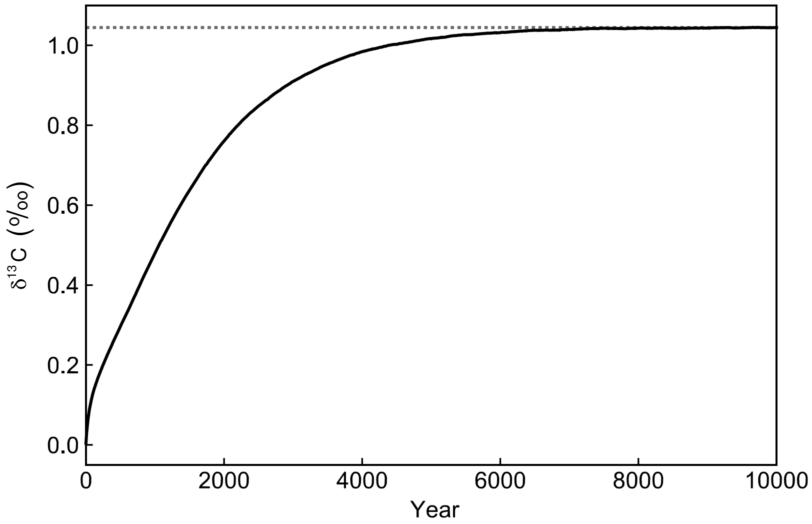

Figure C.1: Global volume-weighted $\delta^{13}C_{DIC}$ integral for the *std* spin-up simulation. The solid line shows the transient isotopic ratio and the dashed line shows the value at equilibrium.

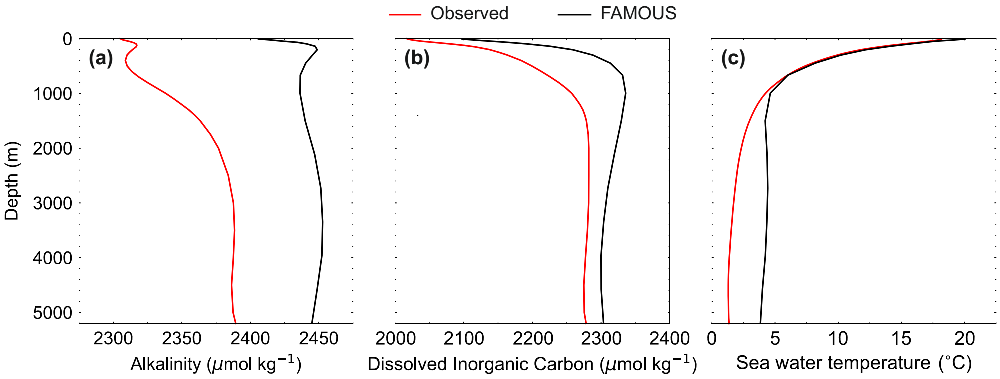

Figure C.2: Depth profiles of globally averaged mean annual (a) alkalinity, (b) DIC, and (c) temperature. The values in the *std* simulation (black) are compared to observed values (red) from GLODAP (Key et al., 2004) and the World Ocean Atlas (Locarnini et al., 2013).

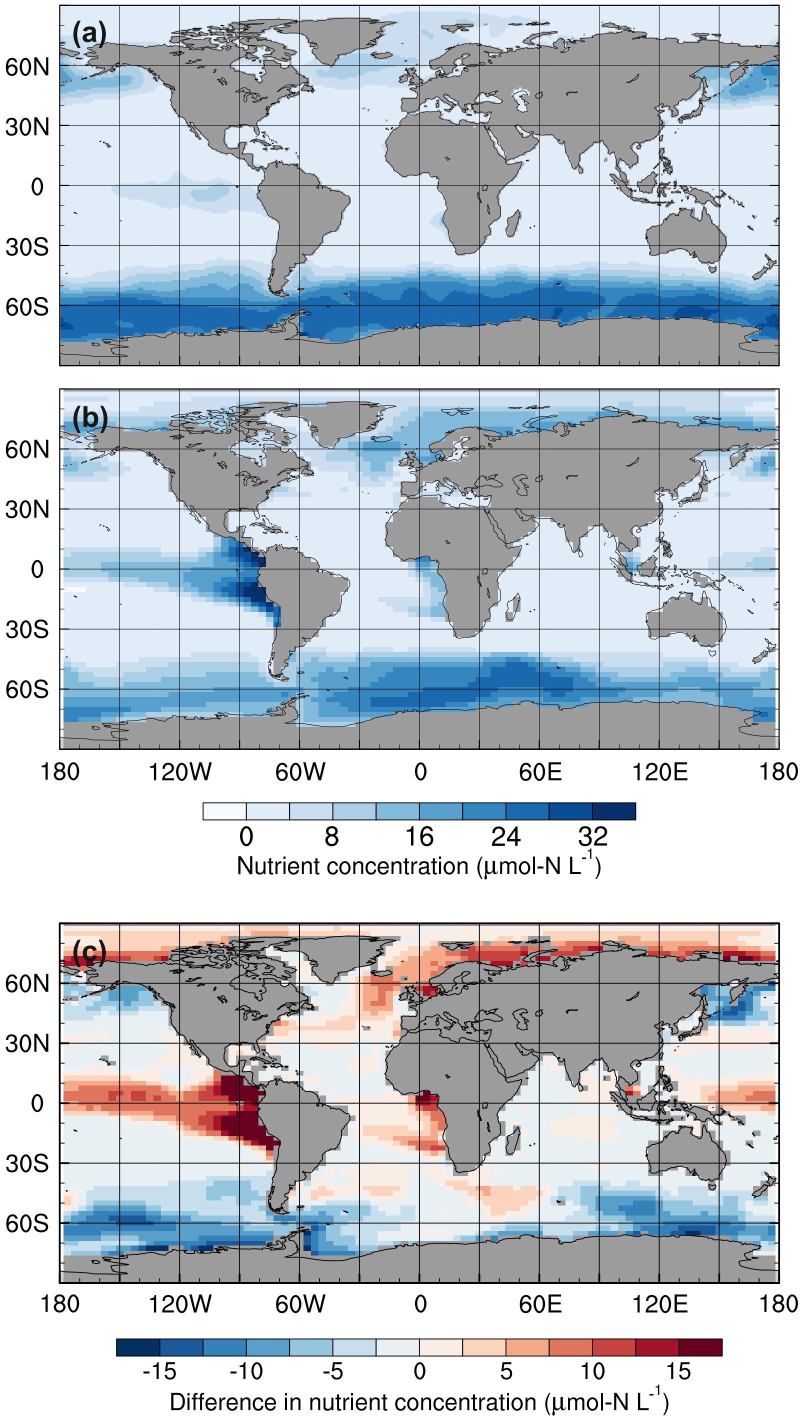

Figure C.3: Mean annual surface nutrient concentrations: (a) World Ocean Atlas observations (Garcia et al., 2014), (b) the *std* simulation in the 1990s, and (c) simulated minus observed.

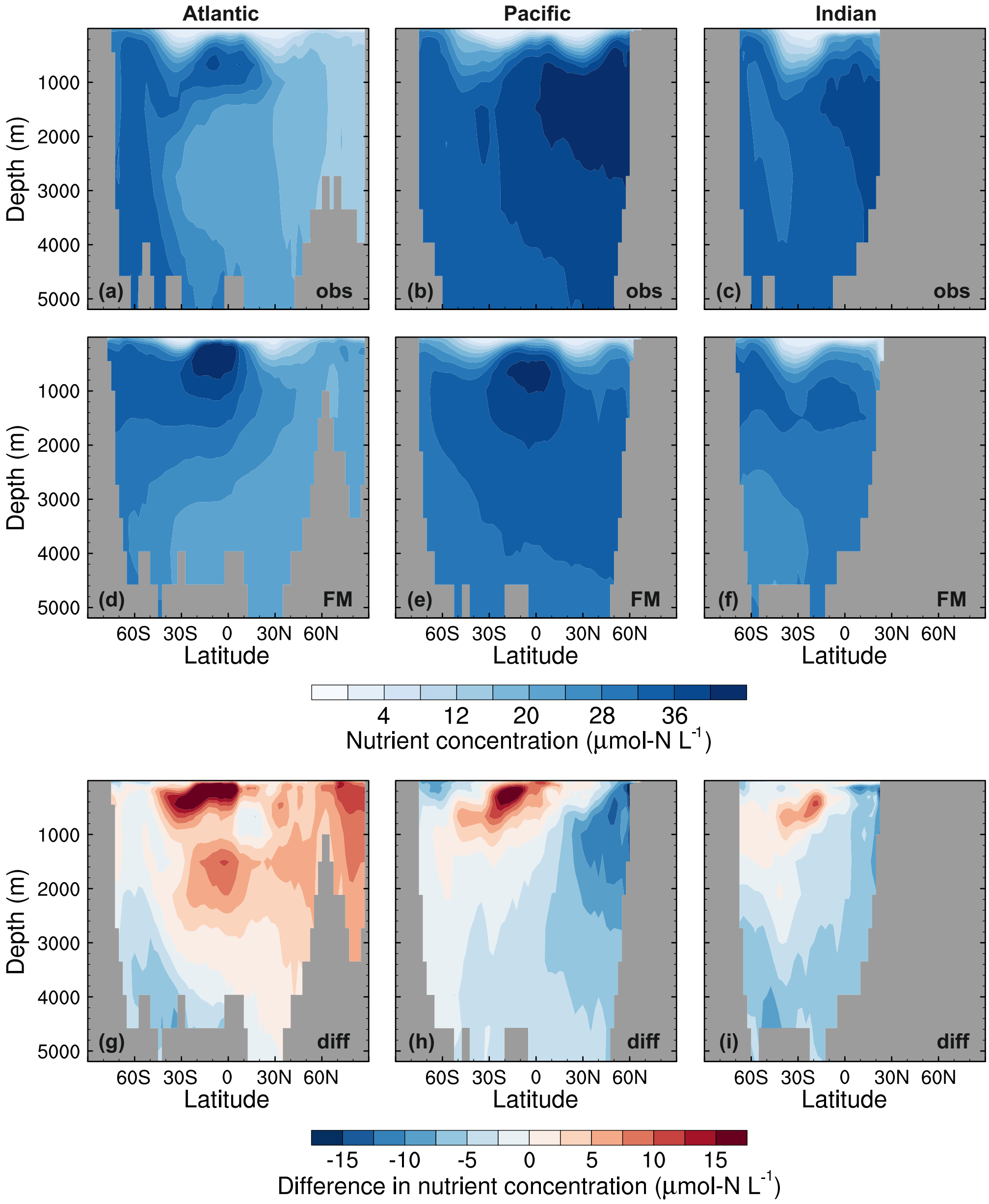

Figure C.4: Zonal mean annual nutrient concentrations in the Atlantic Ocean (left), Pacific Ocean (centre) and Indian Ocean (right): the World Ocean Atlas observations (Garcia et al., 2014, top), the *std* simulation in the 1990s (middle), and simulated minus observed (bottom).

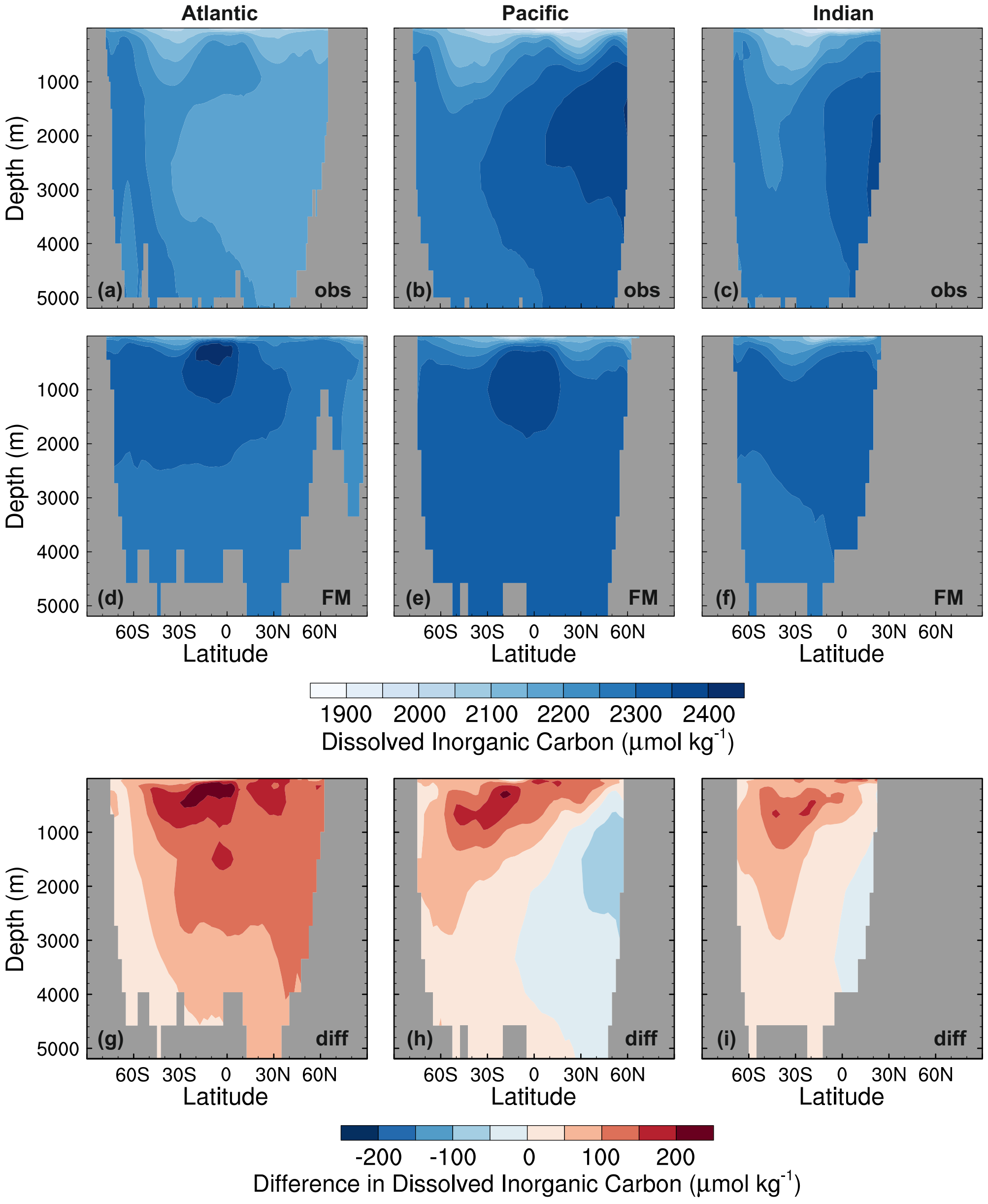

Figure C.5: Zonal mean DIC concentrations in the Atlantic Ocean (left), Pacific Ocean (centre) and Indian Ocean (right): the GLODAP observations (Key et al., 2004, top), the *std* simulation in the 1990s (middle), and simulated minus observed (bottom).

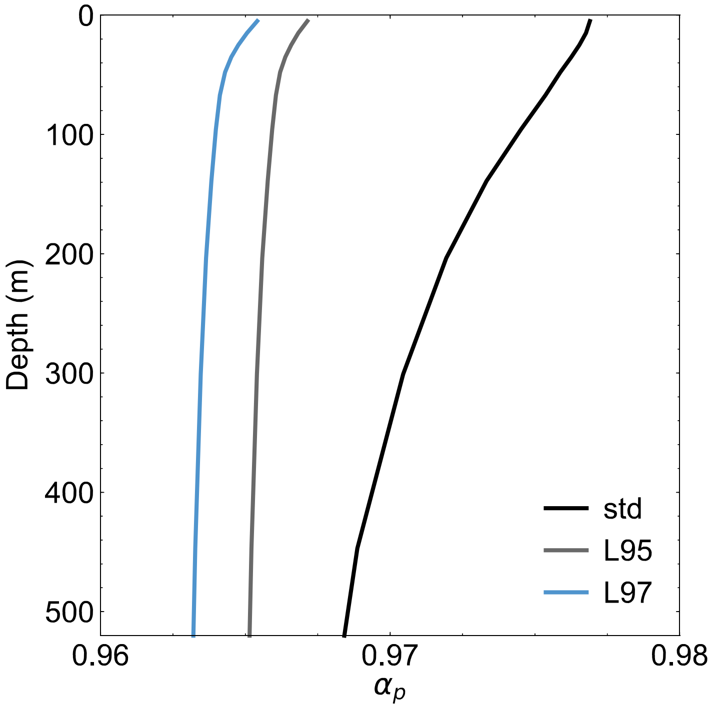

Figure C.6: Depth profiles of globally averaged isotopic fractionation during photosynthesis (α_p) at the end of the spin-up simulations (years 9900 to 10,000): (a) the *std* simulation (black), (b) the *L95* simulation (grey), and (c) the *L97* simulation (blue).

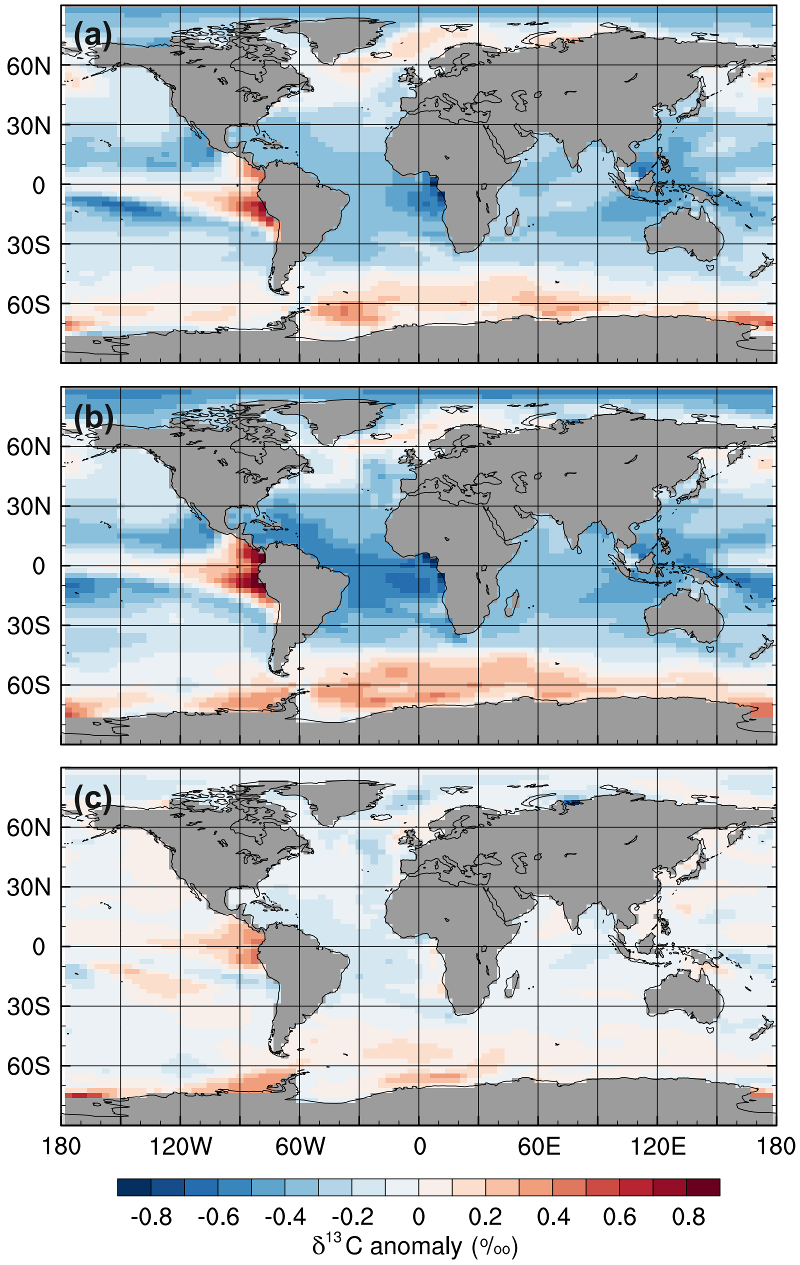

Figure C.7: Differences between the simulated surface ocean $\delta^{13}C_{DIC}$ values in the 1990s: (a) *std* minus *L95*, (b) *std* minus *L97*, and (c) *L95* minus *L97*.

APPENDIX D

Equations for Chapter 4

D.1 Air-sea gas exchange of abiotic ^{14}C

The standard equation for calculating the change in abiotic DI^{14}C due to air-sea gas exchange is:

$$\frac{d^{14}C}{dt} = PV \times \left(C_{\mathrm{sat}} \times \frac{^{14}A}{^{12}A} - C_{\mathrm{surf}} \times \frac{^{14}C}{^{12}C}\right) \tag{D.1}$$

where PV is the piston velocity in cm h^{-1} (Eq. (4.4)), C_{sat} is the saturation concentration of atmospheric CO$_2$ (in mol m^{-3}), C_{surf} is the surface aqueous CO$_2$ concentration (in mol m^{-3}), and $^{14}A/^{12}A$ and $^{14}C/^{12}C$ are the ^{14}C/^{12}C ratios of the atmosphere and DIC, respectively.

The equation for calculating the change in abiotic DI^{14}C/DI^{12}C due to air-sea gas exchange is:

$$\frac{d\left(\frac{^{14}C}{^{12}C}\right)}{dt} = \frac{^{12}C \times \frac{d^{14}C}{dt} - ^{14}C \times \frac{d^{12}C}{dt}}{(^{12}C)^2} \tag{D.2}$$

$$\begin{aligned}\frac{d\left(\frac{^{14}C}{^{12}C}\right)}{dt} &= \frac{1}{^{12}C} \times \left[PV \times \left(C_{\mathrm{sat}} \times \frac{^{14}A}{^{12}A} - C_{\mathrm{surf}} \times \frac{^{14}C}{^{12}C}\right)\right] \\ &\quad - \frac{^{14}C}{\left(^{12}C\right)^2} \times \left[PV \times (C_{\mathrm{sat}} - C_{\mathrm{surf}})\right]\end{aligned} \tag{D.3}$$

$$\begin{aligned}\frac{d\left(\frac{^{14}C}{^{12}C}\right)}{dt} &= \frac{1}{^{12}C} \times PV \times \left[\left(C_{\mathrm{sat}} \times \frac{^{14}A}{^{12}A} - C_{\mathrm{surf}} \times \frac{^{14}C}{^{12}C}\right)\right. \\ &\quad \left. - \left(C_{\mathrm{surf}} \times \frac{^{14}C}{^{12}C} - C_{\mathrm{surf}} \times \frac{^{14}C}{^{12}C}\right)\right]\end{aligned} \tag{D.4}$$

$$\frac{d\left(\frac{^{14}C}{^{12}C}\right)}{dt} = \frac{1}{^{12}C} \times PV \times C_{\mathrm{sat}} \times \left(\frac{^{14}A}{^{12}A} - \frac{^{14}C}{^{12}C}\right) \tag{D.5}$$

D.2 Air-sea gas exchange of biotic ^{14}C

The standard equation for calculating the change in biotic DI^{14}C due to air-sea gas exchange is:

$$\frac{d^{14}C}{dt} = \alpha_{\mathrm{k}} \times \alpha_{\mathrm{aq}\leftarrow\mathrm{g}} \times PV \times \left(C_{\mathrm{sat}} \times \frac{^{14}A}{^{12}A} - \frac{C_{\mathrm{surf}} \times \frac{^{14}C}{^{12}C}}{\alpha_{\mathrm{DIC}\leftarrow\mathrm{g}}} \right) \tag{D.6}$$

where PV is the piston velocity in cm h^{-1} (Eq. (4.4)), C_{sat} is the saturation concentration of atmospheric CO$_2$ (in mol m^{-3}), C_{surf} is the surface aqueous CO$_2$ concentration (in mol m^{-3}), α_{k} is the constant kinetic fractionation factor, $\alpha_{\mathrm{aq}\leftarrow\mathrm{g}}$ is the temperature-dependent fractionation during gas dissolution (Eq. (3.6)), $\alpha_{\mathrm{DIC}\leftarrow\mathrm{g}}$ is the is the temperature-dependent fractionation between aqueous CO$_2$ and DIC (Eq. (3.7)), and $^{14}A/^{12}A$ and $^{14}C/^{12}C$ are the ^{14}C/^{12}C ratios of the atmosphere and DIC, respectively. For each processes, the isotopic enrichment factor (ε, Eq. (4.7)) for ^{14}C is twice that of ^{13}C.

The equation for calculating the change in biotic DI^{14}C/DI^{12}C due to air-sea gas exchange is:

$$\frac{d\left(\frac{^{14}C}{^{12}C}\right)}{dt} = \frac{^{12}C \times \frac{d^{14}C}{dt} -^{14}C \times \frac{d^{12}C}{dt}}{(^{12}C)^2} \tag{D.7}$$

$$\begin{aligned} \frac{d\left(\frac{^{14}C}{^{12}C}\right)}{dt} = {} & \frac{1}{^{12}C} \times \left[\alpha_{\mathrm{k}} \times \alpha_{\mathrm{aq}\leftarrow\mathrm{g}} \times PV \times \left(C_{\mathrm{sat}} \times \frac{^{14}A}{^{12}A} - \frac{C_{\mathrm{surf}} \times \frac{^{14}C}{^{12}C}}{\alpha_{\mathrm{DIC}\leftarrow\mathrm{g}}} \right) \right] \\ & - \frac{^{14}C}{\left(^{12}C\right)^2} \times \left[PV \times (C_{\mathrm{sat}} - C_{\mathrm{surf}}) \right] \end{aligned} \tag{D.8}$$

$$\begin{aligned} \frac{d\left(\frac{^{14}C}{^{12}C}\right)}{dt} = {} & \frac{1}{^{12}C} \times PV \times \left[\alpha_{\mathrm{k}} \times \alpha_{\mathrm{aq}\leftarrow\mathrm{g}} \times \left(C_{\mathrm{sat}} \times \frac{^{14}A}{^{12}A} - \frac{C_{\mathrm{surf}} - \frac{^{14}C}{^{12}C}}{\alpha_{\mathrm{DIC}\leftarrow\mathrm{g}}} \right) \right. \\ & \left. - \left(\frac{^{14}C}{^{12}C} \times [C_{\mathrm{sat}} - C_{\mathrm{surf}}] \right) \right] \end{aligned} \tag{D.9}$$

APPENDIX E

Additional figures and tables for Chapter 4

Table E.1: Number of pre-bomb Δ^{14}C data points in the compilation of Graven et al. (2012b) binned according to the vertical levels in FAMOUS.

Water depth (m)	Number of data points
0 to 10	67
10 to 20	2
20 to 30	0
30 to 40	0
40 to 50	2
50 to 80	2
80 to 120	0
120 to 170	1
170 to 250	4
250 to 375	8
375 to 550	3
550 to 830	9
830 to 1250	13
1250 to 1800	6
1800 to 2400	13
2400 to 3000	14
3000 to 3600	13
3600 to 4250	8
4250 to 4900	4
4900 to 5500	16
5500+*	7

* Not represented in the model, which has a maximum depth of approximately 5500 m.

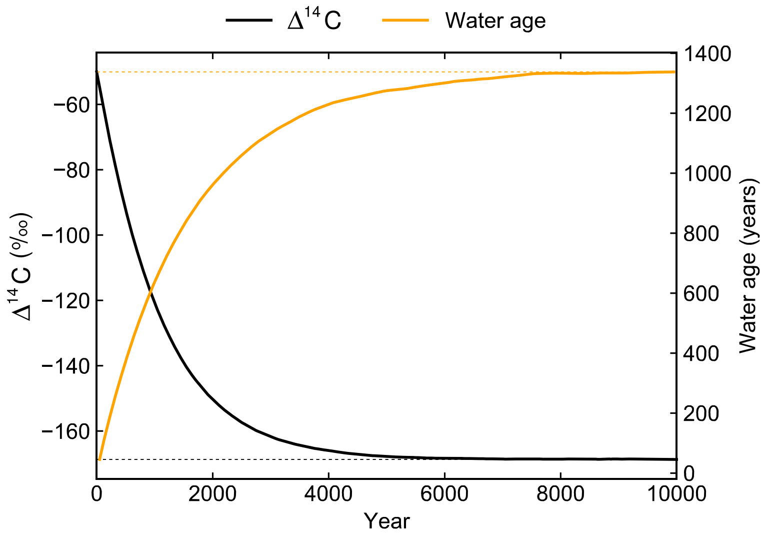

Figure E.1: Global volume-weighted Δ^{14}C (black) and water age (orange) integrals for the spin-up simulation. The solid lines show the transient values and the dashed lines show the values at equilibrium.

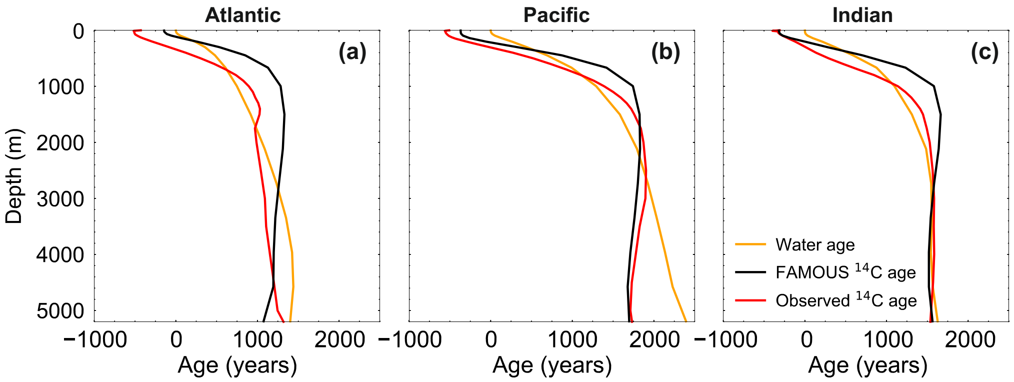

Figure E.2: Basin-averaged depth profiles of ^{14}C age and water age during the 1990s: (a) Atlantic Ocean, (b) Pacific Ocean, and (c) Indian Ocean. The simulated ^{14}C age (black) is compared to the simulated water age (orange) and the ^{14}C age in the gridded GLODAP data (Key et al., 2004, red).

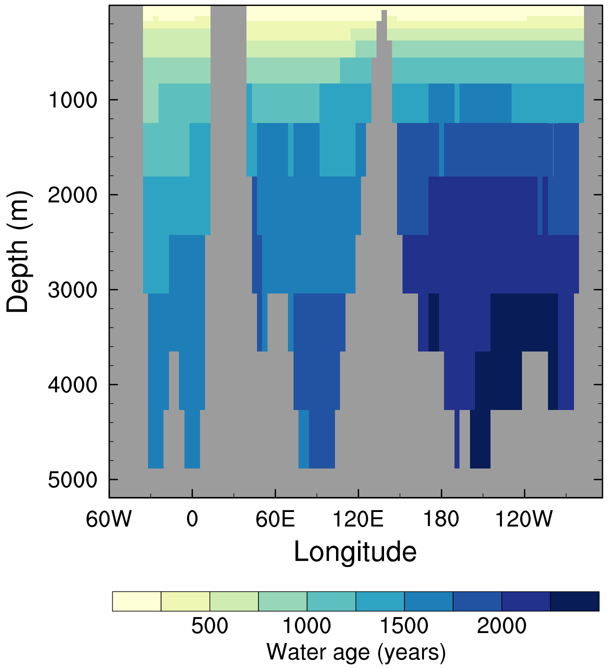

Figure E.3: Idealised water age transect at 10° S at the end of the spin-up simulation (years 9900 to 10,000).

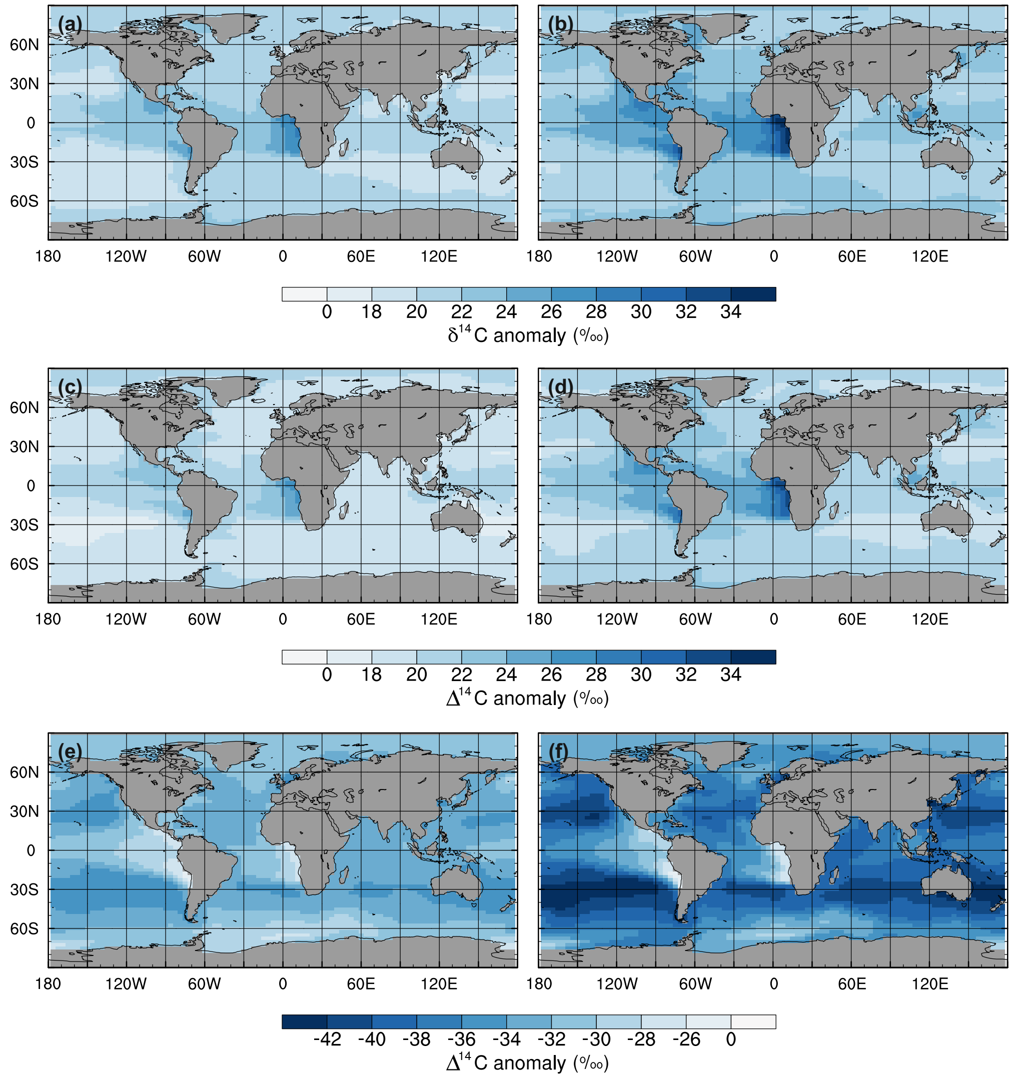

Figure E.4: Differences between the biotic and abiotic tracers in the surface ocean at the end of the spin-up simulation (years 9900 to 10,000, left) and during the 1990s (right): (a, b) uncorrected biotic δ^{14}C minus uncorrected abiotic δ^{14}C (as presented in Figure 4.12), (c, d) corrected biotic Δ^{14}C minus corrected abiotic Δ^{14}C, and (e, f) corrected biotic Δ^{14}C minus uncorrected abiotic δ^{14}C, which is equivalent to abiotic Δ^{14}C in other modelling studies (e.g. Toggweiler et al., 1989a; Jahn et al., 2015). Note that in (d), the isotopic fractionation correction (Eq. (4.8)) has been applied to the abiotic tracer (even though the abiotic tracer is not affected by isotopic fractionation effects) to place both tracers in the same reference frame (Δ^{14}C) as observational studies. Also, note that in (e) and (f), the Δ^{14}C anomalies are negative because (as outlined in Section 4.2.2.4) the isotopic fractionation correction that is applied to the biotic tracer (≈50 ‰) is larger than the uncorrected difference between the two tracers (≈20 ‰). In all six sub-plots, darker colours correspond to the largest absolute anomalies.

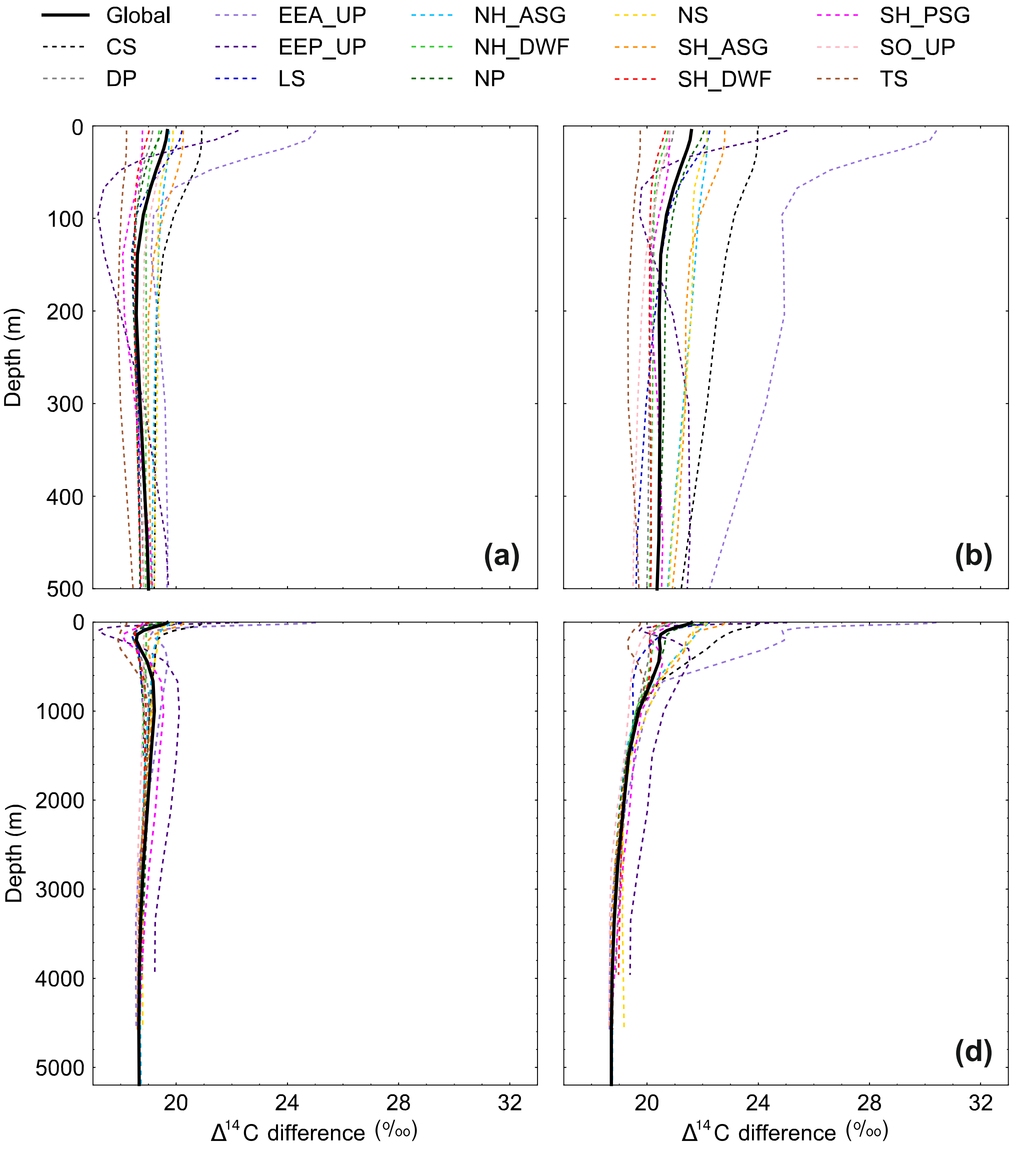

Figure E.5: Global (solid black) and regional (dotted) depth profiles of biotic minus abiotic Δ^{14}C: (a, c) the end of the spin-up simulation (years 9900 to 10,000) and (b, d) the 1990s; (a, b) the uppermost 500 m of the ocean and (c, d) the whole water column. The regions are outlined in Figure 4.7: Caribbean Sea (CS), Drake Passage (DP), eastern equatorial Atlantic upwelling zone (EEA_UP), eastern equatorial Pacific upwelling zone (EEP_UP), Labrador Sea (LS), Northern Hemisphere Atlantic sub-tropical gyre (NH_ASG), Northern Hemisphere deep water formation region (NH_DWF), North Pacific (NP), Nova Scotia (NS), Southern Hemisphere Atlantic sub-tropical gyre (SH_ASG), Southern Hemisphere deep water formation region (SH_DWF), Southern Hemisphere Pacific sub-tropical gyre (SH_PSG), Southern Ocean upwelling zone (SO_UP), and Tasman Sea (TS). Note that the abiotic tracer does not take isotopic fractionation effects into account but, in this figure, the correction has been applied to place both tracers in the same reference frame (Δ^{14}C) as observational studies.

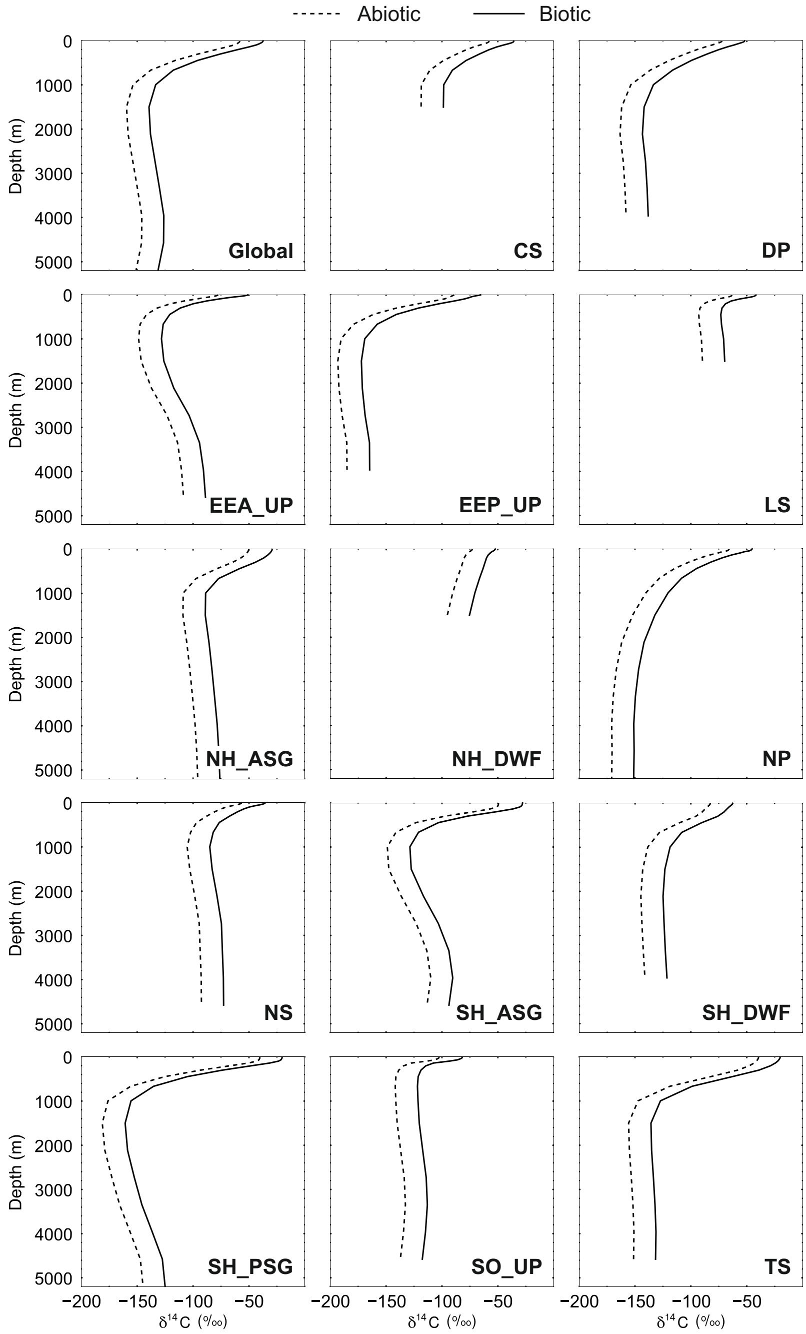

Figure E.6: Global and regional depth profiles of abiotic (dashed) and biotic (solid) δ^{14}C at the end of the spin-up simulation (years 9900 to 10,000). The regions are outlined in Figure 4.7: Caribbean Sea (CS), Drake Passage (DP), eastern equatorial Atlantic upwelling zone (EEA_UP), eastern equatorial Pacific upwelling zone (EEP_UP), Labrador Sea (LS), Northern Hemisphere Atlantic sub-tropical gyre (NH_ASG), Northern Hemisphere deep water formation region (NH_DWF), North Pacific (NP), Nova Scotia (NS), Southern Hemisphere Atlantic sub-tropical gyre (SH_ASG), Southern Hemisphere deep water formation region (SH_DWF), Southern Hemisphere Pacific sub-tropical gyre (SH_PSG), Southern Ocean upwelling zone (SO_UP), and Tasman Sea (TS).

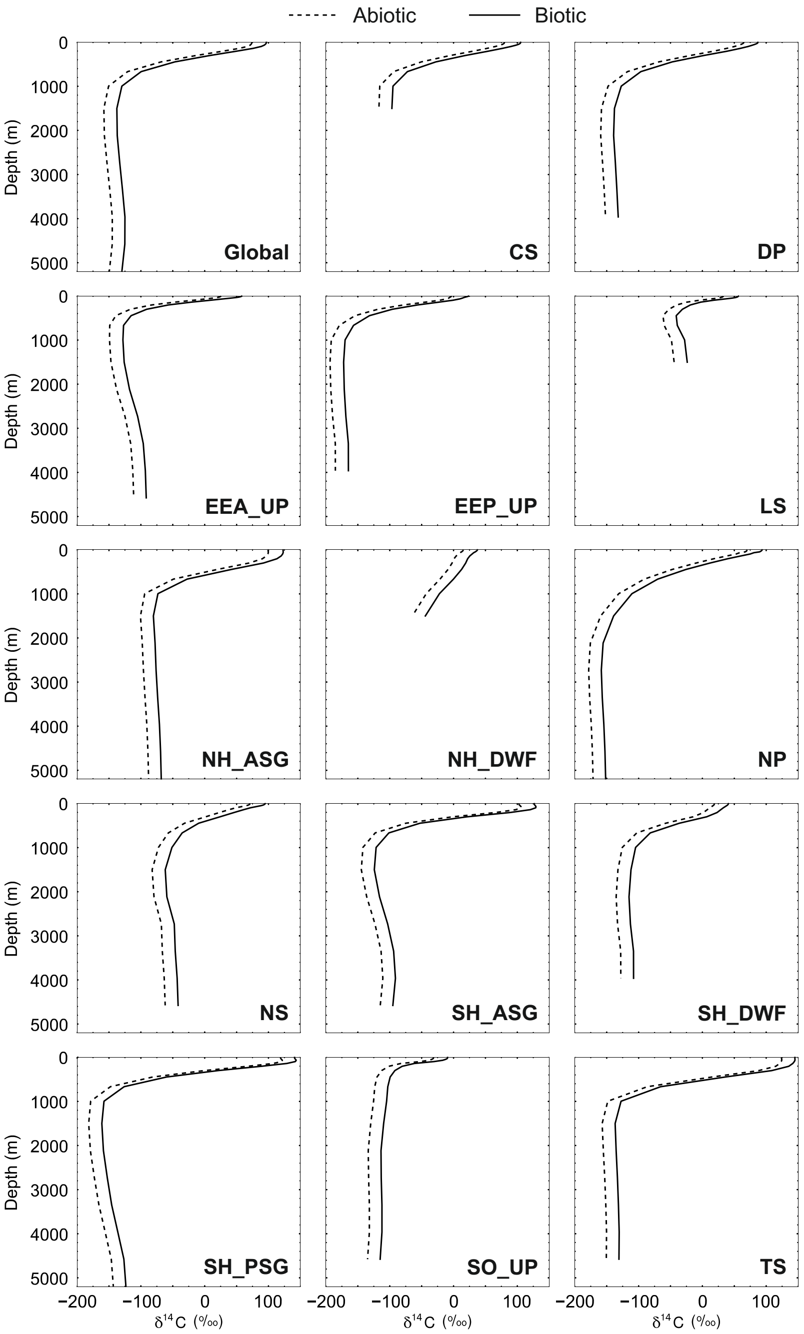

Figure E.7: As for Figure E.6, but for the 1990s.

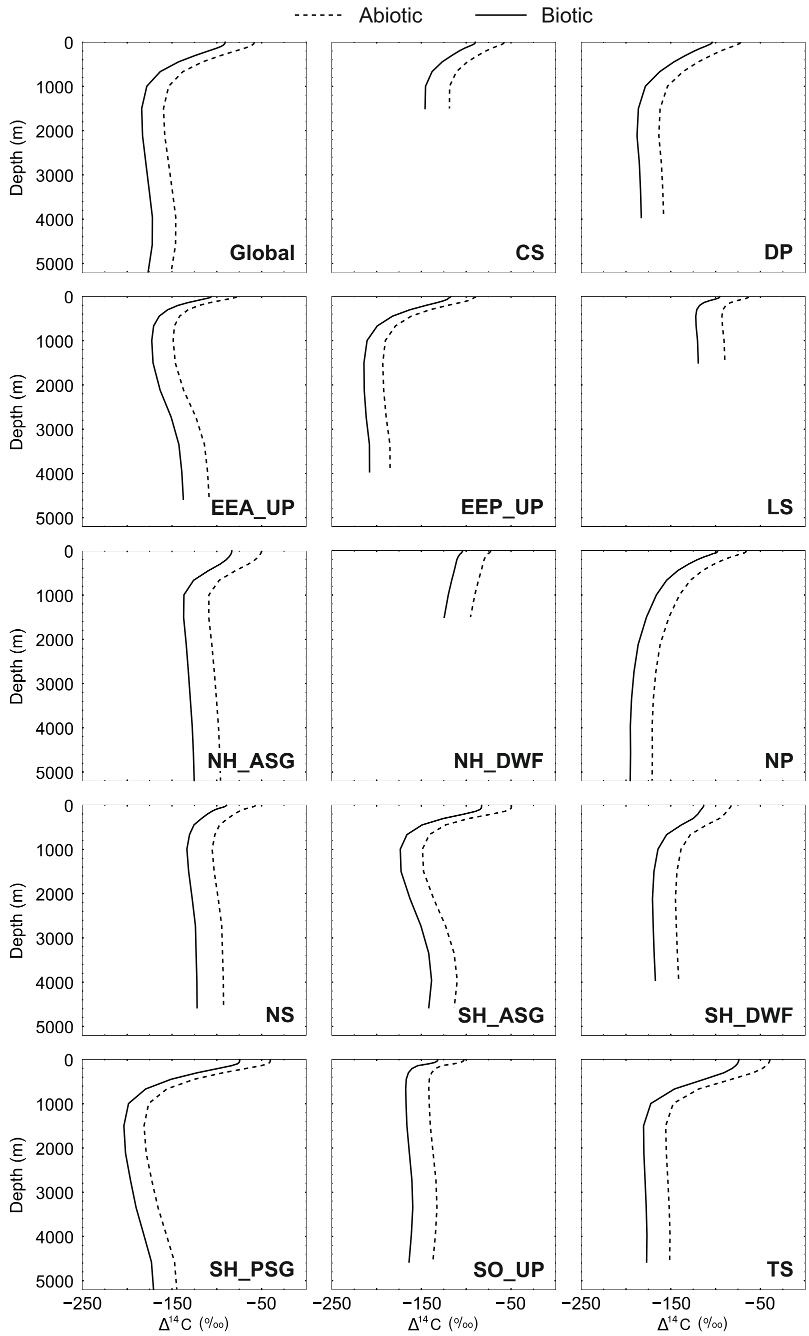

Figure E.8: As for Figure E.6, but for corrected biotic Δ^{14}C (Eq. (4.8)) and uncorrected abiotic δ^{14}C, which (as outlined in Section 4.2.2.4) is equivalent to abiotic Δ^{14}C in other modelling studies (e.g. Toggweiler et al., 1989a; Jahn et al., 2015).

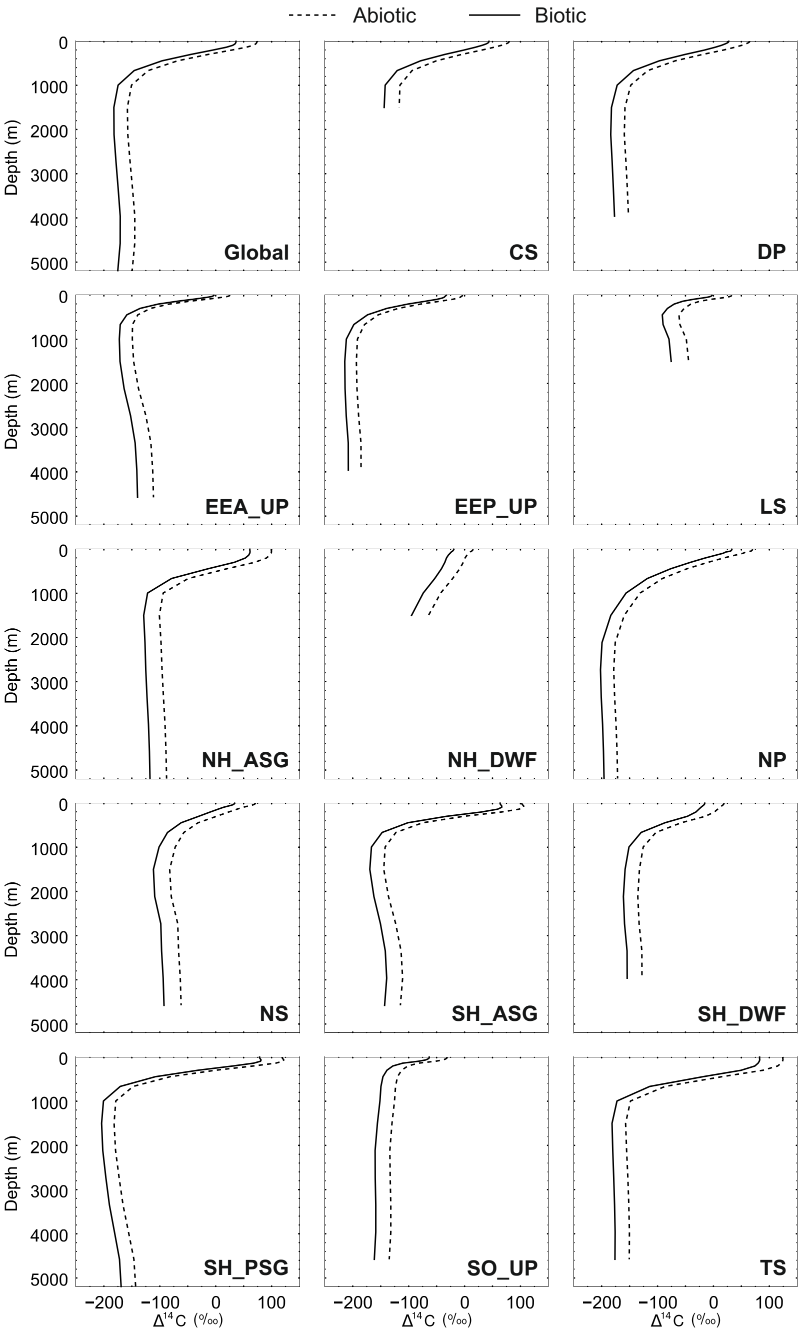

Figure E.9: As for Figure E.8, but for the 1990s.

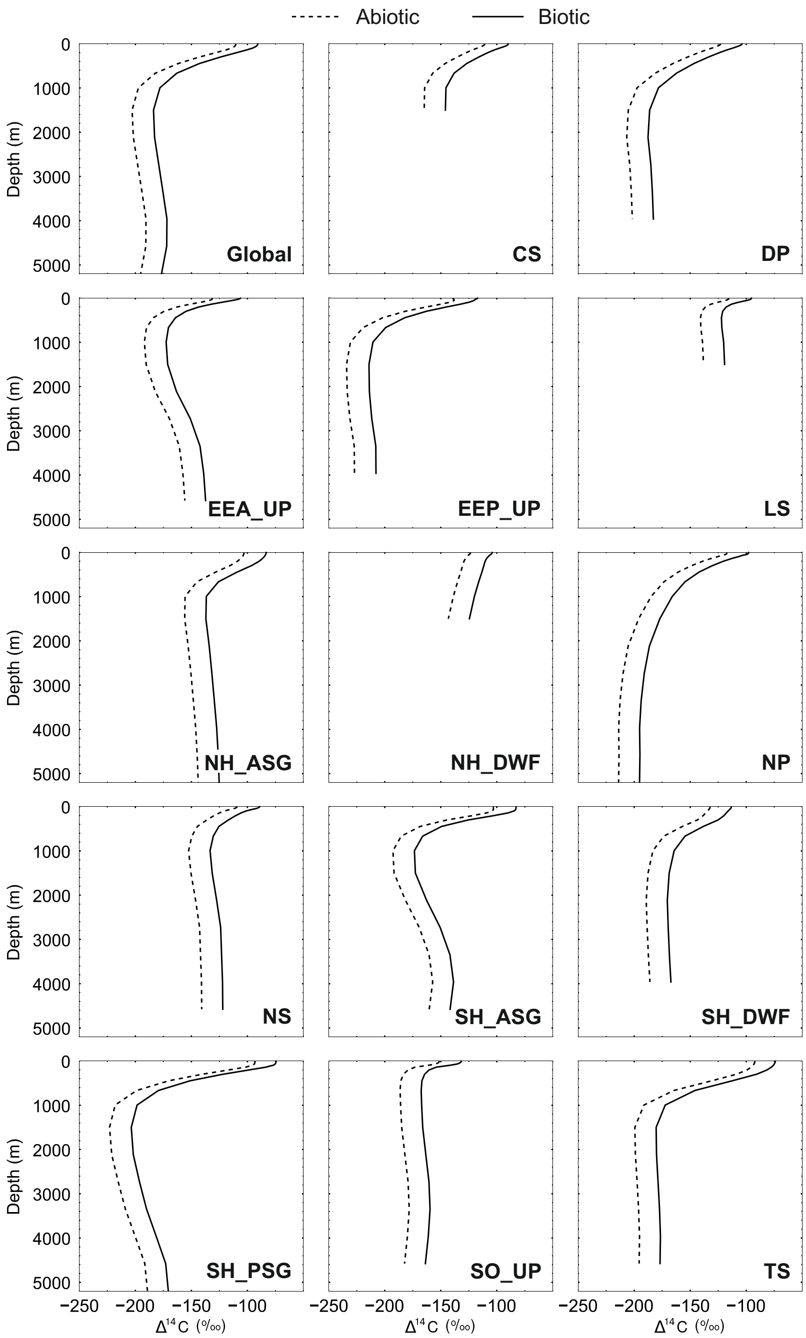

Figure E.10: As for Figure E.6, but for corrected biotic Δ^{14}C (Eq. (4.8)) and corrected abiotic Δ^{14}C. Note that the abiotic tracer does not take isotopic fractionation effects into account but, in this figure, the correction has been applied to place both tracers in the same reference frame (Δ^{14}C) as observational studies.

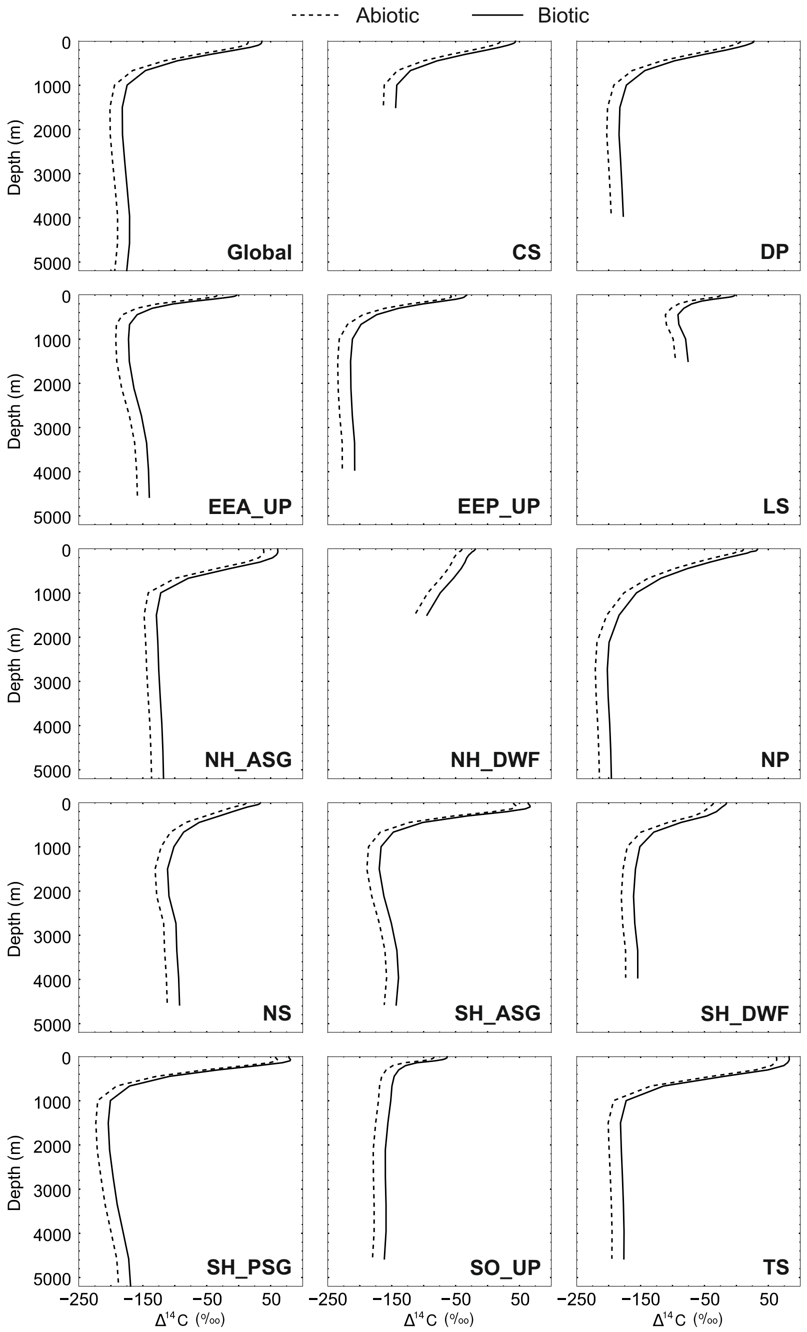

Figure E.11: As for Figure E.10, but for the 1990s.

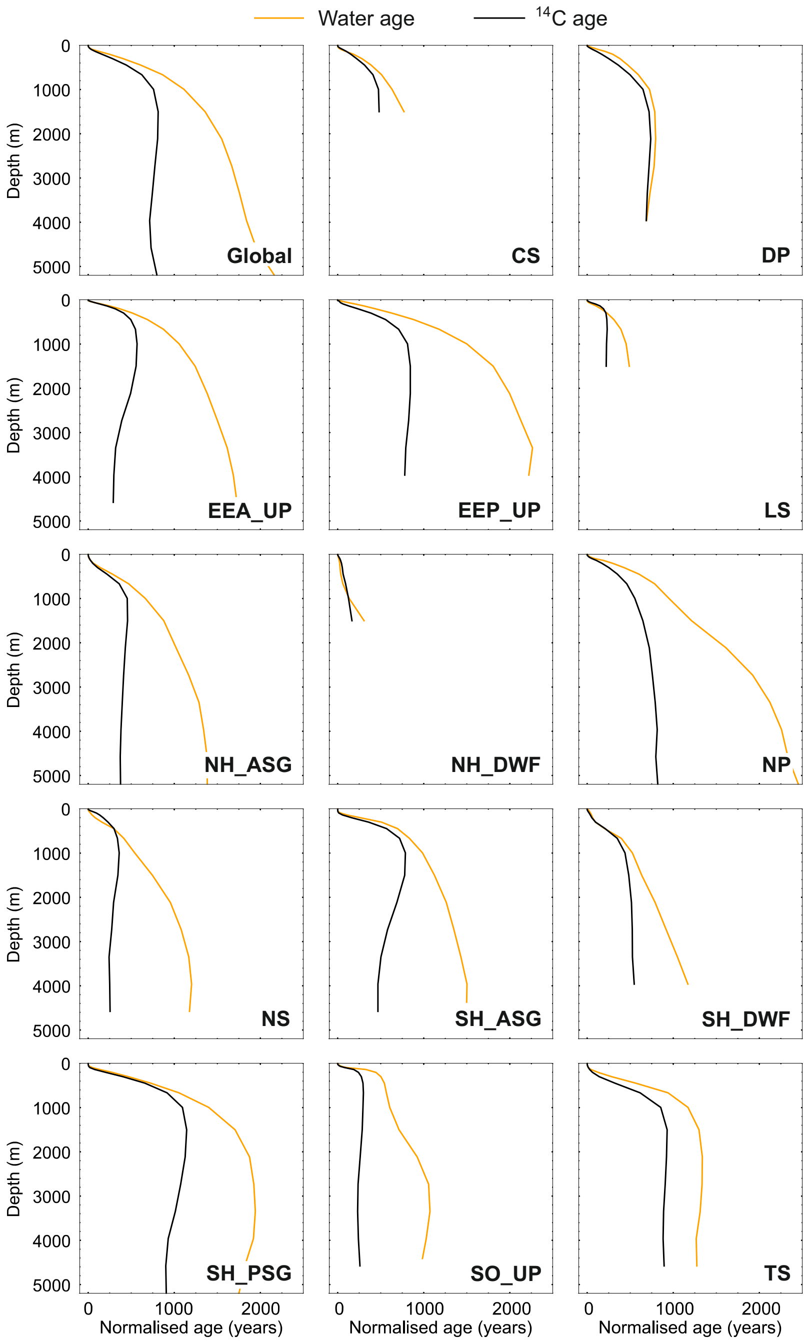

Figure E.12: Global and regional depth profiles of water age (orange) and ^{14}C age (black) at the end of the spin-up simulation (years 9900 to 10,000). The ^{14}C ages have been normalised relative to the surface ocean in each regions, so that both the ^{14}C age and the water age in the uppermost layer are 0 years. The regions are outlined in Figure 4.7: Caribbean Sea (CS), Drake Passage (DP), eastern equatorial Atlantic upwelling zone (EEA_UP), eastern equatorial Pacific upwelling zone (EEP_UP), Labrador Sea (LS), Northern Hemisphere Atlantic sub-tropical gyre (NH_ASG), Northern Hemisphere deep water formation region (NH_DWF), North Pacific (NP), Nova Scotia (NS), Southern Hemisphere Atlantic sub-tropical gyre (SH_ASG), Southern Hemisphere deep water formation region (SH_DWF), Southern Hemisphere Pacific sub-tropical gyre (SH_PSG), Southern Ocean upwelling zone (SO_UP), and Tasman Sea (TS).

APPENDIX F

Code availability

The main repository for the Met Office Unified Model (UM) version 4.5, as presented in this thesis, can be found at:

`http://cms.ncas.ac.uk/code_browsers/UM4.5/UMbrowser/index.html`

The UM configuration ("basis") files for the simulations described in this thesis (as outlined in Table F.1) can be accessed via the Providing Unified Model Access (PUMA) service:

`http://cms.ncas.ac.uk/wiki/PumaService`

Table F.1: Overview of the simulations described in this thesis, as denoted by their unique five letter Met Office UM identifiers and the notation used within this manuscript.

Identifier	**Simulation**	**Duration**
XMDVT	SFLUX spin-up	0 to 5000 years
XNVUA	SFLUX spin-up	5000 to 10,000 years
XMDVU	VFLUX spin-up	0 to 5000 years
XNVUB	VFLUX spin-up	5000 to 10,000 years
XNBQA	FM1 spin-up	0 to 10,000 years
XOAVB	*std* spin-up	0 to 10,000 years
XOAVI	*std* transient	1765 to 2000 CE
XOGNC	*std* control	1765 to 2000 CE
XOAVD	*ki-fract-only* spin-up	0 to 10,000 years
XOAVE	*no-bio-fract* spin-up	0 to 10,000 years
XOAVF	*no-asgx-fract* spin-up	0 to 10,000 years
XOAVK	*L95* spin-up	0 to 10,000 years
XOAVU	*L95* transient	1765 to 2000 CE
XOAVL	*L97* spin-up	0 to 10,000 years
XOAVW	*L97* transient	1765 to 2000 CE

The code for neutralising the unforced salinity drift in FAMOUS-MOSES2.2, as presented in Chapter 2, is available online:

`https://link.springer.com/article/10.1007\%2Fs00382-018-4243-y\#SupplementaryMaterial`

The code, post-processing scripts, and pre-stash files for implementing carbon isotopes and water age in the ocean component of the UM4.5, as presented in Chapters 3 and 4, are available via the Research Data Leeds Repository:

`https://doi.org/10.5518/621`